UNCLASSIFIED

AD NUMBER

AD876698

NEW LIMITATION CHANGE

TO

Approved for public release, distribution unlimited

FROM

Distribution authorized to U.S. Gov't. agencies only; Administrative/Operational Use; JUL 1970. Other requests shall be referred to Army Mobility Equipment Research and Development Center, Fort Belvoir, VA.

AUTHORITY

USAMERDC ltr, 10 Jan 1979

THIS PAGE IS UNCLASSIFIED

AD

AD876698

DDC FILE COPY

HIGH-SPEED CRYOGENIC ALTERNATOR DEVELOPMENT

VOLUME 1

PHASE I FINAL REPORT

by

D. B. Colyer and W. R. Oney

July 1970

Prepared for

DEPARTMENT OF THE ARMY
MOBILITY EQUIPMENT RESEARCH AND DEVELOPMENT CENTER
FORT BELVOIR, VIRGINIA 22060

Prepared under

Contract No. DAAK02-68-C-0320

DDC
RECEIVED
NOV 19 1970
B

Prepared by

Mechanical Engineering Laboratory
Research and Development Center
General Electric Company
Schenectady, New York 12305

Each transmittal of this document outside the agencies of the U. S. Government must have prior approval of the Chief, Electrotechnology Laboratory, U. S. Army Mobility Equipment Research and Development Center, Fort Belvoir, Virginia.

195

PROPERTY OF U. S. GOVERNMENT

S-70-1070

AD

HIGH-SPEED CRYOGENIC ALTERNATOR DEVELOPMENT
VOLUME 1

PHASE I FINAL REPORT

by

D. B. Colyer and W. R. Oney

July 1970

Prepared for

DEPARTMENT OF THE ARMY
MOBILITY EQUIPMENT RESEARCH AND DEVELOPMENT CENTER
FORT BELVOIR, VIRGINIA 22060

Prepared under

Contract No. DAAK02-68-C-0320
Project 6.27.20.01.1, 1T662705 A012

Details of illustrations in this document may be better studied on microfiche

Prepared by

Mechanical Engineering Laboratory
Research and Development Center
General Electric Company
Schenectady, New York 12305

PROPERTY OF U. S. GOVERNMENT

S-70-1070

NOTICES

Destroy this report when no longer needed. Do not return it to the originator.

The findings in this report are not to be construed as an official Department of the Army position, unless so designated by other authorized documents.

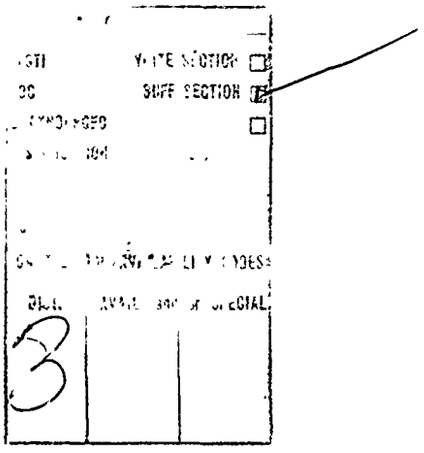

SUMMARY

This final technical report, "High-speed Cryogenic Alternator Development," provides the design methods leading to an experimental high-speed electric power generator operating at cryogenic temperatures.

The goals of this report are to define the basic problems and then establish a sound engineering basis for the design of high-speed high-efficiency compact alternators to operate at cryogenic temperatures.

The engineering basis used was to make an alternator electromagnetic design suitable for an existing General Electric expansion turbine design, all operating on gas-lubricated bearings at speeds up to 180,000 rpm, with an electrical power output of 100 watts.

A permanent magnet alternator was designed, manufactured, and tested at both room temperature and cryogenic temperatures. The alternator was tested with leading, unity, and lagging power factors.

At cryogenic temperatures, in the order of 100°K (-280°F), tests were conducted and the turboalternator was evaluated at speeds up to 220,000 rpm, and with electrical power output values up to 109 watts. An alternator electromagnetic efficiency as high as 98 percent was measured.

This Phase I final report covers the development effort of the high-speed cryogenic alternator.

An extension to this same contract has been made to incorporate the high-speed turbine-driven alternator in a laboratory 80°K cryogenic refrigerator. A Phase II final report covering the cryogenic refrigerator will be delivered after completion of the refrigerator test and evaluation.

Volume 2 of this Phase I report is a continuation of Volume 1.

FOREWORD

This Phase I final technical report was prepared by the Research and Development Center of the General Electric Company in Schenectady, New York, under U.S. Army Mobility Equipment Research and Development Center Contract No. DAAK02-68-C-0320, "High-speed Cryogenic Alternator Development," Project 6.27.20.01.1, IT662705 A012. This contract is administered by the General Electric Research and Development Center for the Power Technology Division, U.S. Army Mobility Equipment Research and Development Center. Mr. A.L. Jokl is the project engineer.

The engineering development work reported covers the period from March 1968 to September 1969. It includes a summary of the alternator electromagnetic design and manufacture and the test and evaluation of the high-speed turbine-driven cryogenic alternator.

This work is under the direction of Mr. D.B. Colyer, project manager. Mr. W.R. Oney is the principal investigator for the alternator electromagnetic design and development.

TABLE OF CONTENTS

Section		Page
	Volume 1	
	SUMMARY	ii
	FOREWORD	iii
1	INTRODUCTION	1
	1.1 Project Objectives and Goals	1
	1.2 Background	1
2	TURBOALTERNATOR ANALYSIS AND DESIGN . . .	5
	2.1 Electromagnetic Analysis	7
	2.1.1 Alternator Analysis	7
	2.2 Electromagnetic Design	32
	2.2.1 Alternator Design	32
	2.2.2 Computed Alternator Performance .	33
	2.3 Mechanical Analysis and Design	36
	2.3.1 Design Approach	37
	2.3.2 Aerodynamic Design	37
	2.3.3 Materials Considerations	43
	2.3.4 Gas Bearings	45
	2.3.5 Thermal Analysis	49
	2.3.6 Thermal Insulation	53
3	ALTERNATOR MANUFACTURE	59
	3.1 Stator Core Assembly	59
	3.2 Wound Stator Core Assembly	59
	3.3 Design Specifications Revised	63
	3.4 Permanent Magnet Field	64
4	TURBOALTERNATOR TESTS, EVALUATION, AND ANALYSIS	65
	4.1 Turboalternator Tests	65
	4.1.1 Test Plan	65
	4.1.2 Test Arrangement	67
	4.1.3 Alternator Stator Tests Before Assembly	70
	4.1.4 Turboalternator Performance Tests .	70
	4.2 Turboalternator Test Evaluation	113
	4.2.1 Room-temperature No-load Operation .	113

TABLE OF CONTENTS (Cont'd)

Section		Page
	4.2.2 Room-temperature Load Operation	119
	4.2.3 Cryogenic-temperature Load Operation	123
	4.3 Turboalternator Contamination Investigators	138
	4.3.1 Turboalternator Tests	140
	4.3.2 Particle Counter Investigation	158
	4.3.3 Wire Mesh Filters	162
	4.3.4 Alternate Filters	167

Volume 2

	SUMMARY	ii
	FOREWORD	iii
5	REFRIGERATOR CYCLE STUDIES	175
	5.1 Liquid-helium-temperature Refrigerators	179
	5.2 20°K Refrigerators	192
	5.3 Liquid-nitrogen-temperature Refrigerator	192
	5.4 100°K Refrigerators	203
6	CONCLUSIONS AND RECOMMENDATIONS	207
	6.1 Conclusions	207
	6.2 Recommendations	207
7	LITERATURE CITED	211
	Appendix I -- TURBOALTERNATOR PERFORMANCE DATA REDUCTION PROGRAM	
	Appendix II -- TURBOALTERNATOR PERFORMANCE TEST DATA REDUCTION RESULTS	

LIST OF ILLUSTRATIONS

Figure		Page
	Volume 1	
1.2-1	Cryogenic Refrigerator Program Development Steps	3
1.2-2	Refrigerator Cycles, Schematic Diagrams	4
2-1	Full-sized Turboalternator Model	6
2-2	Turboalternator Isometric Cutaway	6
2-3	Turboalternator Parts	7
2.1.1.1-1	Demagnetization Curve	9
2.1.1.1-2	Permeance Paths	10
2.1.1.2-1	Line-to-line Waveshape, 3000 Hz, 50 Volts per Centimeter	11
2.1.1.5-1	Line-to-line Waveshape, Approximately 1800 Hz, 10 Volts per Centimeter, One Coil Reversed in Each Phase	13
2.1.1.5-2	Fundamental Component with Reversed Coil in Each Phase	15
2.1.1.5-3	Fundamental Component of Voltage	16
2.1.1.5-4	Fifth Harmonic Voltage, Coil Reversed	17
2.1.1.5-5	Seventh Harmonic Voltage, Coil Reversed	17
2.1.1.14.3-1	Resistance of Molybdenum Permalloy Specimen	23
2.1.1.14.4-1	Molybdenum Permalloy Characteristics at 300°K	25
2.1.1.14.4-2	Molybdenum Permalloy Characteristics at 77°K	26
2.1.1.14.4-3	Hysteresis Loops at 300°K and 400 Hz, Horizontal Calibration 10 Milliamperes per Div	27
2.1.1.14.4-4	Hysteresis Loops at 77°K and 400 Hz, Horizontal Calibration 20 Milliamperes per Div	27
2.1.1.14.4-5	Hysteresis Loops at 300°K and 3000 Hz, Horizontal Calibration 50 Milliamperes per Div	28
2.1.1.14.4-6	Hysteresis Loops at 77°K and 3000 Hz, Horizontal Calibration 50 Milliamperes per Div	28
2.1.1.14.4-7	Outer Loops of Figures 2.1.1.14.4-5 and 2.1.1.14.4-6 Superimposed	29

LIST OF ILLUSTRATIONS (Cont'd)

Figure		Page
2.1.1.14.4-8	Hysteresis Loop at Room Temperature and 5000 Hz, Horizontal Calibration 50 Milliamperes per Div	29
2.1.1.16-1	Calculated Constant Current (0.565 Amperes) Characteristics	31
2.1.1.17-1	Vector Diagram (Scaled for Illustrative Purposes)	32
2.2.1-1	Alternator Final Design	33
2.3.1-1	Turboalternator Assembly	38
2.3.1-2	Open-cycle Turboalternator Test Arrangement	39
2.3.2-1	Turboalternator Performance Test Results (Helium Gas Inlet Temperature 157°R (Typical); Pressure Ratio 1.3)	42
2.3.2-2	Estimated Turbine Performance (Helium Gas Inlet Temperature 80°K; Exhaust Pressure 29.92 in HgA; Speed 180,000 rpm)	44
2.3.3-1	Thermal Contraction of Common Metals with Temperature	46
2.3.5-1	Design Program Parasitic Losses, Helium Gas at 138.8°R	50
2.3.5-2	Design Program Parasitic Losses, Helium Gas at 540°R	51
2.3.5-3	Thermal Circuit	54
2.3.5-4	Thermal Circuit Schematic Diagram	55
3.2-1	Turboalternator Stator	60
3.2-2	One-hundred-percent Pitch -- Six Coils	61
3.2-3	Five-sixth Pitch -- Six Coils	62
3.2-4	Five-sixth Pitch -- Twelve Coil	63
4.1.2-1	Turboalternator Test Station	68
4.1.2-2	Turboalternator Cryogenic Test Arrangement	69
4.1.3-1	Line-to-line Waveforms at 2180 Rpm (Vertical Scale 0.5 Volts per Centimeter)	71

LIST OF ILLUSTRATIONS (Cont'd)

Figure		Page
4.1.4.2-1	Orange Lead, Voltage Waveform across 2985-ohm Resistor, 2.95 Watts, Room Temperature, 180,000 Rpm, Oscilloscope Sensitivity 50 Volts per Centimeter	74
4.1.4.2-2	White Lead, Voltage Waveform across 2985-ohm Resistor, 2.95 Watts, Room Temperature, 180,000 Rpm, Oscilloscope Sensitivity 50 Volts per Centimeter	74
4.1.4.2-3	Black Lead, Voltage Waveform across 2985-ohm Resistor, 2.95 Watts, Room Temperature, 180,000 Rpm, Oscilloscope Sensitivity 50 Volts per Centimeter	75
4.1.4.2-4	Thrust Proximity Probe Signal, 2.95-watt Load, Room Temperature, 180,000 Rpm, Oscilloscope Sensitivity 400 Microinches per Centimeter . . .	75
4.1.4.2-5	Signals from Shaft Orbit Proximity Probes, 2.95-watt Load, Room Temperature, 180,000 Rpm, Oscilloscope Sensitivity 400 Microinches per Centimeter (Lower Signal Turbine End)	76
4.1.4.2-6	Orange Lead, Voltage Waveform across 109.2-ohm Resistor, 66.9 Watts, Room Temperature, 180,020 Rpm, Oscilloscope Sensitivity 50 Volts per Centimeter	76
4.1.4.2-7	White Lead, Voltage Waveform across 109.2-ohm Resistor, 66.9 Watts, Room Temperature, 180,120 Rpm, Oscilloscope Sinsitivity 50 Volts per Centimeter	77
4.1.4.2-8	Black Lead, Voltage Waveform across 2985-ohm Resistor, 66.9 Watts, Room Temperature, 180,120 Rpm, Oscilloscope Sensitivity 50 Volts per Centimeter	77
4.1.4.2-9	Thrust Proximity Probe Signal at 66.9-watt Load, Room Remperature, 180,120 Rpm, Oscilloscope Sensitivity 50 Volts per Centimeter	78
4.1.4.2-10	Signals from Shaft Orbit Proximity Probes, 66.9 Watts, Room Temperature, 180,120 Rpm, Oscilloscope Sensitivity 400 Microinches per Centimeter (Lower Signal Turbine End)	78

Figure		Page
4.1.4.3-1	Orange Lead, Voltage Waveform across 165.5-ohm Resistor, 29.3 Watts, Room Temperature, 140,100 Rpm, Oscilloscope Sensitivity 20 Volts per Centimeter	79
4.1.4.3-2	White Lead, Voltage Waveform across 165.5-ohm Resistor, 29.3 Watts, Room Temperature, 140,100 Rpm, Oscilloscope Sensitivity 20 Volts per Centimeter	79
4.1.4.3-3	Black Lead, Voltage Waveform across 165.5-ohm Resistor, 29.3 Watts, Room Temperature, 140,100 Rpm, Oscilloscope Sensitivity 20 Volts per Centimeter	80
4.1.4.3-4	Thrust Proximity Probe Signal, 29.3-watt Load Room Temperature, 140,100 Rpm, Oscilloscope Sensitivity 400 Microinches per Centimeter	80
4.1.4.3-5	Signals from Shaft Orbit Proximity Probes, 29.3-watt Load, Room Temperature, 140,100 Rpm, Oscilloscope Sensitivity 400 Microinches per Centimeter (Lower Signal Turbine End)	81
4.1.4.3-6	Orange Lead, Voltage Waveform across 109.2-ohm Resistor, 96.2 Watts, Room Temperature, 220,080 Rpm, Oscilloscope Sensitivity 50 Volts per Centimeter	81
4.1.4.3-7	White Lead, Voltage Waveform across 109.2-ohm Resistor, 96.2 Watts, Room Temperature, 220,080 Rpm, Oscilloscope Sensitivity 50 Volts per Centimeter	82
4.1.4.3-8	Black Lead, Voltage Waveform across 109.2-ohm Resistor, 96.2 Watts, Room Temperature, 220,080 Rpm, Oscilloscope Sensitivity 50 Volts per Centimeter	82
4.1.4.3-9	Thrust Proximity Probe Signal at 96.2-watt Load, Room Temperature, 200,080 Rpm, Oscilloscope Sensitivity 400 Microinches per Centimeter	83
4.1.4.3-10	Signals from Shaft Orbit Proximity Probes, 96.2-watt Load, Room Temperature, 220,080 Rpm, Oscilloscope Sensitivity 400 Microinches per Centimeter (Lower Signal Turbine End)	83

LIST OF ILLUSTRATIONS (Cont'd)

Figure		Page
4.1.4.4-1	White-to-orange Leads, Voltage Waveform Line to Line, No Load, Cryogenic Temperature, 180,000 Rpm, Oscilloscope Sensitivity 50 Volts per Centimeter	85
4.1.4.4-2	Black-to-orange Leads, Voltage Waveform Line to Line, No Load, Cryogenic Temperature, 180,000 Rpm, Oscilloscope Sensitivity 50 Volts per Centimeter	85
4.1.4.4-3	Black-to-white Leads, Voltage Waveform Line to Line, No Load, Cryogenic Temperature, 180,000 Rpm, Oscilloscope Sensitivity 50 Volts per Centimeter (TR 103)	86
4.1.4.4-4	Thrust Proximity Probe Signal, No Load, Cryogenic Temperature, 180,000 Rpm, Oscilloscope Sensitivity 400 Microinches per Centimeter . . .	86
4.1.4.4-5	Signals from Shaft Orbit Proximity Probes, No Load, Cryogenic Temperature, 180,000 Rpm, Oscilloscope Sensitivity 400 Microinches per Centimeter (Signal on the Right Turbine End)	87
4.1.4.6-1	Leading Power Factor Circuit	92
4.1.4.6-2	Lagging Power Factor Circuit	92
4.1.4.6-3	Alternator Load Bank	93
4.1.4.6-4	Voltage across 123.5-ohm Resistor with Leading Power Factor at 65.1 Watts, 183,060 Rpm, Oscilloscope Sensitivity 50 Volts per Centimeter . . .	94
4.1.4.6-5	Thrust Proximity Probe Signal with Leading Power Factor at 65.1 Watts, 183,060 Rpm, Oscilloscope Sensitivity 400 Microinches per Centimeter . . .	94
4.1.4.6-6	Signals from Shaft Orbit Proximity Probes with Leading Power Factor at 65.1 Watts, 183,060 Rpm, Oscilloscope Sensitivity 400 Microinches per Centimeter (Smallest Orbit Turbine End) . . .	95
4.1.4.6-7	Voltage across 109.2-ohm Resistor with Lagging Power Factor at 50.9 Watts, 185,580 Rpm, Oscilloscope Sensitivity 50 Volts per Centimeter . . .	95

Figure		Page
4.1.4.6-8	Thrust Proximity Probe Signal with 66.3-watt Pure Resistive Load, 179,640 Rpm, Oscilloscope Sensitivity 400 Microinches per Centimeter . . .	96
4.1.4.6-9	Signals from Shaft Orbit Proximity Probes with 66.3-watt Pure Resistive Load, 179,640 RPM, Oscilloscope Sensitivity 400 Microinches per Centimeter (Smallest Orbit Turbine End)	96
4.1.4.6-10	Thrust Proximity Probe Signal with 43.4-watt Pure Resistive Load, 141,480 Rpm, Oscilloscope Sensitivity 400 Microinches per Centimeter	98
4.1.4.6-11	Signals from Shaft Orbit Proximity Probes with 43.4 Watts Pure Resistive Load, 141,480 Rpm, Oscilloscope Sensitivity 400 Microinches per Centimeter (Smallest Orbit Turbine End)	98
4.1.4.6-12	Thrust Proximity Probe Signal with 96.2 Watts Pure Resistive Load, 220,680 Rpm, Oscilloscope Sensitivity 400 Microinches per Centimeter	99
4.1.4.6-13	Signals from Shaft Orbit Proximity Probes with 96.2 Watts Pure Resistive Load, 220,680 Rpm, Oscilloscope Sensitivity 400 Microinches per Centimeter (Smallest Orbit Turbine End)	99
4.1.4.7-1	Line-to-line Voltage, No Load, 215,520 Rpm, Room Temperature, Oscilloscope Sensitivity 50 Volts per Centimeter	102
4.1.4.7-2	Thrust Proximity Probe Signal at No Load, 215,520 Rpm, Room Temperature, Oscilloscope Sensitivity 400 Microinches per Centimeter	102
4.1.4.7-3	Signals from Shaft Orbit Proximity Probes, No Load, 215,520 Rpm, Room Temperature, Oscilloscope Sensitivity 400 Microinches per Centimeter (Smallest Orbit Turbine End)	104
4.1.4.8-1	Voltage Waveform across 123.5-ohm Resistor, 52.64 Watts, Room Temperature, 180,540 Rpm, Oscilloscope Sensitivity 50 Volts per Centimeter . .	104
4.1.4.8-2	Thrust Proximity Probe Signal, 52.64-watt Load Room Temperature, 180,540 Rpm, Oscilloscope Sensitivity 400 Microinches per Centimeter . . .	105

Figure		Page
4.1.4.8-3	Signals from Shaft Orbit Proximity Probes, 52.64-watt Load, Room Temperature, 180,540 Rpm, Oscilloscope Sensitivity 400 Microinches per Centimeter (Smallest Orbit Turbine End) . . .	105
4.1.4.9-1	Line-to-line Voltage, No Load, 91,920 Rpm, Cryogenic Temperature, Oscilloscope Sensitivity 50 Volts per Centimeter	107
4.1.4.9-2	Thrust Proximity Probe Signal, No Load, 91,920 Rpm, Cryogenic Temperature, Oscilloscope Sensitivity 400 Microinches per Centimeter	107
4.1.4.9-3	Signals from Shaft Orbit Proximity Probes, No Load, 91,920 Rpm, Cryogenic Temperature, Oscilloscope Sensitivity 400 Microinches per Centimeter (Smallest Orbit Turbine End)	108
4.1.4.9-4	Line-to-line Voltage, No Load, 241,800 Rpm, Cryogenic Temperature, Oscilloscope Sensitivity 50 Volts per Centimeter	108
4.1.4.9-5	Thrust Proximity Probe Signal at No Load, 241,800 Rpm, Cryogenic Temperature, Oscilloscope Sensitivity 400 Microinches per Centimeter	109
4.1.4.9-6	Signals from Shaft Orbit Proximity Probes, No Load, 241,800 Rpm, Cryogenic Temperature, Oscilloscope Sensitivity 400 Microinches per Centimeter (Smallest Orbit Turbine End)	109
4.1.4.10-1	Voltage Waveform across 123.5-ohm Resistor, 60.8 Watts, Cryogenic Temperature, 179,340 Rpm, Oscilloscope Sensitivity 50 Volts per Centimeter	111
4.1.4.10-2	Thrust Proximity Probe Signal, 60.8-watt Load, Cryogenic Temperature, 179,340 Rpm, Oscilloscope Sensitivity 400 Microinches per Centimeter	111
4.1.4.10-3	Signals from Shaft Orbit Proximity Probes at 60.8-watt Load, Cryogenic Temperature, 179,340 Rpm, Oscilloscope Sensitivity 400 Microinches per Centimeter (Smallest Orbit Turbine End)	112
4.2.1-1	Room-temperature No-load Performance, Shaft Magnetized, Run 100	115

Figure		Page
4.2.1-2	Room-temperature, No-load Performance, Shaft Not Magnetized, Run 104	116
4.2.1-3	Room-temperature, No-load Performance, Shaft Magnetized, Run 106	117
4.2.1-4	Room-temperature No-load Performance, Composite of Three Runs	118
4.2.1-5	Room-temperature No-load Performance, Turbine Performance Parameters	120
4.2.1-6	Room-temperature No-load Performance, Turbine Versus Speed	121
4.2.2-1	Turboalternator Room-temperature Performance, Power Output Versus Speed	122
4.2.2-2	Turboalternator Room-temperature Performance, Voltage Versus Current	124
4.2.2-3	Turboalternator Room-temperature Performance, Voltage per Cycle Versus Current	125
4.2.2-4	Turboalternator Room-temperature Performance, Efficiency and Bypass Flow Versus Velocity Ratio	126
4.2.2-5	Turboalternator Room-temperature Performance, Temperature Drop Efficiency Versus Velocity Ratio	127
4.2.2-6	Turboalternator Room-temperature Performance, Flow Factor Versus Pressure Ratio	128
4.2.3-1	Turboalternator Cryogenic-temperature Performance, Power Output Versus Speed	130
4.2.3-2	Turboalternator Cryogenic-temperature Performance, Voltage per Cycle Versus Current	131
4.2.3-3	Turboalternator Cryogenic-temperature Performance, Efficiency and Bypass Flow Versus Velocity Ratio	134
4.2.3-4	Turboalternator Cryogenic-temperature Performance, Flow Factor Versus Pressure Ratio	136
4.2.3-5	Turboalternator Cryogenic-temperature Performance, Electromagnetic and Overall Efficiency Versus Power Output	137

Figure		Page
4.3.1-1	Shaft Speed Trace (Sweep -- 0.1 Millisecond per Centimeter; Amplitude -- 0.02 Volt per Centimeter)	144
4.3.1-2	Journal Orbit Traces (Left -- Thrust End; Right -- Turbine End), 400 Microinches per Centimeter	144
4.3.1-3	Journal Pad Trace (Sweep -- 0.1 Millisecond per Centimeter; Amplitude -- 0.1 Volt per Centimeter)	145
4.3.1-4	Thrust Bearing Trace (Sweep -- 2.0 Milliseconds per Centimeter; Amplitude -- 0.2 Volt per Centimeter)	145
4.3.1-5	Shaft Speed Trace (Sweep -- 2.0 Milliseconds per Centimeter; Amplitude -- 0.02 Volt per Centimeter)	146
4.3.1-6	Journal Orbit Traces (Top -- Thrust End; Bottom -- Turbine End), 0.2 Volt per Centimeter	146
4.3.1-7	Journal Pad Trace (Sweep -- 2.0 Milliseconds per Centimeter; Amplitude -- 0.1 Volt per Centimeter)	147
4.3.1-8	Thrust Bearing Trace (Sweep -- 2.0 Milliseconds per Centimeter; Amplitude -- 0.2 Volt per Centimeter)	147
4.3.1-9	Shaft Speed Trace (Sweep -- 0.1 Millisecond per Centimeter; Amplitude -- 0.02 Volt per Centimeter)	149
4.3.1-10	Journal Orbit Traces (Top -- Thrust End; Bottom -- Turbine End), 0.2 Volt per Centimeter	149
4.3.1-11	Journal Pad Trace (Sweep -- 2.0 Milliseconds per Centimeter; Amplitude -- 0.1 Volt per Centimeter)	150
4.3.1-12	Thrust Bearing Trace (Sweep -- 2.0 Milliseconds per Centimeter; Amplitude -- 0.2 Volt per Centimeter)	150
4.3.1-13	Turboalternator Gas System Cleanliness Test Arrangement	152
4.3.2-1	Equipment for Injection of 1.171- and 2.68-micron Particles into Gas Stream	161
4.3.2-2	Method of Introducing Large Particles into Gas Stream	163

Figure		Page
4.3.3-1	Filter Pressure Drop Test Results	166
4.3.4.1-1	Microlite Filter Assembly	169
4.3.4.1-2	Microlite Filter Gas Test Assembly	169
4.3.4.2-1	Nuclepore Membrane Filter, Preliminary Design .	172
4.3.4.2-2	Nuclepore Membrane Filter Pressure Drop Characteristic (Five-micron Hole Size, Helium Gas)	173

Volume 2

5-1	Refrigerator Cycle Diagram	176
5-2	Temperature Entropy Diagram, Liquid-helium Temperature Refrigerator	177
.1-1	Cryogenic Refrigerator Heat Leak	180
.1-2	Liquid-helium Cryogenic Refrigerator System Schematic Diagram	182
.1-3	Effect of Turboalternator Efficiency (4.4°K 2-watt Refrigerator)	184
.1-4	Effect of Turbine Inlet Temperatures (4.4°K 2-watt Refrigerator)	185
.1-5	Effect of a Number of Compressor Stages (4.4°K 2-watt Refrigerator)	186
.1-6	Effect of Heat Exchanger Effectiveness (4.4°K 2-watt Refrigerator)	188
-1	Turboalternator Instrumentation Schematic . . .	216
-2	Turboalternator Performance Data Sheets (Sheet 1).	217
-2	Turboalternator Performance Data Sheets (Sheet 2).	218
-3	Results of Data Reduction for Largest Power Output Obtained at Cryogenic Temperature	219

LIST OF TABLES

Tables		Page
	Volume 1	
2.1.1.15-1	Comparison of Calculated and Tested Characteristics	30
2.2.1-1	Calculated Alternator Features and Performance	34
2.2.2-1	Output Power for Alternator D-90702 (Calculated)	35
2.2.2-2	Alternator Characteristics at 180,000 Rpm and 77°K	35
2.2.2-3	Alternator Characteristics at 180,000 Rpm and 77°K Calculated to 2 Amperes	36
2.2.2-4	Calculated Performance at 180,000 Rpm and 300°K	36
2.3.1-1	Typical Test Data on General Electric Turboalternator	40
2.3.2-1	Aerodynamic Design Geometry	41
2.3.2-2	Estimated Turboalternator Performance for Cryogenic Alternator Tests	43
2.3.3-1	Material Properties	47
2.3.4-1	Comparison of Journal Bearing Types	48
2.3.5-1	Distribution of All Heat Loads at Rated Alternator Condition	52
2.3.5-2	Boundary Conditions	56
2.3.5-3	Alternator Stator Temperature Rise	56
4-1	Turboalternator Performance Tests	65
4.1.4-1	Turboalternator Test Summary	72
4.1.4.4-1	Turboalternator Erratic Operation at Cryogenic Temperatures Possible Causes and Corrections	87
4.1.4.6-1	Turboalternator Load Performance Test Results at Cryogenic Temperatures	89
4.1.4.6-2	Voltmeter Corrections and Power Output for Run 105	90
4.1.4.7-1	Turboalternator Performance Test Results, No-load Conditions at Room Temperature	101

Table		Page
4.1.4.8-1	Turboalternator Performance Test Results, Load Conditions at Room Temperature	103
4.1.4.9-1	Turboalternator Performance Test Results, No-load Conditions at Cryogenic Temperatures . . .	106
4.1.4.10-1	Turboalternator Performance Test Results, Load Conditions at Cryogenic Temperatures	110
4.2-1	No-load Performance Curve Summary	114
4.2-2	Load Performance Curve Summary	114
4.2.3-1	Characteristics of Alternator Design D-90702 with Rotor 11B	132
4.2.3-2	Characteristics of Alternator for Point 4 Load . .	133
4.2.3-3	Comparison of Design and Test Alternator Temperatures	139
4.3-1	Commercial Helium Bottled Gas Specifications .	140
4.3.1-1	Turboalternator Development Tests Summary . .	143
4.3.1-2	Particle Study Report	156
4.3.2-1	1.171-micron Particle Test	160
4.3.2-2	2.68-micron Particle Test	162
4.3.3-1	Comparison of Pressure-drop Tests	165
4.3.3-2	Filter Pressure Drops Relative to Refrigerator Needs	168

Volume 2

5-1	Summary of Refrigeration Cycle Studies	178
5.1-1	Two-watt Liquid-helium-temperature Cryogenic Refrigerator	181
5.1-2	Effect of Heat Exchanger Pressure Drop	187
5.1-3	4.4°K Cryogenic Refrigeration Cycle Study Results .	189
5.1-4	3.6°K Cryogenic Refrigerator Cycle Study Results .	191
5.2-1	20°K Cryogenic Refrigerator Cycle Study Results .	193
5.2-2	20°K Cryogenic Refrigerator Cycle Study Results .	194

LIST OF TABLES (Cont'd)

Table		Page
5.2-3	20°K Cryogenic Refrigerator Cycle Study Results .	195
5.3-1	One-watt 77°K Cryogenic Refrigerator	197
5.3-2	77°K Cryogenic Refrigerators	198
5.3-3	77°K Cryogenic Refrigerators	199
5.3-4	77°K Cryogenic Refrigerators	200
5.3-5	77°K Cryogenic Refrigerators	201
5.3-6	77°K Cryogenic Refrigerators	202
5.4-1	100°K Cryogenic Refrigerators	203
5.4-2	100°K Cryogenic Refrigerators	204
5.4-3	100°K Cryogenic Refrigerators	205
6.1-1	Comparison of Cryogenic-temperature Performance Results (Extreme Conditions)	208
I-1	Turboalternator Test and Computer Program Nomenclature	221

Section 1

INTRODUCTION

1.1 PROJECT OBJECTIVES AND GOALS

The objective of this project was to provide the design methods leading to an experimental high-speed electric power generator operating at cryogenic temperatures.

The goals were to define the basic problems and then establish a sound engineering basis for the design of high-speed high-efficiency compact alternators to operate at cryogenic temperatures. The engineering design basis was then to be used to make an alternator design suitable for operation with a General Electric expansion turbine, operating on gas-lubricated bearings at speeds up to 180,000 rpm. The turbine-driven alternator was then to be built and tested at both room and cryogenic temperatures. Suitable instrumentation was to be incorporated so that a comprehensive performance evaluation could be made.

Originally, the means of obtaining these goals was to build a turbine-driven alternator operating on roller element bearings. These goals were changed to incorporate long-life potential gas-lubricated bearings.

This Phase I final report covers alternator analysis, design, and test evaluation of the high-speed cryogenic turbine-driven alternator operating on gas-lubricated bearings.

After the turboalternator development program was well underway, the project objectives and goals were extended to incorporate the cryogenic turboalternator into a complete cryogenic refrigeration system. This part of the program is underway and will be included in a Phase II final report after refrigerator development has been completed.

1.2 BACKGROUND

Progress has been made in the development of superconducting magnets, superconducting electrical machinery, infrared sensors, superconducting computer logic and memories, and various extremely sensitive electronic devices that are dependent upon cooling at cryogenic temperatures. Applications of these devices require long-life cryogenic refrigerators that are compact and lightweight. A critical component in a cryogenic refrigerator is the expansion turbine that should be highly reliable and should operate at reasonable efficiency.

This work was directed toward the research analysis and design of compact high-efficiency turbine-driven cryogenic alternators. Initial design and

development of miniature alternators had been sponsored by a U. S. Air Force contract (Ref. 1) and the General Electric Company internal funds (Refs. 2 through 5) for use as load devices for expansion turbines as components of cryogenic refrigeration systems.

A typical cryogenic refrigerator uses helium gas compressed at room temperature and delivered to a cold section. This gas is cooled, by counterflow heat exchangers and expansion turbines, down to the required refrigeration temperature. With two turbines and five heat exchangers, the refrigeration temperature reached can be that of liquid helium, 4.2°K (Refs. 6 and 7). The role of the two turbines, operating typically at 75°K and 14°K, provide local refrigeration to the heat exchangers, which in turn provide refrigeration to the refrigerant gas that provides the 4.2°K temperature for the device to be refrigerated.

The principal function of the turbine is to extract energy from the working fluid gas at low temperature and to deliver this energy with minimum loss to ambient temperature. The most efficient means of making this energy transfer is a high efficient alternator. Thus, initial turboalternator analysis indicated that a high-speed permanent magnet alternator was a good choice, and a turbine-driven alternator was built and operated both at room temperatures and at cryogenic temperatures around 80°K (-320°F) (Refs. 3 and 5).

The type of turboalternator discussed in this report is well suited to satisfying the needs of a miniature refrigerator operating at 4.4°K with a 1- to 2-watt refrigeration capacity. A series of program development steps to meet this goal is shown in Figure 1.2-1.

Previous U. S. Air Force and General Electric programs have provided a background in the development of high-speed compressors for miniature refrigerators (Refs. 1, 6, and 8). An advanced permanent-magnet motor-driven high-speed helium compressor is currently being developed under U.S. Army Mobility Equipment Research and Development Center Contract No. DAAK-02-69-C-0171 (Ref. 9).

Also, an advanced high-effectiveness cryogenic heat exchanger development program has been sponsored by the General Electric Company (Refs. 10 through 14). Based on this program, a set of five of these exchangers has been designed, tested, and delivered to the U.S. Air Force (Ref. 15).

The turboalternator discussed in this report will be joined with the high-speed regenerative compressor and one cryogenic heat exchanger to provide an 80°K refrigerator. More components of similar design can be added later to obtain 1 watt of refrigeration at 4.4°K. A schematic showing the components for these two long-life refrigerators is shown in Figure 1.2-2.

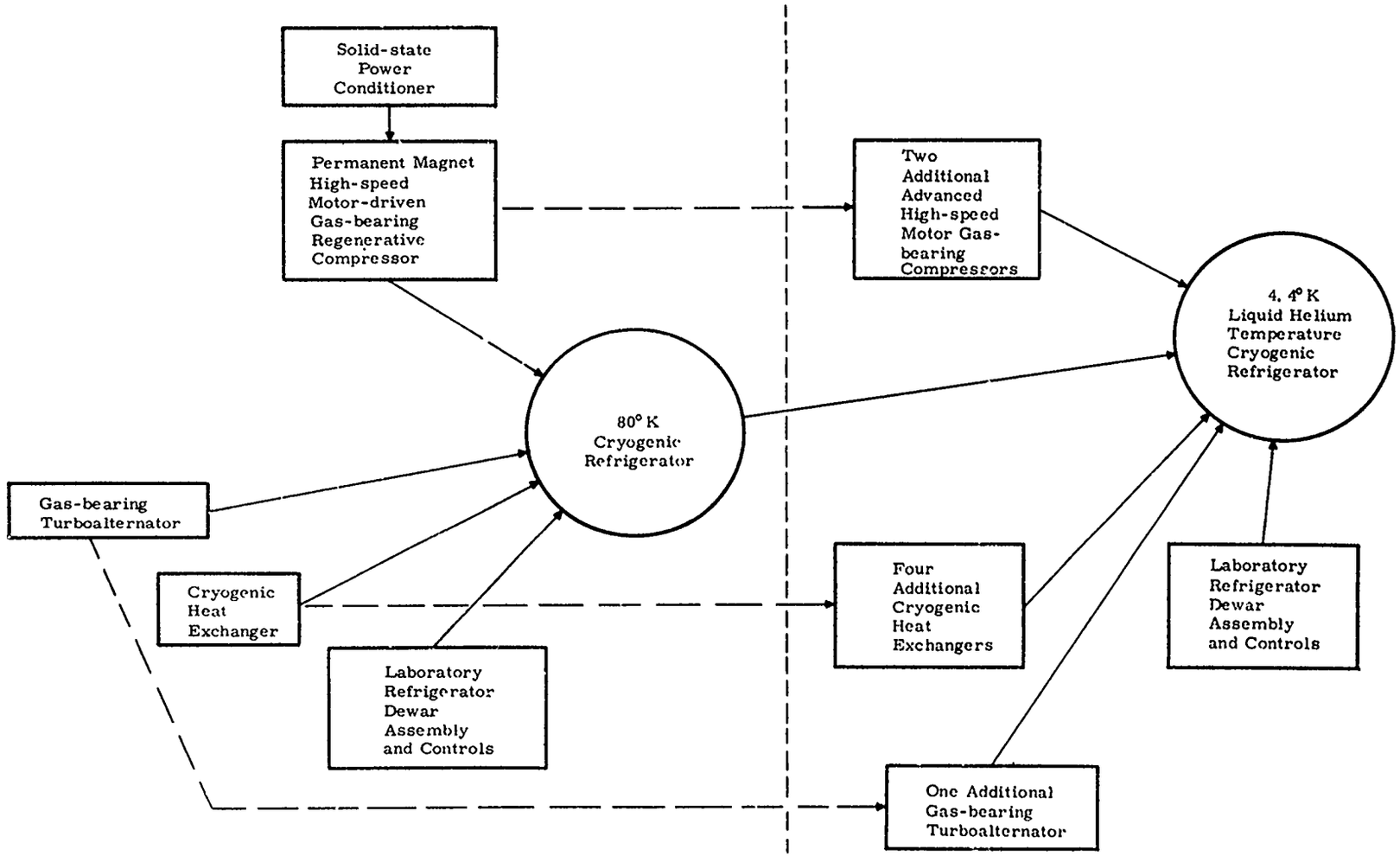

Figure 1.2-1. Cryogenic Refrigerator Program Development Steps

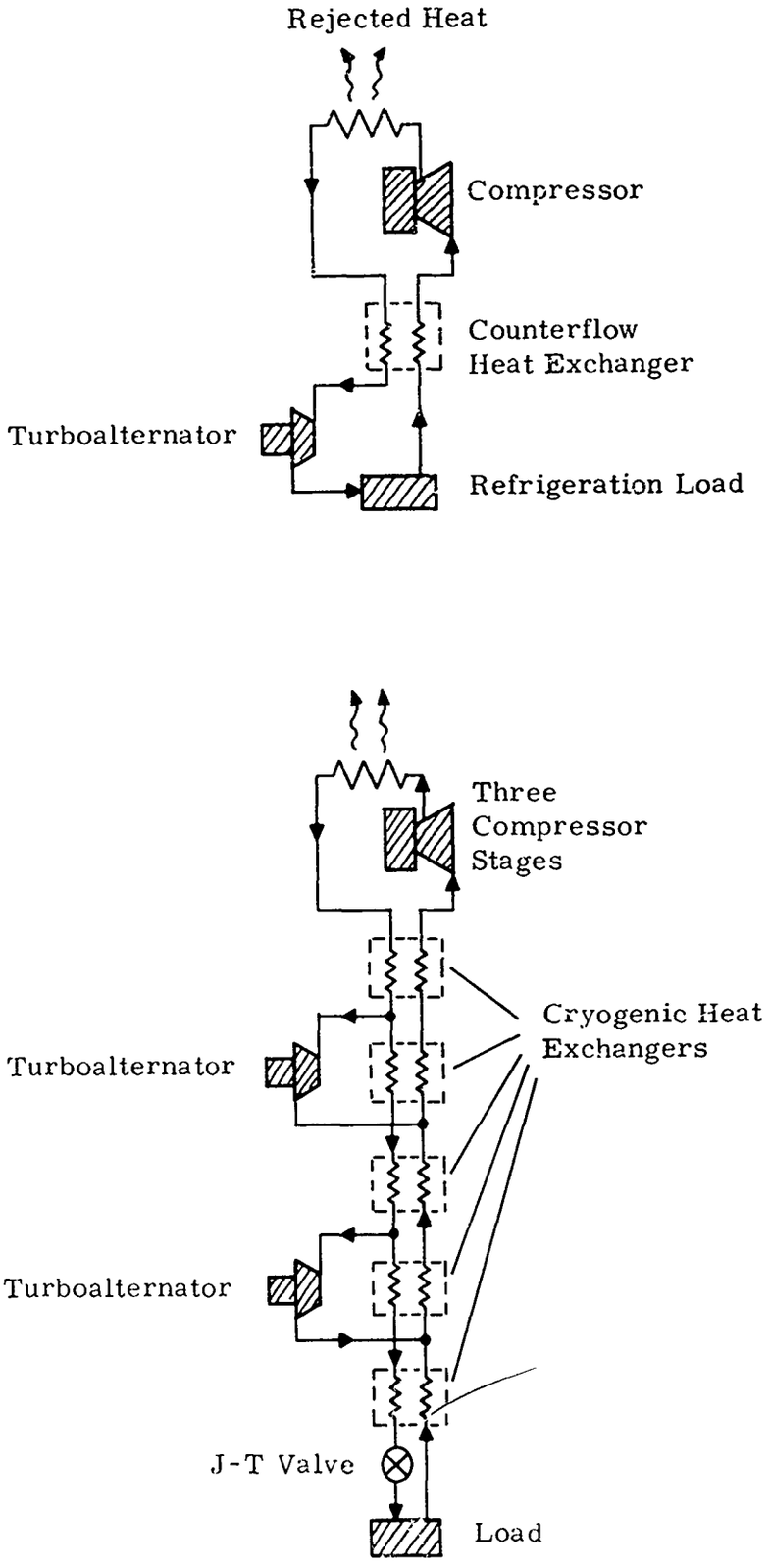

Figure 1.2-2. Refrigerator Cycles, Schematic Diagrams

Section 2

TURBOALTERNATOR ANALYSIS AND DESIGN

The following paragraphs describe the analysis and design steps taken to obtain a 100-watt cryogenic turboalternator.

The General Electric turboalternator was designed to incorporate elements which could readily be developed to provide suitable performance and which would be adaptable to eventual quantity production. A full-size model of the assembled miniature turboalternator is shown in Figure 2-1. The turbine is on the left, and the alternator stator can be seen, in the middle of the assembly, through the transparent plastic.

Figure 2-2 shows an isometric cutaway drawing of the turboalternator. The unit is mounted on gas-lubricated journal bearings. Three hardened pads at each journal bearing support the 1/4-inch-diameter shaft with an operating gas film thickness of about 300 microinches. These journal bearings are of the self-acting tilting-pad type. They were incorporated to ensure stable operation throughout the operating range and at any attitude.

The impulse wheel, which has a 0.625-inch diameter, is radial. The radial flow path lends itself to close blade-tip axial clearances, which minimize leakage. Wheels and nozzles have been produced from aluminum and from titanium by each of three methods: direct milling by tracing from an enlarged pattern, electrical discharge machining, and diffusion bonding of photoetched laminations.

Two inward-pumping spiral-grooved thrust bearings position the shaft axially. Like the journal bearings, the thrust bearings are gas lubricated, typically using a 500-microinch film thickness. Thrust bearing surfaces have been grooved both by photoetching and by electrical discharge machining.

The entire bearing system is self-aligning because the thrust bearings are gimbal mounted and the tilting-pad journal bearings are self-aligning. Satisfactory operation of the complete bearing system is independent of the accuracy with which adjacent parts are manufactured.

The turbine energy is absorbed by the permanent magnet alternator. This compact alternator is the most practical device for extracting energy at cryogenic temperatures when that energy will be expended at ambient temperatures. The two-pole magnet operates within the stator and is wound 3-phase within low-loss iron laminations. These laminations have been made by conventional die punching and by photoetching, a method which eliminates crimped edges. The alternator rotor consists of a high field-strength platinum-cobalt magnet. The rotor is constructed by brazing the magnet to shaft ends. The ground magnet surface has the same diameter as the shaft.

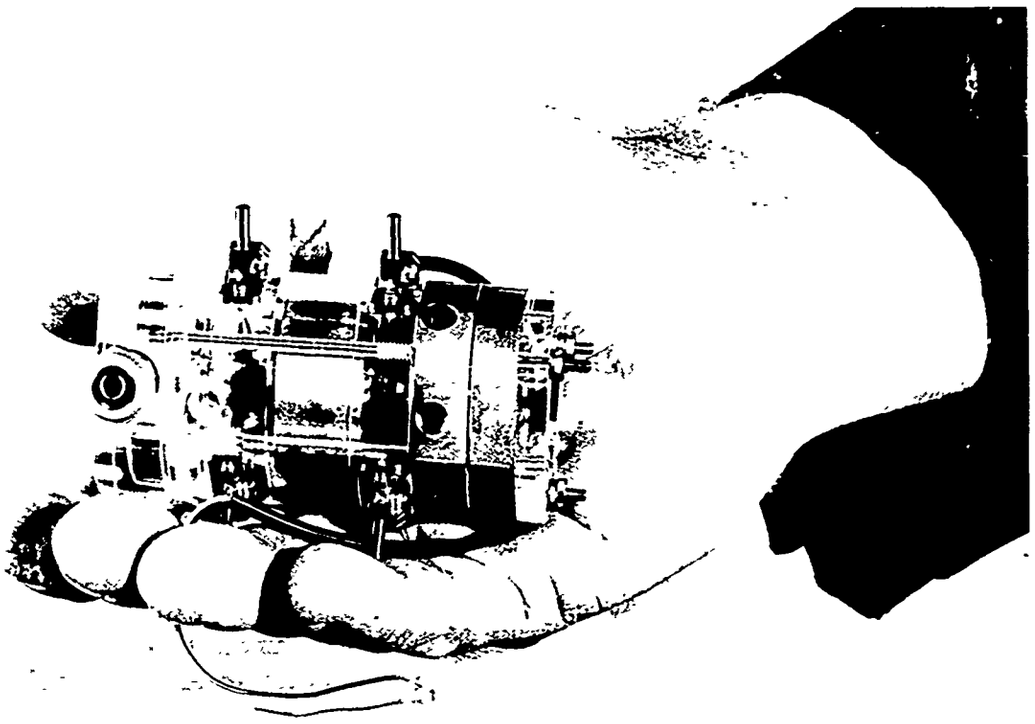

Figure 2-1. Full-sized Turboalternator Model

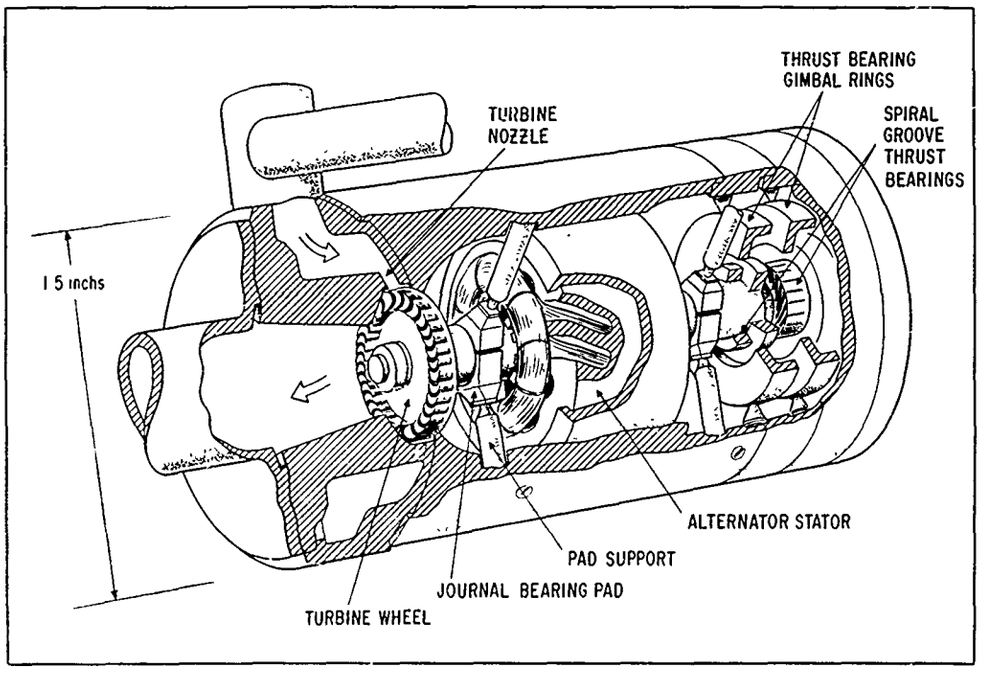

Figure 2-2. Turboalternator Isometric Cutaway

Some turboalternator parts are shown in Figure 2-3. The rotor magnet can be seen in the center of the shaft. The wheel in the foreground was made by electrical discharge machining of low oxygen content titanium. A titanium wheel lamination and one stator lamination are shown; both were photoetched. On the right is one of the two gimbal-mounted spiral-grooved thrust bearings. Three journal bearing tilting pads are shown. Two are finished, with pivot stems inserted, and the third is shown as a casting before machining. The proximity probe shown was used in a special miniaturized design which provided a linear capacitance characteristic over a range of 2/1000 inch. A set of six of these were used to monitor rotor and pad motions.

For the turboalternator developed under this program, the basic design was the same as described above, except for the electromagnetic design.

The General Electric Company alternator was used for establishing the basis for the electromagnetic analysis. Then, using this analysis as a design basis, the contract electromagnetic design was made.

2.1 ELECTROMAGNETIC ANALYSIS

2.1.1 Alternator Analysis

An alternator consisting of a platinum cobalt magnet field and a mechanically compatible stator was available from a General-Electric-sponsored

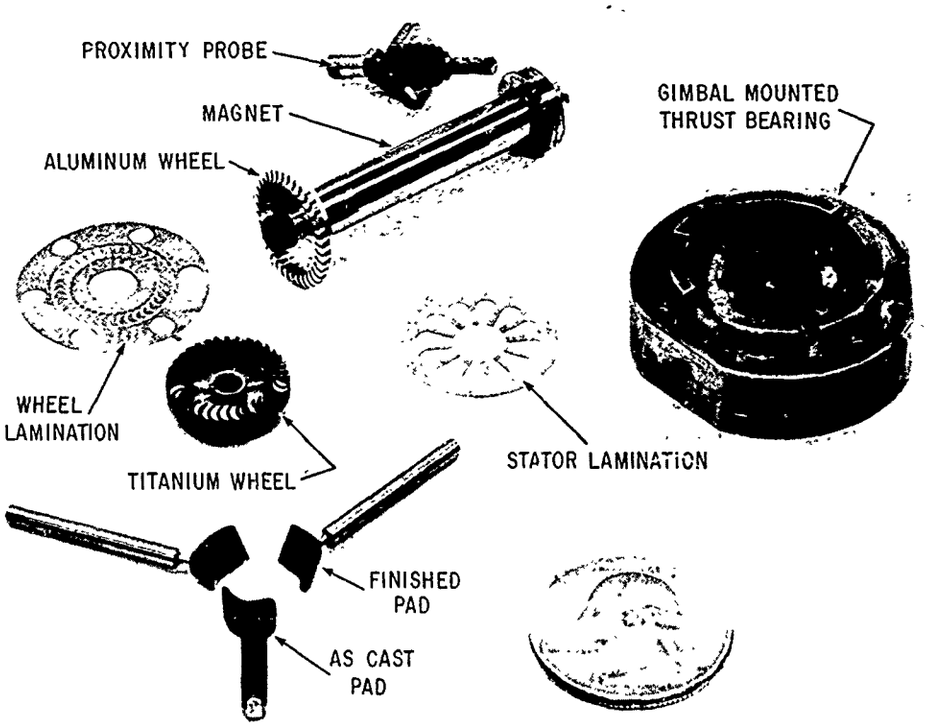

Figure 2-3. Turboalternator Parts

program for testing purposes. A complete electromagnetic analysis of this configuration had not previously been made. Therefore, initial analysis effort for the contract alternator was made by evaluating the General Electric alternator.

2.1.1.1 Field Calculations. The General Electric Company developed an improved fabrication technique, which made it possible to obtain full diameter of the field magnet without the need for a canned magnet configuration. Formerly, the gas bearing design had fixed the shaft diameter. This improved construction now employs a field magnet with a diameter equal to the air bearing diameter. A stronger field and a smaller air gap have been made possible with this shaft. Stator core material and stator configuration were subsequently optimized around this new field configuration.

The existing shaft has a platinum-cobalt magnet 0.261 inch in diameter and 0.375 inch long. The diameter-to-length ratio, D/W, is 0.695 inch. Its demagnetization coefficient (Ref. 16) is:

$$B/H = \sqrt{(D/W)(D/W + 2)}$$

$$= \sqrt{0.695\,(0.695 + 2)} = 1.372 \qquad (1)$$

A line from the origin with the slope of the coefficient, B/H, intersects the demagnetization curve (Ref. 17) of Figure 2.1.1.1-1.

Recoil permeability is approximately 1.13 gauss/oersted and demagnetization is approximately 1.16 gauss/oersted (Ref. 18).

The demagnetization curve is almost linear in the working region of the magnet. Recoil is usually considered parallel to the demagnetization curve at the "y" intercept when more specific information is unavailable.

The assembled permeance coefficient is an order of magnitude greater than the demagnetization coefficient. External flux paths are via five routes shown in Figure 2.1.1.1-2. Flux in paths 1, 2, 3, and 4 link the stator coils and induce an output voltage. Flux in path 5 is lost. Paths 2 and 3 are introduced to trap fringing flux and the ends of the magnet. Flux in path 4 is thereby reduced. Although this flux in path 4 generates voltage, entry is through the long dimension of the outside lamination. Some extra losses result; eddy currents inhibit flux penetration via path 4.

A cursory examination indicates one or two percent of the total flux follows paths 2, 3, 4, and 5. Refined calculations, using the methods of rotors (Ref. 19), were subsequently made.

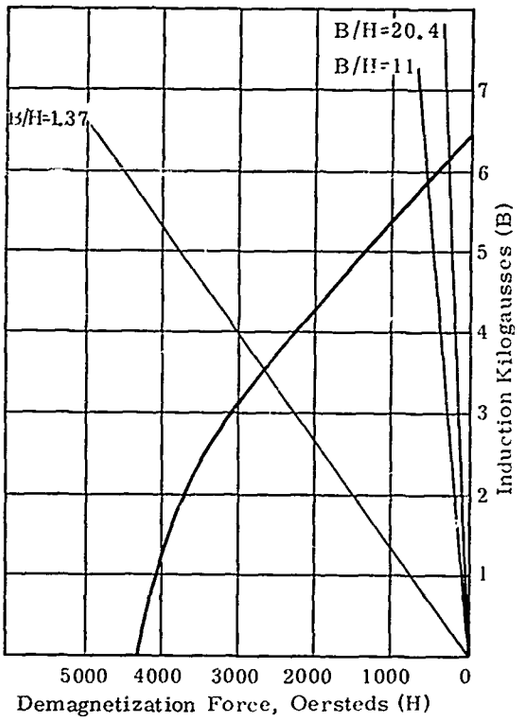

Figure 2.1.1.1-1. Demagnetization Curve

The test rotor and stator had an assembled effective magnetic air gap of 0.0169 inch. If saturation effects are neglected, the permeance coefficient is:

$$(B/H)_{unsaturated} = \frac{\text{Diameter}}{2 \times \text{effective gap}}$$

$$= \frac{0.261}{2 \times 0.0169} = 7.72 \qquad (2)$$

This slope is plotted in Figure 2.1.1.1-1. The operating point of the alternator field is at the intersection of the recoil line, which is about 5.8 kilogausses peak magnet density. Peak yoke density in the stator is 7.9 kilogausses and peak tooth density is about 9.3 kilogausses. This is obviously a saturated condition for Hymu 80* core material. The effective gap is increased by about 3.1 mils, due to saturation effects in the teeth, and by a similar amount, due to saturation in the yoke. The effective gap when saturation effects are included is approximately 20 mils. The saturated permeance coefficient is approximately:

$$(B/H)_{saturated} = \frac{\text{Diameter}}{2 \times \text{effective gap}}$$

$$\approx \frac{0.261}{2 \times 20} = 6.52 \qquad (3)$$

*Trademark of the Carpenter Steel Company

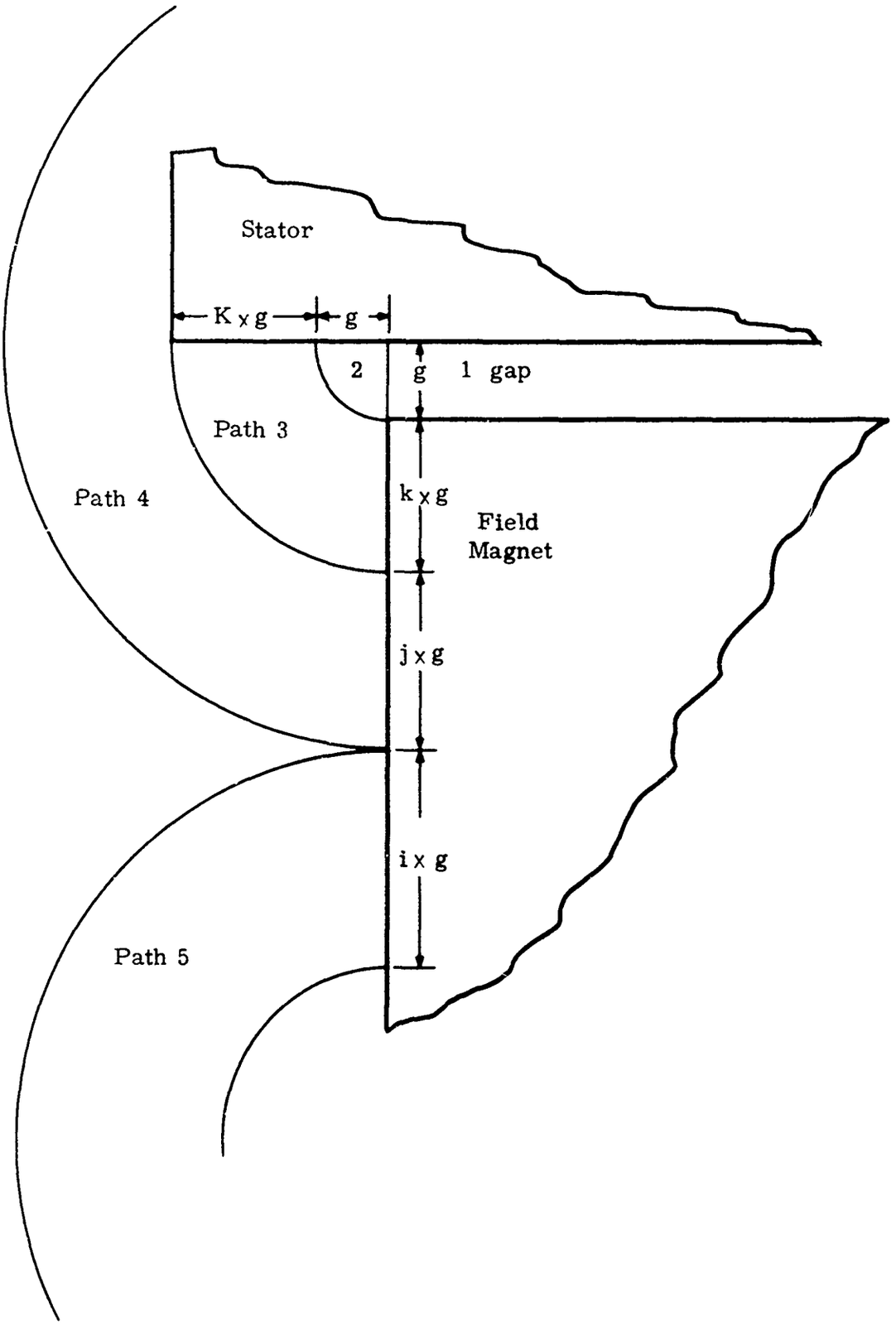

Figure 2.1.1.1-2. Permeance Paths

This slope is also plotted in Figure 2.1.1.1-1. Intersection with the recoil line is at approximately 5.6 kilogausses peak. This is down about 4 percent from the unsaturated point.

2.1.1.2 Tested Open-circuit Voltage for General Electric Alternator. The rotor and stator were operated together. Line-to-line voltage was measured at 98 volts and 3 kilohertz. Figure 2.1.1.2-1 shows its waveshape line to line. It appears to be approximately sinusoidal. However, it is known that saturation has produced large odd harmonic fluxes. No third or ninth harmonics appear at the terminals because the alternator is wye connected. Very little fifth and seventh harmonic voltages appear because the second coil in each phase is offset 30 electrical degrees. Also, a 30-electrical-degree skew greatly reduces the fifth and seventh harmonics and practically eliminates the eleventh and thirteenth harmonics.

The fundamental component of flux appeared to be about 8 percent lower than calculated even when leakage, saturation, and recoil are considered. This was not readily explainable. Evidently, it was the result of one or more of the following, with regard to the magnet:

2.1.1.2.1 Flux Lines. The flux lines emanating from the center of the magnet slug must share the path of greatest reluctance. As a result, the center of the magnet may fall below the knee of the demagnetization curve during air

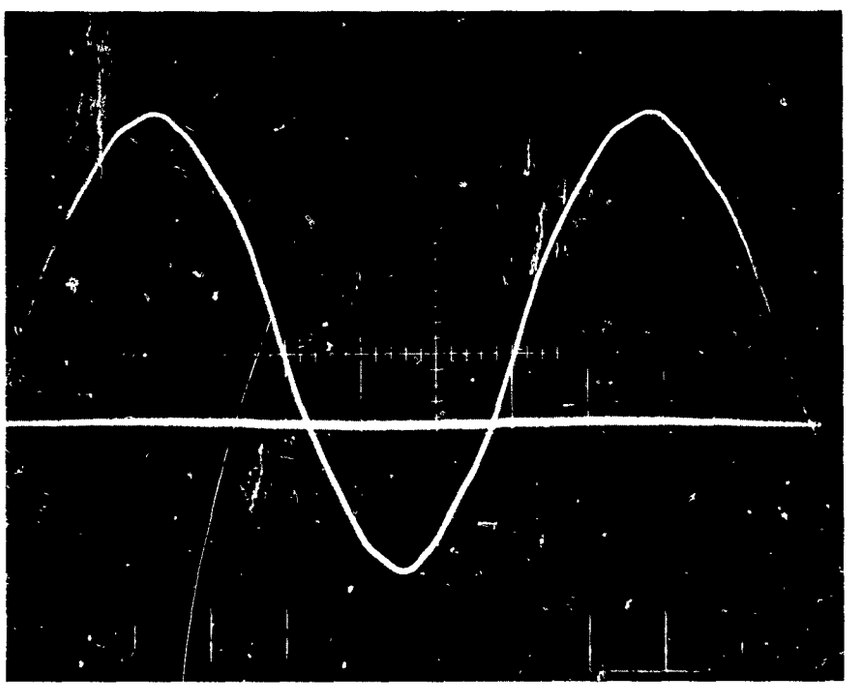

Figure 2.1.1.2-1. Line-to-line Waveshape, 3000 Hz, 50 Volts per Centimeter

stabilization. Recoil by the center section of the magnet would be parallel to and at a lower level than the end sections of the magnet.

2.1.1.2.2 Full Magnetization. Full magnetization may not have been attained.

2.1.1.2.3 Processing with Heat. Processes involving heat, such as brazing and nitriding, may have had a slight deleterious effect on its magnetic properties.

A technique for measuring a magnet property which might be used for process optimization and subsequent quality check appeared desirable. A fixture of approximately zero reluctance, with coils deployed to intercept all magnet flux, would be connected to a gaussmeter to measure accurately total flux from the magnet. Peak density obtained, therefore, is the y intercept with the recoil line. Maximizing this y intercept property will assure the strongest magnet possible. A simple fixture was made and a test procedure was worked out.

2.1.1.3 Separation of Losses by Test. A series of three dynamic tests was proposed to separate the alternator losses:

- Friction and windage (F & W) -- unmagnetized field driven at rated speed
- Open circuit core loss (OCCL) -- fully magnetized field driven at rated speed
- Short circuit core loss (SCCL) -- partially magnetized field driven at rated speed

The OCCL test would include (besides friction and windage) the following losses: 1) fundamental flux core loss, 2) end leakage losses, 3) a component of pole face loss related to ripple flux caused by stator slots, and 4) saturation harmonic flux losses.

The SCCL test would include (besides friction and windage) the following losses: 1) leakage flux losses in the stator teeth and yoke, 2) a component of pole face loss due to stator leakage fluxes passing through the rotor, and 3) skin effect losses in the stator strands.

2.1.1.4 Basic Material Property Tests. Room temperature and cryogenic temperature material property tests were planned. This enabled the designer to extrapolate more accurately to design conditions. These property tests were:

2.1.1.4.1 Stator Core Material. A technique for evaluating available standard core material was subsequently determined and applied.

2.1.1.4.2 Stator Copper. Accurate dc measurements of resistance of the actual winding at cryogenic temperatures were made. Effect of stresses and stretch incurred in placing the winding were included by this measurement.

2.1.1.4.3 Cobalt Platinum Magnet. Improved field strength at cryogenic temperatures was determined.

2.1.1.5 Effect of Stronger Magnet Field. While the canned magnet slug configuration of the earlier design possessed many attributes, it was replaced with the full-diameter magnet field. This full-diameter field is stronger and the air gap permeance can be several times larger. A configuration to make optimum use of these parameters was investigated.

An existing stator operating with a canned magnet slug (20-mil gap) was assembled and run with a new full diameter field, which had a 5-mil air gap. Saturation of stator teeth and yoke was predicted by simple calculation. The full effect of saturation on flux harmonics was not directly observable in the line-to-line voltage.

As was previously noted, harmonic voltages largely cancel themselves in the winding when its two coils per phase are offset 30 electrical degrees. However, with one coil reversed, the line-to-line voltage waveshape appears as shown in Figure 2.1.1.5-1. A computer analysis of 12 measured points indicates a strong fifth and seventh harmonic:

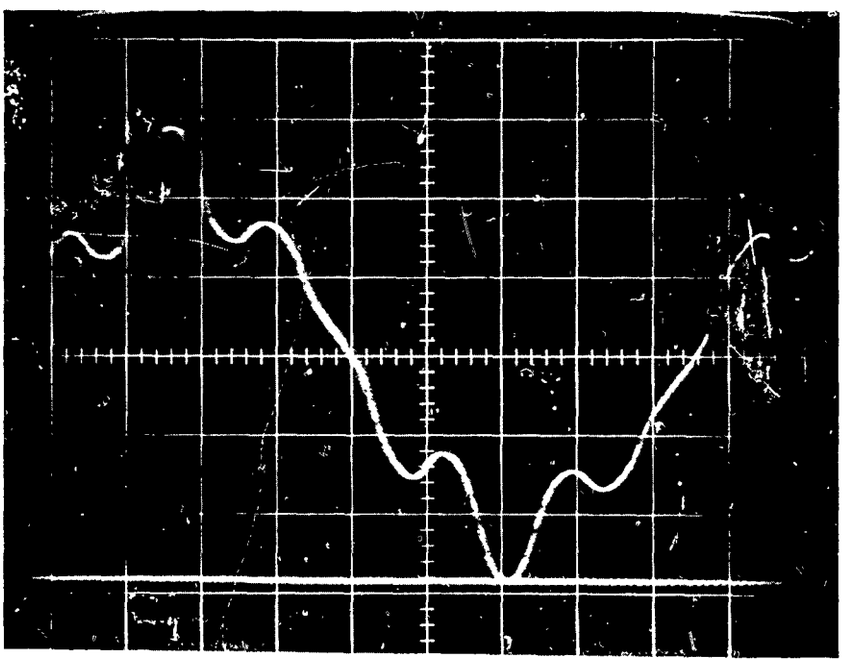

Figure 2.1.1.5-1. Line-to-line Waveshape, Approximately 1800 Hz, 10 Volts per Centimeter, One Coil Reversed in Each Phase

Measured Point	Analysis
Fundamental	16.0 volts rms
Fifth harmonic	2.45 volts rms
Seventh harmonic	2.32 volts rms

With this information, it is possible to calculate the actual harmonic flux density in the stator iron. For example, the fundamental vector relationships, Figure 2.1.1.5-2, illustrate how phase and terminal voltages are built up from coil voltages. In this case, one coil is backward in each phase, and 2.32 inches of scale in the figure equals 16 volts rms of fundamental line-to-line voltage. Thus, it can be deduced that 2.5 inches of coil voltage in Figure 2.1.1.5-2 equals 17.9 volts.

Figure 2.1.1.5-3, which uses the same scale for coil voltage, shows that when the coils are properly connected, the terminal voltage is 8.34 inches or 59.8 volts. The actual value by measurement is just under 59 volts. The agreement is probably accidental; it is much better than is warranted by the crudeness of the method.

Fifth and seventh harmonic voltages can be treated in the same manner. Angular shifts are multiplied by the harmonic order. Figure 2.1.1.5-4 shows the fifth harmonic. The scale is changed to 4.22 inches and equals 2.45 volts. Coil voltage (1.25 inches) is 0.725 volt rms for the fifth harmonic.

The seventh harmonic coil voltage is given in Figure 2.1.1.5-5. Another arbitrary scale is used with 4.22 inches, which equals 2.32 volts. Coil voltage (1.25 inches) is 0.687 volt rms for the seventh harmonic.

Voltage and flux are directly related. However, actual harmonic flux is larger by the inverse of the skew factor for that harmonic. A summary of the findings for harmonic voltages, which have been obtained graphically and calculated for relative flux densities, are:

Order of Harmonic, K	Coil Voltage	Skew Factor	$\left(\frac{B_K}{B_1}\right) 100$
1	17.9	0.99	100%
3	Unknown	0.90	Unknown
5	0.725	0.74	5.4%
7	0.687	0.53	7.2%

The third harmonic cannot be demonstrated with line-to-line measurements in a wye-connected machine. Losses associated with harmonic fluxes appear to be significant.

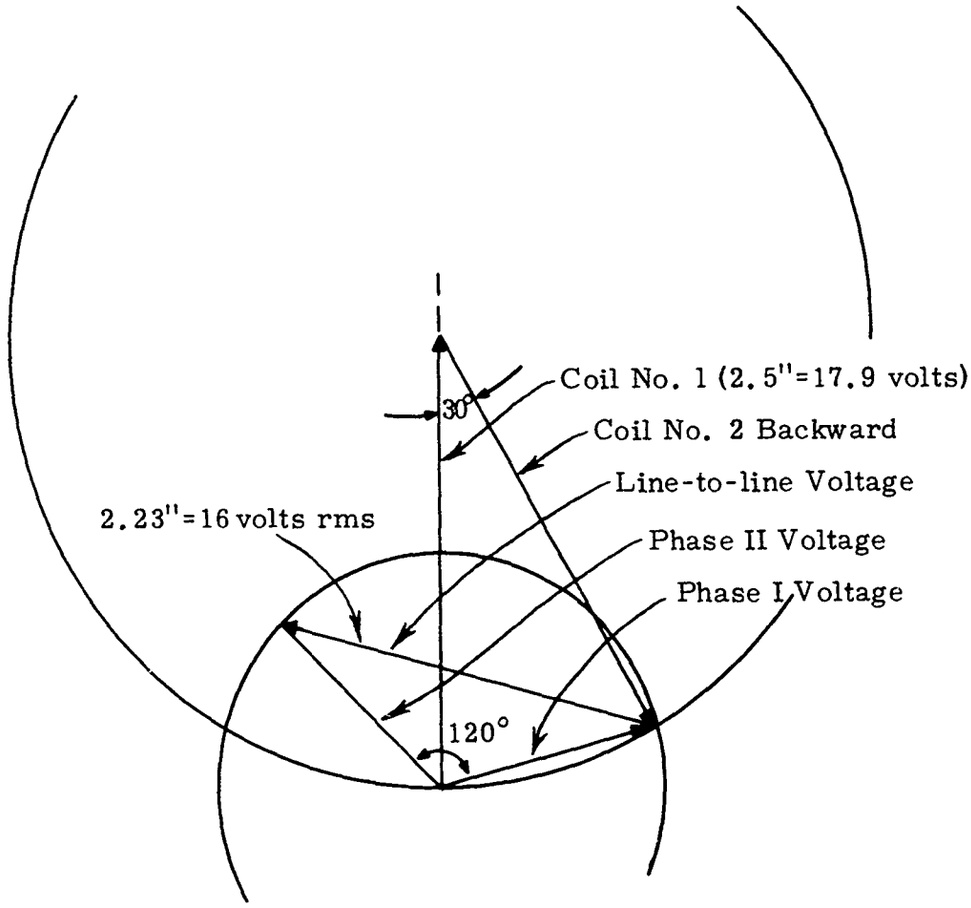

Figure 2.1.1.5-2. Fundamental Component with Reversed Coil in Each Phase

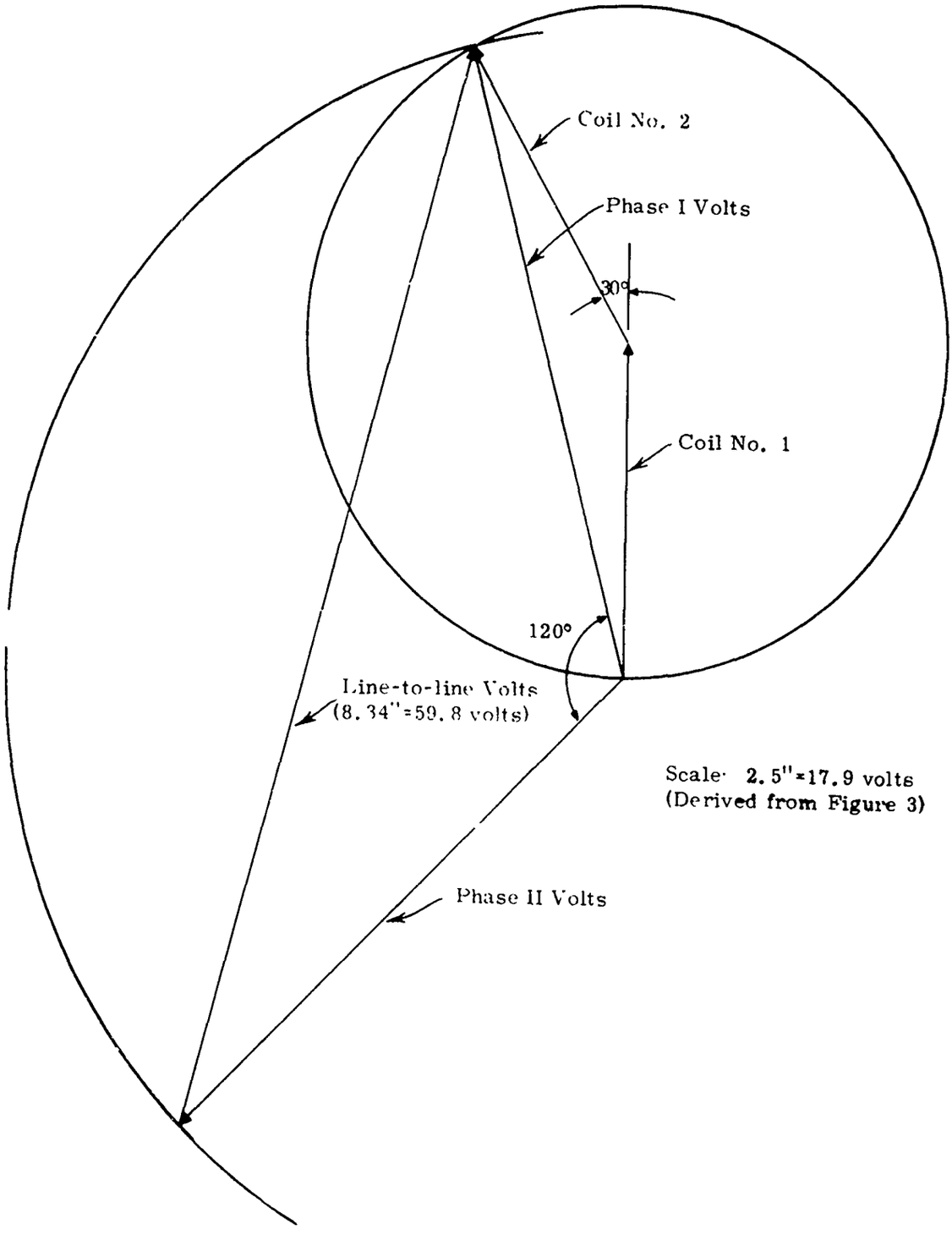

Figure 2.1.1.5-3. Fundamental Component of Voltage

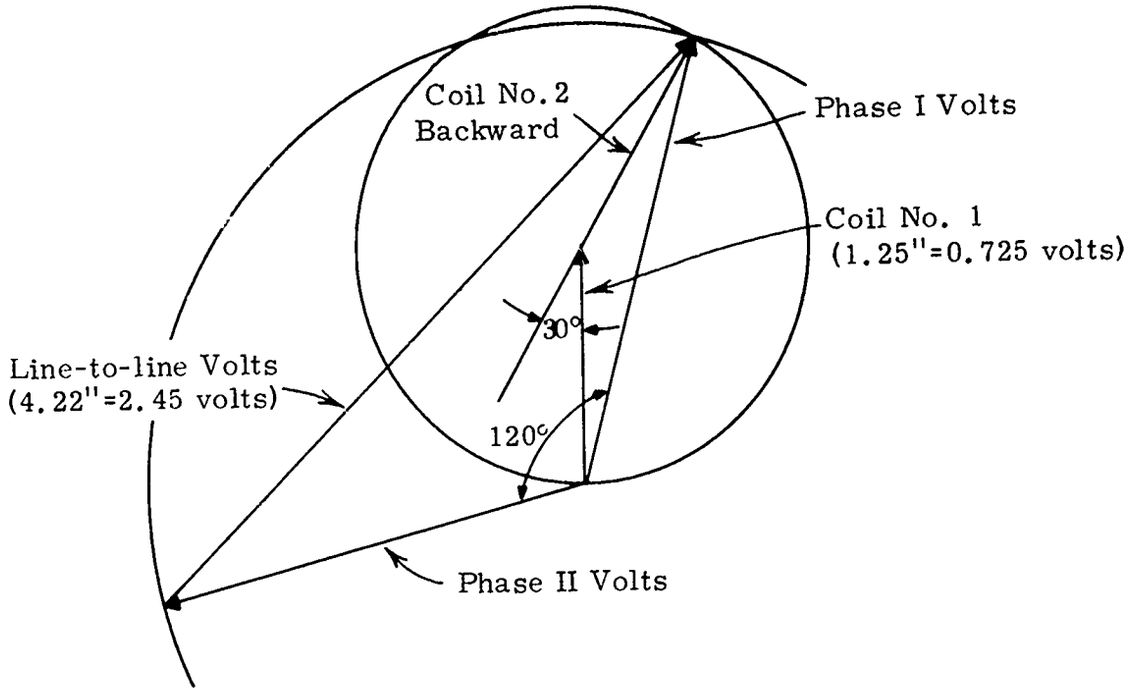

Figure 2.1.1.5-4. Fifth Harmonic Voltage, Coil Reversed

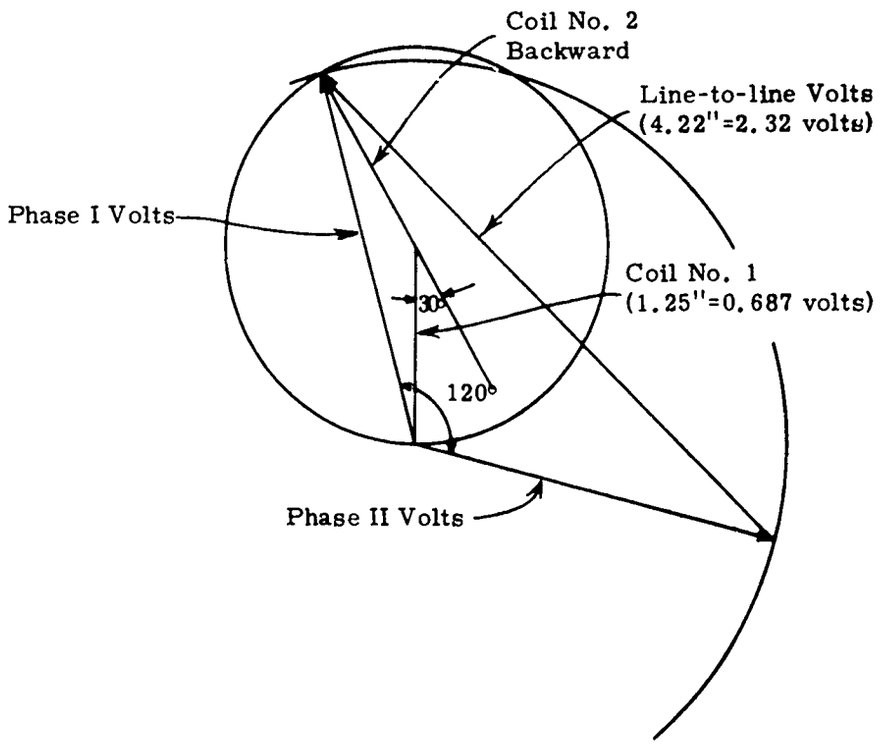

Figure 2.1.1.5-5. Seventh Harmonic Voltage, Coil Reversed

2.1.1.6 Eddy Current Losses. In a magnetic circuit containing a volume (V) of laminated core material of thickness (t), the eddy current loss (Pe) (Ref. 20) for all practical purposes is:

$$Pe = \frac{\pi^2 f^2 t^2 B_{max}^2 V}{6\rho} \tag{4}$$

where

ρ = resistivity

B_{max} = maximum flux density

f = frequency

There is evidence that hysteresis loss may be relatively large in some types of 4-mil material. In any case, the losses do not follow Equation 4 for commercially available materials (Ref. 21).

The following paragraphs discuss the effect on the core loss if eddy current losses predominate. Harmonic loss relative to the fundamental loss is:

$$\left(\frac{Pe_K}{Pe_1}\right) = K^2 \times \left(\frac{B_K}{B_1}\right)^2 \tag{5}$$

where K is the harmonic order. Tabulated results are:

Harmonic Order	$\left(\frac{B_K}{B_1}\right) \times 100$	$\left(\frac{Pe_K}{Pe_1}\right) \times 100$
1	100%	100%
3	Unknown	Unknown
5	5.4%	73%
7	7.2%	254%

These results show that eddy current losses, which result from saturation harmonics, can be relatively large. However, the experimental data from which these results were obtained are not sufficiently accurate to conclude anything other than a general trend. A simple dynamic experiment was planned wherein coil voltage was to be sensed directly and a harmonic analyzer was employed to directly measure harmonic fluxes. The results are reported in paragraph 2.1.1.11.

2.1.1.7 Field Magnetization. The apparent fundamental component of flux was found to be about 8 percent lower than typical vendor data would indicate. This was reported on the basis of observed open-circuit dynamic test voltage. Subsequently, a flip-coil test fixture and gaussmeter confirmed the

dynamic test results. Three possibilities were postulated for this seeming degradation of material property.

The most likely possibility of incomplete magnetization was eliminated by upping the magnetizing field to 25,000 gausses. An increase of less than 2 percent in lines was observed. Upon receipt of more unnitrided shafts, tests were repeated to determine what effect, if any, the nitriding process has on magnetization.

The field magnet was subjected to 25 kilogausses at room temperature. A magnetic short circuit (after field was air stabilized) was imposed on the field. This produced 3620 lines at room temperature. Then the magnet was cooled to 77°K, where it produced 3760 lines of flux, and magnetized at 77°K (25 kg), producing 3860 lines. Upon warming to room temperature, it again produced 3620 lines, which is the same as when magnetized at room temperature. It appears that magnetization is not permanently enhanced by magnetizing at 77°K. However, the field, as expected, did get a little stronger (about 3.8 percent) at 77°K.

2.1.1.8 Stator Measurements and Armature Leakage Reactance. End turn, slot and zig-zag leakage reactances were calculated by conventional motor methods to be about 33 ohms per phase at 3000 Hz. Line-to-line impedance was measured with the rotor in place (demagnetized and stationary). This value was 38.7 ohms (4.10 millihenries line to line). The rotor was taken out of the stator and the impedance reading taken again. This value was 35.3 ohms (3.85 millihenries line to line). Additional zig-zag leakage, due to the presence of the rotor, appeared to be small. The change in apparent resistance was too small to be detected, so there was probably very little eddy current loss in the field. Armature leakage reactance is nearly twice as large as resistance at room temperature and nearly 16 times as large as resistance at 77°K.

2.1.1.9 Armature Resistance. Existing material data indicate that mechanical stresses in the winding do not seriously affect the linear resistance of copper, except at temperatures much below 77°K. Tests were made to determine winding resistance at room temperature, dry ice temperature, and liquid nitrogen temperatures. Two thermocouples were imbedded in the winding at one location on the end turns. Results show a linear relationship as follows:

Temperature	Line-to-line Resistance, Ohms
Room (296°K)	32.8
Dry Ice (194°K)	19.42
LN_2 (77°K)	4.22

Results of this nature can be used in conjunction with the thermocouple readings and phase current to determine I^2R at any test point.

2.1.1.10 Core Loss Data. The need for core loss data was projected by analysis of Magnetic Metals data for Centrimu 20 (Hymu 80). The 8-kilogauss data were extrapolated from 4- and 6-kilogauss data. The 3000-Hz and 4000-Hz data were interpolated between 1000-Hz and 5000-Hz data, with the following results:

Frequency (Hz)	Flux Density (Kilogauss)	Loss Watts per Pound		
		Hysteresis	Eddy	Total
3000	6	1.89	3.60	5.50
	8	3.0	6.3	9.3
4000	6	2.52	6.30	8.82
	8	4.0	11.2	15.2
5000	6	3.15	9.85	13.0
	8	5.0	17.5	22.5

2.1.1.11 Harmonic Fluxes. Measurement of harmonic fluxes was made on a stator having 21.5-degree spiral. A 200-turn search coil of 100 percent pitch was inserted. Harmonic fluxes were determined by direct measurement with a Hewlett-Packard harmonic analyzer.

Core loss values are proportional to the square of both harmonic order and harmonic flux density. On this basis, the measured harmonic fluxes and calculated losses are:

Harmonic	Megavolts	Spiral Factor	Harmonic Flux (Percent)	Core Loss (Percent)
1 (24 Hz)	217	0.995	100	100
3	23.0	0.95	11.2	11.3
5	3.1	0.86	1.7	0.7
7	7.5	0.74	4.7	10.6
9	4.9	0.59	3.8	11.6
			Total	134

If it is assumed core loss associated with harmonic fluxes is proportional to magnitude squared times harmonic order square, the core loss summation

for fundamental through the ninth harmonic is 134 percent of that due to fundamental alone.

2.1.1.12 Calculated Core Loss. Peak flux densities in the stator and teeth were recalculated using the newly developed data for magnet strength. The values are at 8.11 kilogausses and 6.14 kilogausses, respectively. Extrapolating by a square relationship from the tabulated data above, the following core losses, which include 34 percent added for harmonic losses, are:

Speed (rpm)	Frequency (Hz)	Total Core Loss (Watts)
180,000	3000	0.35
240,000	4000	0.58
300,000	5000	0.83

2.1.1.13 Core Loss at Low Temperatures. The core loss for Hymu 80 is so low that direct measurements at low temperatures are very difficult without the aid of some sophisticated instrumentation. Data of some nature were needed, and direct measurement was investigated as a possible methodology. An alternate approach would have been to 1) photograph the hysteresis loop for various frequency fluxes and temperatures and 2) measure resistivity as a function of temperature. Assuming knowledge of the hysteresis and eddy current losses at room temperature, the core loss at other lower temperatures could then be calculated.

2.1.1.14 Basic Core Loss Data. Very little core loss data are available for Hymu-80-type materials at cryogenic temperatures. A series of tests was made on the material to determine the effect of cold on its properties.

2.1.1.14.1 Core Specimen. A toroidal wound core of 79 ring laminations of molybdenum permalloy was used for the core loss test. Lamination thickness was 3.5 mils. The ring had an outside diameter of 2 inches and an inside diameter of 1.5 inches.

Excitation was by a toroidal winding of 40 turns of 0.032-inch HF wire. A bifilar secondary of 40 turns of 0.0285-inch HF wire fed the voltage coil on a wattmeter as well as an integrator input to the oscilloscope.

2.1.1.14.2 Instrumentation for Core Loss Measurements. The BH loop was displayed on an oscilloscope. A type O operational amplifier plug-in unit converted (integrated) the voltage signal from the core to flux (density), β, which was displayed on the vertical of a Tektronix Type 536 Oscilloscope. A Tektronix current probe (P6042) (dc to 50 millihertz) fed its signal to a type CA plug-in unit for the horizontal display of amperes (turns), H.

A McIntosh amplifier (M1-200AB), which supplied the power, was driven by a Hewlett-Packard Wide-range Oscillator. The output voltage waveshape was monitored by another oscilloscope. A 50-ohm resistor was connected in parallel across the 8-ohm tap on the output transformer for an auxiliary load. Frequency was checked with a Beckman counter.

Watts and volts were measured with a Fluke Model 102 VAW meter. Linearity in the integrator was checked at 5000 Hz with a squarewave signal generator.

2.1.1.14.3 Resistance Measurements of Molybdenum Permalloy. A tape specimen (from Arnold 12P1000-10 core) 0.001 inch thick, 0.125 inch wide, and approximately 19 inches long was tested at various temperatures with a Rubicon Portable Resistance Bridge, with the following results:

Temperature (°K)	Measured Resistance	Lead Resistance	Tape Resistance
297	3.686	0.0280	3.658
194.5	3.416	0.0257	3.390
77	3.196	0.0235	3.173

The resulting resistance ratio at temperature, T, referred to 300°K is:

$$\frac{R(T)}{R(300°K)} = \frac{3.053 + 0.16233 \times 10^{-2} \times (T) - 7.5 \times 10^{-7} \times (T)^2 + 7.167 \times 10^{-7} \times (T)^3}{3.666} \quad (5)$$

where T is temperature in degrees Kelvin. A curve of R(T) is shown in Figure 2.1.1.14.3-1. Three test points are indicated. Note that the resistivity drops about 15 percent from room to liquid-nitrogen temperature.

2.1.1.14.4 Core Loss Measurements on Molybdenum Permalloy. Core loss tests are complete on the ring core specimen. Tests were conducted at 2, 3, 4, and 5 kilohertz and 2.2, 3.3, 4.4, 5.5, 6.6, and 7.35 kilogausses at 300°K and 77°K. Empirical equations which fit the test data are:

At 300°K

$$\left(\frac{Pc}{f}\right) = 0.23 \times 10^{-3} \times \left(\frac{\beta}{4.4}\right) + 0.207 \times 10^{-6} \left(\frac{\beta}{4.4}\right)^{2.5} \times f \quad (6)$$

where

β = kilogausses

f = Hz

The equation for (Pc/f) is in watts per pound per cycle.

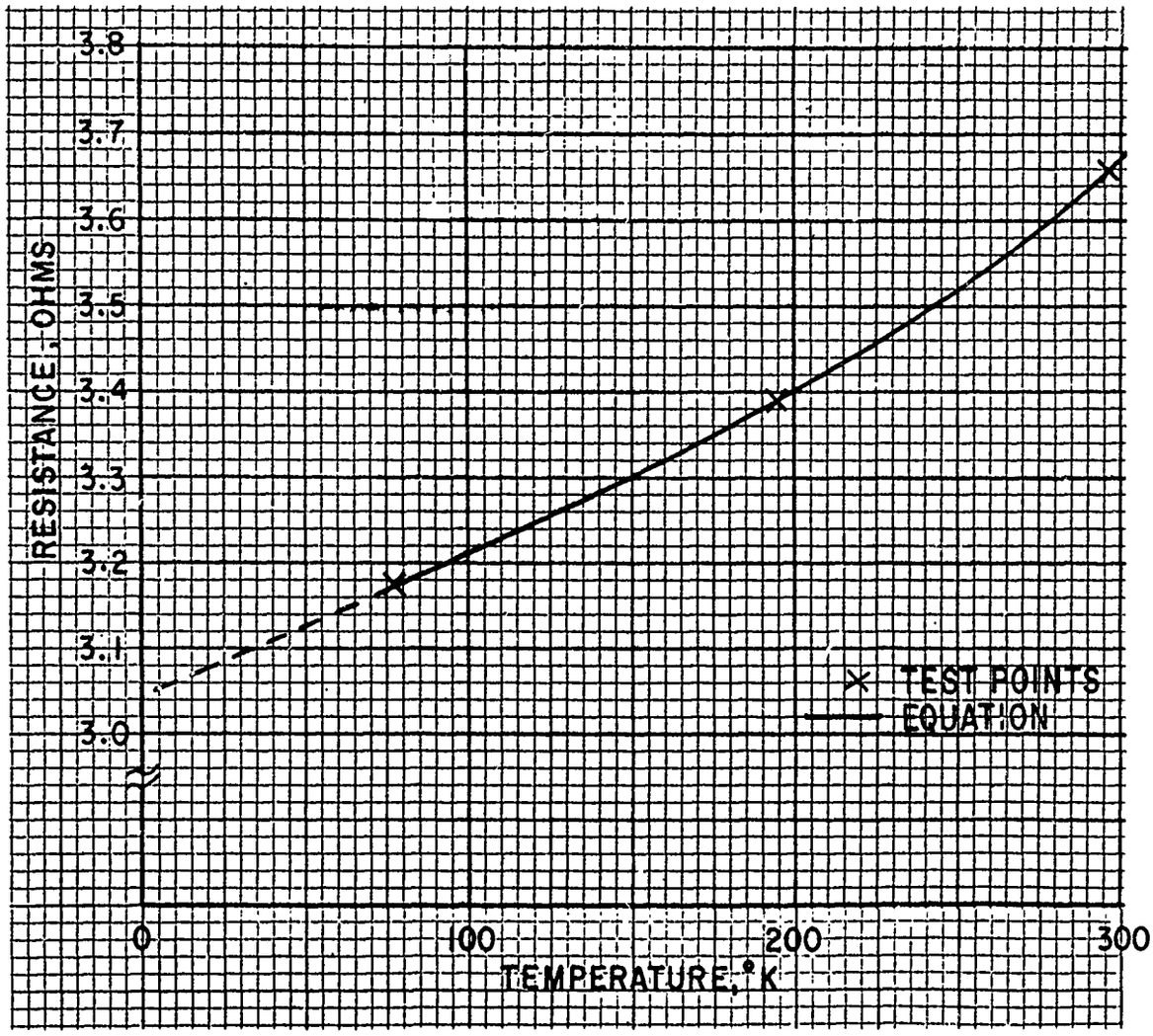

Figure 2.1.1.14.3-1. Resistance of Molybdenum Permalloy Specimen

At 77°K

$$\left(\frac{Pc}{f}\right) = 0.60 \times 10^{-3} \times \left(\frac{\beta}{4.4}\right)^{1.5} + 0.33 \times 10^{-6} \left(\frac{\beta}{4.4}\right)^{2.0} \times f \qquad (7)$$

Families of these curves are shown in Figures 2.1.1.14.4-1 and 2.1.1.14.4-2, respectively. Tested results are plotted along with these curves. Scatter is ralatively small and the fit for these data is good.

Generally, the first factor in the equation is the energy of the hysteresis loop, and the second term relates to eddy current loss. BH loop pictures roughly indicate an increase in area of the loop of approximately 50 percent at 77°K. The coefficient in the first term of the equation almost doubles at 77°K.

Resistivity measurements (reported above) on material similar to Hymu 80 indicate an increase of 15 percent in conductance at 77°K. The coefficient of the second term increases almost 50 percent at 77°K. Note that flux density, β, is a part of the coefficients. Exponents of β for the various terms are reasonable.

Figure 2.1.1.14.4-3 shows the effect of flux density on the hysteresis loop at 400 Hz and room temperature. A sine wave of voltage was applied to the test specimen. Voltage was raised in steps of about one-fourth to saturation. The horizontal scale is the exciting current -- 10 milliamperes per division.

Figure 2.1.1.14.4-4 shows similar data at 77°K. The horizontal scale has been increased to 20 milliamperes per division; otherwise the loops would have been excessively distorted.

Figures 2.1.1.14.4-5 and 2.1.1.14.4-6 show hysteresis loops at room temperature and 77°K, respectively, for 3000 Hz. These illustrations have the same horizontal calibration. Figure 2.1.1.14.4-7 shows the outer loops of Figures 2.1.1.14.4-5 and 2.1.1.14.4-6 superimposed to indicate the relative size, hot and cold. The larger loop is for the cold condition.

The pregnant look beginning to appear in Figure 2.1.1.14.4-5 at 3000 Hz is very pronounced in Figure 2.1.1.14.4-8 at 5000 Hz. Eddy currents in the iron are probably affecting the results. If they do affect the results, then it may be difficult, if not impossible, to determine a true hysteresis loop on any but the thinnest specimens of core material.

2.1.1.15 Computer Program. A computer program was written and debugged as an aid to optimize alternator performance. The program was initially written for a unity and leading power factor load because that was the most likely mode of operation. Later, a modification was prepared to predict performance for a lagging power factor load. The purpose of this mode of operation was to

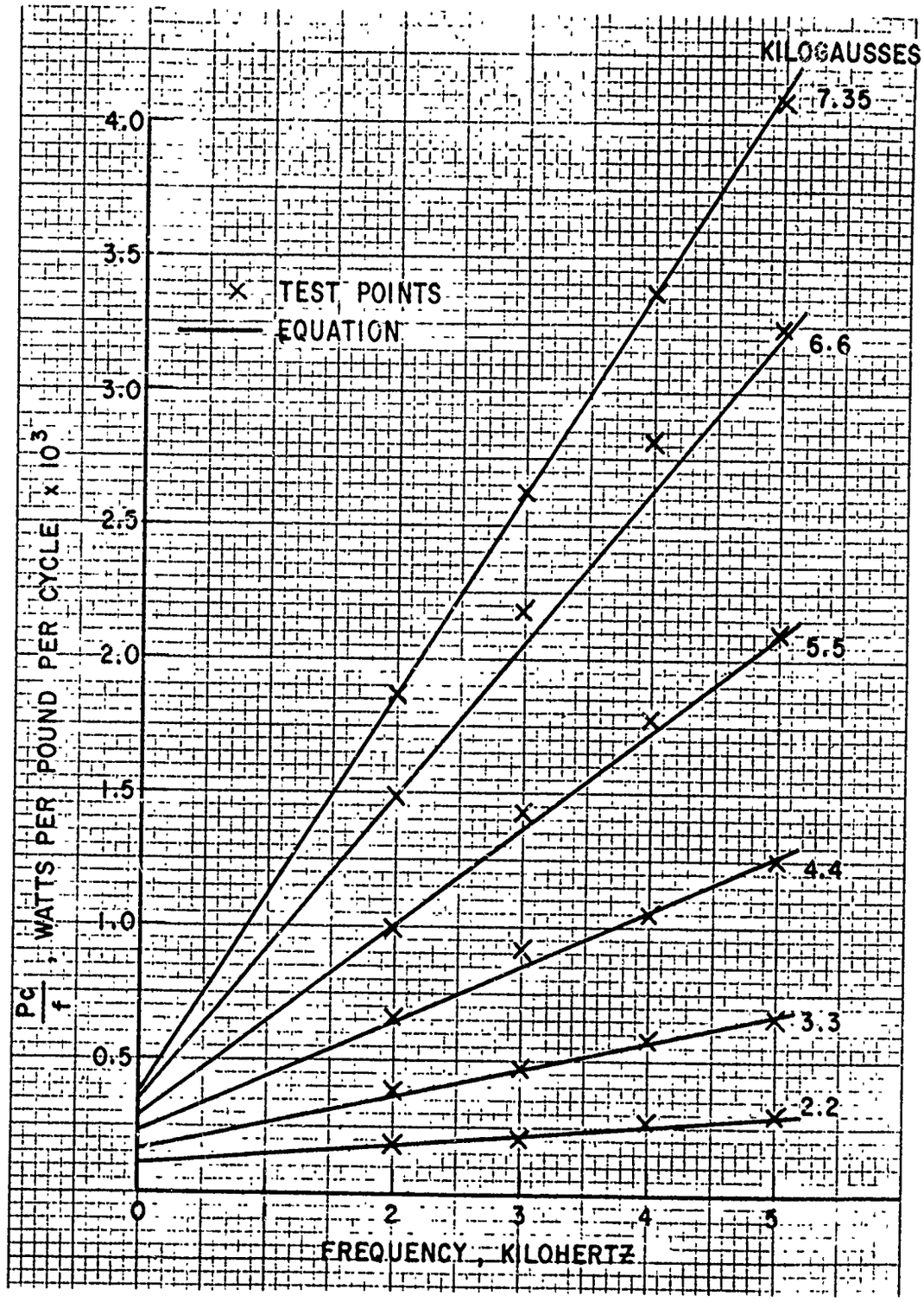

Figure 2.1.1.14.4-1. Molybdenum Permalloy Characteristics at 300°K

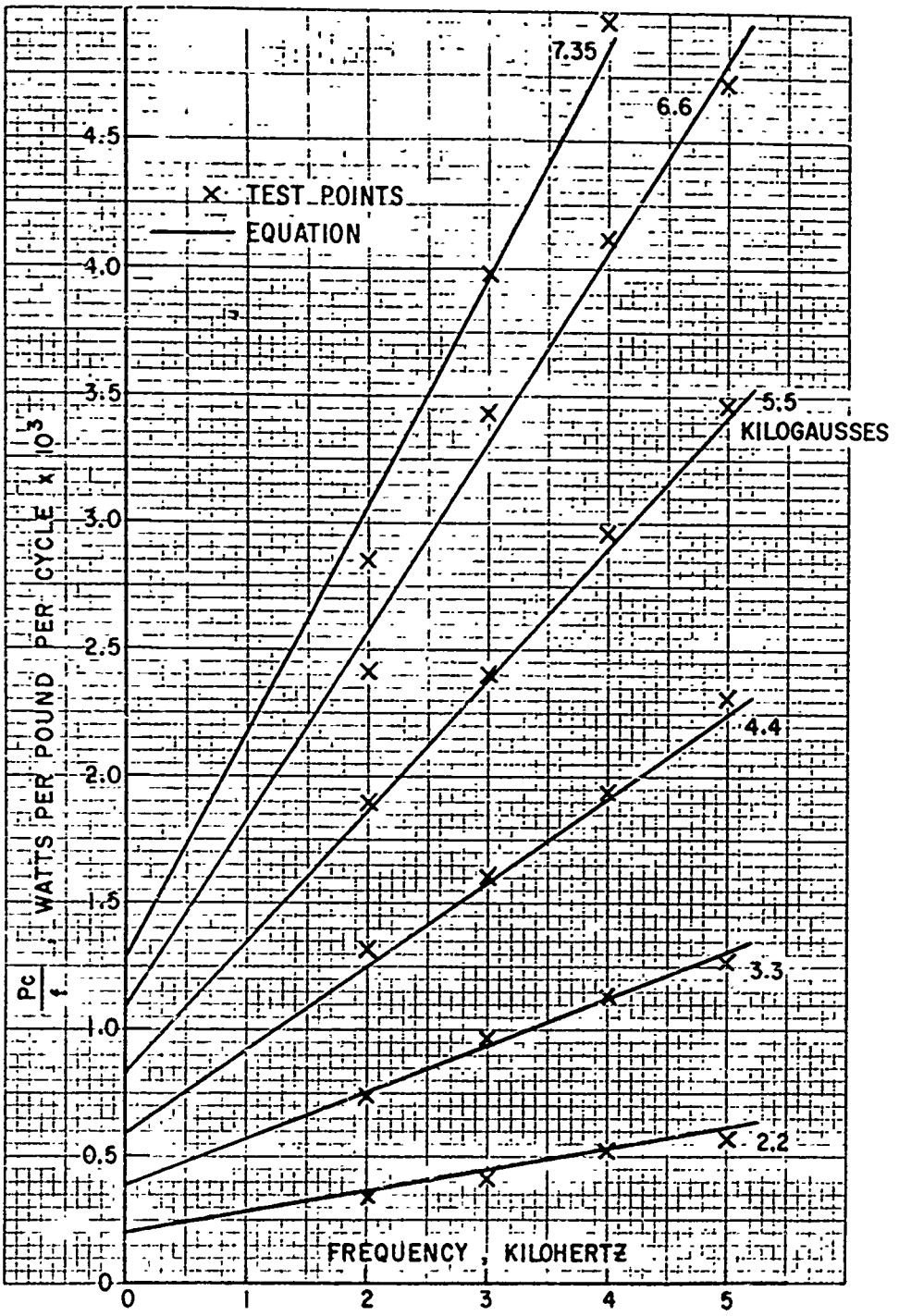

Figure 2.1.1.14.4-2. Molybdenum Permalloy Characteristics at 77°K

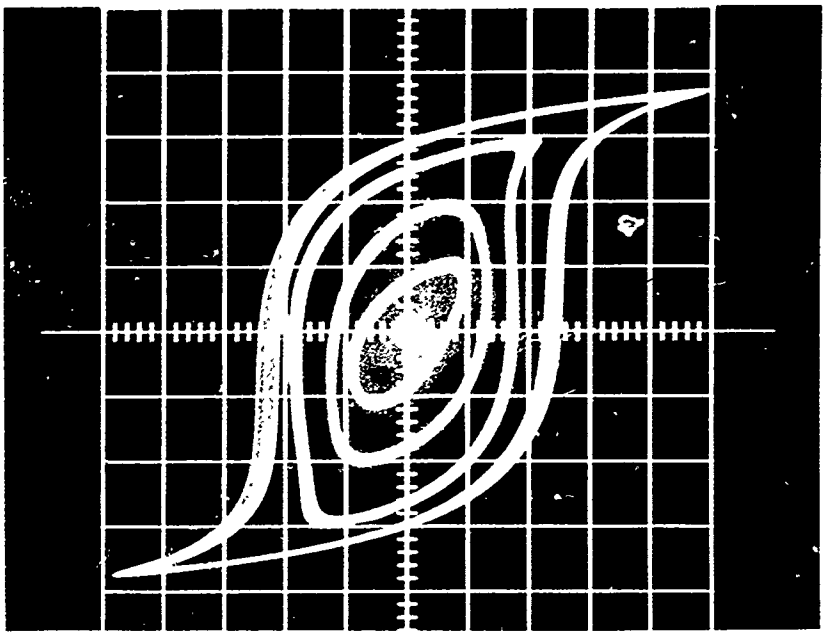

Figure 2.1.1.14.4-3. Hysteresis Loops at 300°K and 400 Hz, Horizontal Calibration 10 Milli-amperes per Div

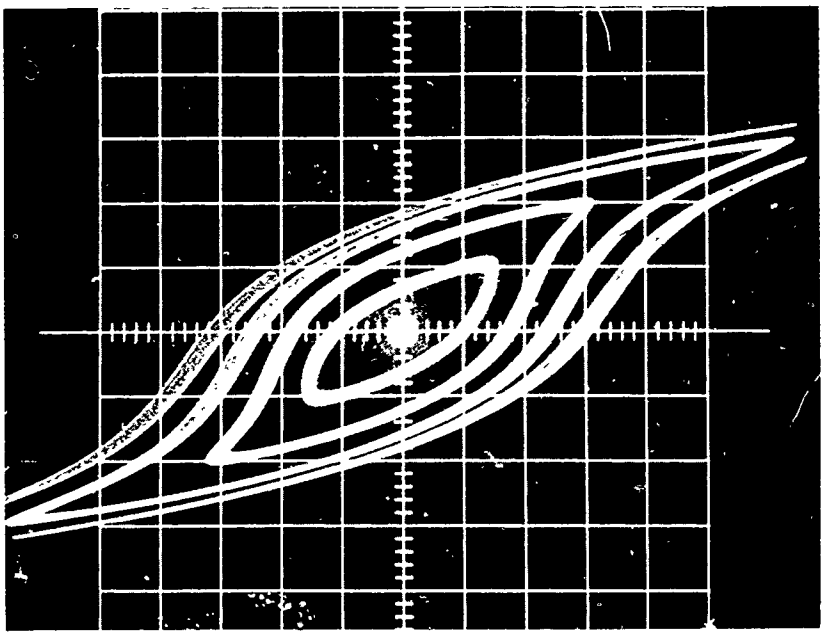

Figure 2.1.1.14.4-4. Hysteresis Loops at 77°K and 400 Hz, Horizontal Calibration 20 Milli-amperes per Div

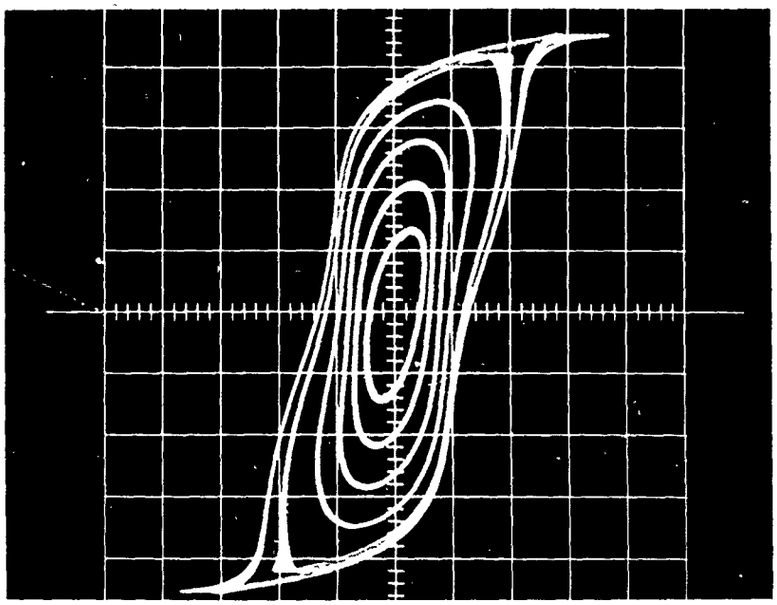

Figure 2.1.1.14.4-5. Hysteresis Loops at 300°K and 3000 Hz, Horizontal Calibration 50 Milli-amperes per Div

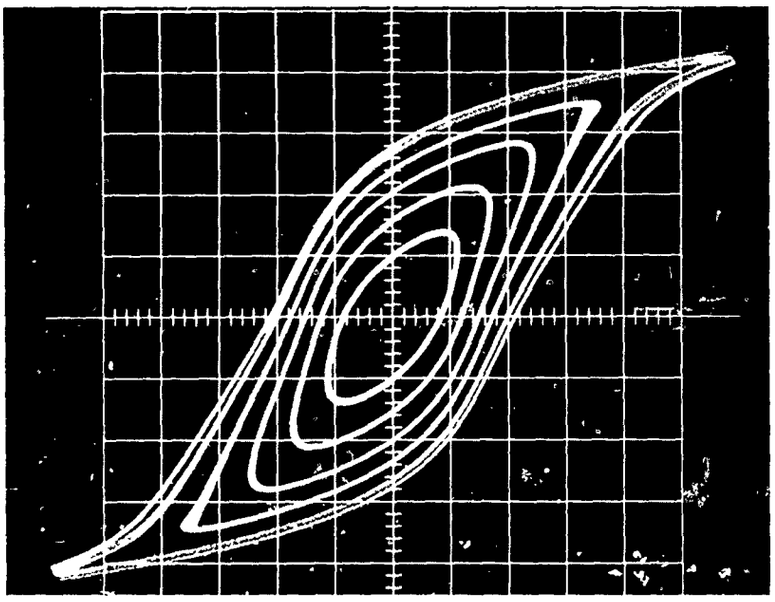

Figure 2.1.1.14.4-6. Hysteresis Loops at 77°K and 3000 Hz, Horizontal Calibration 50 Milli-amperes per Div

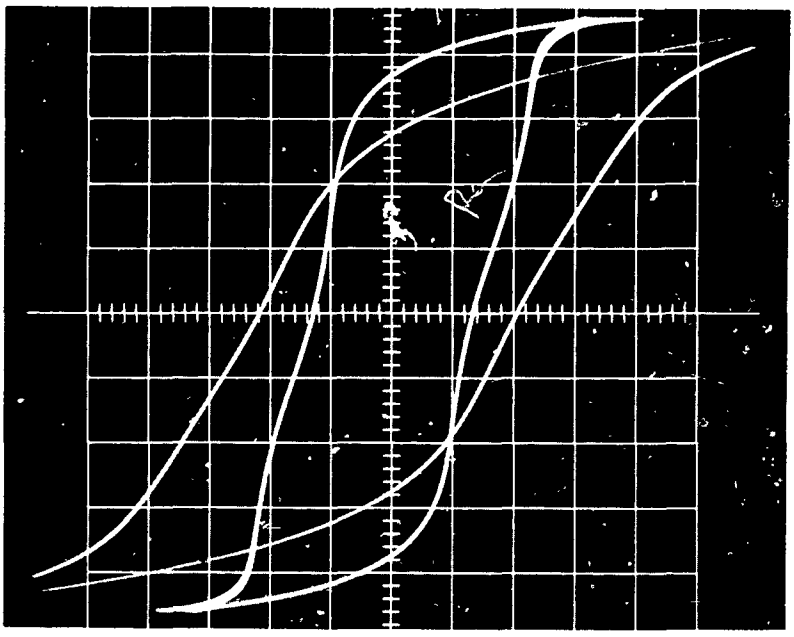

Figure 2.1.1.14.4-7. Outer Loops of Figures 2.1.1.14.4-5 and 2.1.1.14.4-6 Superimposed

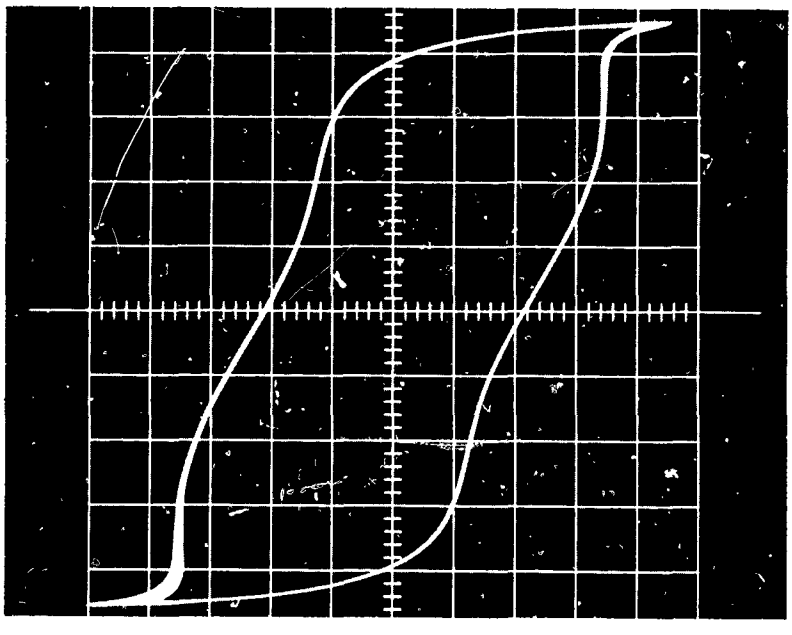

Figure 2.1.1.14.4-8. Hysteresis Loop at Room Temperature and 5000 Hz, Horizontal Calibration 50 Milliamperes per Div

accentuate the effect of alternator reactance so it could be determined indirectly from the tested characteristics.

On the basis of four test points, the program results appeared acceptable. Table 4.1.1.15-1 shows the correlation of phase volts for a wide range of output power and frequency.

Table 2.1.1.15-1

COMPARISON OF CALCULATED AND TESTED CHARACTERISTICS

Run 24 (Point)	Hz	Phase (L-N) (Volts)		Output Power (Watts)	
		Calculated	Tested	Calculated	Tested
1	3578	66.4	65.9	19.0	19.4
2	2790	48.0	47.4	38.8	39.4
3	2474	40.8	40.1	39.7	39.8
4	2994	43.0	42.6	72.2	73.0

2.1.1.16 Leading Power Factor. Self-excitation of the alternator by armature reaction can be useful in raising terminal voltage and thereby lowering line current for a fixed power output requirement. Lower I^2R loss and improved efficiency will result. Counterbalancing this effect is the increasing penalty for juggling reactive power; that is, the I^2R of the reactive component of current. One optimizing approach which will lead to lowest I^2R for a specified output power is to 1) assume a line current and 2) calculate the optimum power factor which occurs at the crest of the output power against the power factor. By successively assuming values of line current until the optimum (crested) output power equals the specified power, the optimum leading power factor is determined. Minimum copper loss will result. Because the copper loss is the significant alternator loss, self-excitation of the alternator by the leading power factor may prove of considerable importance in critical applications.

Figure 2.1.1.16-1 indicates the output capability of an alternator for one value of line current with a changing load power factor.

2.1.1.17 Vector Diagram. Figure 2.1.1.17-1 is a diagram of pertinent electromagnetic vectors. The d and q components are not identified formally for the sake of simplicity, but the calculations include their effect.

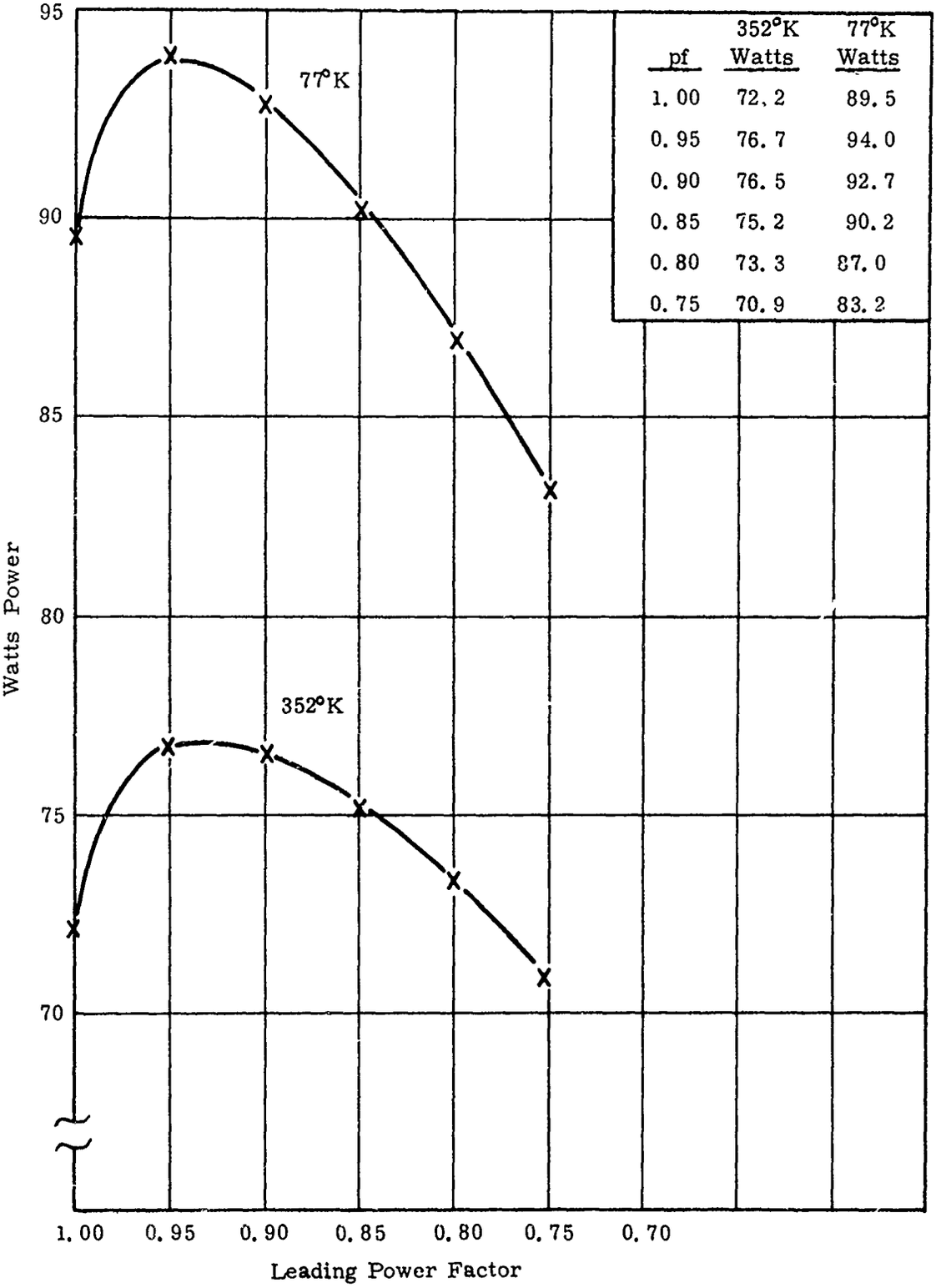

pf	352°K Watts	77°K Watts
1.00	72.2	89.5
0.95	76.7	94.0
0.90	76.5	92.7
0.85	75.2	90.2
0.80	73.3	87.0
0.75	70.9	83.2

Figure 2.1.1.16-1. Calculated Constant Current (0.565 Amperes) Characteristics

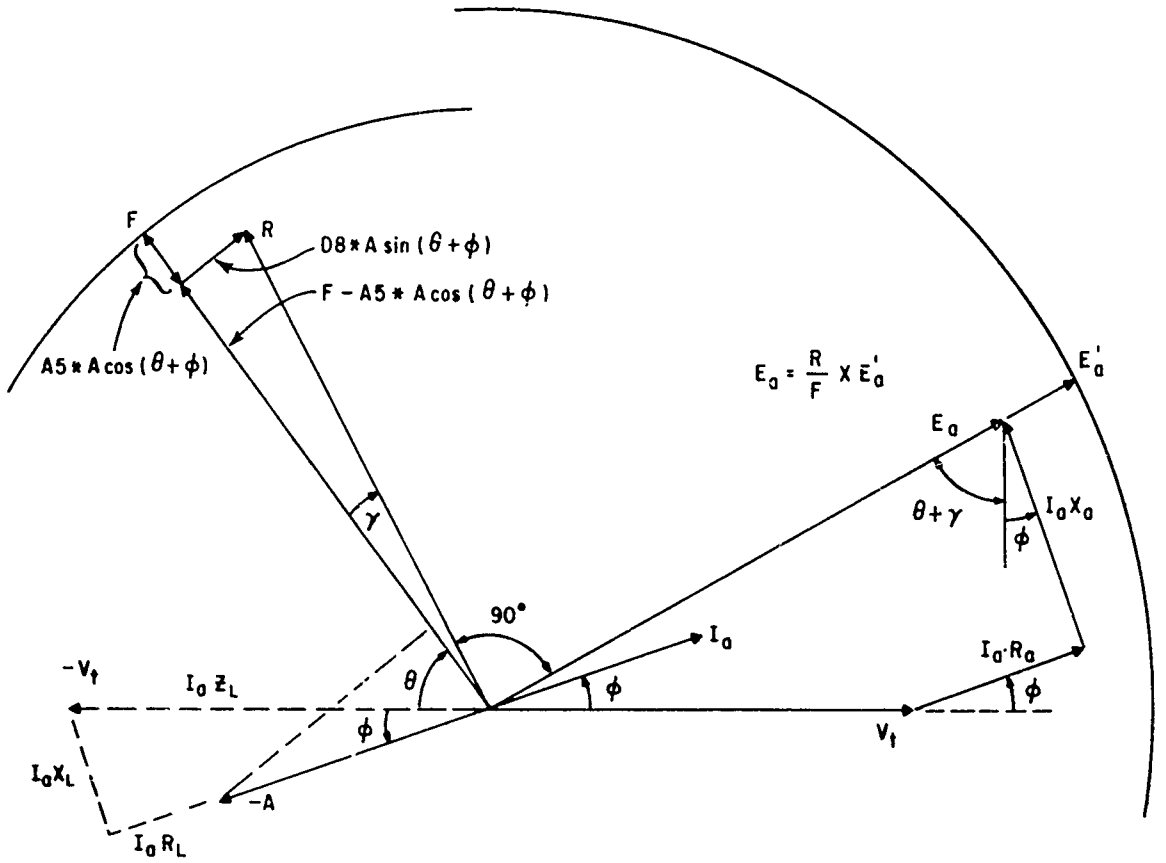

Figure 2.1.1.17-1. Vector Diagram (Scaled for Illustrative Purposes)

2.2 ELECTROMAGNETIC DESIGN

2.2.1 Alternator Design

The contract alternator design is shown in Figure 2.2.1-1. The stack length, rotor magnet, and cage outside diameter are the same as those of the General Electric alternator. The iron laminations were designed to provide more slot space for windings, and the housing is relieved on the turbine end to allow more clearance for end turns. The alternator stator detail and assembly drawing number is 542C692.

The alternator design evolved in three stages. A preliminary design was superceded by computer design D-81368, which included features suggested by the contracting officer's representative. A final computer design, D-90702 (Table 2.2.1-1) included the new winding configuration development discussed in section 3. Limited end turns space comprised the copper section slightly but lowered the strand insulation stress.

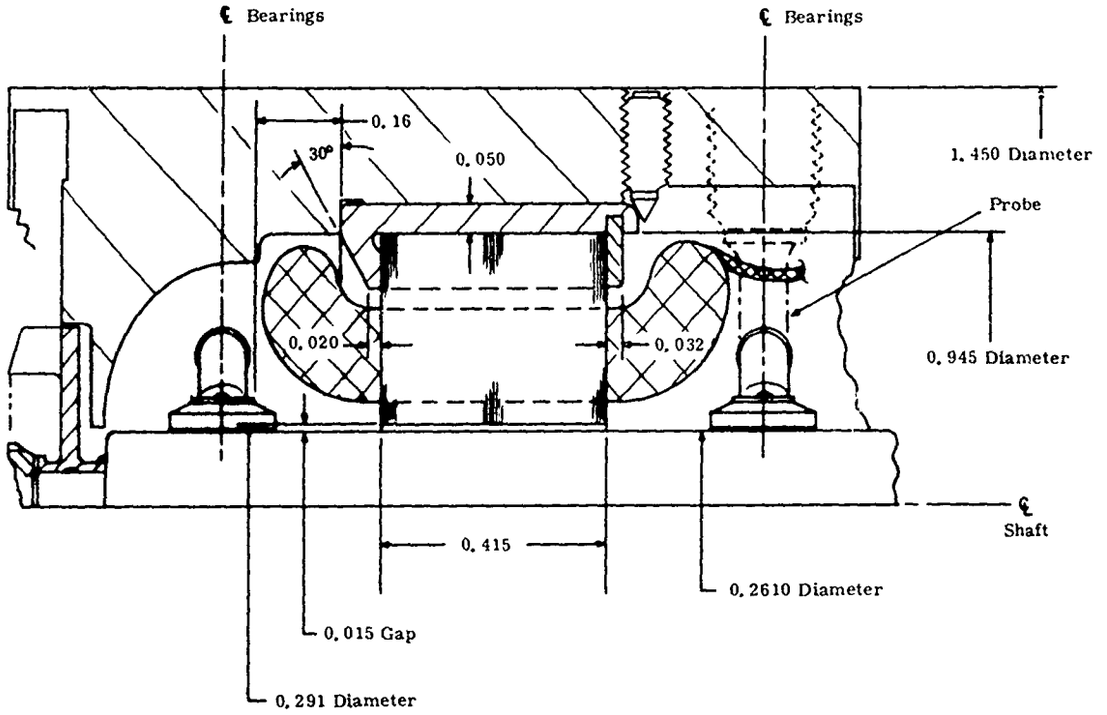

Figure 2.2.1-1. Alternator Final Design

2.2.2 Computed Alternator Performance

Output power for speeds of interest, unity and 0.8-power-factor lag, and 300°K and 77°K is tabulated in Table 2.2.2-1. The effect of lagging power factor is to lower terminal voltage and raise line current for a given output power. The increased copper loss results in a lower efficiency.

A better evaluation of the effect of power factor is shown in Table 2.2.2-2 where temperature (77°K) and speed (180,000 rpm) are held constant. Output power crests with varying power factor for a given output current. These crests are shown asterisked. For example, at 0.6 amperes and 0.95-power-factor lead, the maximum output power is 96.0 watts. To interpolate between four points in Table 2.2.2-2 for 100 watts, it would appear the optimum condition would be 0.628 amperes and 0.925-power-factor lead. The contract alternator would, by calculation for this power factor, produce 14.5 percent less copper loss.

To try to squeeze the most from this alternator, output power does not increase indefinitely with increasing current. For example, if the 0.85-power-factor lead data in Table 2.2.2-2 were calculated beyond the 1 ampere shown to 2 amperes, calculated characteristics shown in Table 2.2.2-3 would be obtained. The maximum possible output in this table is 239.4 watts at 1.7

Table 2.2.1-1

CALCULATED ALTERNATOR FEATURES AND PERFORMANCE

Alternator Features	Performance	
	Computer Design D-81368	Computer Design D-90702
Stator		
Outside diameter punching (inch)	0.945	0.965
Inside diameter (inch)	0.291	0.291
Length (inch)	0.415	0.415
Material (inch)	0.004 Hymu 80	0.004 Hymu 80
Number of slots	12	12
Spiral (degrees)	21	21
Tooth width (inch)	0.044	0.044
Circuits	1	1
Connection	Wye	Wye
Pitch (percent)	100	83.3
Conductors per slot	103	70
Wire	1-0.0080 HF	1-0.0080 HF
Turns in series per phase	206	140
Pitch factor	1	0.967
Distribution factor	0.967	0.965
Skew factor	0.995	0.993
Stacking factor	0.95	0.94
Resistance (77°K) (ohms)	1.33	0.84
Leakage reactance (ohms)	56	24.7
Rotor Field		
Diameter (inch)	0.261	0.261
Length (inch)	0.375	0.375
Material	Co-Pt	Co-Pt
Air gap (inch)	0.015	0.015
Performance (77°K)		
Power factor	1	1
Output (watts)	100	100
Line-to-line volts -- no load	138	93
Line-to-line volts -- full load	125	85
Current (amperes)	0.416	0.680
Current density (amperes per square inch)	8,280	13,600
Core loss (watts)	0.43	0.50
Copper loss (watts)	0.70	1.17
Electromagnetic efficiency (percent)	98.8	98.3

Table 2.2.2-1

OUTPUT POWER FOR ALTERNATOR D-90702 (CALCULATED)

Speed (rpm)	Power Factor (per Unit)	Temperature (°K)	Total Output (Watts)										
			0 Ampere	0.1 Ampere	0.2 Ampere	0.3 Ampere	0.4 Ampere	0.5 Ampere	0.6 Ampere	0.7 Ampere	0.8 Ampere	0.9 Ampere	1.0 Ampere
180,000	1.0	300	0	15.9	31.3	46	59.8	72.6	84.1	94.1	102.4	108.8	112.9
180,000	1.0	77	0	16.1	32	47.5	62.5	76.7	90	102.2	113.1	122.3	129.5
140,000	1.0	300	0	12.4	24.2	35.4	45.8	55.4	63.9	71.1	77	81.2	83.6
140,000	1.0	77	0	12.5	24.9	36.9	48.5	59.5	69.8	79.2	87.6	94.7	100.2
220,000	1.0	300	0	19.5	38.5	56.6	73.8	89.8	104.3	117.1	127.9	136.4	148.2
220,000	1.0	77	0	19.7	39.1	58.1	76.5	93.9	110.3	125.2	138.6	149.9	158.9
180,000	0.8 lag	300	0	12.3	23.5	33.4	42	49.1	54.9	59.1	61.8	62.8	62.1
180,000	0.6 lag	77	0	12.4	23.9	34.2	43.4	51.4	58	63.1	66.8	68.8	69

Table 2.2.2-2

ALTERNATOR CHARACTERISTICS AT 180,000 RPM AND 77°K

Power Factor (per Unit)	Output Power (Watts)									
	0.1 Ampere	0.2 Ampere	0.3 Ampere	0.4 Ampere	0.5 Ampere	0.6 Ampere	0.7 Ampere	0.8 Ampere	0.9 Ampere	1.0 Ampere
0.80 lag	12.4	23.9	34.2	43.4	51.4	58	63.1	66.8	68.8	69
0.85 lag	13.3	25.6	36.8	46.9	55.8	63.2	69.2	73.5	76.1	76.8
0.90 lag	14.1	27.4	39.6	50.8	60.6	69.1	76.1	81.4	84.9	86.4
0.95 lag	15	29.3	42.7	55.1	66.4	76.3	84.7	91.5	96.3	99
Unity	16.1*	32*	47.5	62.5	76.7	90	102.2	113.1	122.3	129.5
0.95 lead	15.6	31.5	47.7*	63.9*	80.1*	96*	111.5*	126.4	140.3	153.3
0.90 lead	14.9	30.3	46.2	62.4	78.8	95.2	111.5*	127.6*	143.2*	158.2
0.85 lead	14.1	28.9	44.3	60.2	76.5	93	109.6	126.3	142.8	158.9*
0.80 lead	13.3	27.5	42.3	57.7	73.6	89.9	106.5	123.4	140.3	157.1

*Power crest

Table 2.2.2-3

ALTERNATOR CHARACTERISTICS AT 180,000 RPM AND 77°K CALCULATED TO 2 AMPERES

Power Factor (per Unit)	Output Power (Watts)										
	1.0 Ampere	1.1 Amperes	1.2 Amperes	1.3 Amperes	1.4 Amperes	1.5 Amperes	1.6 Amperes	1.7 Amperes	1.8 Amperes	1.9 Amperes	2.0 Amperes
0.85 lead	158.9	176.6	189.5	203.4	215.9	226.6	234.8	239.4*	238.4	228.3	184

*Power Crest

amperes. For another power factor, the results would be slighlty different. It is speculated that the very most output would be obtained at about 0.75-power-factor lead and about 2.5 amperes, but this maximum was not searched out.

The alternator is expected to operate at room temperature prior to cooldown. Room temperature characteristics may be obtained from Table 2.2.2-2 by subtracting, from the output, the increased I^2R loss at 300°K.

Table 2.2.2-4 shows calculated output power at room temperature for various line currents for unity and 0.95-power-factor lead. Note that the leading power factor of 0.95 is beneficial above about 45 watts. Generally, it appears that a leading power factor will be most beneficial for high loads.

Table 2.2.2-4

CALCULATED PERFORMANCE AT 180,000 RPM AND 300°K

Power Factor (per Unit)	Output Power (Watts)									
	0.1 Ampere	0.2 Ampere	0.3 Ampere	0.4 Ampere	0.5 Ampere	0.6 Ampere	0.7 Ampere	0.8 Ampere	0.9 Ampere	1.0 Ampere
Unity	15.9	31.3	46	59.8	72.6	84.1	94.1	102.4	108.8	112.9
0.95 lead	15.4	30.9	46.3	61.3	76	90	103.1	115.2	125.9	134.9

2.3 MECHANICAL ANALYSIS AND DESIGN

In the following paragraphs, the turboalternator design approach is outlined for application in refrigerators. The aerodynamic design of the turboalternator operating at 180,000 rpm and 100 watts output is based on the design and performance results of a General Electric Company turboalternator. Turboalternator material considerations are discussed for both room and cryogenic temperatures. The gas-bearing design criteria are described. From the aerodyamic and electromagnetic design, a thermal analysis of the alternator was made, and thermal insulation results are presented.

2.3.1 Design Approach

The turboalternator design approach was directed toward eventual application to operation in cryogenic refrigeration systems. The design was to be adaptable first, for use in an 80°K cryogenic refrigerator, and then, with a change of turbine wheel and nozzle, for use of the same turboalternator as one of the two units required in a 4.4°K cryogenic refrigeration system. The design point for a typical 80°K refrigerator and a 4.4°K refrigerator are shown in Tables 5.1-1 and 5.3-1.

The turboalternator operating environment will influence the design. The eventual system application will be in a cryogenic refrigerator where the flow is ducted to and from the cryogenic heat exchangers. The entire assembly of exchangers and turboalternators will be within a dewar to provide vacuum insulation. A radiation shield will also be wrapped around the components. The complete turboalternator will be enclosed in a vacuum-tight can. Only instrumentation and alternator leads will be brought in and out of the can. The turboalternator mounted inside the can is shown in Figure 2.3.1-1.

For initial purposes of testing the turboalternator at cryogenic temperatures, an open cycle test arrangement is most practical. A system found effective at the Research and Development Center is shown in Figure 2.3.1-2. The turboalternaotr is shown vertically, with the turbine wheel end down. Helium gas is ducted through a liquid-nitrogen cooling coil to the turbine inlet. The turbine exhaust is directed downward and is then guided, close to the turbine housing, upward to cool the alternator housing. The gas then reverses again and spills through the holes, shown on the platform holding the bell jar.

A typical set of test data during this type of operation of the General Electric turboalternator (for Run 25, Data Point 5) is shown in Table 2.3.1-1

The data of specific interest for alternator test results are shown along with gas temperatures and flow rates. The 15°K difference between the turbine inlet and winding temperature is a result of both the winding temperature joule heat generation and degree of cooling available from the cooling gas flow. The gas cooling is primarily from the turbine discharge as described above. In addition, there is bypass leakage from the turbine wheel tip to the alternator housing, resulting from the wheel inlet pressure. This bypass flow is considered further in the alternator heat transfer design analysis, because it is the source of cooling gas available in all modes of operation.

2.3.2 Aerodynamic Design

The turbine aerodynamic design is based on previous design and development sponsored by the General Electric Company. A variety of turbines has

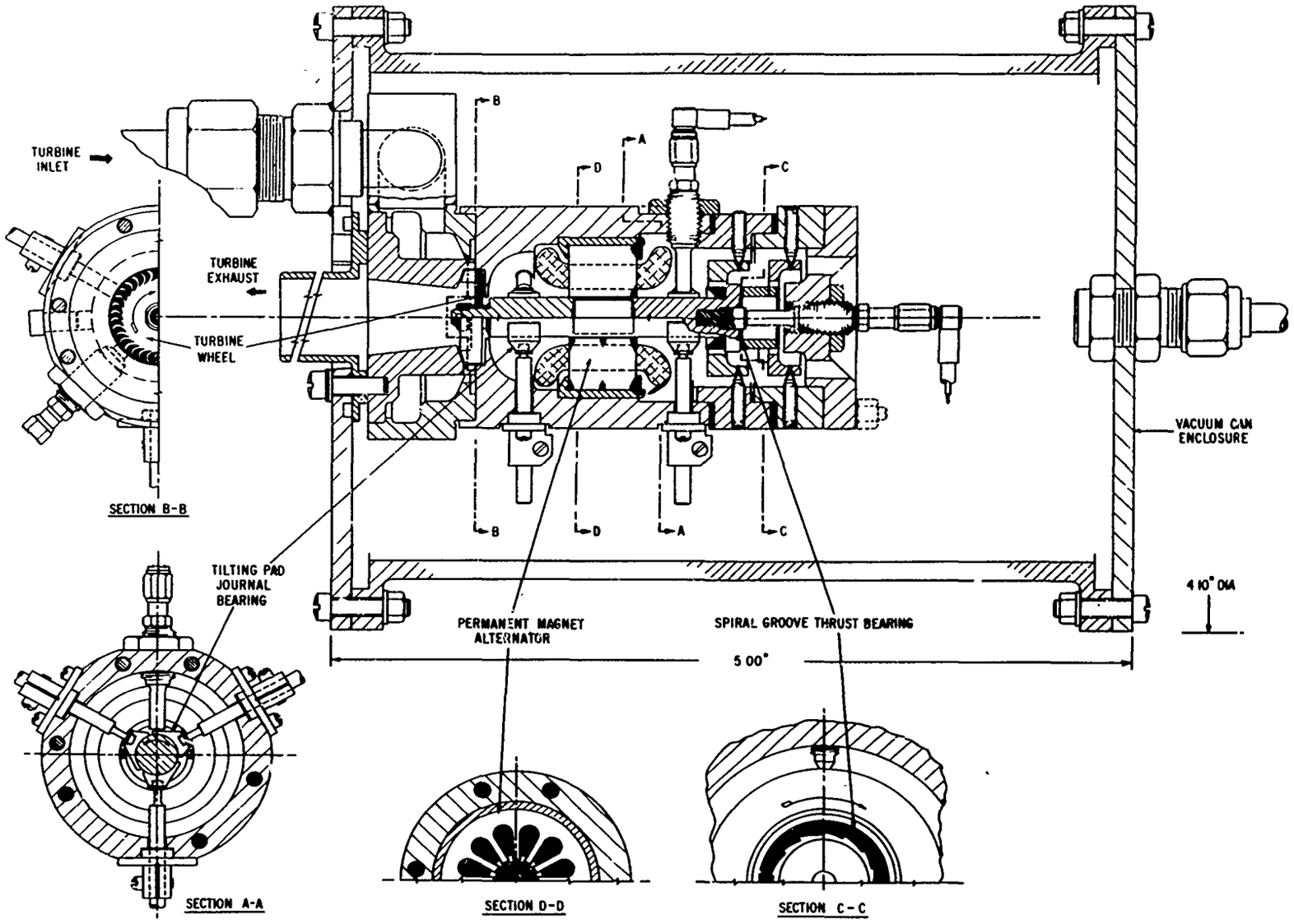

Figure 2.3.1-1. Turboalternator Assembly

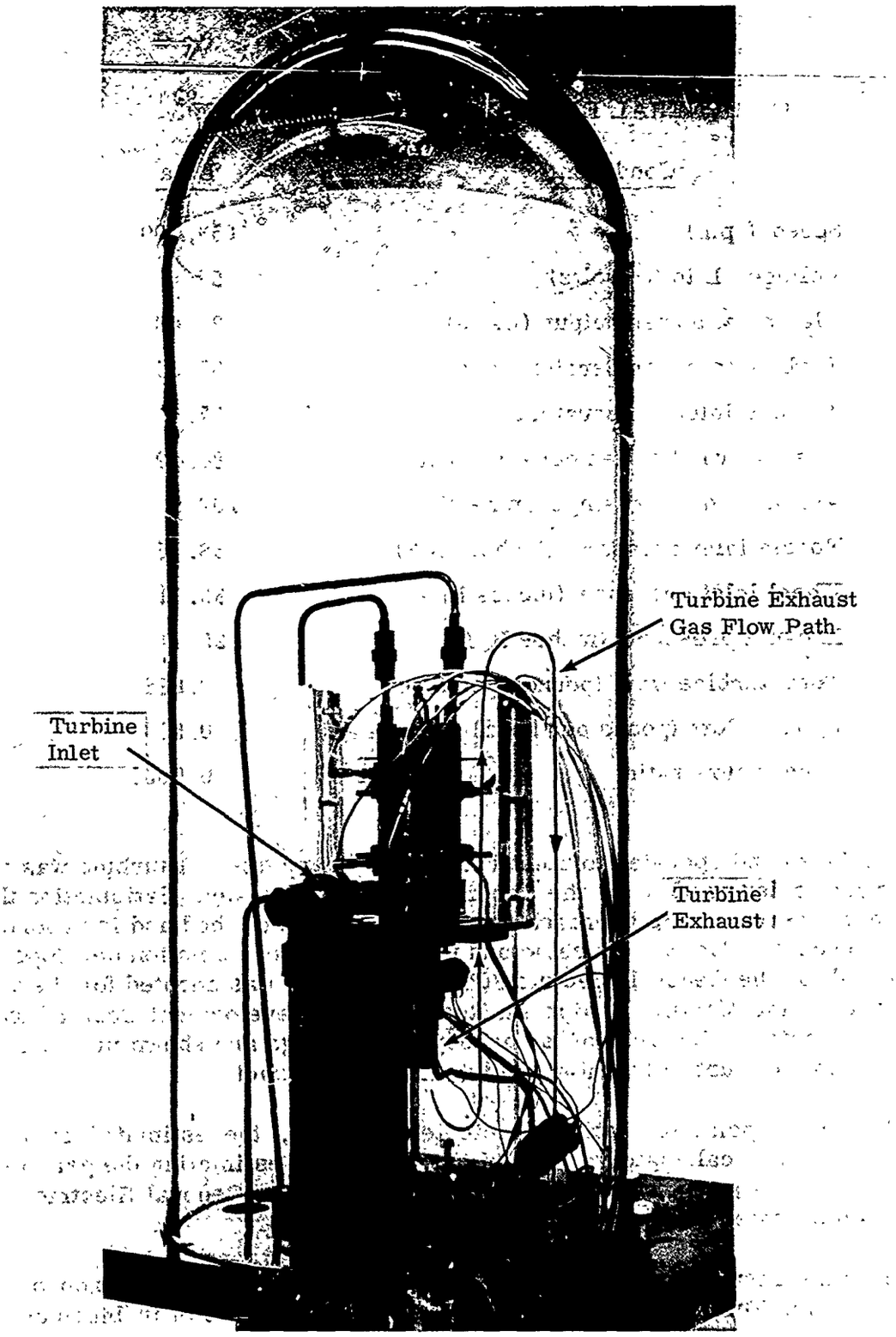

Figure 2.3.1-2. Open-cycle Turboalternator Test Arrangement

Table 2.3.1-1

TYPICAL TEST DATA
ON GENERAL ELECTRIC TURBOALTERNATOR

Condition	Data
Speed (rpm)	153,300
Voltage, L to N (volts)	52
Electrical power output (watts)	21.48
Turbine inlet temperature (°R)	157.65
Turbine inlet temperature (°K)	87.5
Average winding temperature (°R)	184.49
Average winding temperature (°K)	102.5
Nozzle inlet pressure (inches HgA)	38.76
Wheel inlet pressure (inches HgA)	33.81
Exhaust pressure (inches HgA)	29.61
Total turbine flow (pounds per hour)	9.088
Bypass flow (pound per hour)	0.593
Bypass flow ratio	0.0653

been designed and operated to meet varying requirements. A turbine was designed and tested at 80°K for the General Electric Company. Satisfaction that the general aerodynamic approach was sound was established and is reported in Reference 3. The same turbine and nozzle design combination developed and tested for the General Electric 80°K refrigerator was adopted for the turbine to drive the Mobility Equipment Research and Development Center high-speed alternator. Features of the aerodynamic design are shown in Table 2.3.2-1, for the turboalternator used under this contract.

For the design point test at cryogenic temperature, the estimated overall performance was calculated. The primary basis for estimating the performance was the results shown in Figure 2.3.2-1 for the General Electric turboalternator tested at cryogenic temperatures.

Performance results are shown with overall efficiency as a function of velocity ratio. This non-dimensional ratio is characteristic of turbines and is the wheel speed divided by the isentropic expansion velocity of the gas. The bypass ratio shown is the fraction of the total flow leaking from the nozzle exit to the alternator housing. The flow factor is a normalized parameter

Table 2.3.2-1

AERODYNAMIC DESIGN GEOMETRY

Design Feature	Data
Turbine wheel	
Drawing	422D343
Blades	36
Blade spacing (inch)	0.0545
Outside diameter (inch)	0.0625
Inside diameter (inch)	0.4608
Chord (inch)	0.08206
Cutter diameter (inch)	0.01615
Inlet angle (degrees)	60
Blade height at outside diameter (inch)	0.0730
Blade height at inside diameter (inch)	0.0993
Turbine nozzle	
Drawing	587E589
Admission (percent)	36.5
Openings	8
Angle (degrees)	72
Height (inch)	0.0734
Throat width (inch)	0.0244
Total nozzle area (square inch)	0.01425
Inside diameter (inch)	0.625

characteristic of the nozzle-turbine operation, and is also a function of pressure ratio. Appendix I completely defines these parameters.

Testing the newly designed contract alternator with this turbine design requires slightly different operating conditions. These were estimated based on the test results in Figure 2.3.2-1. An increase of flow factor with pressure ratio was estimated, and the overall efficiency and bypass flow ratio were assumed not to vary with pressure ratio.

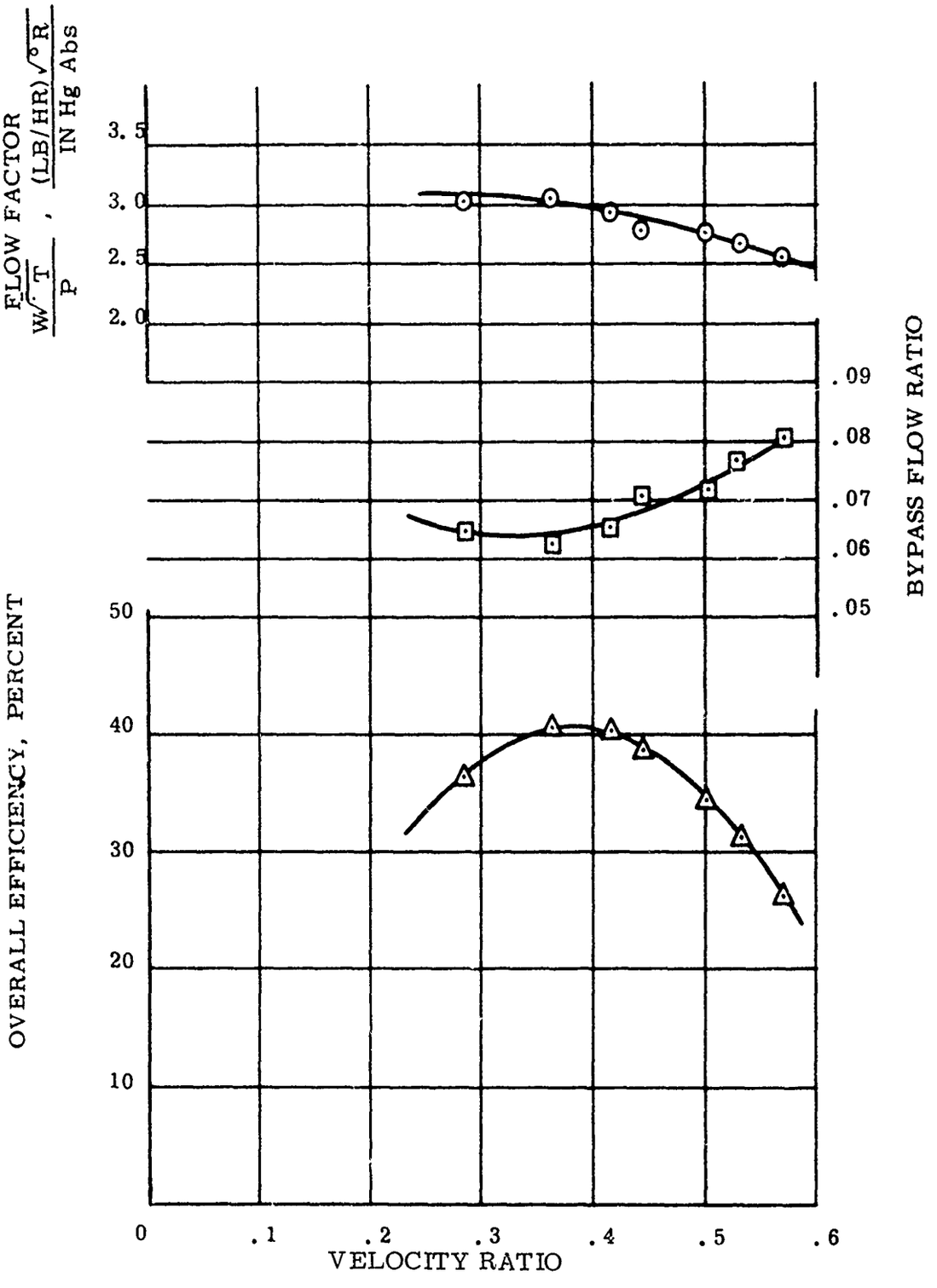

Figure 2.3.2-1. Turboalternator Performance Test Results (Helium Gas Inlet Temperature 157°R (Typical); Pressure Ratio 1.3)

At the ambient exhaust pressure and with an 80°K turbine inlet temperature, the power output at 180,000 rpm is shown in Figure 2.3.2-2. Also shown as a function of inlet pressure is the bypass flow available for alternator cooling. The operating parameters, Table 2.3.2-2, are at the rated power for the alternator design. These values were estimated to be within 10 percent of the actual operating conditions that would be experienced when the alternator was tested.

Table 2.3.2-2

ESTIMATED TURBOALTERNATOR PERFORMANCE FOR CRYOGENIC ALTERNATOR TESTS

Characteristic	Parameter
Electrical power output (watts)	100
Speed (rpm)	180,000
Inlet temperature (°K)	80
Inlet pressure (inches Hg A)	62.0
Exhaust pressure (inches Hg A)	29.92
Pressure ratio	2.075
Total mass flow (pounds per hour)	19.2
Bypass flow (pounds per hour)	1.2
Velocity ratio	0.324
Overall efficiency assumed (percent)	39.5
Gas	Helium

2.3.3 Materials Considerations

One of the principal materials properties which must be taken into consideration is the embrittlement of carbon steels at low temperatures. The safest technique is to avoid the use of this material, except where it is needed for magnetic properties. In those areas, and where it could be subject to structural loads or especially shock loads, other materials with superior low-temperature properties are needed. Carbon steel should be avoided for parts such as bolts, snap rings, springs, and so forth, but should be capable of carrying compressive and light tensile loads if significant shock and vibration are not present.

The tendency of a metal to brittle fracture and lose ductility with decreasing temperature depends to a great extent upon its crystal structure. Metal with body-centered cubic crystal structures is generally severely embrittled at low temperatures. Common metals in this group are iron, chromium, columbium, molybdenum, and tungsten. Many of the face-centered cubic metals retain considerable ductility at cryogenic temperatures. Metals in this group are aluminum, copper, and nickel. Unalloyed metals with a

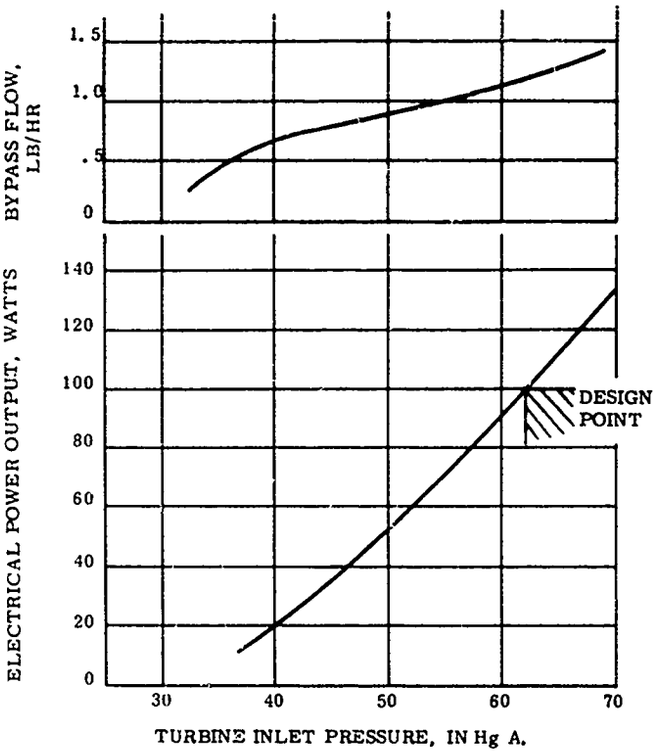

Figure 2.3.2-2. Estimated Turbine Performance (Helium Gas Inlet Temperature 80°K; Exhaust Pressure 29.92 in Hg A; Speed 180,000 rpm)

hexagonal close-packed structure also tend to retain their ductility at low temperatures. Examples of these are titanium, magnesium, and beryllium.

Aluminum alloys tend to increase in yield strength and decrease in ductility as temperature drops. The extent to which these changes take place varies with the alloy. Age-hardened 2000 and 7000 series aluminum alloys provide the highest strengths, but their ductilities could be marginal at very low temperatures. Welding reduces the ductility of these alloys still further. The 5000 series aluminum alloys offer considerably higher ductilities and are not appreciably affected by welding. These alloys are the weakest of the aluminums, however. Aluminum casting alloys have strengths the same as 5000 series alloys, but are ductile only to around -320°F or 77°K.

Stainless steels of the 300 series and some modifications of them are composed of a single phase austenite structure. Because austenite has a face-centered crystal structure, many of these steels are suited for low-temperature service. Yield strength tends to increase at low temperature and ductilities remain high.

Titanium alloys are good choices for low-temperature use when weight considerations or some other property of the metal is important. At tem-

peratures below 77°K, some titanium alloys are reported to decrease in ductility. Mechanical properties of titanium alloys are highly sensitive to interstitial element contant.

There are many sources of information on low-temperature properties of metals and alloys (Refs. 22 through 26).

The mechanical design of machinery for cryogenic service is complicated primarily by the dissimilar thermal contractions of the materials. At any mating joint of dissimilar materials the effects of these contraction or expansion differences must be accommodated. The thermal coefficient of expansion is not constant and varies considerably with temperature for a given material. Furthermore, the coefficient is a nonlinear function of temperature. For these reasons, it is not practical to work with expansion coefficients except over small temperature ranges. When temperature ranges are wide, it is more useful to refer to a curve or table showing the change of length per unit length at room temperature as a function of temperature. Such a curve for several common materials is presented in Figure 2.3.3-1. These curves have been cut off at 160°K, but if extended, all the curves would converge and cross at 293°K and at zero on the ordinate axis.

Interference fits are frequently used on conventional machines. It is evident, Figure 2.3.3-1, that contraction differences between metals can lead to failure of these interference fits, either from loosening of the fit or tightening it to beyond the elastic limits of the materials involved.

Materials selections for the turboalternator for mechanical design are based principally on low-temperature ductility and compatible thermal expansion characteristics throughout the range of operation. Austenitic stainless steels (300 series) are most suitable at low temperatures. Although it is a difficult process, 304 stainless can be nitrided for a hard gas bearing surface, while 303 stainless is preferred for ease of machining.

Both titanium and aluminum are good turbine wheel materials. Titanium is required for very high peripheral speeds because it has a high strength-to-weight ratio.

Beryllium copper is a wear-resistant material of high strength, and has expansion characteristics similar to 300 series stainless steel. It is also adaptable to photoetching for thrust bearing use.

A compilation of pertinent material properties is shown in Table 2.3.3-1.

2.3.4 Gas Bearings

The bearing selection is critical to the overall turboalternator as a system because low losses and consistent operation are required. Ball bearings for

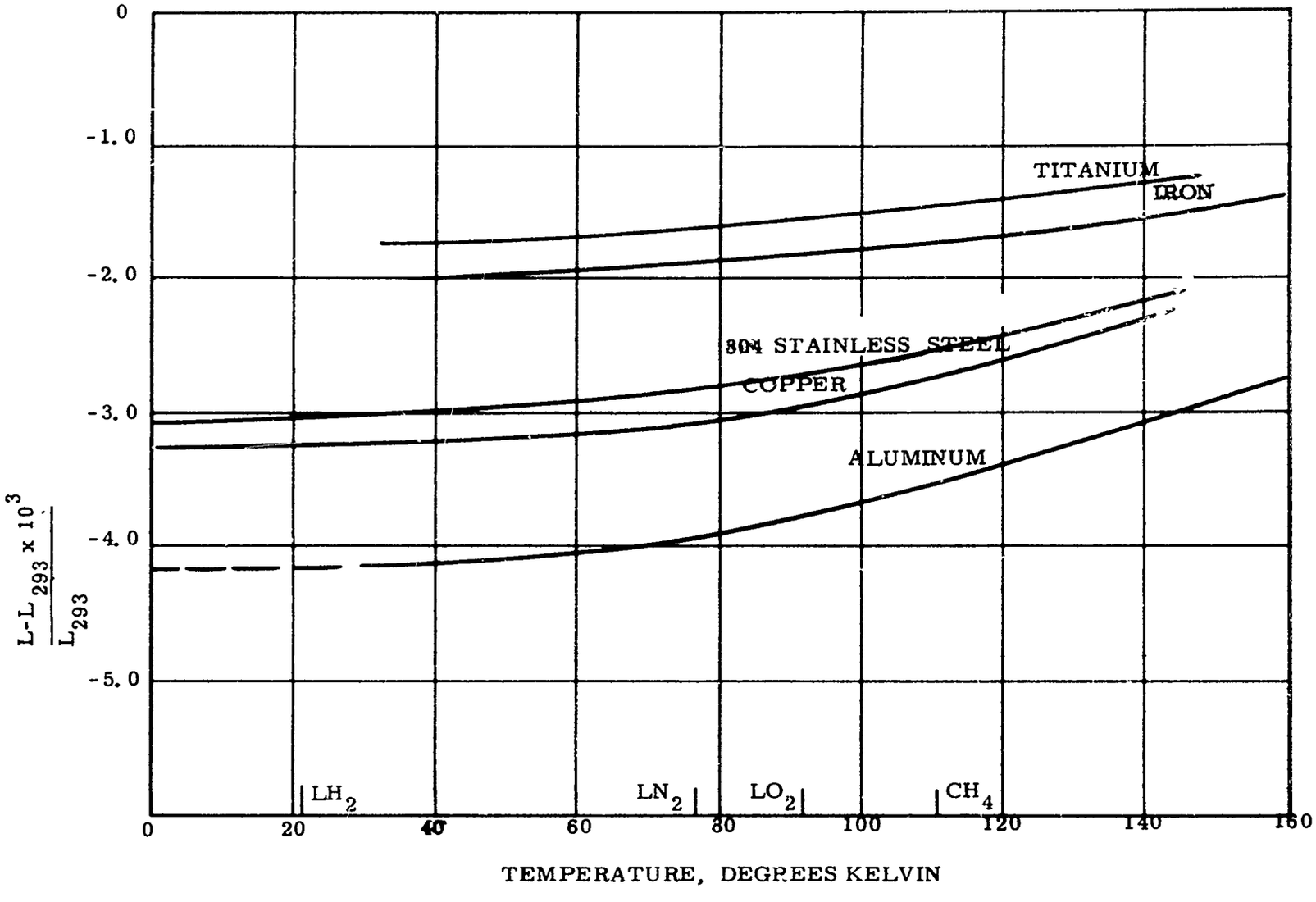

Figure 2.3.3-1. Thermal Contraction of Common Metals with Temperature

Table 2.3.3-1

MATERIAL PROPERTIES

Material	Alloy	Thermal			Mechanical							Electrical Resistivity (Micro-ohm-cm)
		Coefficient of Expansion (1/°F)	Specific Heat (B/Lb°R)	Conductivity (B/Hr-ft°R)	Yield Strength (Psi)	Tensile Strength (Psi)	Impact Charpy V (ft-lb)	Hardness	Density (Lb/In^3)	Modulous Elasticity in Tension (Psi)	Poissons Ratio (Nondimensional)	
310 stainless steel	310	8×10^{-6} (68-212°F)	0 12 (68-212°F)	8 (212°F)	30,000 (68°F)	75,000 (68°F)	70 (68°F)	R_b90	0 ?9	30×10^6 (68°F)	0.26	78 (68°F)
		7.06×10^{-6} (68-300°F)			88,000 (-380°F)	774,500 (-380°F)	45 (-380°F)			32×10^6 (-380°F)		
Titanium	6AL-4V ELI	4.9×10^{-6} (32-212°F)	0.135 (68°F)	4.2 (68°F)	120,000 (68°F)	130,000 (68°F)	18 (68°F)	R_c36	0.160	$16\ 5 \times 10^6$	0 34	171
		3.77×10^{-6} (68-300°F)			220,000 (-380°F)	240,000 (-380°F)				18×10^6 (-380°F)		
PLACOVAR Pl-Co magnet	50-50 Pl-Co AT ≤ 76.7% Pl by weight	7.67×10^{-6} (0-300°C)	0.05 (est)	40 (est)		100,000 (68°F)		R_c52	0.567	37.7×10^6	0.05 (est)	30
Hymu 80 laminations	B3F7C	7.17×10^{-6} (-70-200°C)		90 (77°K)		135,000		R_b95	0.316	33.7×10^6		
Beryllium copper	B11H51D3 (Alloy 25)	9.77×10^{-6} (25-300°C)	0.10	7	110,000 140,000	135,000			0.301	19×10^6		
Aluminum	7075-T6		0.216	67 (+50°F)	74,000 (+50°F)	85,000 (+50°F)	6 5 (+50°F)	180 dph (+30°F)	0 096	10.6×10^6 (+50°F)		
		40×10^{-6} (70-350°F)		31 (-350°F)	92,000 (-350°F)	102,000 (-350°F)	4.0 (-350°F)	220 dph (-350°F)		$11\ 2 \times 10^6$ (-350°F)		

operating at speeds up to 180,000 rpm are not attractive for low friction losses. Also, operation at cryogenic temperatures would require design and development steps to advance the state of the art. Gas bearings are the only practical approach.

Gas journal bearing selection can first be made on either self-acting or an externally pressurized basis, where the latter requires a high-pressure gas source prior to starting. This results in a refrigerator system loss of high-pressure gas and, further, a subsystem would be required to provide gas to the bearings during operation. Candidate journal bearing types are shown in Table 2.3.4-1. The externally pressurized porous version has been attempted

Table 2.3.4-1

COMPARISON OF JOURNAL BEARING TYPES

Bearing Type	Load Capacity	Any-attitude Stability	Manufacture and Development Risk	Refrigeration Loss	
				Friction	Gas Supply
Externally pressurized					
Orifice fed	Good	Possible whirl and hammer	High	Low	Some
Porous	Good	Possible whirl and hammer	High	Low	Some
Self-acting					
Cylindrical	Moderate	Possibly unstable	High	Moderate	None
Tree lobe	Moderate	Good	High	Moderate	None
Spiral groove	Moderate	Good	Low	Moderate	None
Tilting Pad	Moderate	Good	Low	Moderate	None

by the General Electric Company but was not completely developed. The orifice-fed bearings have been successfully developed, based on pioneering efforts by Sixsmith at the National Bureau of Standards.

The other self-acting journal bearings listed are in various stages of research and development. The first three have not been successfully reduced to practice in high-speed miniature machinery and were not considered seriously because considerable development effort might be required. The tilting

pad journal had been reduced to practice in many large machines and one miniature cryogenic turbine. The development successes behind the tilting pad made it a logical journal bearing candidate for the General Electric turboalternator.

A similar comparison can be made for thrust bearing selection. Externally pressurized thrust bearings were passed over because refrigerator system gas is required. The choices of self-acting gas thrust bearings are:

- Inward-pumping spiral groove
- Outward-pumping spiral groove
- Step bearings
- Tilting pad

The first has the best load capability, superior to the other three. Spiral groove thrust bearings have had a good record of development success in large and small machinery. Step bearings have been successfully developed for large machinery, when the mechanical configuration excludes spiral groove thrust bearings. At the General Electric Company, the gimbal-mounted spiral groove thrust bearing has proven to be a suitable choice.

A recent independent study under contract to the U. S. Air Force (Ref. 27) concluded that for miniature cryogenic turbines, tilting pad journal bearings and spiral groove thrust bearings were the best selection.

A complete discussion on the turboalternator gas bearing design is given in Reference 1.

2.3.5 Thermal Analysis

Heat loads for the turboalternator to be used in the thermal design and analysis have been estimated. Alternator electrical losses were established above. The pole face and stray load loss heat loads were assumed to be insignificant.

Windage and bearing friction losses were calculated with the General Electric Company turboalternator design computer program. Computer design parasitic losses for helium gas operation are shown in Figures 2.3.5-1 and 2.3.5-2 for room temperature and liquid nitrogen temperatures. The alternator gap is the annular section between the magnet and the toothed stator. The word "shaft" refers to the free shaft area. The bearing loss includes both the journal and the thrust elements. The turbine disc is the back side of the turbine wheel. The total of these friction and windage losses is shown for each operating temperature. Prior to test results, it must be confirmed that the total of the bearing and windage parasitic losses were in reasonable agreement with the summation of the calculated parasitic losses.

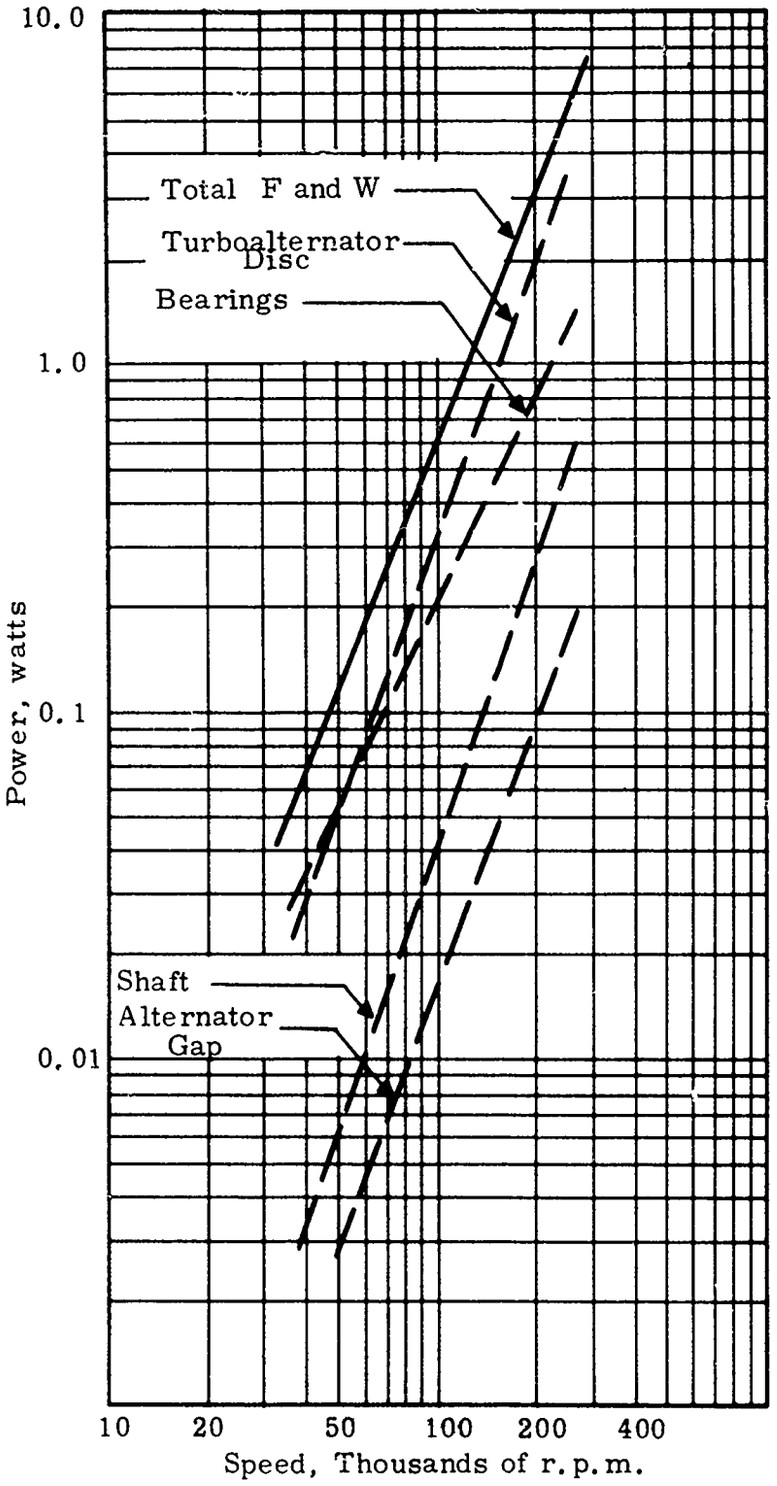

Figure 2.3.5-1. Design Program Parasitic Losses, Helium Gas at 138.8°R

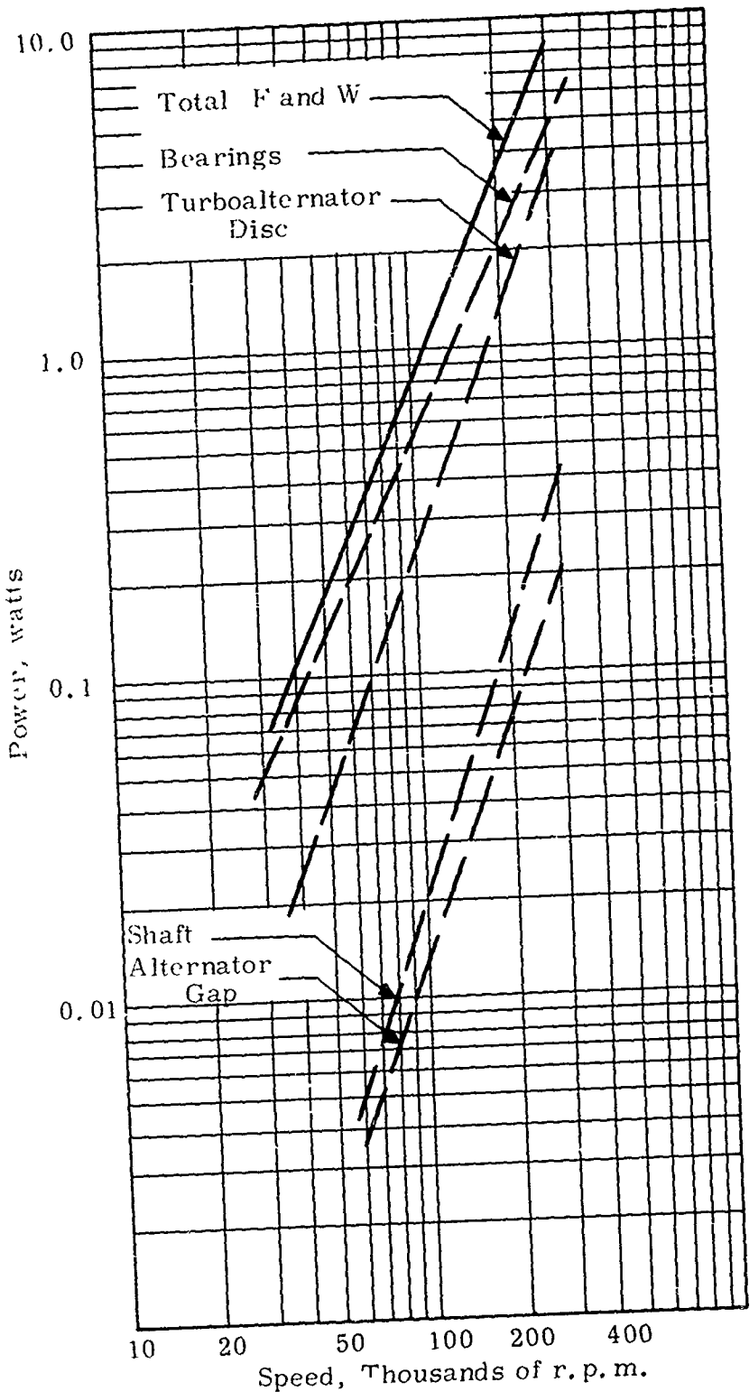

Figure 2.3.5-2. Design Program Parasitic Losses, Helium Gas at 540°R

Alternator joule (I^2R) losses were determined in paragraph 2.1 above. A complete distribution of all heat loads at the rated alternator condition is listed in Table 2.3.5-1.

Table 2.3.5-1

DISTRIBUTION OF ALL HEAT LOADS
AT RATED ALTERNATOR CONDITION

Turboalternator Component	Head Load (Watts) (80°K, 180,000 rpm)	
	Individual Load	Total
Alternator		
Core	0.430	
Copper	0.700	
Pole face	nil	
Stray load	nil	
Total		1.130
Windage		
Disc	1.385	
Shaft	0.213	
Gap	0.072	
Total		1.670
Bearings		
Each journal	0.253	
Both thrust faces	0.160	
Total		0.666
Total heat loss		3.466

To obtain extreme conditions and limits of the turboalternator as a thermal system, order of magnitude calculations were made. Based on the heat loads given in Table 2.3.5-1 and the estimated overall performance shown in Table 2.3.2-2, calculations were made for extreme operating conditions.

Assuming no turbine bypass flow to cool the alternator, and assuming the entire heat load is absorbed by the turbine inlet gas flow, the turbine inlet temperature would rise 0.282°K. This assumes perfect conduction of all heat paths to the turbine inlet gas. Then, assuming no conduction from the heat loads to housing, and all of the heat absorbed by the turbine bypass flow, the 1.2 pounds per hour turbine bypass flow temperature would rise 4.51°K.

The detailed thermal analysis was initiated for the alternator design rating. The thermal circuit in Figure 2.3.5-3 shows the basis for the gas flow through the stator-rotor gap and the conduction paths to the shell and end turns. An electrical analog of this thermal circuit is shown schematically, in Figure 2.3.5-4, with the node temperatures and thermal conductances.

Heat balances at the nodes result in a set of equations:

$$Q1 = (TM1FE - TM2)\ G1 + (TM1FE - TM4FE)\ G2 \quad (8)$$

$$Q2 = (TM2 - TM1FE)\ G1 + (TM2 - TM3)\ G4 + (TM2 - TM1DE)\ G1 \quad (9)$$

$$Q1 = (TM1DE - TM2)\ G1 - (TM1DE - TM4DE)\ G2 \quad (10)$$

$$Q3 = (TM3 - TM2)\ G4 + (TM3 - TM4S)\ G7A + (TM3 - TM4G)\ G5A \quad (11)$$

Using these equations, the boundary temperatures were calculated, local heat inputs were established, and conductance values were determined. Results are shown on Table 2.3.5-2.

It was assumed that there was no heat conducted down the shaft. Also, it was assumed that there was no conduction from the laminations to the cage, which is a requirement to prevent an interference fit that would work harden the lamination iron.

With these boundary conditions, the solution of the simultaneous equations is shown on Table 2.3.5-3. Here the temperatures are shown as rises above the turbine inlet temperature of 80°K.

2.3.6 Thermal Insulation

Thermal insulation requirements for the turboalternator are considered for both the open-cycle turboalternator cryogenic test arrangement and the eventual refrigerator system application.

The open-cycle test arrangement previously used at the General Electric Company was described above, in conjunction with Figure 2.3.1-2. This system had allowed testing the GE alternator at a turbine inlet temperature of about 100°K. A lower alternator temperature can be achieved when a greater load is applied to the turbine because a greater turbine flow is avail-

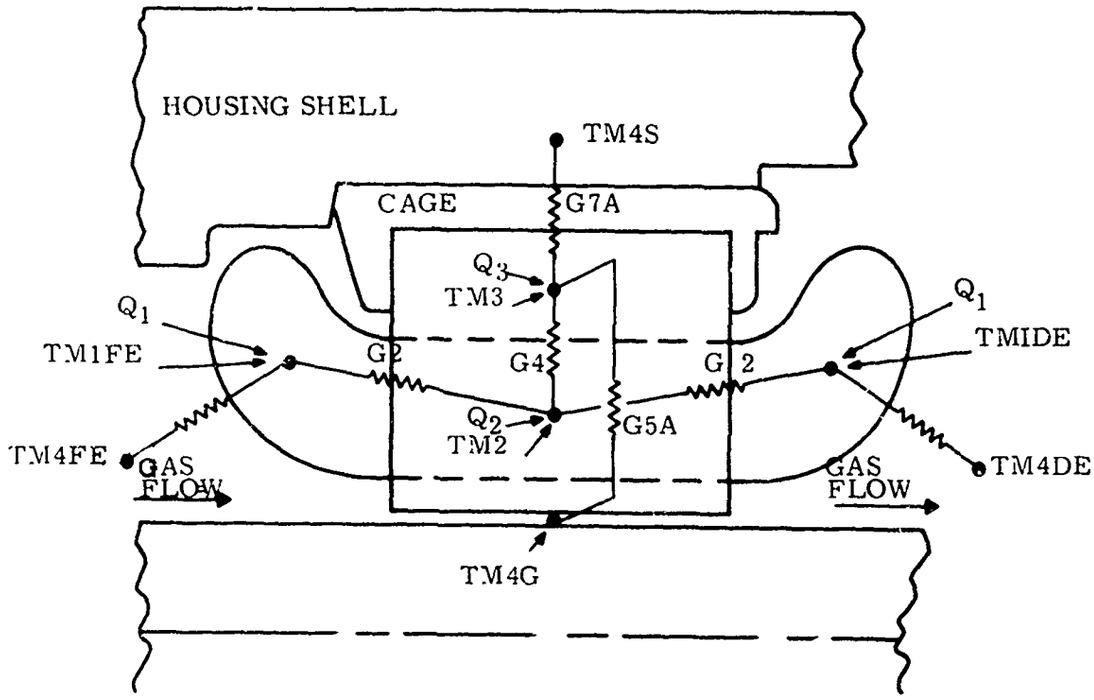

Figure 2.3.5-3. Thermal Circuit

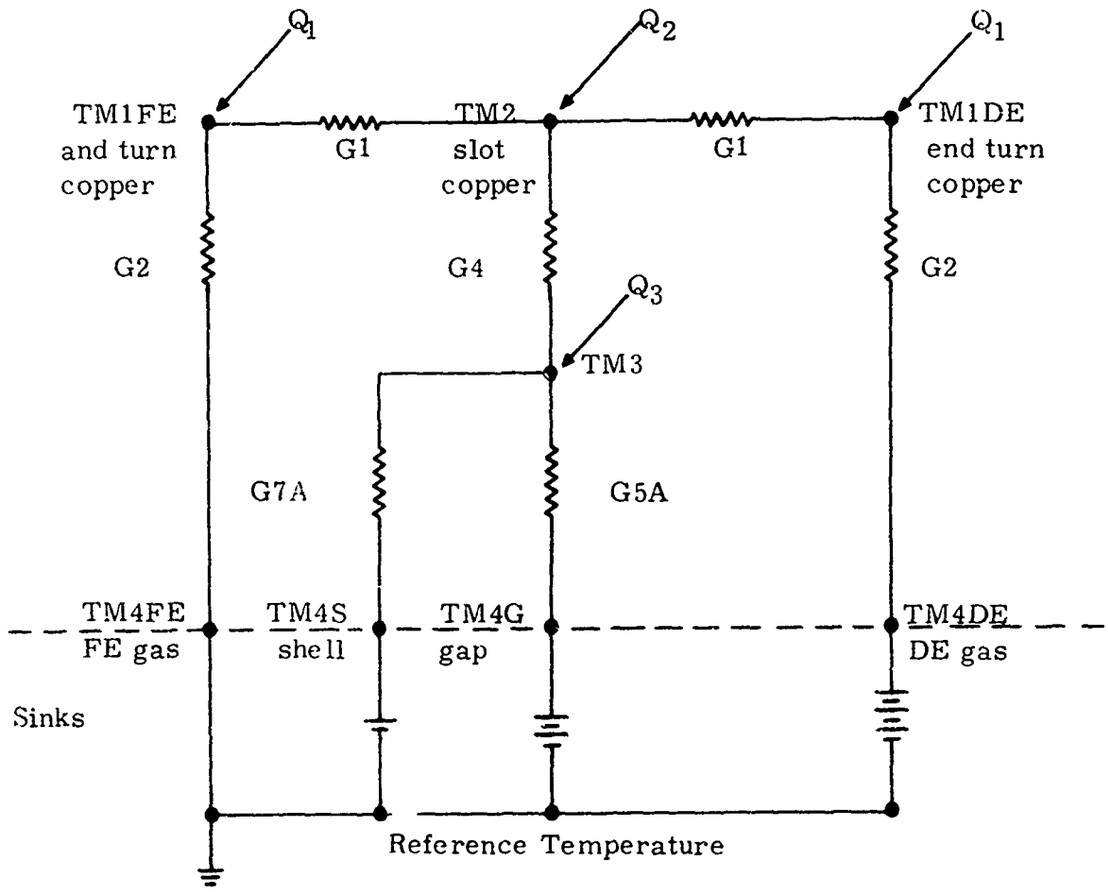

Figure 2.3.5-4 Thermal Circuit Schematic Diagram

Table 2.3.5-2

BOUNDARY CONDITIONS

Condition	Boundary
Temperature, T (°F)	
TM4FE	3.69
TM4G	3.78
TM4DE	4.10
Heat input, Q (watts)	
Q1	0.172
Q2	0.356
Q3	0.430
Conductances, G, B/hr (°F)	
G1	11.1
G2	33.4
G4	89.0
G5A	10.1
G7A	0

Table 2.3.5-3

ALTERNATOR STATOR TEMPERATURE RISE

Temperatures Above Turbine Inlet of 80°K	°F	°K	Symbol
End turn at gas inlet	5.70	3.16	TM1FE
Slot copper	10.80	6.00	TM2
End turn at gas outlet	14.64	8.14	TM1DE
Core	6.16	3.42	TM3

able from both the turbine bypass leakage and the turbine exhaust. If further cooling is required, a blanket of aluminized Mylar* could be used to wrap the bell jar. Another method to depress the temperature would be to duct an auxiliary helium gas flow, also precooled in liquid nitrogen, to the bell jar.

For thermal insulation requirements in a refrigeration system application, the turboalternator should be considered enclosed in a case, as shown in Figure 2.3.1-1. Local cooling of the alternator is provided by conduction and turbine bypass flow. This cooling flows along the alternator shaft, out the alternator housing inside the case, and then is ducted to the turbine exhaust line. Thus, it can be assumed that the turboalternator is at essentially constant temperature for system insulation purposes.

Convection heat leaks would be eliminated with vacuum insulation, with the system in a 10^{-5} torr vacuum, external to the case.

Radiation heat leaks have been calculated with and without radiation shielding. For the 3.5-inch diameter by 5-inch-long turboalternator can, radiation from the 300°K dewar wall to the can allows a 4.5-watt heat leak. An emissity of 0.2 was assumed. With the addition of a 0.5-inch layer of superinsulation, the turboalternator can heat leak would be reduced to 0.5 watts.

Conduction to and from the can is primarily through the plumbing which is essentially at the same temperature as the can. Other insignificant conduction paths would be the instrumentation leads and alternator power leads.

*Trademark of E. I. du Pont de Nemours and Company, Inc.

Section 3

ALTERNATOR MANUFACTURE

3.1 STATOR CORE ASSEMBLY

A quantity of commercial-grade photoetched laminations was obtained. These proved less economical than a laboratory grade because the wide dimensional tolerances required careful inspection and selection. The oxide coating, as received, was inadequate for interlaminar insulation. A polyimide coating 4 microns thick was applied. A 300-megohm interlaminar resistance was measured. No degradation of adherence was observed after repeated immersions in liquid nitrogen. The laminations were stacked in a stainless steel can with a 21-degree slot skew, and the can lip was rolled according to Figure 2.2.1-1.

3.2 WOUND STATOR CORE ASSEMBLY

The journal bearing pad stems, Figure 2.3.1-1, impose a space limitation on the end turns. However, it is permissible to extend the end turns 0.22 inch beyond the end of the stack. As the stator winding investigation continued, it became evident that the special restriction on the end turns would be the critical dimensions with which to contend.

Previous alternator stator designs fit comfortably within the allotted space. Our goal for the Mobility Equipment Research and Development Center stator, which was to increase the copper section to 365 percent, was achieved for the slots. However, it proved to be too ambitious in regard to the end turns with the space available, so in order to expedite the goal, an increase to 250 percent of the old copper section has been achieved, without much difficulty. Figure 3.2-1 shows the wound stator with thermocouple leads.

Six thermocouples have been imbedded in the windings. Two are in the end turns on the connection end and two are on the opposite end. Two thermocouples are in the bottom of the slot, in the middle of the stack (Figure I-1 shows a schematic representation of the instrumentation).

Three techniques for winding the stator core with more copper have been evaluated. Attributes of each technique are discussed below:

- One-hundred-percent Pitch Winding (Figure 3.2-2). In this three-phase winding configuration, there can be only one coil side per slot because there are only 12 slots. Belts in the same phase are shifted 30 electrical degrees. Therefore, the effectiveness in utilizing the magnetic flux is 0.67. This factor is comparable to pitch and distribution factors. The major drawback to this configuration is the lumping at three points in the end windings where belts in the same phase overlap. Also, the conductors from two additional slots must pass

Preceding page blank

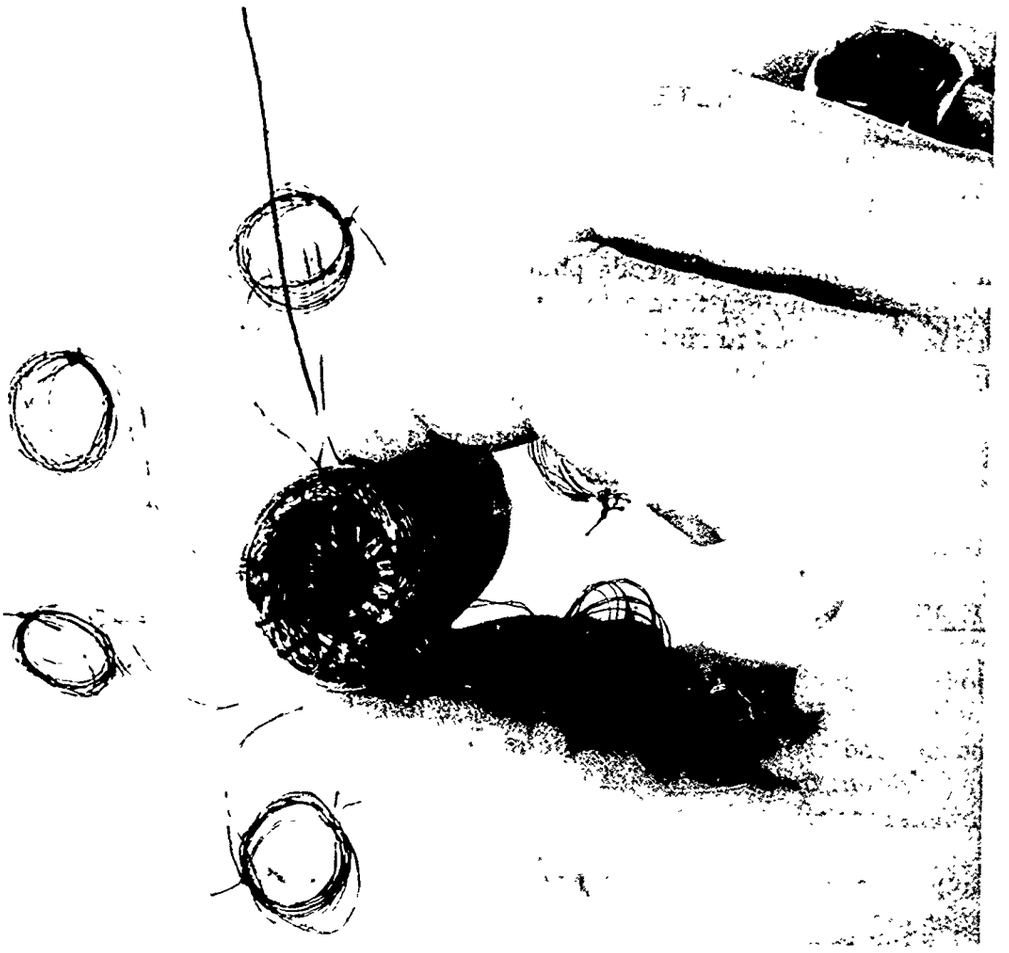

Figure 3.2-1. Turboalternator Stator

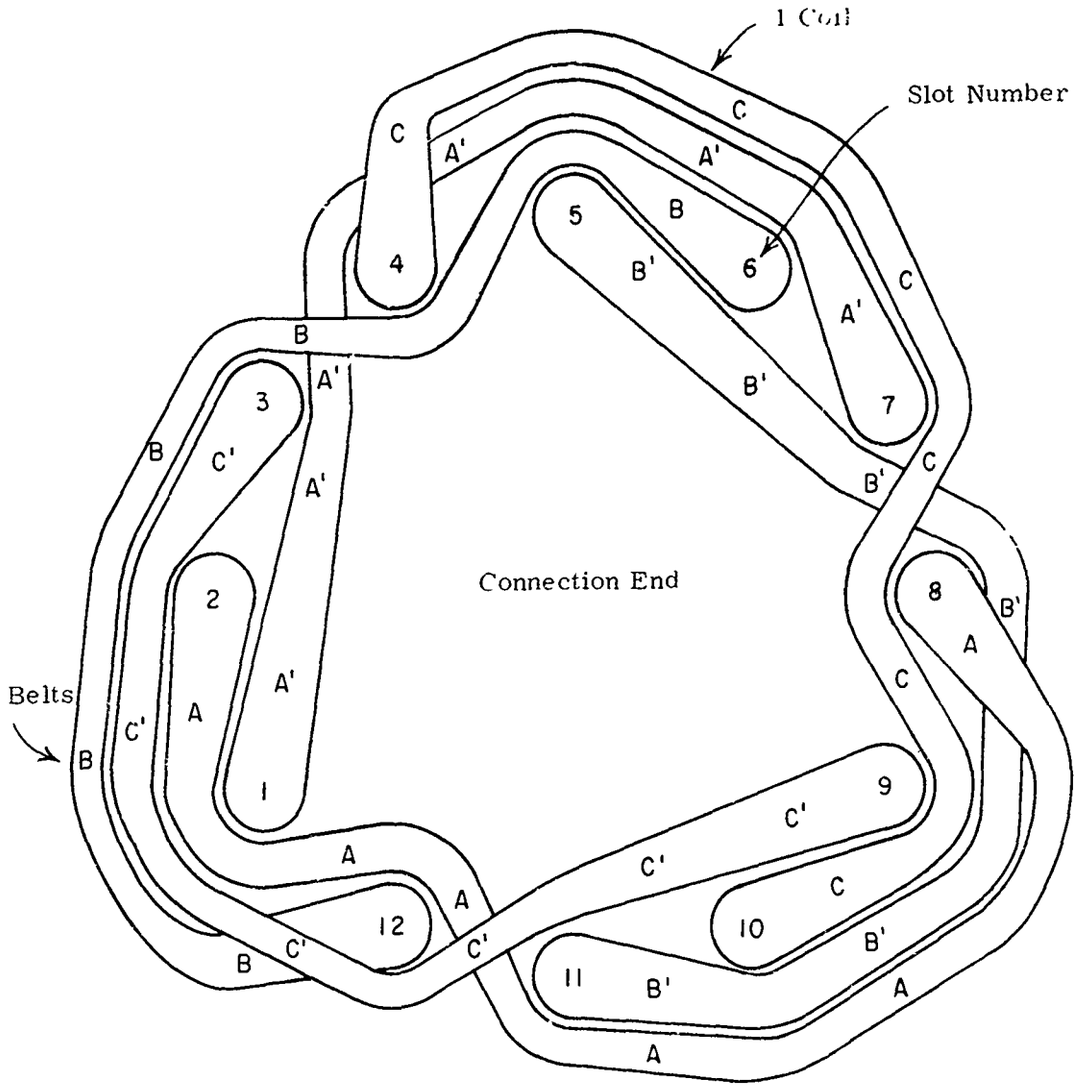

Figure 3.2-2. One-hundred-percent Pitch -- Six Coils

each other at these lumps. While this technique worked satisfactorily for previous designs which had a small copper section, it would prevent obtaining the goal of a section with more copper.

- Five-sixth-pitch Winding (Figure 3.2-3). Like the 100-percent pitch configuration, this winding has one coil side per slot. Belts in the same phase are symmetrical and do not overlap. Conductors from a maximum of three slots pass each other in the end turn region. The pitch factor is 0.967 and the distribution factor is 1.0. After insertion of four coils, it became apparent that still another technique was needed to come anywhere near the goal for an increased-copper section.

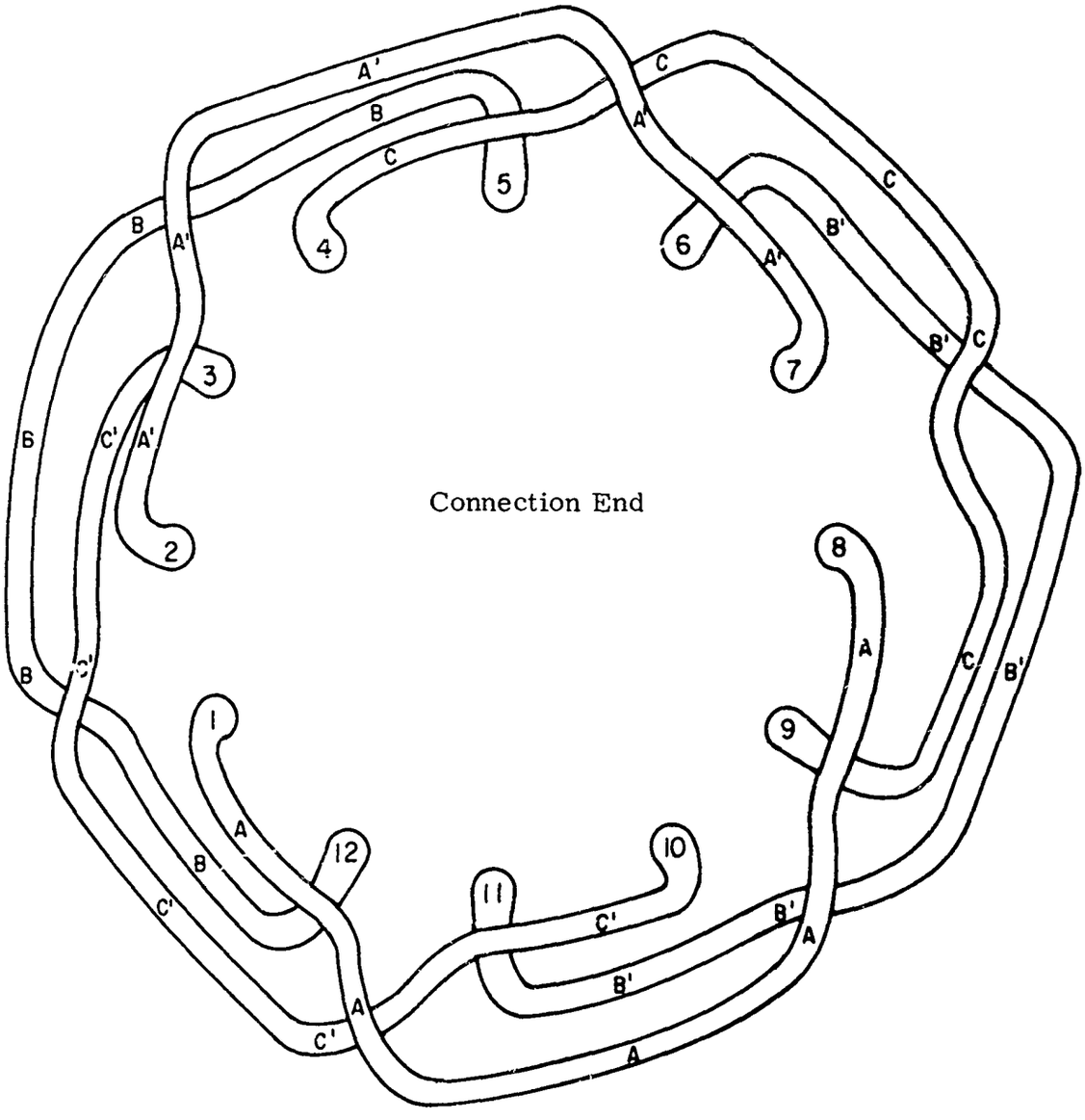

Figure 3.2-3. Five-sixth Pitch -- Six Coils

- Five-sixth-pitch Winding (Figure 3.2-4). The best winding is the standard distributed symmetrical winding. This allows two coil sides per slot, which is twice the number of coils for the two methods above, but with half the turns per coil. Twelve coils having 35 turns of 8-mil wire were inserted with ease. Pitch factor (Kp) is 0.967 and distribution factor (Kd) is 0.967. End turns from 2-1/2 slots nested uniformly about the periphery. This configuration results in better magnetic symmetry (armature reaction) and electrical (impedance) symmetry. End-turn nesting is greatly enhanced and bunching of end turns is eliminated.

  A major problem associated with this technique is the larger number of individual coils. Stripping insulation and soldering leads was performed with relative ease; however, it proved tedious to keep the 24 fine wires in sequence as they emerged from the tangle. Joints were insulated with a flag of Mylar tape.

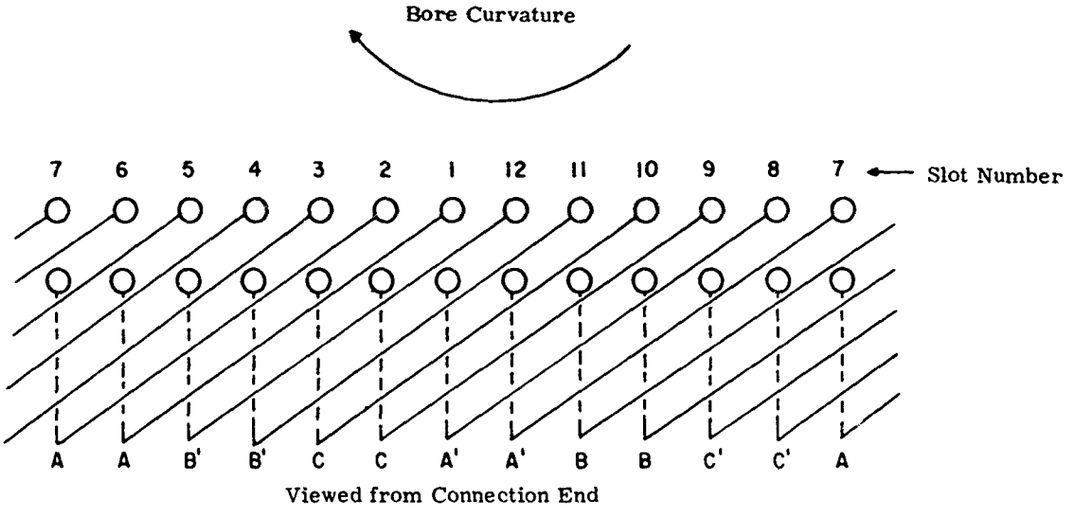

Figure 3.2-4. Five-sixth Pitch -- Twelve Coils

3.3 DESIGN SPECIFICATIONS REVISED

The following changes were adapted for the stator after encountering the previously discussed problems:

Characteristic	Change
Outside diameter (inch)	0.965
Pitch	5/6
Conductors per slot	70
Turns in series per phase	140

Pitch factor (Kp)	0.967
Resistance at 77°K (ohm)	0.84
Armature reactance (Xa) (ohms)	26

No reduction in power output capability was anticipated. Increased phase current, due to the lower terminal voltage, resulted in an increase in copper loss of 0.47 watt.

3.4 PERMANENT MAGNET FIELD

The platinum-cobalt magnets for alternators previously manufactured were not of uniform strength. One batch of fields, which was processed, exhibited a degradation of 4.7 percent after nitriding. A degradation of 10.6 percent was our immediate past experience on other fields.

Either of two phenomena was suspected. First, a time-temperature relationship for nitriding could possibly carry the Co-Pt permanent magnet characteristic beyond optimum B_r, or second, chemical contamination could be causing the deterioration of performance.

Subsequently another batch of fields was processed. Copper masks covered the magnets completely during nitriding. Test results before and after nitriding showed magnet deterioration exceeded 12 percent. It appears that the time-temperature relationship should be anticipated in the heat treat to obtain optimal properties for the Co-Pt magnet.

Discovering the right time to stop heat treating the virgin magnet, so nitriding will carry magnetization properties to optimum, could be an extended process. This development, which is beyond the scope of the present investigation, represents a potential saving of about 10 percent in alternator size, and is a worthwhile future development program.

Section 4

TURBOALTERNATOR TESTS, EVALUATION, AND ANALYSIS

In Section 4, turboalternator tests are described and then evaluated. Pertinent analyses of tests are made.

A brief summary of all pertinent performance tests conducted is shown in Table 4-1. At room or cryogenic temperature, the greatest speed, power, and efficiency among all the data points for the particular run are listed. Also shown for each run are the greatest overall and electromagnetic efficiencies determined.

Table 4-1

TURBOALTERNATOR PERFORMANCE TESTS

Test	Run	Temperature	Maximums			
			Electrical Load (Watts)	Speed (Rpm)	Overall Efficiency (Percent)	Electromagnetic Efficiency (Percent)
No load	100	Room	0	249, 540	0	0
No load	104	Room	0	219, 960	0	0
No load	106	Room	0	220, 680	0	0
No load	108	Cryogenic	0	180, 960	0	0
Load	101	Room	66. 9	181, 200	29. 79	96. 52
Load	102	Room	96. 2	220, 140	31. 38	96. 59
Load	103	Cryogenic	55. 26	247, 680	35. 7	96. 97
Load	105	Cryogenic	109. 03	219, 960	47. 90	98. 28
Load	107	Room	52. 64	215, 520	33. 55	96. 29
Load	109	Cryogenic	60. 83	180, 480	48. 06	98. 30

4. 1 TURBOALTERNATOR TESTS

The following paragraphs present all the pertinent tests conducted on the turboalternator. First the test plan for the tests conducted outlines the test requirements; then the laboratory test arrangement used in conducting the tests is described. Specific tests on the alternator stator, conducted before installing in the turboalternator, are described. Then a description of all turboalternator performance tests is presented, for both the room and cryogenic tests conducted.

4. 1. 1 Test Plan

The original test plan approved to test and evaluate the turboalternator follows.

4. 1. 1. 1 Magnetize Magnet. The magnet, as an integral part of the turboalternator shaft, will be magnetized in a field of 25, 000 gausses. The magnet strength will be measured with the flip coil test fixture and gaussmeter.

4. 1. 1. 2 Stator Resistance. Resistance measurements of all three phases will be made as a function of temperature. Room ambient and liquid nitrogen temperatures will be used. Thermocouples embedded in the stator windings will be the basis for temperature measurements.

4. 1. 1. 3 Waveform Test. Prior to assembly in the gas-bearing turboalternator housing, the magnet will be operated in the stator on a miniature lathe at a speed of about 2000 rpm. Photos of voltage waveform will be taken.

4. 1. 1. 4 Turboalternator Calibration Tests (Breakdown of Running Light Losses). Bearing friction, disc and shaft windage, and no-load core losses will be determined by operating the turboalternator at no load (both unmagnetized and magnetized). Tests will be conducted at both room and cryogenic temperatures, but with cryogenic instrumentation inaccuracies, qualification may have to be made with analysis. A prior flow leak characteristic calibration from the turbine to the housing will be used to determine bypass leakage. Pressure and temperature measurements across the turbine will be used to determine the work from the turbine wheel. The net power to the alternator will be the wheel power less the parasitic losses and housing bypass flow. The housing bypass flow will be gas available to cool the stator between the shaft and stator.

4. 1. 1. 5 Turboalternator Performance Instrumentation Checkout. The alternator will be instrumented to measure:

- Voltages, each leg
- Winding temperature, two thermocouples at each end of winding
- Yoke outside diameter temperature, two thermocouples at mid length
- Stator slot temperature, two thermocouples at mid length
- Alternator gas temperature, two thermocouples at outlet
- Alternator gas flow rate (this will be the same as the precalibrated flow leak rate from turbine tip to housing)
- Turbine performance (pressures, temperatures, flow rate, and proximity probes as required)

4. 1. 1. 6 Turboalternator Performance Tests. Performance tests will be conducted at room temperature and liquid-nitrogen temperatures, at speeds up to 180, 000 rpm and at loads up to 100 watts. Load power factors under test will include at least unity and 0. 8 lagging. Waveform pictures will be taken under various loads.

4. 1. 1. 7 Short Circuit Test. To attempt to get short circuit core loss information, tests will be conducted at 77°K, to be used for checking calculated machine reactance and irreversible demagnetization effect on the magnet.

4. 1. 1. 8 Test Data Reduction. An existing computer program will be modified to present test data as recorded, along with performance parameters deduced from test data. Items to be included will be:

- Voltages
- Resistance
- Frequency, speed
- Wheel power
- Friction power
- Electric power output
- Alternator gas flow
- Alternator temperatures
- Current
- Current density
- Joule losses

The instrumentation installed for testing is shown schematically in Figure I-1; the performance data reduction program appears in Appendix I.

4. 1. 2 Test Arrangement

The turboalternator performance evaluation tests were conducted at both room and cryogenic temperatures with the turboalternator operating open cycle.

Helium gas supplied from a high pressure bottle was directed to the turbine and then discharged to the laboratory air for room-temperature tests. For cryogenic-temperature tests, the helium gas was cooled by a heat exchanger with a coiled gas tube in a dewar of liquid nitrogen.

Figure 4. 1. 2-1 is a photograph of the turboalternator test station. The equipment is shown set up for testing the turboalternator in a horizontal position at cryogenic temperatures. The turboalternator is mounted off a bench through two indexing tables to allow freedom of rotation in both horizontal and vertical planes. A bell jar covers the turboalternator assembly to prevent the moist room air from contaminating the helium gas system and freezing the turboalternator components. The stainless steel dewar located below the turboalternator contains a copper coil connected into the helium gas line to the turboalternator and as liquid nitrogen is added to the dewar, it precools the helium

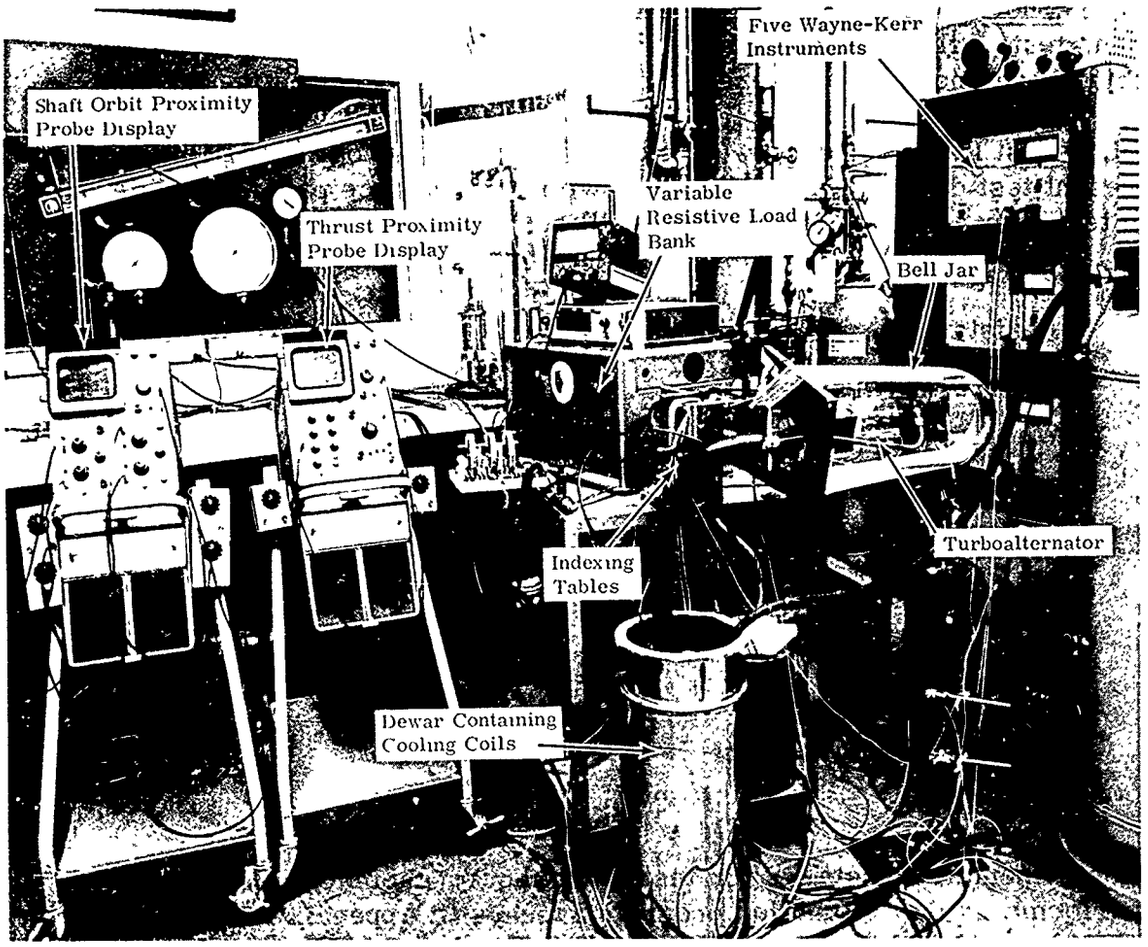

Figure 4. 1. 2-1. Turboalternator Test Station

gas. The Wayne-Kerr instruments and oscilloscopes used in conjunction with the proximity probes are located in the background along with the variable resistive-load bank for applying loads to the turboalternator.

Figure 4. 1. 2-2 shows a close-up of the turboalternator cryogenic test arrangement. The shields around the turboalternator are used for cryogenic-temperature tests to direct the cold gas coming out of the turbine exhaust across the turboalternator housing to provide cooling of the entire assembly. The cold gas then reverses again within the bell jar and exhausts to the laboratory atmosphere. This flow path is illustrated in Figure 2. 3. 1-2.

Turboalternator assembly procedures are not discussed in this report because a separate document (Ref. 28) was prepared for this purpose and was previously delivered under this contract. The document details all assembly and disassembly procedures used during the course of performance testing. Contents of the report include:

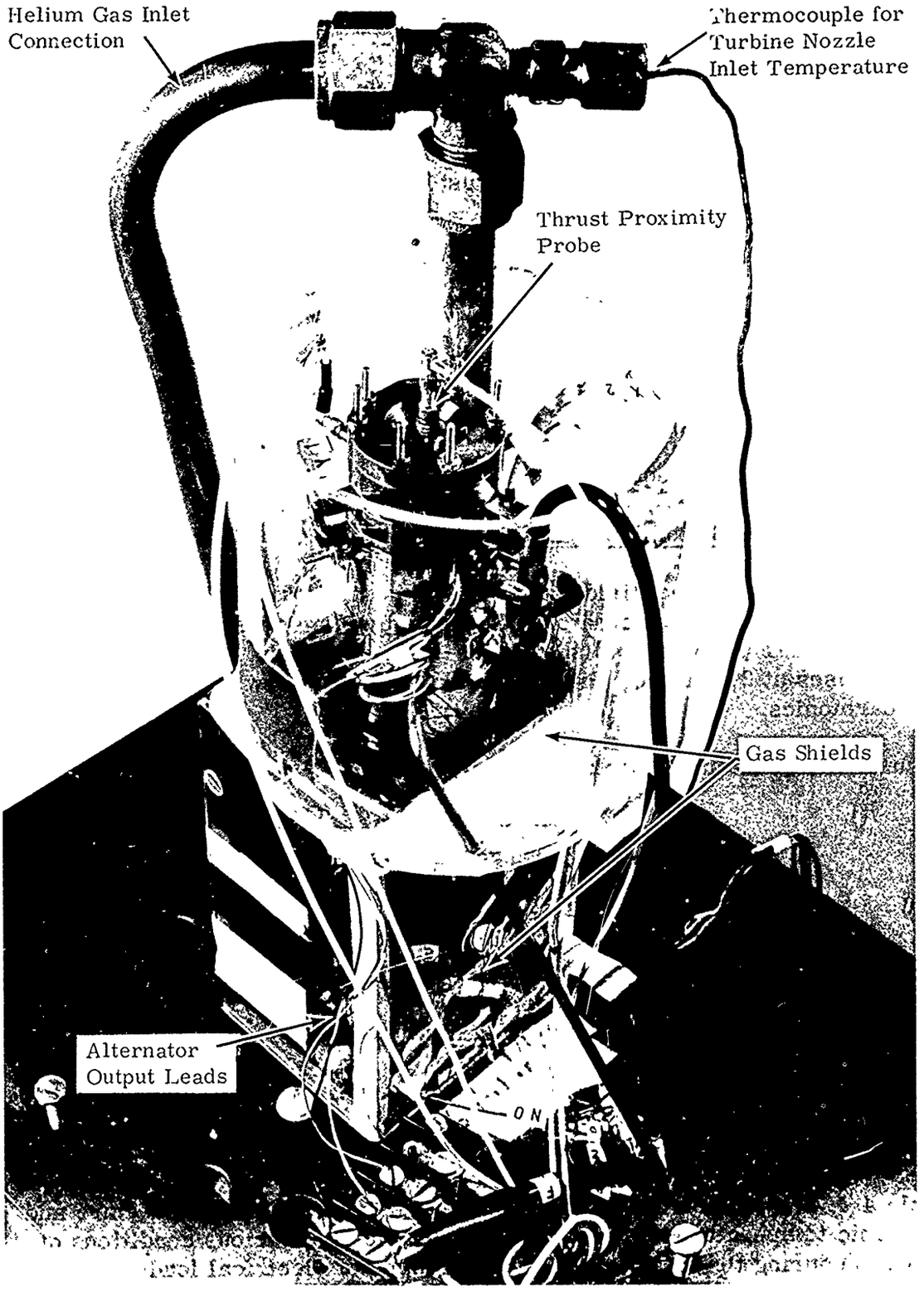

Figure 4.1.2-2. Turboalternator Cryogenic Test Arrangement

- Turboalternator assembly procedure

  Preliminary cleaning
  Balancing the rotating assembly
  Preliminary pad positioning and stator installation
  Assembling the inner thrust bearing
  Assembling the outer thrust bearing
  Installing the shaft
  Installing the turbine wheel
  Setting the thrust bearings
  Installing the thrust proximity probe
  Making the final pad adjustment
  Magnetizing the shaft magnet
  Demagnetizing the shaft magnet

- Turboalternator disassembly procedure
- Shaft balance equipment

4.1.3 Alternator Stator Tests Before Assembly

A test rotor with magnet field was spun with a miniature lathe inside the wound stator for the contract alternator. Generated voltages were as expected. Figure 4.1.3-1 (A, B, and C) shows line-to-line waveshapes for each of the three phases at 2180 rpm. Pitch, distribution, and skew greatly reduced the flux harmonics.

Results of a resistance check were:

	Resistance (Ohms)		
Temperature	Orange to White	White to Black	Black to Orange
299°K (78°F)	12.74	12.76	12.64
77°K	1.675	1.680	1.666

4.1.4 Turboalternator Performance Tests

All the turboalternator performance tests are presented in the order that the tests were conducted. Oscilloscope traces of the voltage waveforms are shown, in addition to the oscilloscope traces of the gas-bearing proximity probes.

Table 4.1.4-1 summarizes all the test runs made at room temperature and cryogenic temperatures. The table also outlines the various conditions of operation during the test runs. The maximums of electrical loads, speeds, and efficiencies are listed for each run. These three entries on the table represent maximums among all of the data points for that particular run; therefore, it would be erroneous to quote the three values as a set of test data common to a single data point.

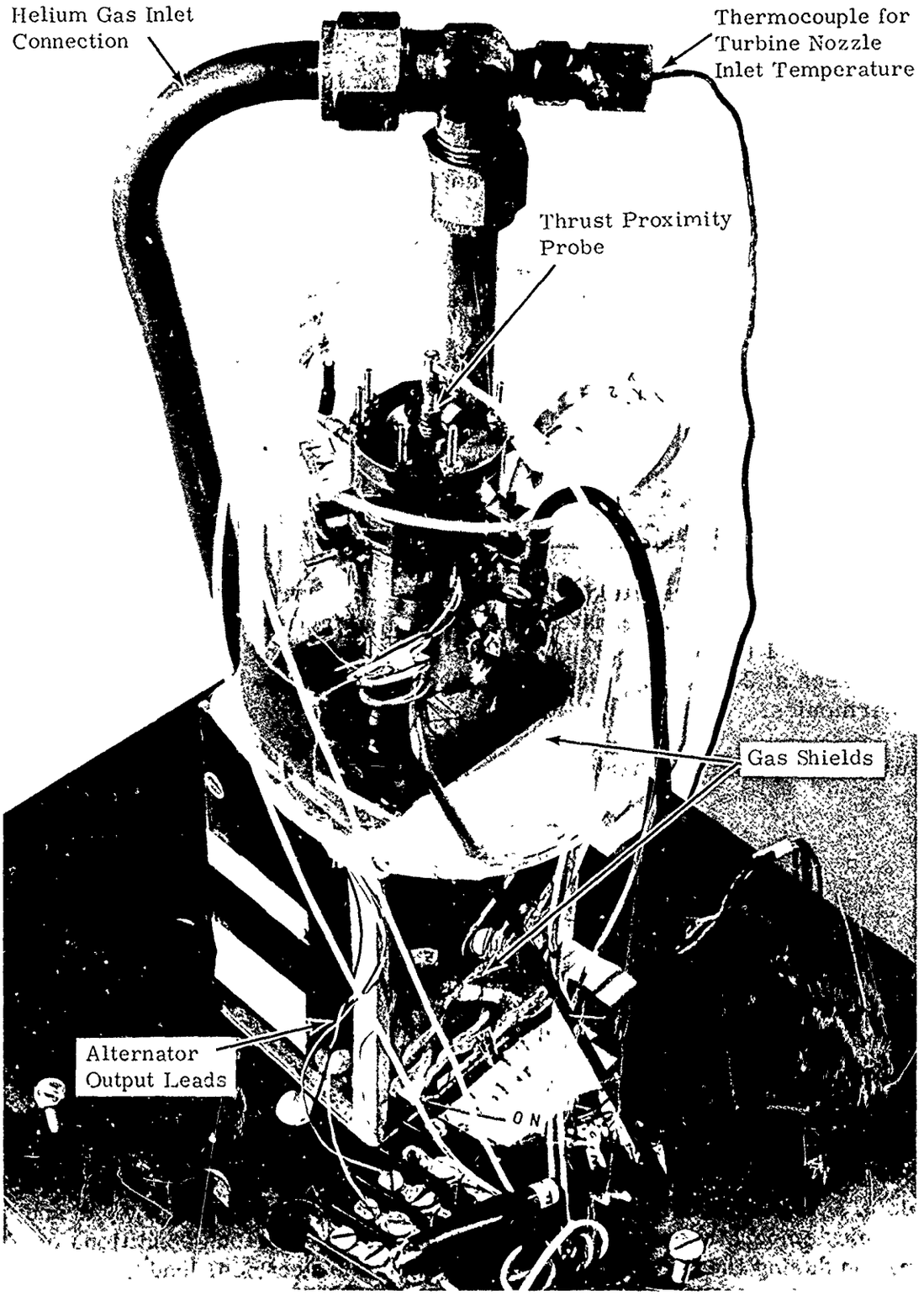

Figure 4.1.2-2. Turboalternator Cryogenic Test Arrangement

- Turbcalternator assembly procedure

  Preliminary cleaning
  Balancing the rotating assembly
  Preliminary pad positioning and stator installation
  Assembling the inner thrust bearing
  Assembling the outer thrust bearing
  Installing the shaft
  Installing the turbine wheel
  Setting the thrust bearings
  Installing the thrust proximity probe
  Making the final pad adjustment
  Magnetizing the shaft magnet
  Demagnetizing the shaft magnet

- Turboalternator disassembly procedure
- Shaft balance equipment

4. 1. 3 Alternator Stator Tests Before Assembly

A test rotor with magnet field was spun with a miniature lathe inside the wound stator for the contract alternator. Generated voltages were as expected. Figure 4. 1. 3-1 (A, B, and C) shows line-to-line waveshapes for each of the three phases at 2180 rpm. Pitch, distribution, and skew greatly reduced the flux harmonics.

Results of a resistance check were:

	Resistance (Ohms)		
Temperature	Orange to White	White to Black	Black to Orange
299°K (78°F)	12. 74	12. 76	12. 64
77°K	1. 675	1. 680	1. 666

4. 1. 4 Turboalternator Performance Tests

All the turboalternator performance tests are presented in the order that the tests were conducted. Oscilloscope traces of the voltage waveforms are shown, in addition to the oscilloscope traces of the gas-bearing proximity probes.

Table 4. 1. 4-1 summarizes all the test runs made at room temperature and cryogenic temperatures. The table also outlines the various conditions of operation during the test runs. The maximums of electrical loads, speeds, and efficiencies are listed for each run. These three entries on the table represent maximums among all of the data points for that particular run; therefore, it would be erroneous to quote the three values as a set of test data common to a single data point.

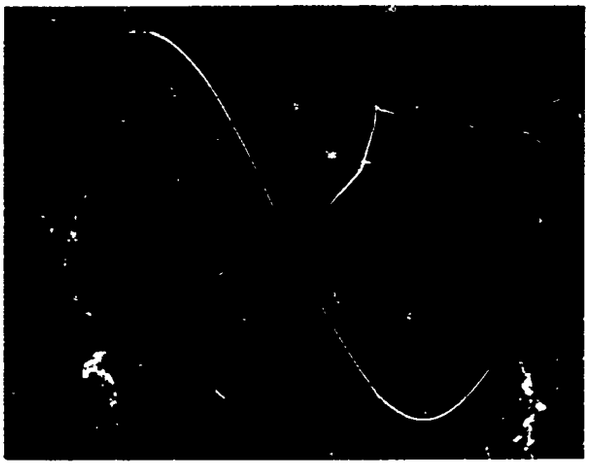

N 2

A (N 2)
Orange to White

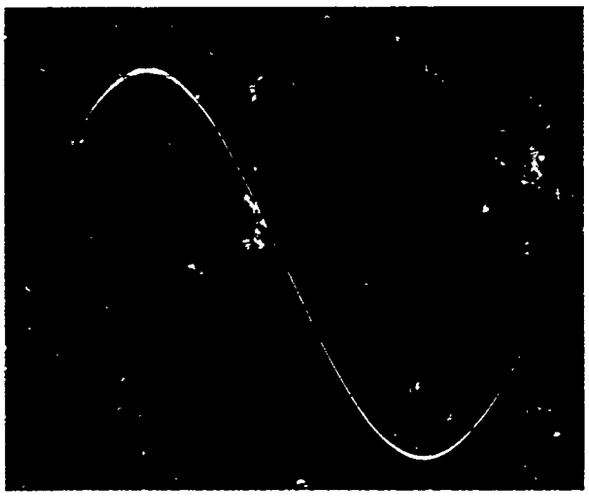

N 3

B (N 3)
Orange to Black

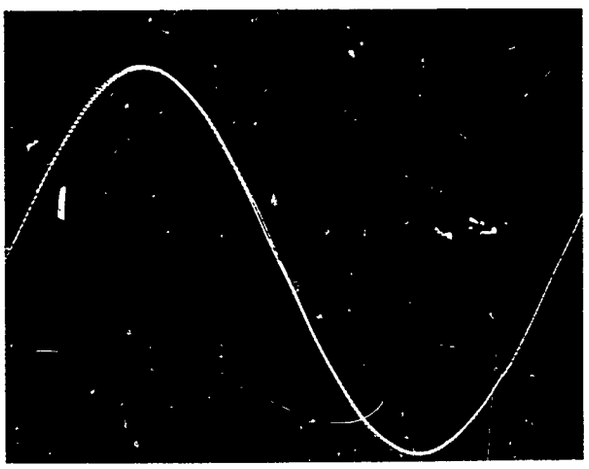

N 6

C (N 6)
White to Black

Figure 4.1.3-1. Line-to-line Waveforms at 2180 Rpm (Vertical Scale 0.5 Volts per Centimeter)

Table 4.1.4-1

TURBOALTERNATOR TEST SUMMARY

Condition	Run 100	Run 101	Run 102	Run 103	Run 104	Run 105	Run 106	Run 107	Run 108	Run 109
Data points	10	8	11	12	5	15	5	5	6	5
Temperature	Room	Room	Room	Cryogenic	Room	Cryogenic	Room	Room	Cryogenic	Cryogenic
Maximum electrical load (watts)	0	66.9	96.2	55.26	0	109.03	0	52.64	0	60.83
Maximum speed (rpm)	249,540	181,200	220,140	247,680	219,960	219,960	220,680	215,520	180,960	180,480
Maximum overall efficiency (percent)	0	29.79	31.38	35.7	0	47.90	0	33.55	0	48.06
Maximum electromagnetic efficiency (percent)	0	96.52	96.59	96.97	0	98.28	0	96.29	0	98.30
Turbine wheel										
Axial clearance (mils)	1.5	1.5	1.5	1.5	1.5	1.5	1.5	1.5	1.5	1.5
Radial clearance (mils)	2	2	2	2	2	4	4	4	4	4
Bearing settings										
Turbine journal radial clearance (microinches)	379	379	379	413	395	303	303	303	303	303
Aft journal radial clearance (microinches)	443	443	443	378	391	295	295	295	295	295
Thrust bearing travel (microinches)	1000	1000	1000	1200	1200	1000	1000	1000	1000	1000
Magnet strength* (gausses)	6070	6070	6070	5700 (approximate)		5510	5510	5510	5510	5510
Operation	Vertical	Vertical	Vertical	Vertical	Vertical	Horizontal	Horizontal	Horizontal	Horizontal	Horizontal
Test purpose	No-load performance	Load performance	Load performance	No-load performance, load performance	Load performance	Capacitive inductive and resistive load performance	No load	Load check data	No load	Load check data
Remarks	Shaft magnetized				Shaft not magnetized	Load-speed limitations were reached operating TA in H position	Shaft magnetized		Shaft magnetized	

*B intercept with recoil line

Other entries on the table show the important clearances settings used during turboalternator assembly. The turbine wheel axial clearance is with the shaft resting on the inner thrust runner; this then represents a minimum turbine wheel operating clearance. The radial wheel clearance was obtained from measurements of the wheel and nozzle diameters. The journal-bearing radial clearances are based on actual measurements of clearance triangles (Ref. 28). The thrust bearing total travel is the assembled clearance the thrust runner can move between the two thrust phases.

The nine test runs are presented in chronological order.

4. 1. 4. 1 Test Run 100 (25 November 1968). The turboalternator was first operated at room temperature for no-load performance and in a vertical (turbine-end down) position with speeds ranging from 99, 480 rpm to 249, 540 rpm.

4. 1. 4. 2 Test Run 101 (26 November 1968). The turboalternator assembly used in Test Run 100 was then operated with loads from 2. 95 watts to 66. 9 watts at room temperature and approximately 180, 000 rpm in a vertical (turbine-end down) position.

Figures 4. 1. 4. 2-1 through 4. 1. 4. 2-3 show waveforms of the voltage across each 2985-ohm resistor connected between line to neutral at the lowest power of 2. 95 watts and 180, 000 rpm. Figures 4. 1. 4. 2-4 and 4. 1. 4. 2-5 show the signals from the proximity probes for the 2. 95-watt load condition. The horizontal sweep used on the oscilloscope for this and all subsequent thrust bearing traces was two milliseconds for each grid centimeter.

Figures 4. 1. 4. 2-6 through 4. 1. 4. 2-8 show the voltage waveform across each 109. 2-ohm resistor connected between line to neutral for 66. 9 watts and 180, 120 rpm. Figures 4. 1. 4. 2-9 and 4. 1. 4. 2-10 show the signals from the proximity probes at the 66. 9-watt load.

4. 1. 4. 3 Test Run 102 (27 November 1968). This test was a continuation of Test Run 101 to obtain higher power outputs. The turboalternator was operated at room temperature, in a vertical (turbine-end down) position, with loads from 1. 78 watts to 96. 2 watts at speeds of approximately 140, 000 rpm and 220, 000 rpm to bracket the 180, 000-rpm design speeds.

Figures 4. 1. 4. 3-1 through 4. 1. 4. 3-3 show the voltage waveforms across each 165. 5-ohm resistor connected between line to neutral for 29. 3 watts, 140, 100 rpm. Figures 4. 1. 4. 3-4 and 4. 1. 4. 3-5 show the signals from the proximity probes at the 29. 3-watt load.

Figures 4. 1. 4. 3-6 through 4. 1. 4. 3-8 show the voltage waveform of the voltage across each 109. 2-ohm resistor connected between a line to neutral, 96. 2 watts and 220, 080 rpm. Figures 4. 1. 4. 3-9 and 4. 1. 4. 3-10 show the signals from the proximity probes at the 96. 2-watt load condition.

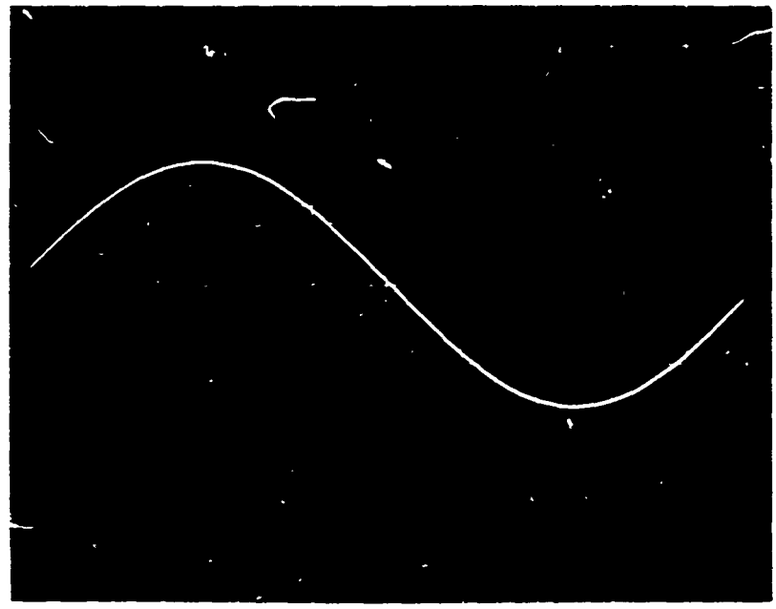

Figure 4.1.4.2-1. Orange Lead, Voltage Waveform across 2985-ohm Resistor, 2.95 Watts, Room Temperature, 180,000 Rpm, Oscilloscope Sensitivity 50 Volts per Centimeter

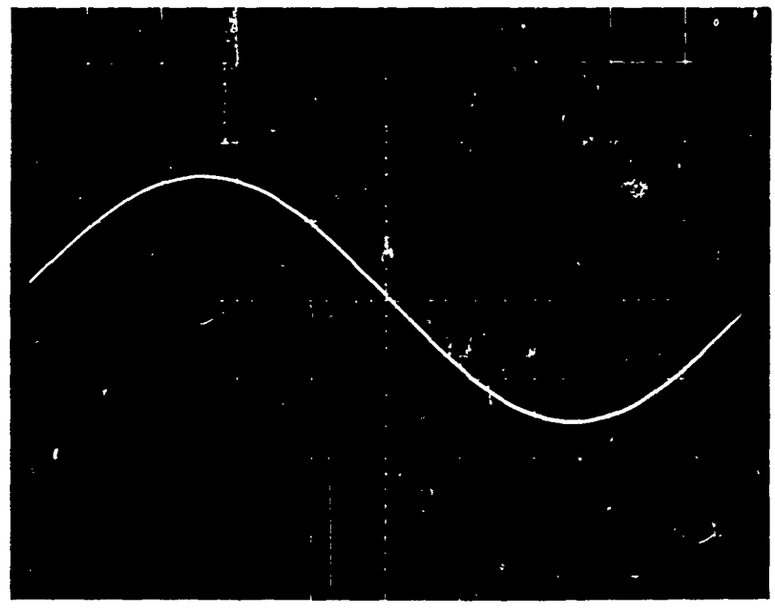

Figure 4.1.4.2-2. White Lead, Voltage Waveform across 2985-ohm Resistor, 2.95 Watts, Room Temperature, 180,000 Rpm, Oscilloscope Sensitivity 50 Volts per Centimeter

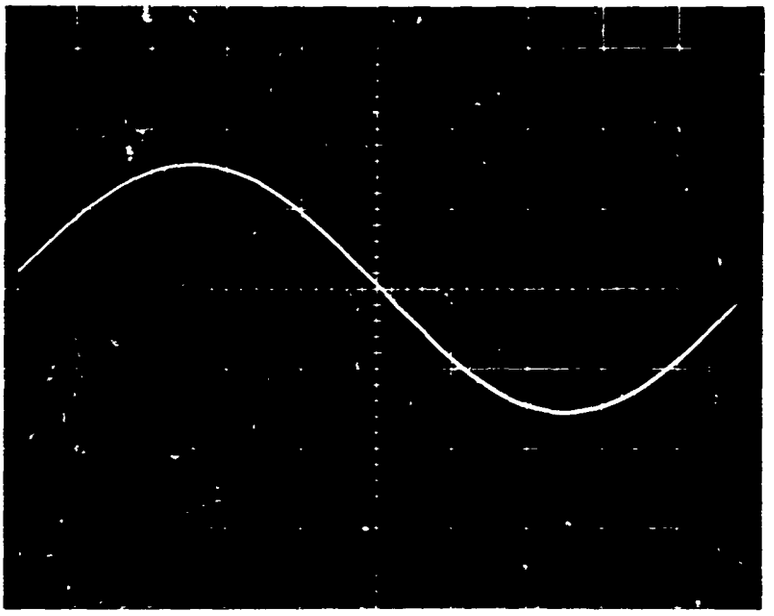

Figure 4.1.4.2-3. Black Lead, Voltage Waveform across 2985-ohm Resistor, 2.95 Watts, Room Temperature, 180,000 Rpm, Oscilloscope Sensitivity 50 Volts per Centimeter

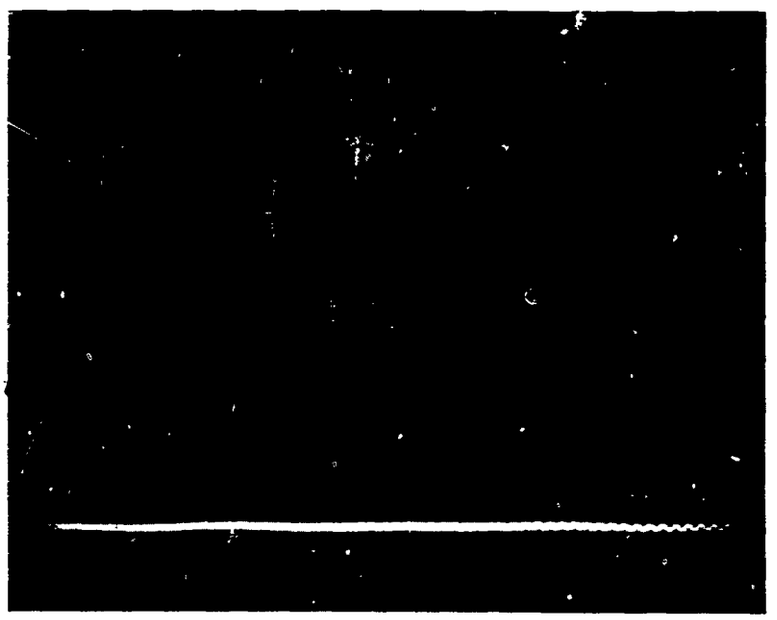

Figure 4.1.4.2-4. Thrust Proximity Probe Signal, 2.95-watt Load, Room Temperature, 180,000 Rpm, Oscilloscope Sensitivity 400 Microinches per Centimeter

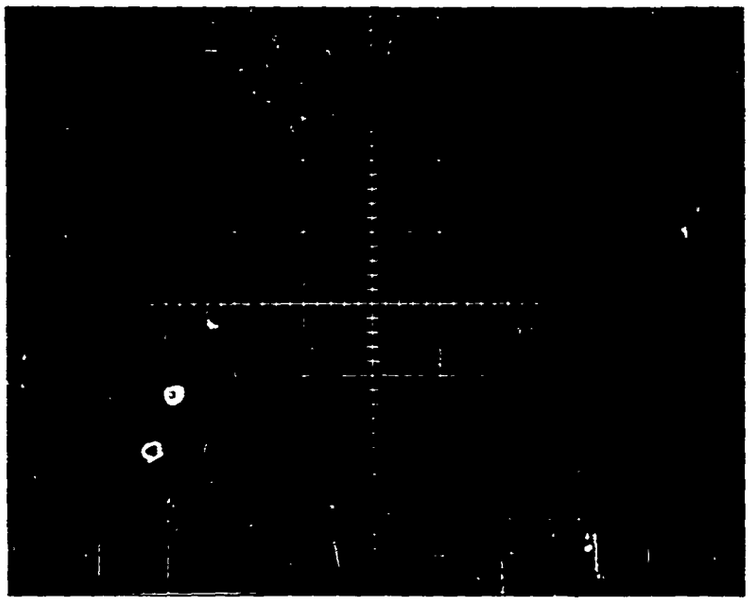

Figure 4.1.4.2-5. Signals from Shaft Orbit Proximity Probes, 2.95-watt Load, Room Temperature, 180,000 Rpm, Oscilloscope Sensitivity 400 Microinches per Centimeter (Lower Signal Turbine End)

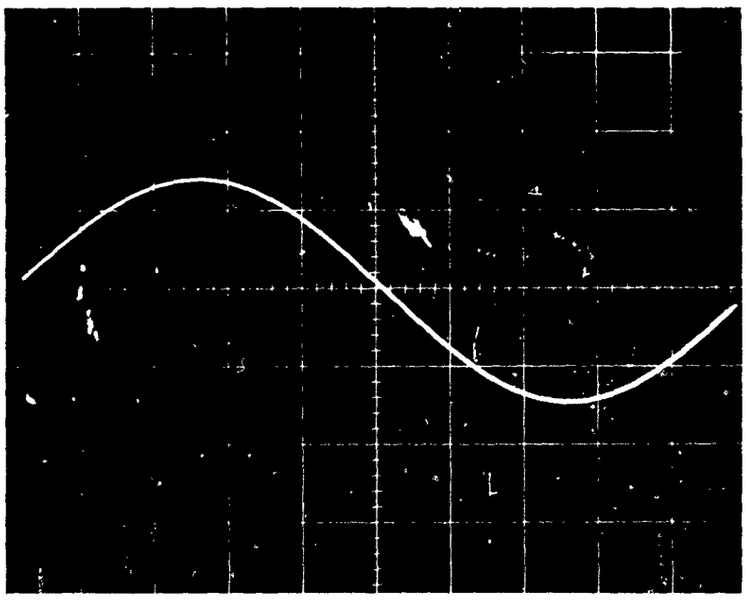

Figure 4.1.4.2-6. Orange Lead, Voltage Waveform across 109.2-ohm Resistor, 66.9 Watts, Room Temperature, 180,020 Rpm, Oscilloscope Sensitivity 50 Volts per Centimeter

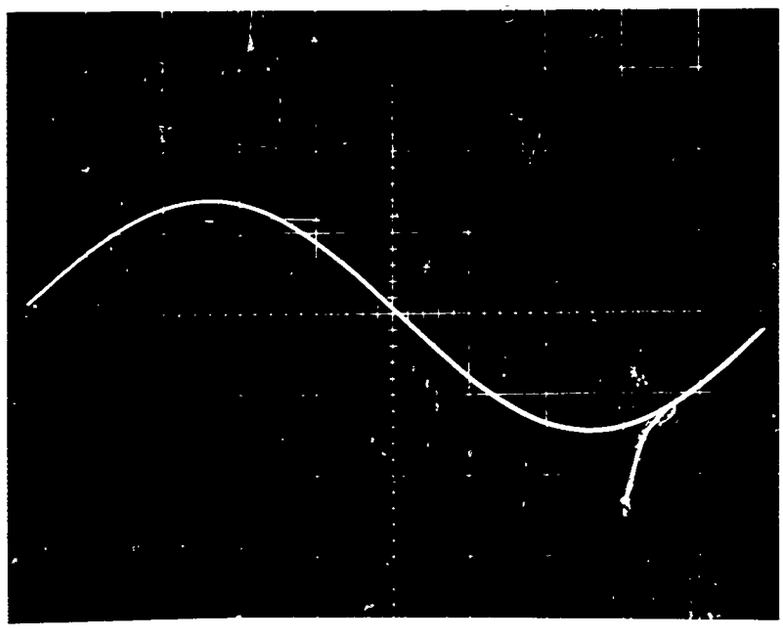

Figure 4.1.4.2-7. White Lead, Voltage Waveform across 109.2-ohm Resistor, 66.9 Watts, Room Temperature, 180,120 Rpm, Oscilloscope Sensitivity 50 Volts per Centimeter

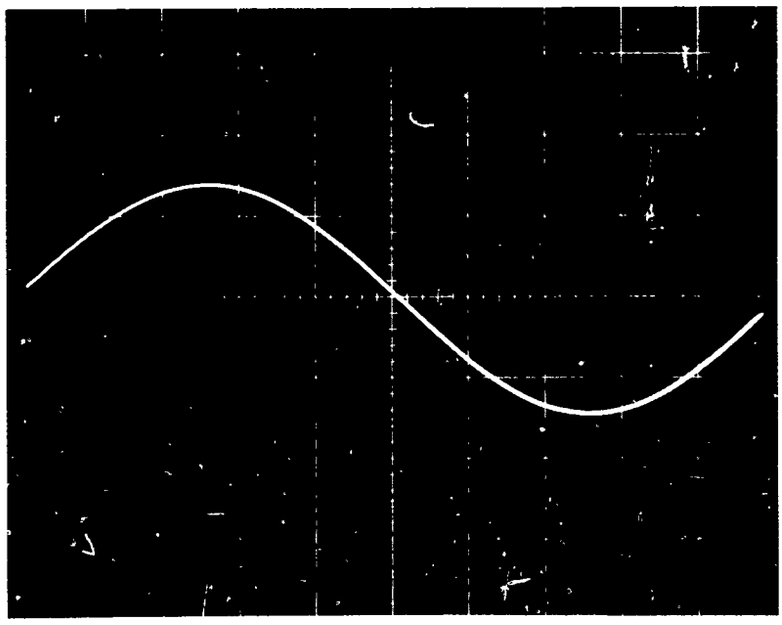

Figure 4.1.4.2-8. Black Lead, Voltage Waveform across 2985-ohm Resistor, 66.9 Watts, Room Temperature, 180,120 Rpm, Oscilloscope Sensitivity 50 Volts per Centimeter

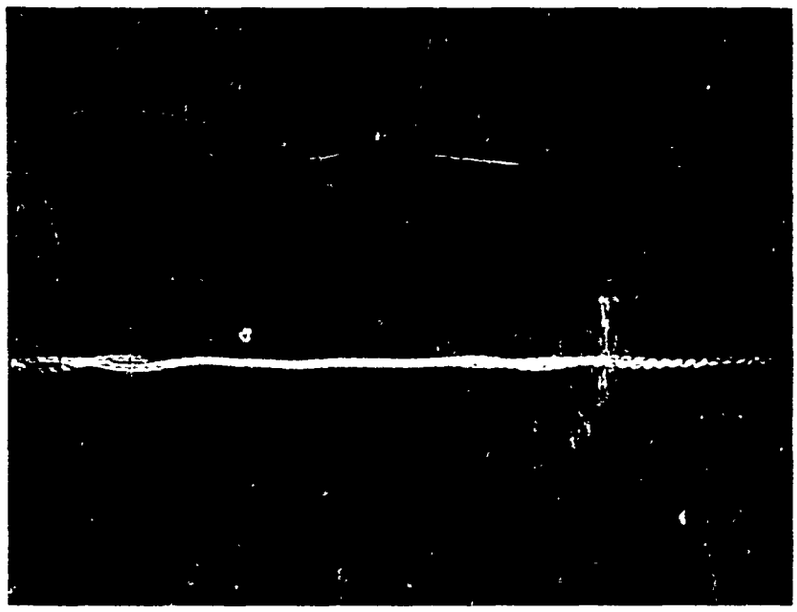

Figure 4.1.4.2-9. Thrust Proximity Probe Signal at 66.9-watt Load, Room Temperature, 180,120 Rpm, Oscilloscope Sensitivity 50 Volts per Centimeter

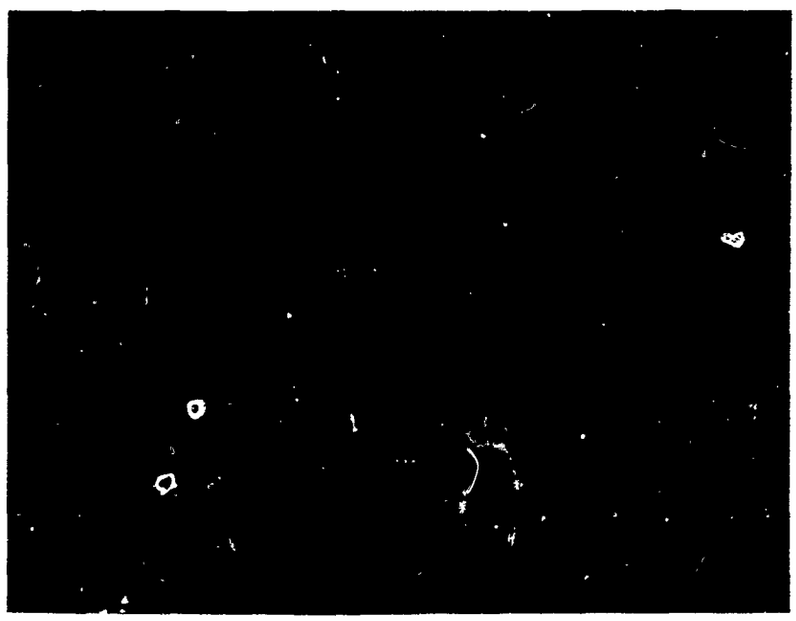

Figure 4.1.4.2-10. Signals from Shaft Orbit Proximity Probes, 66.9 Watts, Room Temperature, 180,120 Rpm, Oscilloscope Sensitivity 400 Microinches per Centimeter (Lower Signal Turbine End)

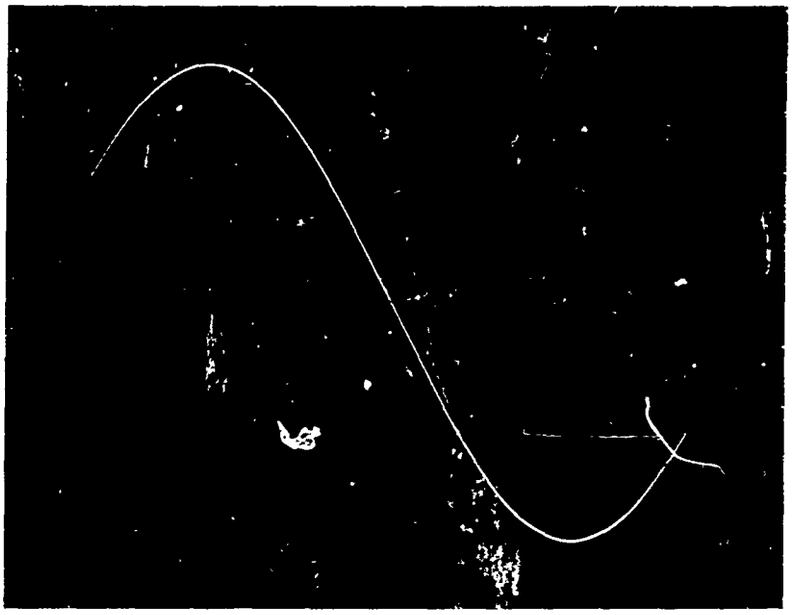

Figure 4.1.4.3-1. Orange Lead, Voltage Waveform across 165.5-ohm Resistor, 29.3 Watts, Room Temperature, 140,100 Rpm, Oscilloscope Sensitivity 20 Volts per Centimeter

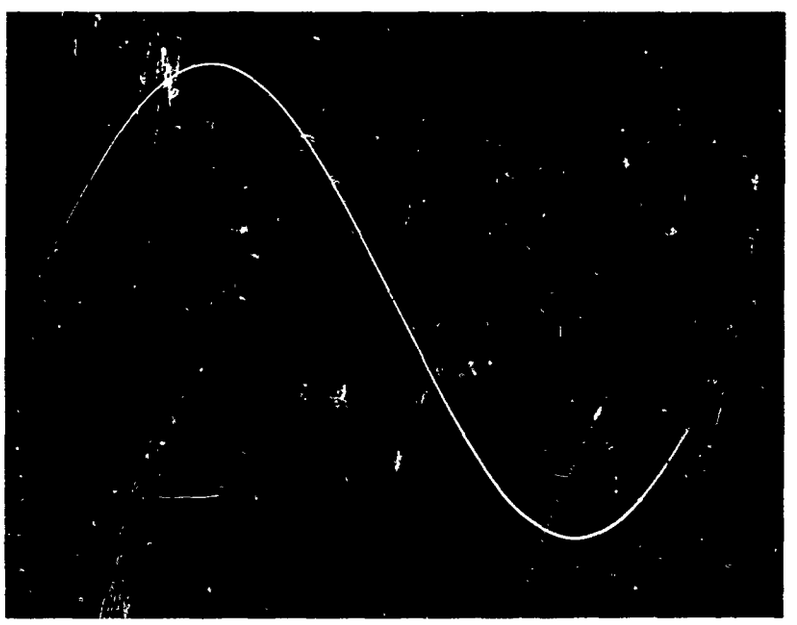

Figure 4.1.4.3-2. White Lead, Voltage Waveform across 165.5-ohm Resistor, 29.3 Watts, Room Temperature, 140,100 Rpm, Oscilloscope Sensitivity 20 Volts per Centimeter

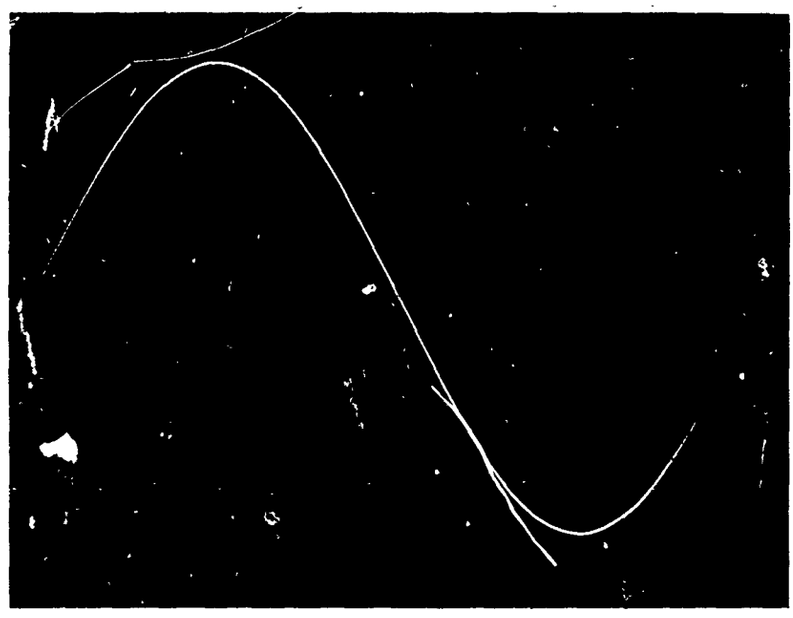

Figure 4.1.4.3-3. Black Lead, Voltage Waveform across 165.5-ohm Resistor, 29.3 Watts, Room Temperature, 140,100 Rpm., Oscilloscope Sensitivity 20 Volts per Centimeter

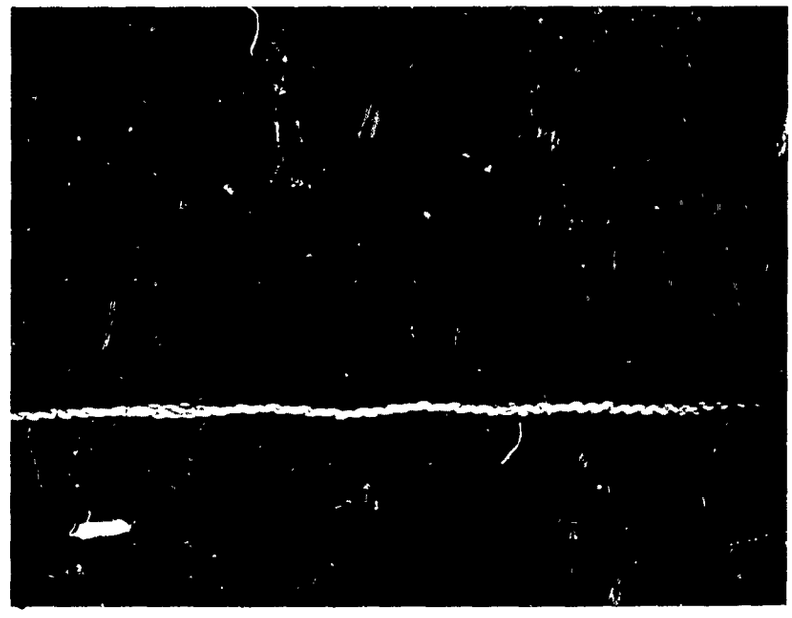

Figure 4.1.4.3-4. Thrust Proximity Probe Signal, 29.3-watt Load, Room Temperature, 140,100 Rpm, Oscilloscope Sensitivity 400 Microinches per Centimeter

Figure 4.1.4.3-5. Signals from Shaft Orbit Proximity Probes, 29.3-watt Load, Room Temperature, 140,100 Rpm, Oscilloscope Sensitivity 400 Microinches per Centimeter (Lower Signal Turbine End)

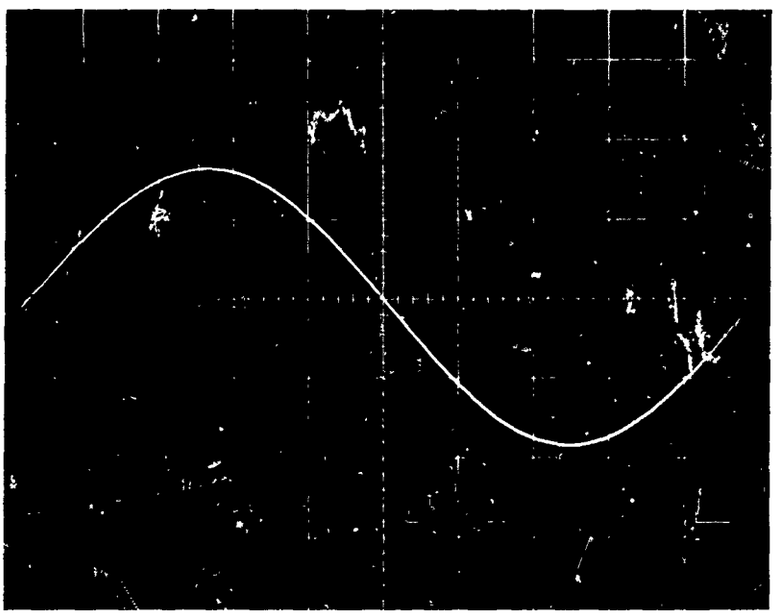

Figure 4.1.4.3-6. Orange Lead, Voltage Waveform across 109.2-ohm Resistor, 96.2 Watts, Room Temperature, 220,080 Rpm, Oscilloscope Sensitivity 50 Volts per Centimeter

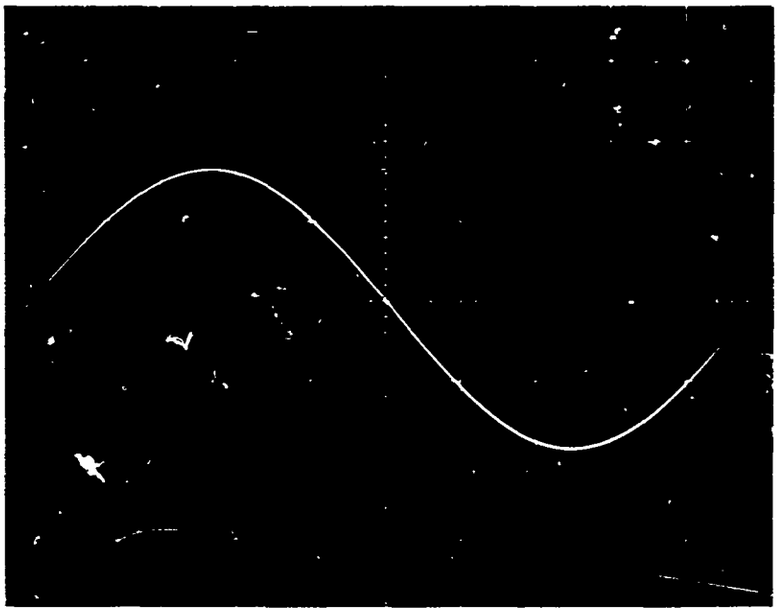

Figure 4.1.4.3-7. White Lead, Voltage Waveform across 109.2-ohm Resistor, 96.2 Watts, Room Temperature 220,080 Rpm, Oscilloscope Sensitivity 50 Volts per Centimeter

NOT REPRODUCIBLE

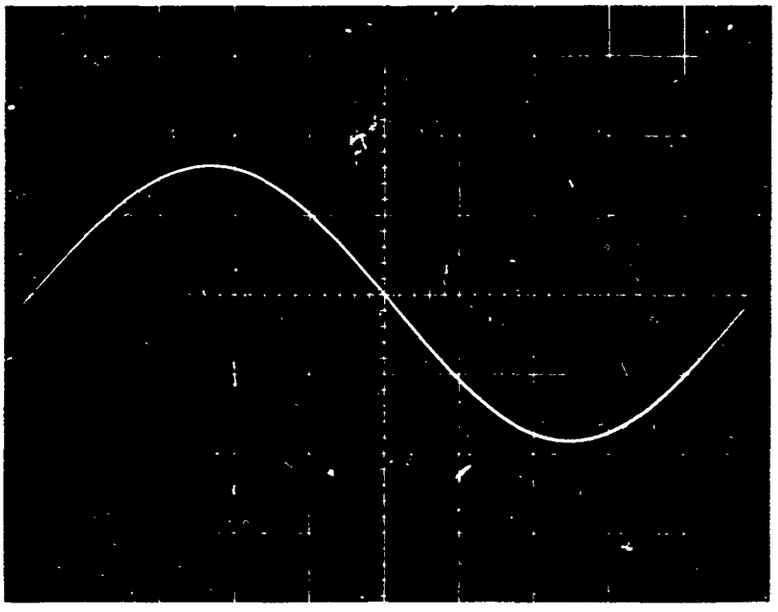

Figure 4.1.4.3-8. Black [illegible]oltage Waveform across 109.2-ohm Resistor, 96.2 Watts, Room Temperature, 220,080 Rpm, Oscilloscope Sensitivity 50 Volts per Centimeter

NOT REPRODUCIBLE

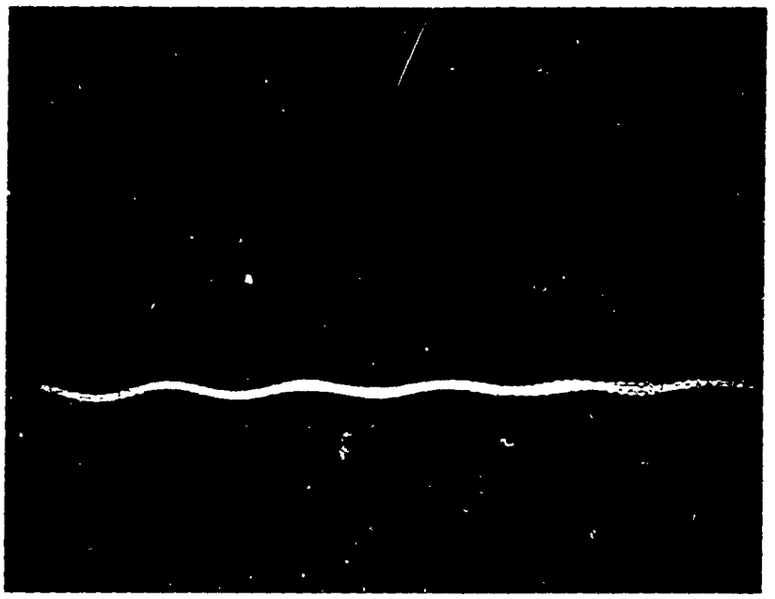

Figure 4.1.4.3-9. Thrust Proximity Probe Signal at 96.2-watt Load, Room Temperature, 200,080 Rpm, Oscilloscope Sensitivity 400 Microinches per Centimeter

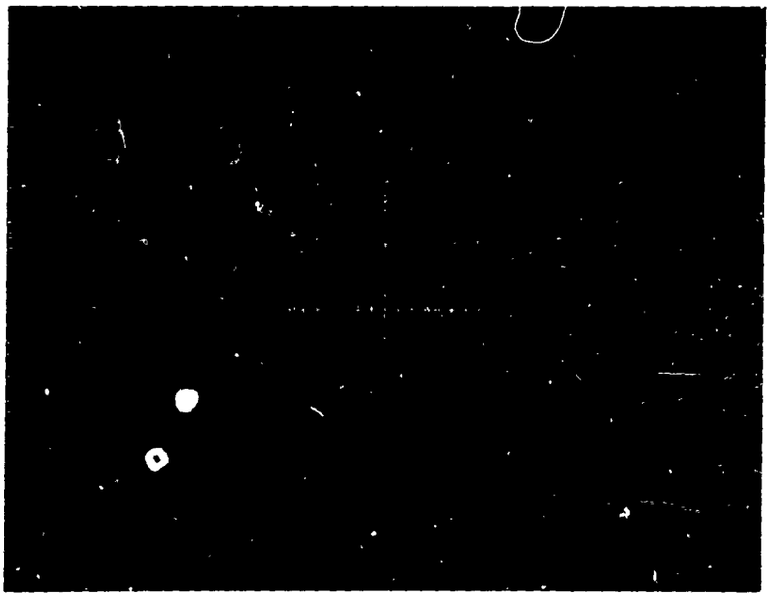

Figure 4.1.4.3-10. Signals from Shaft Orbit Proximity Probes, 96.2-watt Load, Room Temperature, 220,080 Rpm, Oscilloscope Sensitibity 400 Microinches per Centimeter (Lower Signal Turbine End)

Cryogenic temperature tests were first conducted on 3 December 1968. The turboalternator assembly used in the first three test runs was operated with liquid-nitrogen precooling of the helium gas. During the cooldown toward liquid-nitrogen temperature, the bearing operation appeared erratic, so the test was stopped. It was postulated that something was rubbing because of differences in thermal contraction or possibly ice crystals forming from a wet source of helium gas.

The turboalternator assembly was disassembled and inspected. The shaft inner thrust surface showed considerable wear and the journal bearing surfaces on the shaft were also worn.

The worn parts were replaced and the turboalternator was reassembled. All clearances in the turboalternator assembly were rechecked and a charcoal trap was added to the helium gas system to remove moisture from the gas. The assembly operated well at room temperature, so the next test run was made.

4. 1. 4. 4 Test Run 103 (6 December 1968). The turboalternator was operated with liquid-nitrogen precooling in a vertical turbine end-down position at no load, with speeds ranging from 117, 480 rpm to 247, 680 rpm. Also runs with loads of 2. 65 watts to 55. 3 watts at approximately 180, 000 rpm were made.

Figures 4. 1. 4. 4-1 through 4. 1. 4. 4-3 show the voltage waveforms line to line at cryogenic temperature with no load and at 180, 000 rpm. Figures 4. 1. 4. 4-4 and 4. 1. 4. 4-5 show the signals from the proximity probes at the no-load condition. The shaft orbits are approximately two times larger than in the previous room-temperature test runs. The reason for this was probably that the shaft and wheel balance, as assembled, was not good.

The turboalternator, as assembled for Test Run 103, was then operated with liquid-nitrogen precooling to obtain more data at cryogenic temperature. During the cooldown, the proximity probe signals became erratic, so the test was stopped. An inspection of the turboalternator parts showed considerable wear on the shaft inner thrust surface and at the journal bearing surfaces on the shaft. The inner thrust bearing also showed considerable wear.

Possible causes for the erratic operation are shown on Table 4. 1. 4. 4-1. All modifications were made and tests were conducted with liquid-nitrogen precooling, but the operation was not satisfactory until the charcoal trap was removed and a fine filtering system was installed in the helium gas line.

The filtering system consisted of three stainless steel wire mesh filters connected in parallel to minimize the pressure drop. The filters were a product of the Aircraft Porous Media Division of the Pall Corporation and removes 98 percent of the particles in the 3. 5-micron range and 100 percent of all particles 13 microns or larger. The filter elements should be stainless steel

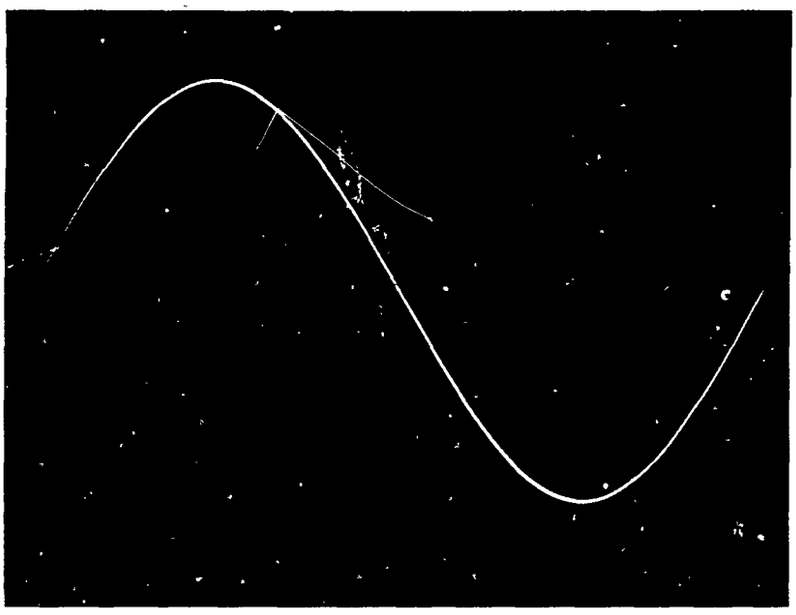

Figure 4.1.4.4-1. White-to-orange Leads, Voltage Waveform Line to Line, No Load, Cryogenic Temperature, 180,000 Rpm, Oscilloscope Sensitivity 50 Volts per Centimeter

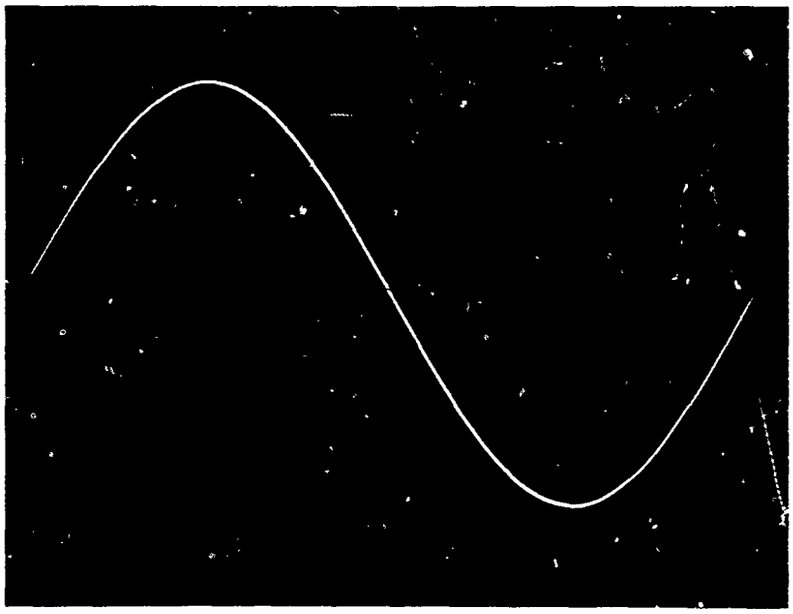

Figure 4.1.4.4-2. Black-to-orange Leads, Voltage Waveform Line to Line, No Load, Cryogenic Temperature, 180,000 Rpm, Oscilloscope Sensitivity 50 Volts per Centimeter

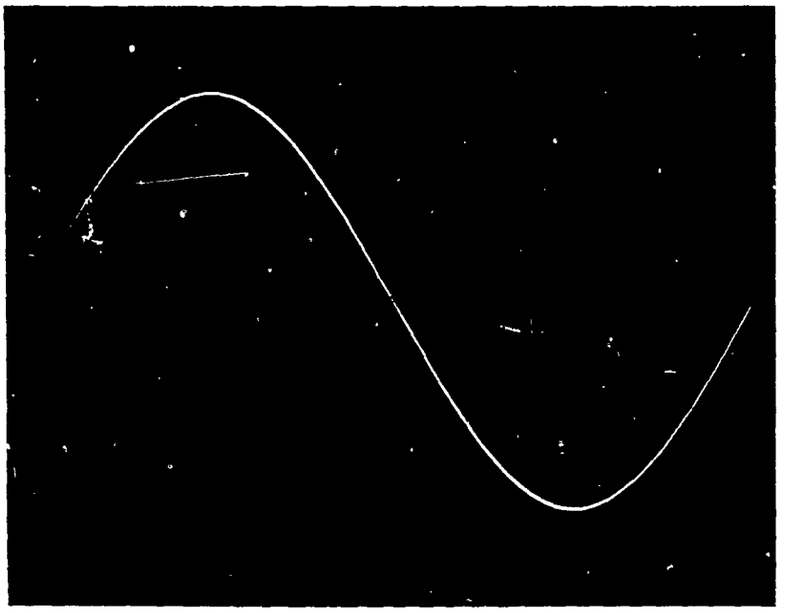

Figure 4.1.4.4-3. Black-to-white Leads, Voltage Waveform Line to Line, No Load, Cryogenic Temperature, 180,000 Rpm, Oscilloscope Sensitivity 50 Volts per Centimeter (TR 103)

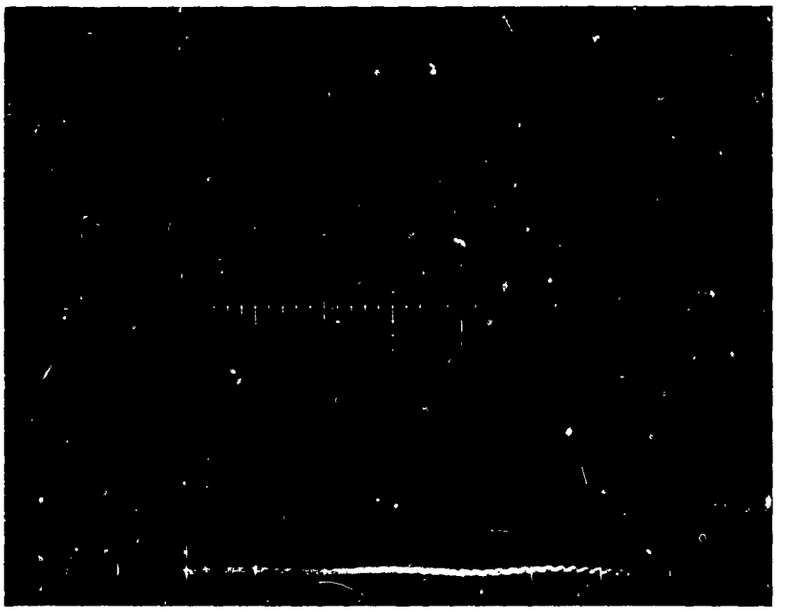

Figure 4.1.4.4-4. Thrust Proximity Probe Signal, No Load, Cryogenic Temperature, 180,000 Rpm, Oscilloscope Sensitivity 400 Microinches per Centimeter

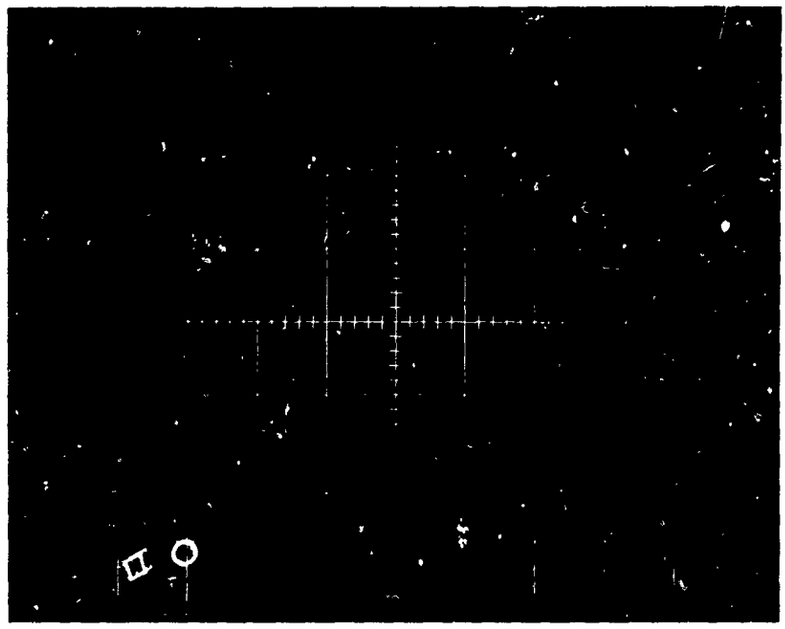

Figure 4. 1. 4. 4-5. Signals from Shaft Orbit Proximity Probes, No Load, Cryogenic Temperature, 180, 000 Rpm, Oscilloscope Sensitivity 400 Micro-inches per Centimenter (Signal on the Right Turbine End)

Table 4. 1. 4. 4-1

TURBOALTERNATOR ERRATIC OPERATION
AT CRYOGENIC TEMPERATURES
POSSIBLE CAUSES AND CORRECTIONS

Possible Cause	Correction
Proximity probe touching	Backed probe out
Turbine wheel rubbing	Decreased wheel outside diameter
Weak inner thrust bearing	Decreased thrust bearing spiral groove depth 8×10^{-4} inches
Weak journal pad bearings	Decreased radial clearance and polished bottom of pad socket
Fine particles of charcoal coming through glass wool filter in charcoal trap	Removed charcoal trap
Dirt or ice particles coming through helium gas system	Installed fine wire mesh filtering system in helium gas line

and contain no epoxy (to seal irregularities in the wire mesh), which would flake off at cryogenic temperatures. Problems with these filters and corrections are described in paragraph 4. 3. 3.

4. 1. 4. 5 Test Run 104 (16 January 1969). A test run was made with a turboalternator assembly at room temperature and with no load, because the shaft magnet was left unmagnetized. The speed ranged from 139, 980 rpm to 219, 960 rpm. Record oscilloscope proximity probe traces taken are not presented because the operation appeared satisfactory.

A subsequent test attempt at cryogenic temperature resulted in erratic operation. Therefore, a complete contamination investigation was conducted from February to August 1969. Highlights of the contamination investigations are described in Section 4. 3.

4. 1. 4. 6 Test Run 105 (18 August 1969). The turboalternator was operated to complete evaluation tests with liquid-nitrogen precooling. The unit was operated in a horizontal position because preliminary cold tests with this turboalternator assembly operating vertically indicatad the possibility of a weak inner thrust bearing at the liquid-nitrogen temperature.

The tests scheduled were run in the following order:

- Cryogenic tests at 0. 95 leading power factor, with a target output of 50 watts at 180, 000 rpm
- Cryogenic tests at 0. 95 lagging power factor, with a target output of 50 watts at 180, 000 rpm
- Cryogenic tests at unity power factor toward 100 watts output at 180, 000 rpm
- Cryogenic tests at unity power factor toward 100 watts output at 140, 000 rpm and at 220, 000 rpm

A fifth test, the internal reactance test, was combined with the first and third tests because leakage reactance measurements could be obtained from these data.

All test data taken are shown in Table 4. 1. 4. 6-1. There are blanks for alternator temperatures. Complete temperature data were not taken for every run because it was very time consuming to record every thermocouple installed, and the data shown were believed sufficient for evaluation.

Electrical power output and voltages shown on the table have been adjusted for the voltmeter calibration after the test. Table 4. 1. 4. 6-2 shows the recorded and corrected readings for Run 105.

Tests were made with capacitors, in series with a resistive load, to provide a nominal leading power factor of 0. 95 at 50 watts and 180, 000 rpm. The

Table 4.1.4.6-1

TURBOALTERNATOR LOAD PERFORMANCE TEST RESULTS AT CRYOGENIC TEMPERATURES
(Run 105, 18 August 1969)

Load Type		Data Point (D1)														
		Capacitive			Inductive			Resistive								
		1	2	3	4	5	6	7	8	9	10	11	12	13	14	15
Frequency (hertz)	(C1)	3051	3058	3047	3093	3035	3035	3072	3150	2994	3678	3637	3637	2322	2410	2358
Speed (rpm)		183060	183480	182820	185580	182100	182100	184320	189000	179640	220680	218220	218220	139320	144600	141480
Flowmeter pressure (psig)	(P0)	87.13	77.0	78.2	78.1	78.2	80.15	78 8	77.65	79 3	77.5	74.8	75 65	81 3	80.2	79.3
Turbine inlet pressure (inches of mercury)	(P1)	17 5	16 02	14.32	15.01	14 22	13.61	17.09	19.82	17 37	22 39	23.89	25.62	10.03	12 89	13.54
Flowmeter (percent)	(J)*	63.8	61 4	57.1	60.02	58.2	55 5	60 9	65 2	58 9	66 9	72.5	76.1	50 01	57 9	60 1
Housing pressure (inches of water)	(H9)	0 095	0.080	0.072	0.075	0 070	0 072	0 09	0.11	0 088	0 147	0 145	0.155	0 045	0 054	0.06
Load resistance (L-N) (ohms)	(R)	123.5	142.0	165.5	109.2	123 5	142.0	123.5	98.5	109 2	109 2	98.5	89.5	165 5	123 5	109.2
Voltage per phase, across resistance (volts)	(V1)	52 3	52.9	52.9	43.8	44.9	46 7	51 9	51.6	49 9	59 9	58.7	57.8	40.6	41 4	40.3
Voltage per phase, across resistance (volts)	(V2)	52.7	53 1	53 1	43.8	44 9	46.8	52 0	51 8	49.9	59 9	58 7	57.8	40.7	41.7	40 3
Voltage per phase, across resistance (volts)	(V3)	52.2	52 8	52 7	43.4	44 6	46 3	51.8	51 3	49 6	59 6	58.2	57.3	40 2	41.2	40 1
Voltage, average output (volts)		52 4	52.9	52 9	43 7	44.8	46.6	51.9	51.6	49 8	59.8	58.5	57.6	40 5	41.4	40.2
Current, voltage across 10-ohm shunt (volts)	(B1)	4.22	3.72	3.22	3.98	3.62	3.29	4.21	5 22	4 52	5 44	5 88	6.39	2 41	3.36	3.69
Current, voltage across 10-ohm shunt (volts)	(B2)	4 21	3.71	3.21	3 97	3.67	3.29	4.19	5.21	4 51	5 42	5.83	6.36	2 41	3.35	3.67
Current, voltage across 10-ohm shunt (volts)	(B3)	4.24	3.75	3.22	3 99	3.63	3.30	4.22	5 25	4.54	5 47	5 89	6 39	2.42	3.38	3.70
Electrical power output (watts) (approximate)		66 3	59.0	50 6	52.4	48.8	45.9	65 0	81.3	68.1	98 5	104 3	111 2	29 8	41.6	44.3
Voltage per phase, across capacitor or inductance (volts)	(V11)	23.2	20.3	17.5	18 5	16.7	15.1									
Voltage per phase, across capacitor or inductance (volts)	(V12)	23.2	20.4	17 6	18.6	16.7	15.2									
Voltage per phase, across total impedance (volts)	(V21)	57.2	57.0	55 9	47.7	48.1	49 1									
Voltage per phase, across total impedance (volts)	(V22)	57.8	57 2	56.0	47 8	48 1	49 1									
Voltage per phase, across total impedance (volts)	(V23)	57.2	56 8	55.8	47.3	47 9	48.9									
Rotameter reference temperature (°K)	(T0)	298.0	298 2	298 4	298.0	298.0	297.8	298 2	298 2	298 2	298 2	298 2	298.2	298.2	298 2	298.2
Turbine nozzle inlet temperature (°K)	(T1)	105.2	101 9	100.6	94.9	95.1	96.1	113 0	120.3	125 2	160 0	123 7	121.7	86.0	90.5	91.0
Turbine exhaust temperature (°K)	(T4)	98.0	105 1	93 9	88.2	89.7	90.4	103 9	109.3	114.5	117.5	110 3	108.0	83.9	85.5	85.5
Turbine exhaust temperature (°K)	(T5)	97.2	110.0	88.8	88.5	89.9	90 4	103.1	104 6	113.6	116 2	108 8	106.9	83.9	85 0	85 0
Turbine exhaust temperature (°K)	(T6)	97.8	95.8	94.8	89.3	90.2	90.4	103.7	110.4	113.6	116 8	109 1	107.1	83.9	85.0	85.0
Turbine exhaust temperature (°K)	(T7)	97.4	93.0	93.8	88.1	89.2	90 2	103.2	110.4	113.6	115.8	108.2	106.6	82.6	85.0	85 0
Turbine end winding temperature (°K)	(S0)	109.3	105.1	104 8	98.9	99.8	99 8	112.1	121.0	125.5	105.4	125.0	122.7	94.9		93.7
Turbine end winding temperature (°K)	(S1)	112.7	107.0	105.8	100.8	101.2	100 9			126 9	131.9			96.9		95.2
Stator shell temperature (°K)	(S2)	107.9	104.1	103 9	97.6	98.0	98.1			124 3	128 2			94 9		94.2
Stator shell temperature (°K)	(S3)	107 2	103.8	103.0	96.6	97.0	97 2			123 3	126.8			93.2		92.6
Stator slot temperature (°K)	(S4)	106.9	105.0	104.4	96.6	97.6	98.3			127 2	131.0			94.2		96 2
Stator slot temperature (°K)	(S5)	113.9	109.8	109 2	102 9	103.3	104 1			129 2	133 5			96.9		98 9
Aft end winding temperature (°K)	(S6)	112.1	107.0	106.0	100 9	100.9	101 0			126 8	131 5			93.7		95.2
Aft end winding temperature (°K)	(S7)	112.9	109.0	108 2	102 6	102.8	102 9			128 3	132 8			95 9		97.9
Aft end gas temperature (°F)	(S8)	112 5	107.8	107.6	102.3	102 4	102.8			127.1	131 5			94.9		97 3
Aft end gas temperature (°K)	(S9)	112.5	107 6	106.3	101.4	101.8	101.9			125 9	128.9			94 9		94 9

*Flowmeter
Float GSVT-44
Tube FP-1/2-27G-10

Table 4.1.4.6-2

VOLTMETER CORRECTIONS AND POWER OUTPUT FOR RUN 105

Reading		Data Point (D1)														
		1	2	3	4	5	6	7	8	9	10	11	12	13	14	15
	V_1	52 3	52 9	52 9	43 8	44.9	46.7	51 9	51 6	49 9	59 9	58.7	57 8	40 6	41 4	40 3
Corrected	V_1	51 9	52.5	52 5	43 3	44.5	46.3	5 15	51 2	49.5	59 5	58 3	57 4	40 1	40 9	39.8
	V_2	52 7	53 1	53 1	43 8	44.9	46.8	52.0	51 8	49 9	59.9	58 7	57 8	40 7	41 7	40 3
Corrected	V_2	52 3	52 7	52 7	43.3	44.5	46.4	51.6	51.4	49 5	59.5	58.3	57 4	40 2	41 2	39 8
	V_3	52 2	52 8	52 7	43 4	44.6	46.3	51.8	51.3	49.6	59.6	58 2	57 3	40 3	41 2	40 1
Corrected	V_3	51 8	52 4	52 3	42 9	44.2	45.9	51.4	50.9	49.2	59.2	57 8	56 9	39 7	40.7	39 6
	B_1	4 22	3 72	3 22	3.98	3.62	3 29	4.21	5.22	4.52	5.44	5.88	6 39	2 41	3 36	3 69
Corrected	B_1	4.17	3.66	3 16	3.93	3 57	3 24	4.16	5 18	4.47	5.40	5 84	6 36	2 40	3 31	3 64
	B_2	4.21	3 71	3.21	3.97	3.61	3 29	4.19	5.21	4.51	5.42	5 83	6 36	2.41	3 35	3.67
Corrected	B_2	4 16	3.65	3.15	3.92	3.56	3.24	4.14	5.17	4.46	5.37	5.79	6.33	2.40	3.30	3.62
	B_3	4 24	3.75	3.22	3.99	3.63	3 30	4.22	5.25	4.54	5.47	5.89	6.39	2.42	3.38	3 70
Corrected	B_3	4.19	3.69	3 16	3 94	3.58	3 25	4.17	5.21	4.49	5.42	5.85	6.36	2.41	3.33	3.65
	V_{11}	23 2	20.3	17.5	18.5	16.7	15.1									
Corrected	V_{11}	23 1	20.2	17.4	18.4	16.6	15.0									
	V_{12}	23.2	20.4	17.6	18.6	16.7	15 2									
Corrected	V_{12}	23.1	20.3	17.5	18.5	16.6	15.1									
	V_{13}	23.1	20.2	17 4	18.4	16.6	15.0									
Corrected	V_{13}	23 0	20 1	17.3	18 3	16.5	14 9									
	V_{21}	57.2	57.0	55.9	47 7	48.1	49.1									
Corrected	V_{21}	56.8	56 6	55.5	47 3	47.7	48.7									
	V_{22}	57.8	57.2	56.0	47.8	48.1	49.1									
Corrected	V_{22}	57 4	56.8	55 6	47 4	47.7	48 7									
	V_{23}	57.2	56 8	55 8	47.3	47 9	48.9									
Corrected	V_{23}	56.8	56.4	55.4	46.9	47.5	48.5									
Electrical power		66.3	50.0	50.6	52.4	48.8	45.9	65.0	81.3	68 1	98 5	104 3	111.2	29.8	41 6	44.3
Output (watts)		65.1	57.8	49.7	50.9	47.6	45.0	64.2	79.6	66 3	96.2	101 7	109.0	28 8	40.7	43.4

circuit is shown in Figure 4. 1. 4. 6-1. The values of the circuit parameters for these tests were:

Line	Series Capacitor
Orange	0. 942 microfarad
Black	0. 944 microfarad
White	0. 942 microfarad

Data were taken at power levels of 65. 1, 57. 8, and 49. 7 watts at approximately 180, 000 rpm.

The load circuit was then changed to test for lagging power factor, Figure 4. 1. 4. 6-2, with series reactors replacing the capacitors. The values of the circuit parameters for these tests were:

Line	Inductance	Coil Resistance
Orange	2. 38 millihenries	0. 256 ohms
Black	2. 36 millihenries	0. 257 ohms
White	2. 37 millihenries	0. 259 ohms

Data were taken at power levels of 50. 9, 47. 6, and 45 watts at approximately 180, 000 rpm.

Figure 4. 1. 4. 6-3 shows the variable resistor load bank, used to load the turboalternator, and the breadboard, used to connect the capacitors or inductors into the circuit for the leading or lagging power factors.

Figure 4. 1. 4. 6-4 shows the voltage waveform of the voltage across the resistor obtained with the leading power factor at 65. 1 watts. Figures 4. 1. 4. 6-5 and 4. 1. 4. 6-6 show the signals from the proximity probes at this load condition. Figure 4. 1. 4. 6-7 shows the voltage waveform of the voltage across the resistor, with a lagging power factor at 50. 9 watts.

Next, the turboalternator was operated at unity power factor, with pure resistive loads, to determine the maximum output power operating at 180, 000 rpm. First, the 123. 5-ohm (per phase) load was repeated, because this was the greatest load obtained during previous cryogenic tests. Data were taken at 64. 2 watts and 184, 320 rpm. As the resistive load was increased, the thrust probe indicated that the shaft was riding closer to the outer thrust bearing. With a load of 89. 5 ohms, the shaft started intermittently touching the outer thrust bearing. The load was therefore reduced to 98. 5 ohms and data were taken, Table 4. 1. 4. 6-1. The speed was 189, 000 rpm operating at 79. 6 watts. To obtain an intermediate power point, the load was reduced to 109. 2 ohms at 179, 640 rpm, where 66. 3 watts were obtained. Figures 4. 1. 4. 6-8 and 4. 1. 4. 6-9 show the signals from the proximity probes with the 66. 3-watt load. The thrust probe signal indicated the thrust runner was closer to the outer thrust bearing when operating at the lower load conditions.

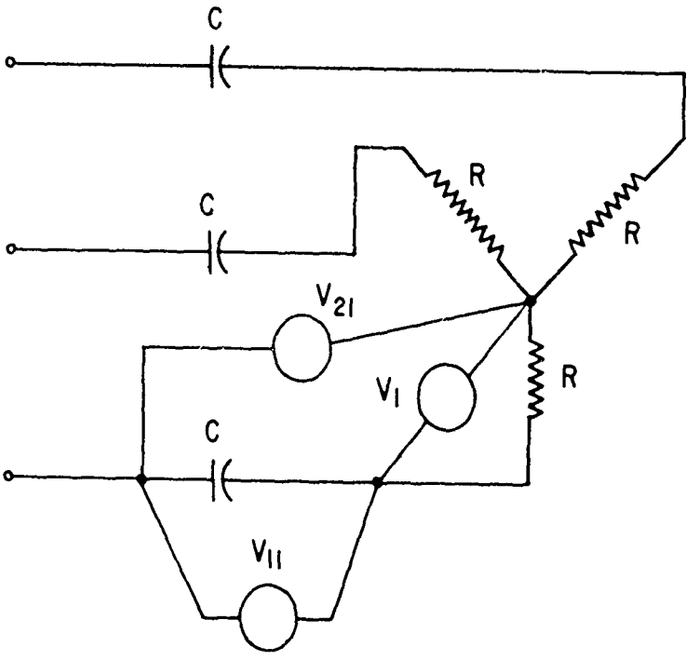

Figure 4.1.4.6-1. Leading Power Factor Circuit

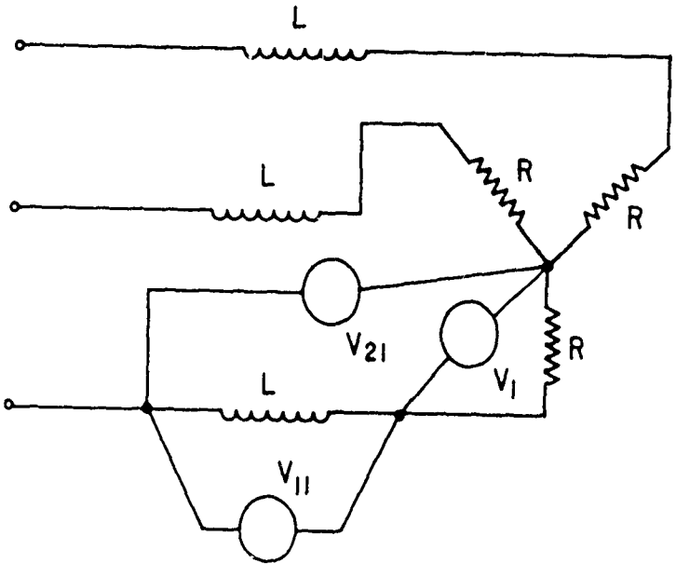

Figure 4.1.4.6-2. Lagging Power Factor Circuit

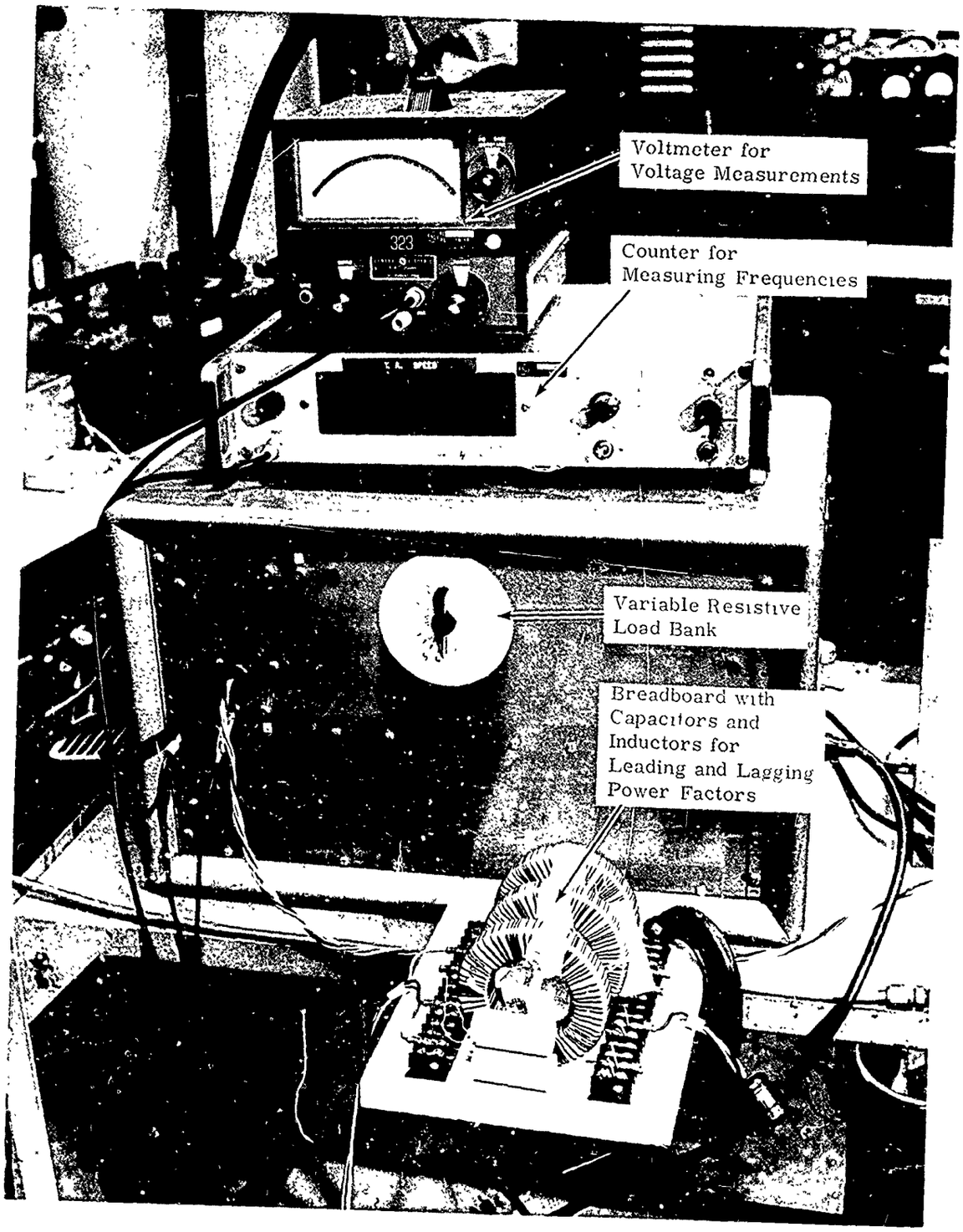

Figure 4.1.4.6-3. Alternator Load Bank

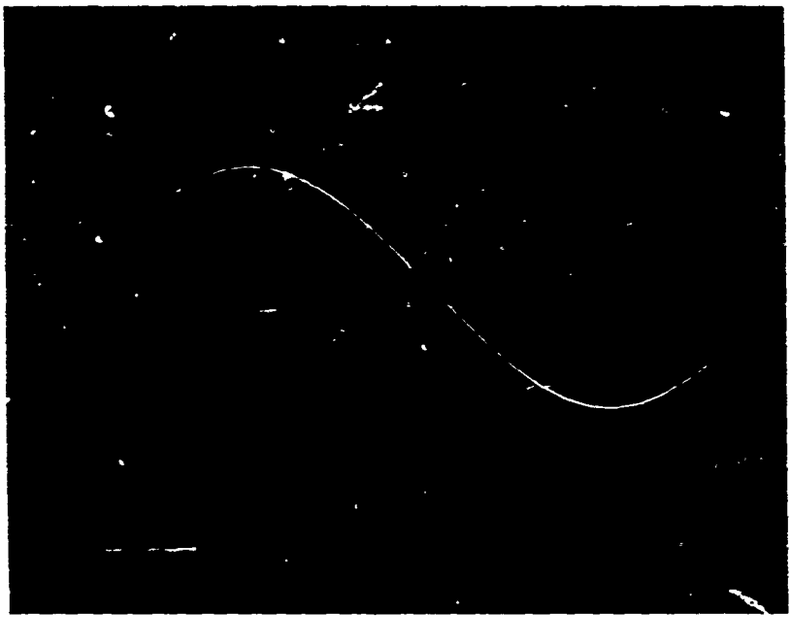

Figure 4.1.4.6-4. Voltage across 123.5-ohm Resistor with Leading Power Factor at 65.1 Watts, 183,060 Rpm, Oscilloscope Sensitivity 50 Volts per Centimeter

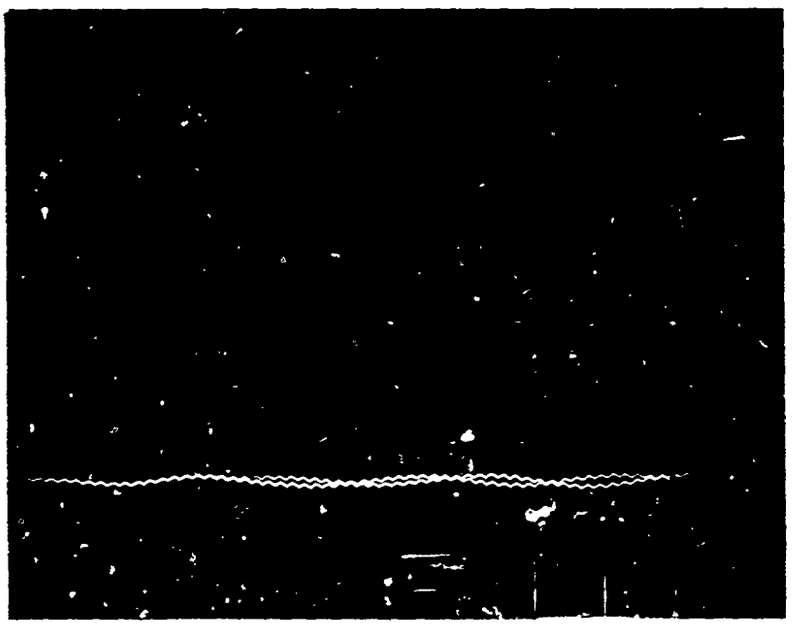

Figure 4.1.4.6-5. Thrust Proximity Probe Signal with Leading Power Factor at 65.1 Watts, 183,060 Rpm, Oscilloscope Sensitivity 400 Microinches per Centimeter

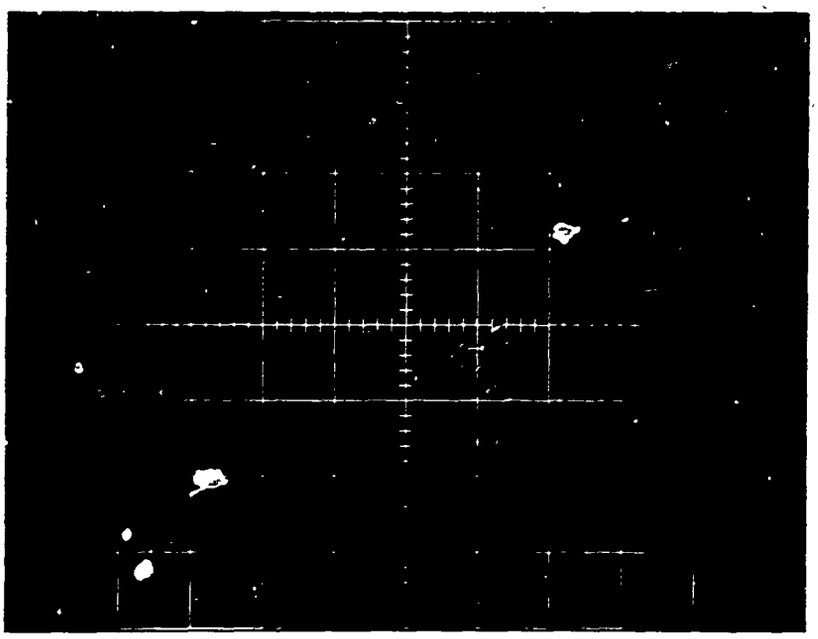

Figure 4.1.4.6-6. Signals from Shaft Orbit Proximity Probes with Leading Power Factor at 65.1 Watts, 183,060 Rpm, Oscilloscope Sensitivity 400 Microinches per Centimeter (Smallest Orbit Turbine End)

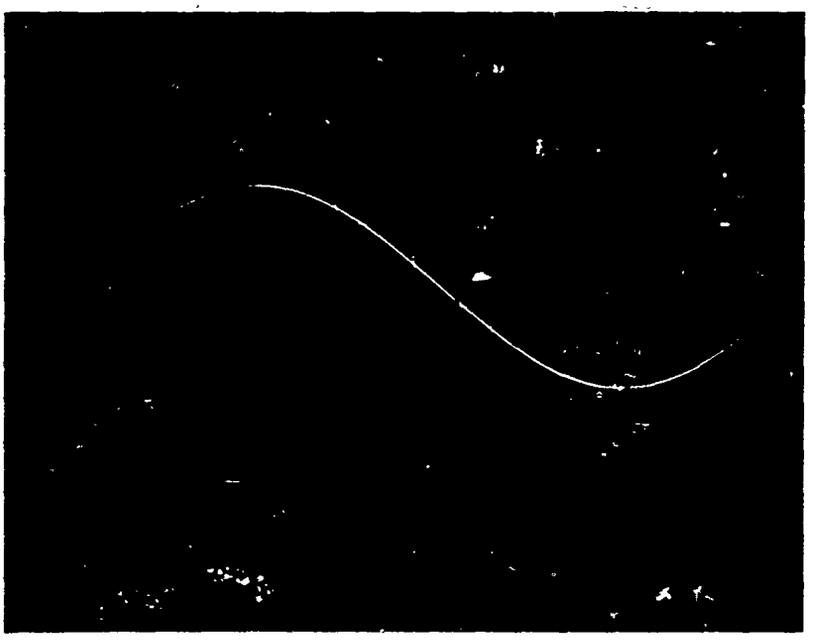

Figure 4.1.4.6-7. Voltage across 109.2-ohm Resistor with Lagging Power Factor at 50.9 Watts, 185,580 Rpm, Oscilloscope Sensitivity 50 Volts per Centimeter

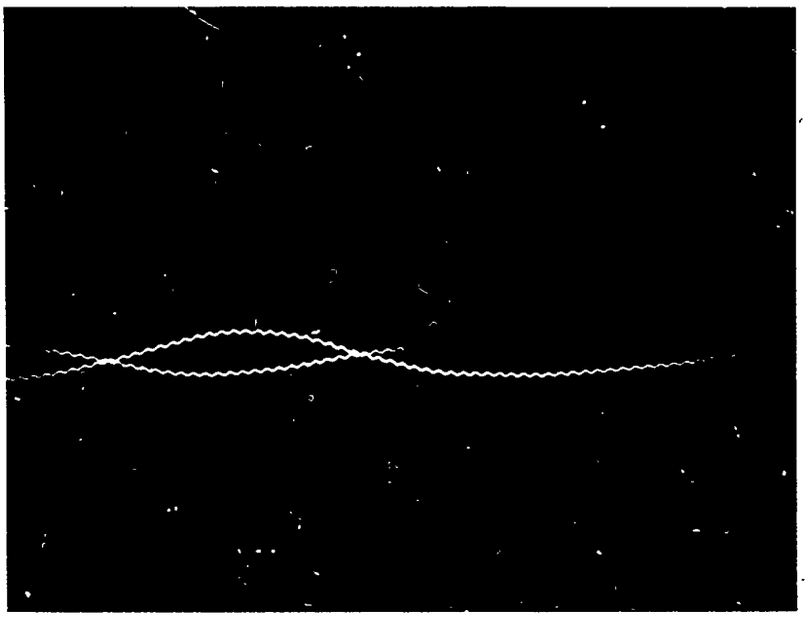

Figure 4.1.4.6-8. Thrust Proximity Probe Signal with 66.3-watt Pure Resistive Load, 179,640 Rpm, Oscilloscope Sensitivity 400 Microinches per Centimeter

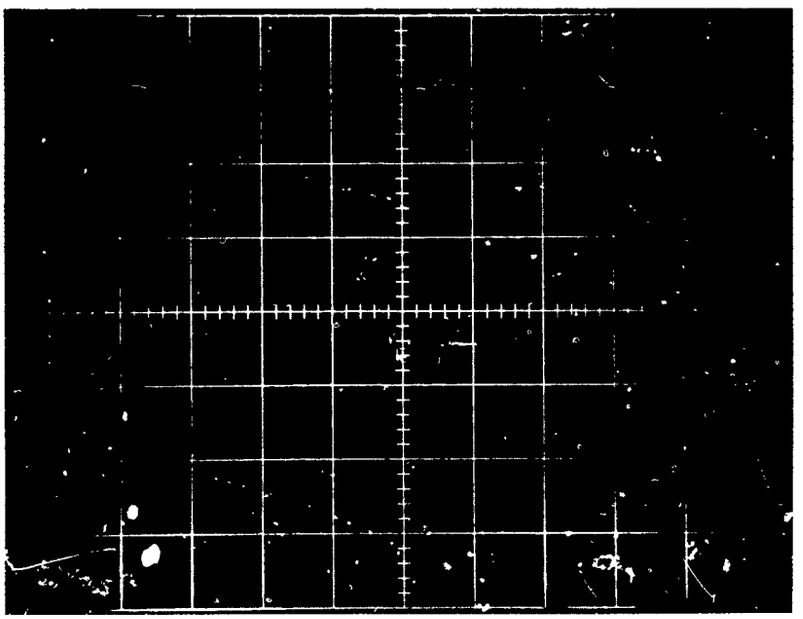

Figure 4.1.4.6-9. Signals from Shaft Orbit Proximity Probes with 66.3-watt Pure Resistive Load, 179,640 Rpm, Oscilloscope Sensitivity 400 Microinches per Centimeter (Smallest Orbit Turbine End)

Unity power factor tests were also made at 220, 000 and 140, 000 rpm to obtain maximum operating powers at each of these speed extremes. An output of 109. 0 watts was obtained at 220, 000 rpm and 43. 4 watts at 140, 000 rpm. A further increase in load at both speeds would cause undesirable thrust bearing loads. See Figures 4. 1. 4. 6-10 through 4. 1. 4. 6-13 for the proximity probe signals at 140, 000 and 220, 000 rpm.

Not all alternator thermocouple readings were recorded for these large power outputs because helium gas consumption was very high. For the operating period from the startup of the turbine warm through completion of the tests, 16 bottles of grade A helium were used. The period of time was 3 hours and 5 minutes.

In general, the turboalternator operated very well at liquid-nitrogen temperature, but with the thrust-bearing load limitations that were reached operating in the horizontal position. The maximum loads for horizontal operation were found to be:

Speed (Rpm)	Electrical Power Output (Watts)
141, 480	43. 4
189, 000	79. 6
218, 220	109. 0

Operating vertically with the turbine-end down allows a greater power output before the load limitation on the outer thrust bearing occurs.

After the above test data were taken, the turboalternator was turned off and restarted five times to test the restarting ability at cryogenic temperature.

The turbine inlet pressure required to start the turboalternator with no load was determined. Then the gas was turned off and the unit coasted to a stop. The last counter frequency observed and the corresponding speed were determined. Results were:

Turbine Inlet Pressure to Restart (Inches Mercury Gage)	Speed (Rpm)	Last Counter Frequency Observed at Coastdown (Hertz)
4. 5	19, 100	318
4. 6	22, 800	380
4. 6	20, 400	341
4. 6	13, 880	231
4. 6	14, 000	234
4. 6	15, 000	250

After warming up to room temperature, the turboalternator started at a turbine inlet pressure of 3. 3 inches of mercury.

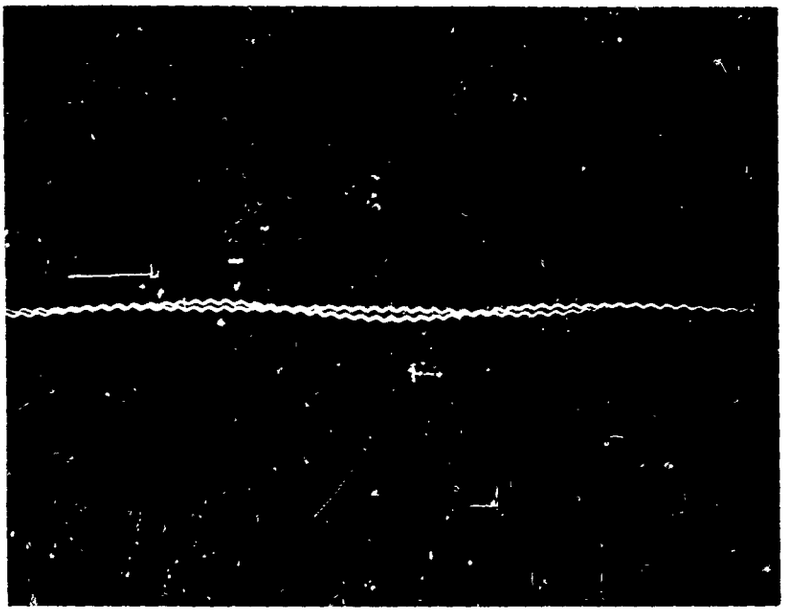

Figure 4.1.4.6-10. Thrust Proximity Probe Signal with 43.4-watt Pure Resistive Load, 141,480 Rpm, Oscilloscope Sensitivity 400 Microinches per Centimeter

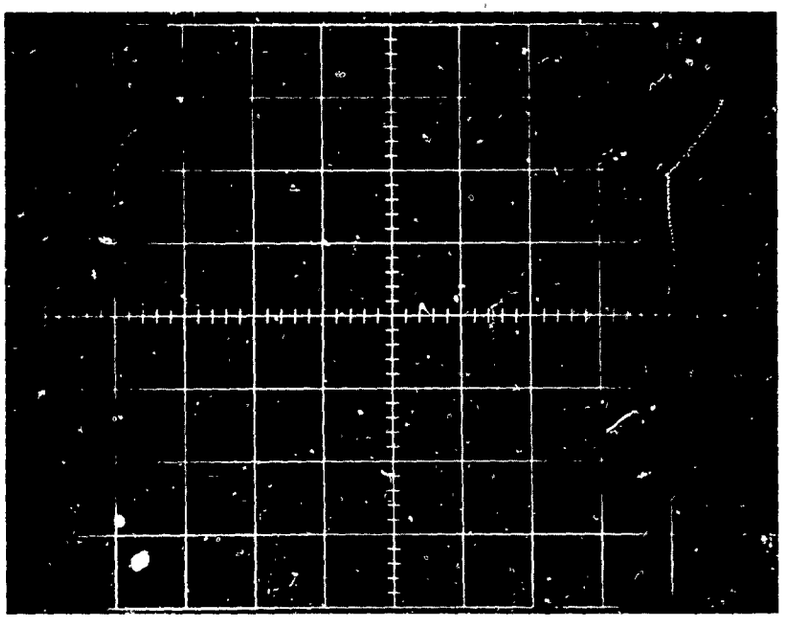

Figure 4.1.4.6-11. Signals from Shaft Orbit Proximity Probes with 43.4 Watts Pure Resistive Load, 141,480 Rpm, Oscilloscope Sensitivity 400 Microinches per Centimeter (Smallest Orbit Turbine End)

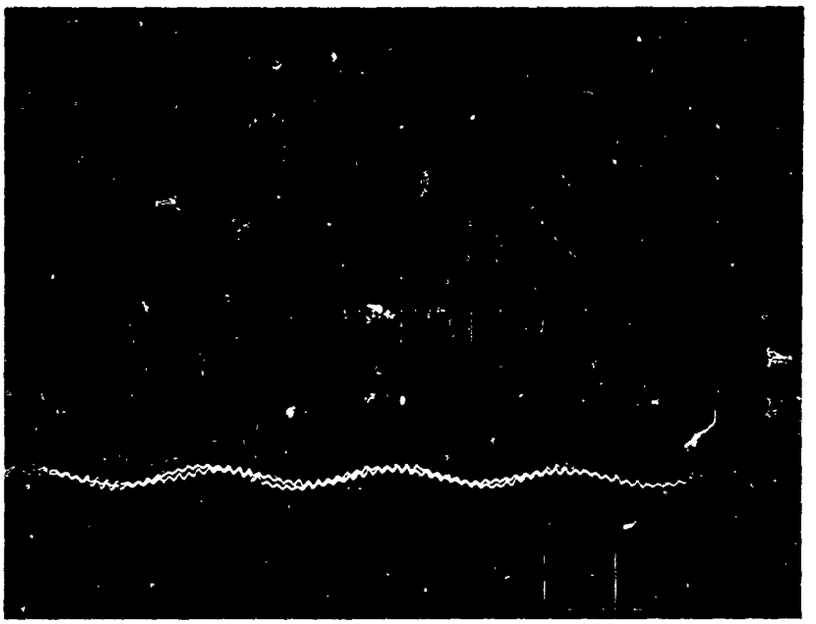

Figure 4.1.4.6-12. Thrust Proximity Probe Signal with 96.2 Watts Pure Resistive Load, 220,680 Rpm, Oscilloscope Sensitivity 400 Microinches per Centimeter

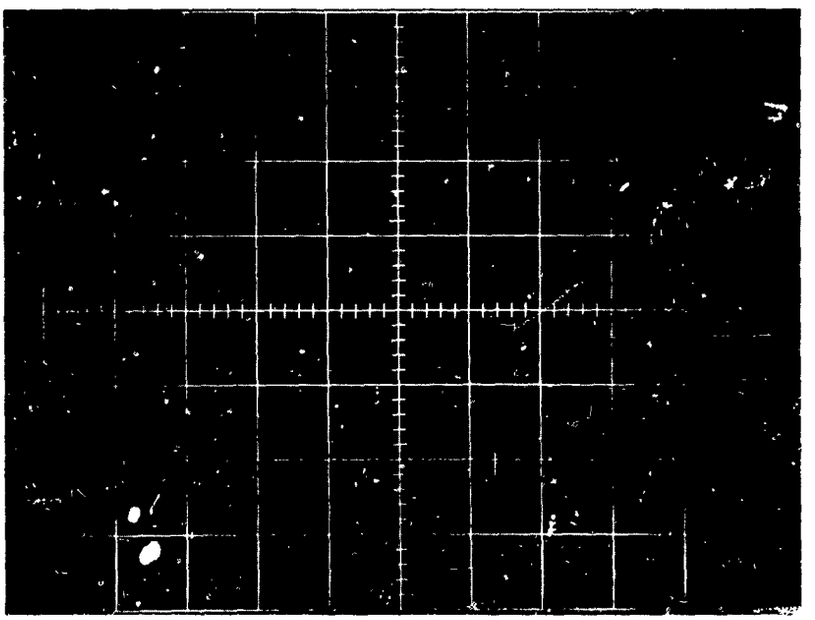

Figure 4.1.4.6-13. Signals from Shaft Orbit Proximity Probes with 96.2 Watts Pure Resistive Load, 220,680 Rpm, Oscilloscope Sensitivity 400 Microinches per Centimeter (Smallest Orbit Turbine End)

With the majority of the tests conducted, a review was made to determine whether any additional tests were desired.

It was found desirable to obtain more data on the turboalternator assembly used in Test Run 105 at no load and low loads to compare with earlier data on the other turboalternator assemblies and to make the turboalternator available for operation and indoctrination of P. Pemberton of Ft. Belvoir. Hence test Runs 106 through 109 were conducted.

4. 1. 4. 7 Test Run 106 (22 September 1969). The turboalternator was operated at room temperature, with no load and in a horizontal position, with speeds ranging from 92, 280 to 215, 520 rpm.

All test data are shown in Table 4. 1. 4. 7-1. Figure 4. 1. 4. 7-1 shows the line-to-line voltage waveform at 215, 200 rpm. Figures 4. 1. 4. 7-2 and 4. 1. 4. 7-3 show the signals from the proximity probes at 215, 200 rpm.

4. 1. 4. 8 Test Run 107 (22 September 1969). The turboalternator was operated at room temperature with loads from 2. 55 watts to 52. 6 watts at room temperature and approximately 180, 000 rpm in the horizontal position.

All test data are shown in Table 4. 1. 4. 8-1.

Figure 4. 1. 4. 8-1 shows the voltage waveform of the voltage across the 123. 5-ohm resistor at 52. 6 watts and 180, 540 rpm. Figures 4. 1. 4. 8-2 and 4. 1. 4. 8-3 show the signals from the proximity probes at the 52. 64-watt load condition.

4. 1. 4. 9 Test Run 108 (23 September 1969). The turboalternator was operated with liquid-nitrogen precooling at no load in the horizontal position with speeds ranging from 241, 800 rpm to 91, 920 rpm.

All test data taken are shown in Table 4. 1. 4. 9-1. Figure 4. 1. 4. 9-1 shows the line-to-line voltage waveform at 91, 920 rpm. Figures 4. 1. 4. 9-2 and 4. 1. 4. 9-3 show the signals from the proximity probes at 91, 920 rpm; corresponding figures for 241, 800 rpm are shown on Figures 4. 1. 4. 9-4 through 4. 1. 4. 9-6.

4. 1. 4. 10 Test Run 109 (23 September 1969). The turboalternator was operated with loads from 2. 76 watts to 60. 8 watts at cryogenic temperatures and at approximately 180, 000 rpm in the horizontal position.

All test data taken are shown in Table 4. 1. 4. 10-1. Figure 4. 1. 4. 10-1 shows the voltage waveform of the voltage across the 123. 5-ohm resistor for 60. 8 watts at 179, 340 rpm. Figures 4. 1. 4. 10-2 and 4. 1. 4. 10-3 show the signals from the proximity probes at this 60. 8-watt load condition.

The turboalternator operated very well during these last five test runs, both at room temperature and liquid-nitrogen temperature. After Test Run 109,

Table 4.1.4.7-1

TURBOALTERNATOR PERFORMANCE TEST RESULTS,
NO-LOAD CONDITIONS AT ROOM TEMPERATURE
(Test Run 106, 22 September 1969)

Load Type		Data Point (D1)				
		1	2	3	4	5
Frequency (Hertz)	(C1)	3592	3011	2517	1963	1538
Speed (rpm)		215,520	180,660	151,020	117,780	92,280
Flowmeter pressure (psig)	(P0)	87.79	88.42	88.58	88.95	89.27
Turbine inlet pressure (inches of mercury)	(P1)	2.65	2.02	1.58	1.09	0.82
Flowmeter (percent)	(J)*	40.9	35.7	31.4	26.9	23.2
Housing pressure (inches of water)	(H9)	0.088	0.070	0.052	0.038	0.025
Load resistance (L-N) (ohms)	(R)	0	0	0	0	0
Voltage (L-L) black-orange (volts)	(V4)	104	87.5	73.4	57	44.7
Voltage (L-L) black-white (volts)	(V5)	104	87.9	73.7	57.5	45
Voltage (L-L) white-orange (volts)	(V6)	104	87.9	73.7	57.5	45
Voltage, average output (volts)		104	87.8	73.6	57.3	45.2
Rotameter reference temperature (°K)	(T0)	298 8	298.9	299	299.1	298.9
Turbine nozzle inlet temperature (°K)	(T1)	299.2	299.2	299.2	299.1	299.1
Turbine exhaust temperature (°K)	(T4)	295.2	296.5	296.8	297.7	298.1
Turbine exhaust temperature (°K)	(T5)	295.2	296.5	296.8	297.7	298.1
Turbine exhaust temperature (°K)	(T6)	295.2	296.5	296.8	297.7	298.1
Turbine exhaust temperature (°K)	(T7)	295.6	296.7	297.1	297.7	298.1
Turbine-end winding temperature (°K)	(S0)	302.4	302.4	301.6	301.7	300.7
Turbine-end winding temperature (°K)	(S1)	302.2	301.8	301.1	300.6	300
Stator shell temperature (°K)	(S2)	302.2	301.8	301.1	301.4	300
Stator shell temperature (°K)	(S3)	302.2	301.9	301.9	300.7	301.1
Stator slot temperature (°K)	(S4)	302.4	301.9	301	300.5	300
Stator slot temperature (°K)	(S5)	302.4	301.9	301	300.5	300
Aft end winding temperature (°K)	(S6)	302.8	301.9	301.2	300.6	300.1
Aft end winding temperature (°K)	(S7)	302.5	301.9	301.1	300.6	300.1
Aft end gas temperature (°K)	(S8)	305.7	304	302.9	301.9	300.7
Aft end gas temperature (°K)	(S9)	304.9	303.6	302.5	301.4	300.7

*Flowmeter
Float GSVT-40
Tube FP-1/2-17G-10

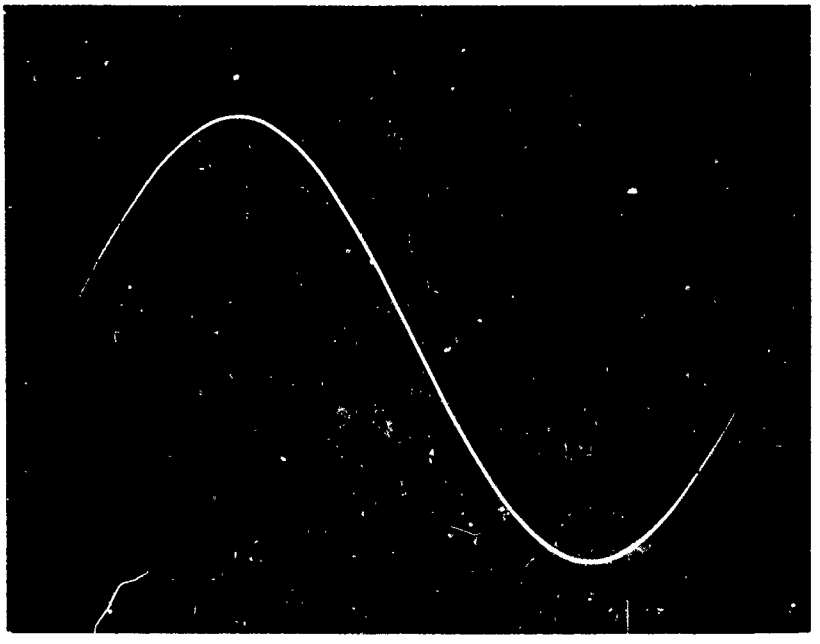

Figure 4.1.4.7-1. Line-to-line Voltage, No Load, 215,520 Rpm, Room Temperature, Oscilloscope Sensitivity 50 Volts per Centimeter

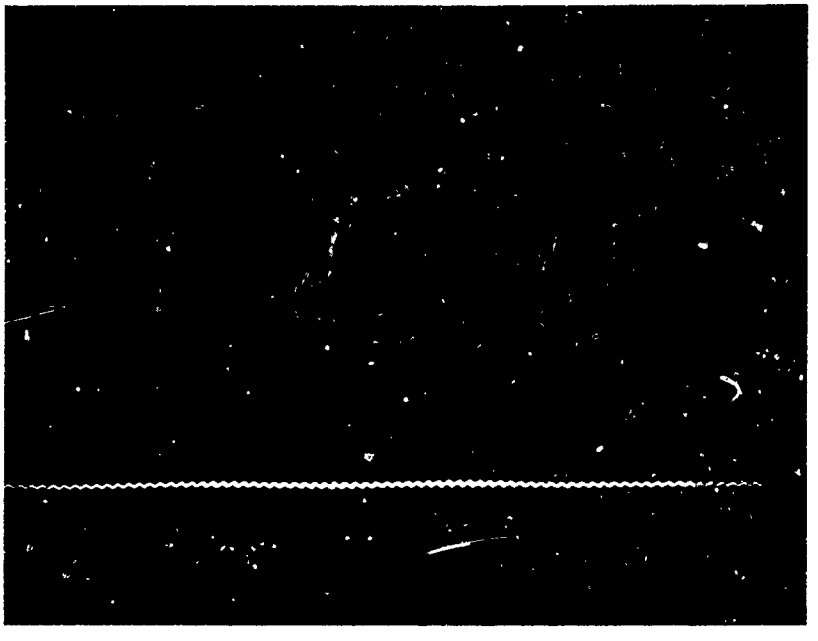

Figure 4.1.4.7-2. Thrust Proximity Probe Signal at No Load, 215,520 Rpm, Room Temperature, Oscilloscope Sensitivity 400 Microinches per Centimeter

Table 4.1.4.8-1

TURBOALTERNATOR PERFORMANCE TEST RESULTS, LOAD CONDITIONS AT ROOM TEMPERATURE (Test Run 107, 22 September 1969)

Load Type		Data Point (D1)				
		1	2	3	4	5
Frequency (Hertz)	(C1)	3009	3016	3012	3010	3009
Speed (rpm)		180,540	180,960	180,720	180,600	180,540
Flowmeter pressure (psig)	(P0)	88.34	88.00	86.97	86.20	85.17
Turbine inlet pressure (inches of mercury)	(P1)	2.60	3.76	6.89	9.63	13.55
Flowmeter (percent)	(J)*	12	15	21.7	26.5	32.2
Housing pressure (inches of water)	(H9)	0.065	0.069	0.072	0.103	0.168
Load resistance (L-N) (ohms)	(R)	2985	990	326.5	199	123.5
Voltage per phase, across resistance (volts)	(V1)	50.5	50.5	49.6	48.7	47
Voltage per phase, across resistance (volts)	(V2)	50.8	50 8	49.7	48.8	47.2
Voltage per phase, across resistance (volts)	(V3)	50.7	50.5	49.5	48.6	46.8
Voltage, average output (volts)		50.7	50.6	49.6	48.7	47
Current, voltage across 10-ohm shunt (volts)	(B1)	0.167	3.504	1.50	2.42	3.76
Current, voltage across 10-ohm shunt (volts)	(B2)	0.168	0.504	1.49	2.41	3.75
Current, voltage across 10-ohm shunt (volts)	(B3)	0.169	0.507	1.51	2.44	3.69
Electrical power output (watts)		2.55	7.67	22.3	35.4	52.6
Rotameter reference temperature (°K)	(T0)	299.2	299.2	299.1	299.1	299.1
Turbine nozzle inlet temperature (°K)	(T1)	299.3	299.3	299.4	299.4	299.5
Turbine exhaust temperature (°K)	(T4)	294.5	292.9	287.6	283.9	280.2
Turbine exhaust temperature (°K)	(T5)	294.5	292.0	287 1	283.3	279.5
Turbine exhaust temperature (°K)	(T6)	294 5	291 8	287 5	284	279.8
Turbine exhaust temperature (°K)	(T7)	294.5	291 8	287 4	284	280.7
Turbine-end winding temperature (°K)	(S0)	300.9	299.3	297.7	297.2	298.1
Turbine-end winding temperature (°K)	(S1)	300.5	299.4	297.7	296.7	298
Stator shell temperature (°K)	(S2)	300 5	299.4	297.5	295.5	297
Stator shell temperature (°K)	(S3)	300.8	299.2	297	296	294 5
Stator slot temperature (°K)	(S4)	300 5	299.4	297.5	296.8	297 8
Stator slot temperature (°K)	(S5)	300.5	299.4	297 5	296 7	297.7
Aft-end winding temperature (°K)	(S6)	300 5	299.5	297.6	296 8	298
Aft-end winding temperature (°K)	(S7)	300 4	299.5	297 5	297.4	298.4
Aft-end gas temperature (°K)	(S8)	302 8	301.8	299	298	298.1
Aft-end gas temperature (°K)	(S9)	302.3	301 2	297.9	296.8	296 5

*Flowmeter

Float GSVT-44
Tube FP-1/2-27G-10

NOT REPRODUCIBLE

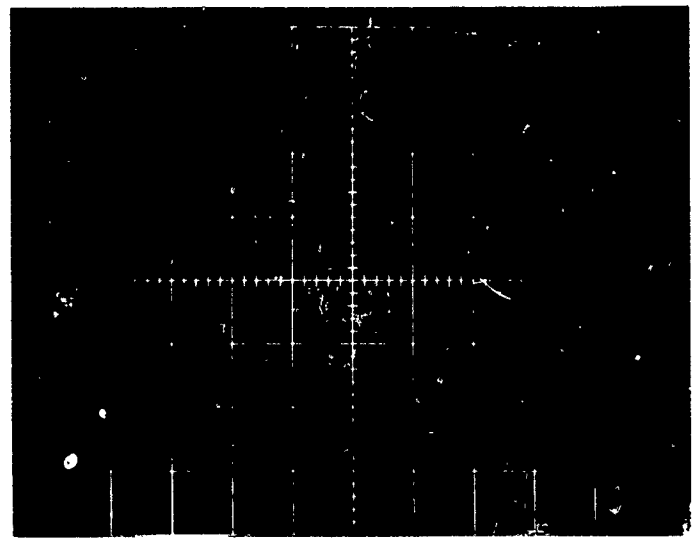

Figure 4.1.4.7-3. Signals from Shaft Orbit Proximity Probes, No Load, 215,520 Rpm, Room Temperature, Oscilloscope Sensitivity 400 Microinches per Centimeter (Smallest Orbit Turbine End)

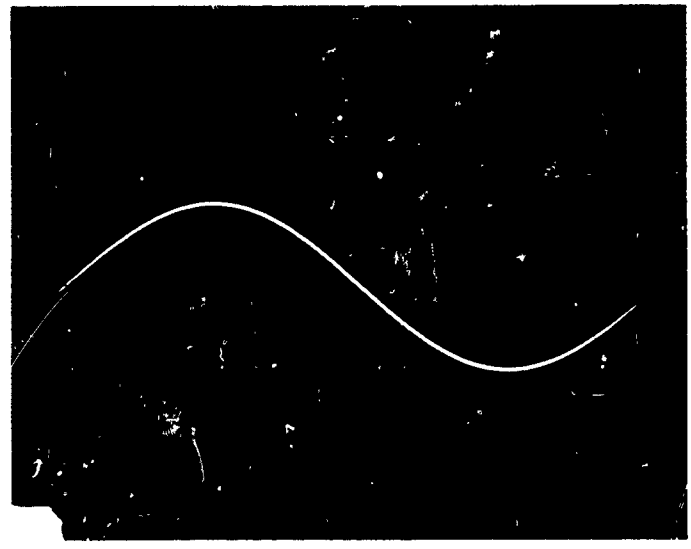

Figure 4.1.4.8-1. Voltage Waveform across 123.5-ohm Resistor, 52.64 Watts, Room Temperature, 180,540 Rpm, Oscilloscope Sensitivity 50 Volts per Centimeter

NOT REPRODUCIBLE

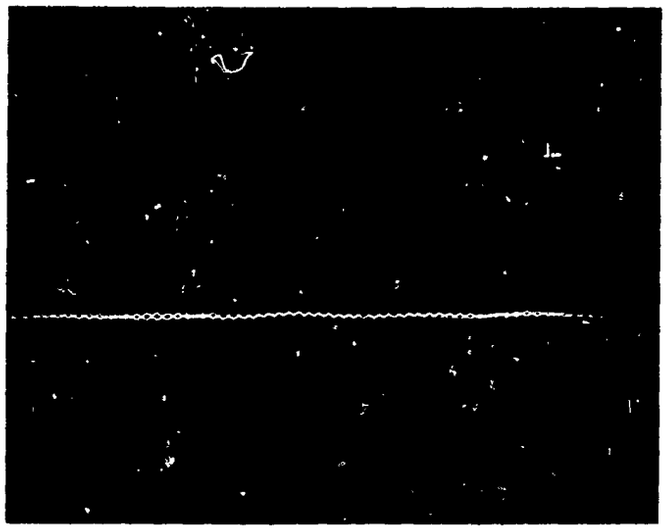

Figure 4.1.4.8-2. Thrust Proximity Probe Signal, 52.64-watt Load, Room Temperature, 180,540 Rpm, Oscilloscope Sensitivity 400 Microinches per Centimeter

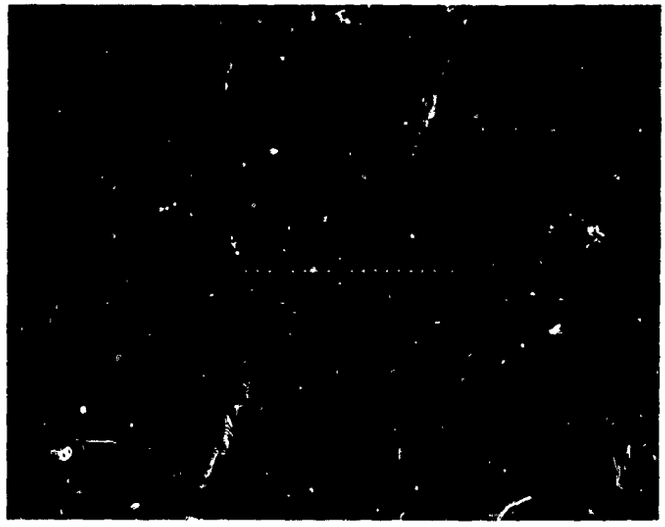

Figure 4.1.4.8-3. Signals from Shaft Orbit Proximity Probes, 52.64-watt Load, Room Temperature, 180,540 Rpm, Oscilloscope Sensitivity 400 Microinches per Centimeter (Smallest Orbit Turbine End)

Table 4.1.4.9-1

TURBOALTERNATOR PERFORMANCE TEST RESULTS NO-LOAD CONDITIONS AT CRYOGENIC TEMPERATURES (Test Run 108, 23 September 1969)

Load Type		Data Point (D1)					
		1	2	3	4	5	6
Frequency (Hertz)	(C1)	4030	3577	3002	2514	2003	1532
Speed (rpm)		241,800	214 620	180,120	150,840	120,180	91,920
Flowmeter pressure (psig)	(P0)	85.25	86 66	87.36	87.55	88.17	88.50
Turbine inlet pressure (inches of mercury)	(P1)	6.55	5 07	3 46	2.39	1.55	0.94
Flowmeter (percent)	(J)*	25.9	22.4	18.4	15.1	12.5	10
Housing pressure (inches of water)	(H9)	0.136	0.101	0.071	0.052	0.045	0.030
Load resistance (L-N) (ohms)	(R)	0	0	0	0	0	0
Voltage (L-L) black-orange (volts)	(V4)	122	108	89.6	76.2	60.8	46.5
Voltage (L-L) black-white (volts)	(V5)	123	109	90	76.8	61.3	46.7
Voltage (L-L) white-orange (volts)	(V6)	123	109	90	76.8	61.4	46.8
Voltage, average output (volts)		123.7	108.7	89.8	76.6	61.2	46.7
Rotameter reference temperature (°K)	(T0)	295.8	295.9	296	296.2	296.3	296.1
Turbine nozzle inlet temperature (°K)	(T1)	93.1	94.2	97	100.7	104.6	117.6
Turbine exhaust temperature (°K)	(T4)	100.6	102.8	108.6	115.6	124.4	142.6
Turbine exhaust temperature (°K)	(T5)	100.8	103.1	108.8	116.2	124.8	142.8
Turbine exhaust temperature (°K)	(T6)	101.6	103.9	109.2	116.2	125.2	143.2
Turbine exhaust temperature (°K)	(T7)	102	104.5	110	117.2	125.7	143.8
Turbine-end winding temperature (°K)	(S0)	108	109.8	116.2	123.2	132.6	152.6
Turbine-end winding temperature (°K)	(S1)	111.8	112.8	118	125.2	133.2	151.2
Stator shell temperature (°K)	(S2)	111.8	115.6	120.8	127.3	135.2	152.9
Stator shell temperature (°K)	(S3)	113.3	114.6	123.2	126.8	135	155.5
Stator slot temperature (°K)	(S4)	114.6	116.8	121.8	128.7	136.2	153.6
Stator slot temperature (°K)	(S5)	110.8	112 4	117.8	125.2	134	151.9
Aft-end winding temperature (°K)	(S6)	109.8	111.5	116.5	124.2	132.9	151
Aft-end winding temperature (°K)	(S7)	112.2	113.6	117.6	124.6	133.2	151.5
Aft-end gas temperature (°K)	(S8)	112.8	114.7	119.3	126.7	135.3	153.7
Aft-end gas temperature (°K)	(S9)	113 3	115	120.2	127.5	136.3	154.6

*Flowmeter
Float GSVT-44
Tube FP-1/2-27G-10

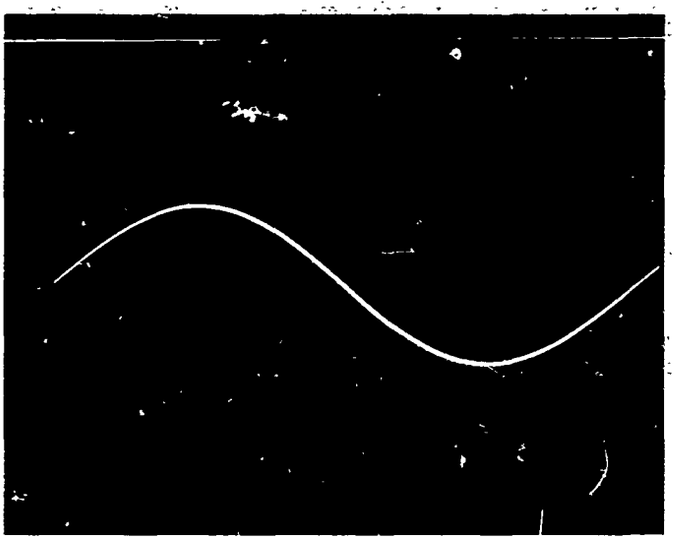

Figure 4.1.4.9-1. Line-to-line Voltage, No Load, 91,920 Rpm, Cryogenic Temperature, Oscilloscope Sensitivity 50 Volts per Centimeter

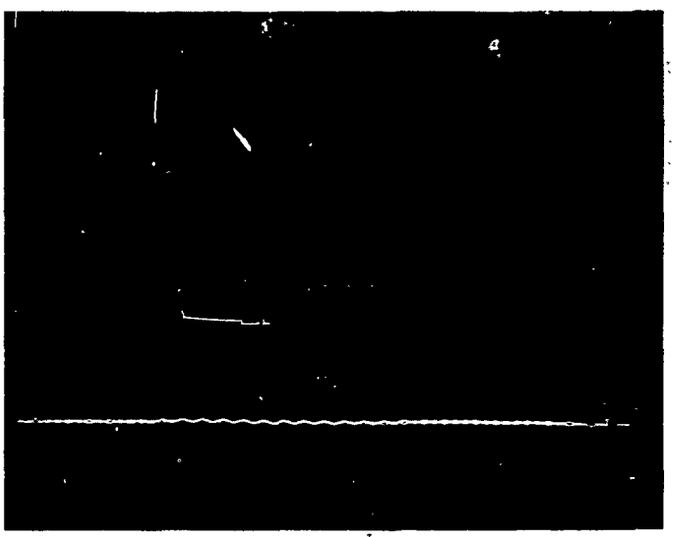

Figure 4.1.4.9-2. Thrust Proximity Probe Signal, No Load, 91,920 Rpm, Cryogenic Temperature, Oscilloscope Sensitivity 400 Microinches per Centimeter

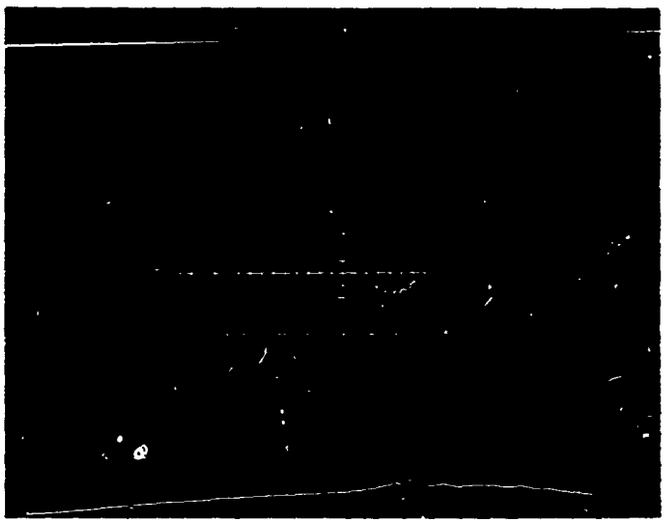

Figure 4.1.4.9-3. Signals from Shaft Orbit Proximity Probes, No Load, 91,920 Rpm, Cryogenic Temperature, Oscilloscope Sensitivity 400 Microinches per Centimeter (Smallest Orbit Turbine End)

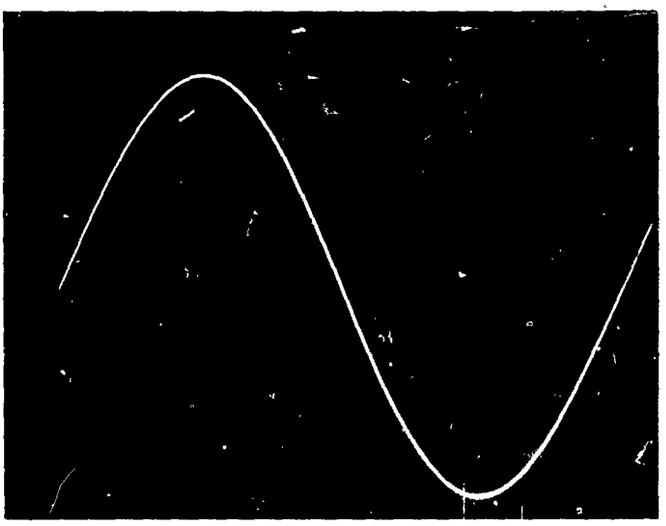

Figure 4.1.4.9-4. Line-to-line Voltage, No Load, 241,800 Rpm, Cryogenic Temperature, Oscilloscope Sensitivity 50 Volts per Centimeter

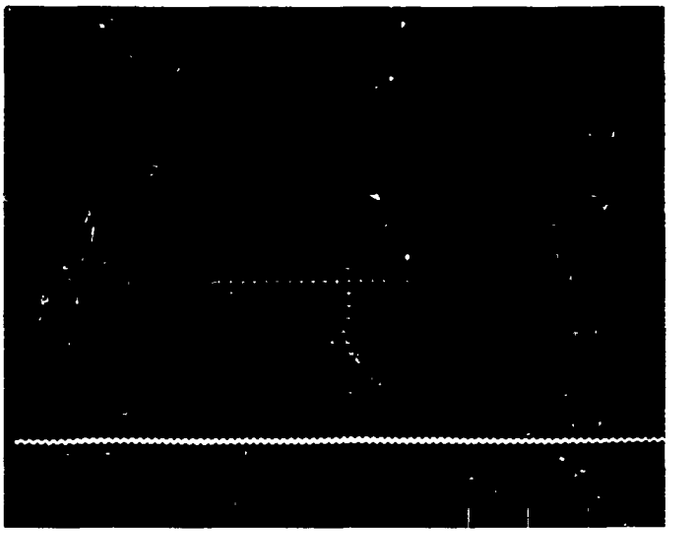

Figure 4.1.4.9-5. Thrust Proximity Probe Signal at No Load, 241,800 Rpm, Cryogenic Temperature, Oscilloscope Sensitivity 400 Microinches per Centimeter

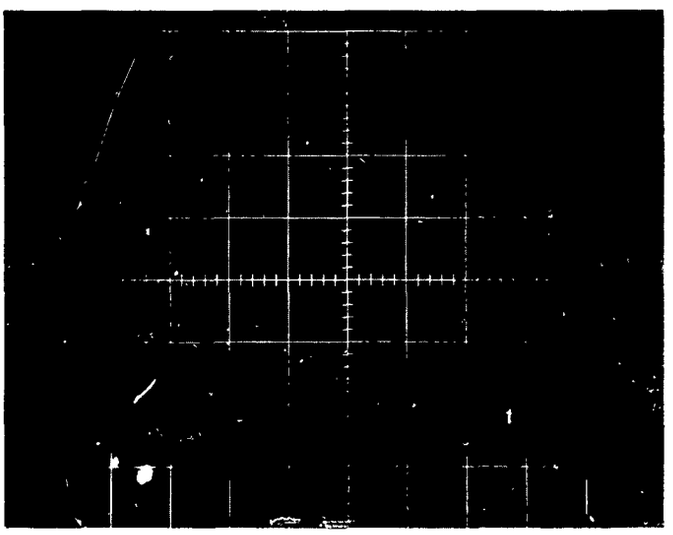

Figure 4.1.4.9-6. Signals from Shaft Orbit Proximity Probes, No Load, 241,800 Rpm, Cryogenic Temperature, Oscilloscope Sensitivity 400 Microinches per Centimeter (Smallest Orbit Turbine End)

Table 4.1.4.10-1

TURBOALTERNATOR PERFORMANCE TEST RESULTS,
LOAD CONDITIONS AT CRYOGENIC TEMPERATURES
(Test Run 109, 23 September 1969)

Load Type		Data Point (D1)				
		1	2	3	4	5
Frequency (Hertz)	(C1)	2995	3008	3006	2993	2989
Speed (rpm)		179,700	180,480	180,360	179,580	179,340
Flowmeter pressure (psig)	(P0)	85.20	83.88	80.91	77.92	78.26
Turbine inlet pressure (inches of mercury)	(P1)	4.28	5.98	9.78	14.31	16.82
Flowmeter (percent)	(J)*	22.8	30.5	45.9	60	63.7
Housing pressure (inches of water)	(H9)	0.069	0.080	0.078	0.080	0.089
Load resistance (L-N) (ohms)	(R)	2985	990	326.5	165.5	123.5
Voltage per phase, across resistance (volts)	(V1)	52.6	52.7	52.5	51.5	50.3
Voltage per phase, across resistance (volts)	(V2)	52.9	52.9	52.7	51.6	50.5
Voltage per phase, across resistance (volts)	(V3)	52.6	52.6	52.4	51.1	49.9
Voltage, average output (volts)		52.7	52.7	52.5	51.4	50.2
Current, voltage across 10-ohm shunt (volts)	(B1)	0.174	0.528	1.59	3.04	4.04
Current, voltage across 10-ohm shunt (volts)	(B2)	0.175	0.527	1.58	3.03	4.02
Current, voltage across 10-ohm shunt (volts)	(B3)	0.175	0.533	1.60	3.06	4.05
Electrical power output (watts)		2.76	8.37	25.1	46.9	60.8
Rotameter reference temperature (°K)	(T0)	296.2	296.2	296.2	296.2	296.2
Turbine nozzle inlet temperature (°K)	(T1)	94.8	89.3	85.6	89.6	100.3
Turbine exhaust temperature (°K)	(T4)	103	91.6	83.1	83.1	92.6
Turbine exhaust temperature (°K)	(T5)	103	91.6	83.1	83.1	91.6
Turbine exhaust temperature (°K)	(T6)	103.2	91.6	82.9	83.7	92.3
Turbine exhaust temperature (°K)	(T7)	103.9	92	83	82.8	91.4
Turbine-end winding temperature (°K)	(S0)	110.2	98.8	93	94.8	101.8
Turbine-end winding temperature (°K)	(S1)	114.5	103.9	96.6	93.3	103.8
Stator shell temperature (°K)	(S2)	115.2	102	95.2	92	100.2
Stator shell temperature (°K)	(S3)	116.2	102.9	93.5	91.2	98.8
Stator slot temperature (°K)	(S4)	117.9	104.2	93.5	91.6	100.4
Stator slot temperature (°K)	(S5)	113.8	103.2	97.1	97.2	104.6
Aft-end winding temperature (°K)	(S6)	112.3	111.9	94.8	94.6	102.6
Aft-end winding temperature (°K)	(S7)	114	103.8	94.9	97	103.2
Aft-end gas temperature (°K)	(S8)	115.9	104.5	97.9	96.1	102.9
Aft-end gas temperature (°K)	(S9)	116.2	104.5	97.1	95.8	102.4

*Flowmeter
Float GSVT-44
Tube FP-1/2-27G-10

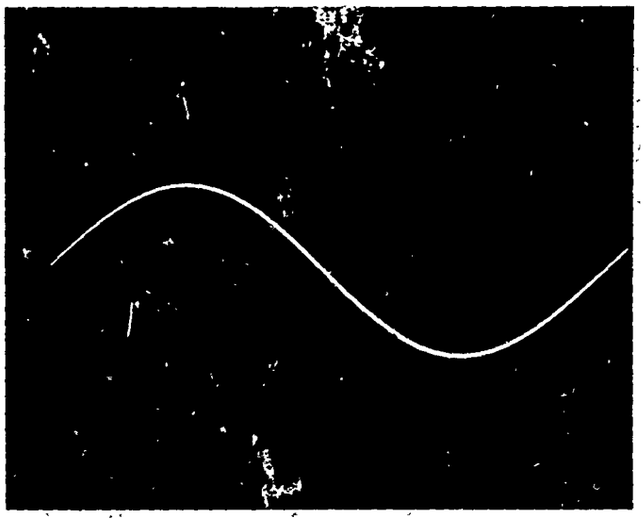

Figure 4.1.4.10-1. Voltage Waveform across 123.5-ohm Resistor, 60.8 Watts, Cryogenic Temperature, 179,340 Rpm, Oscilloscope Sensitivity 50 Volts per Centimeter

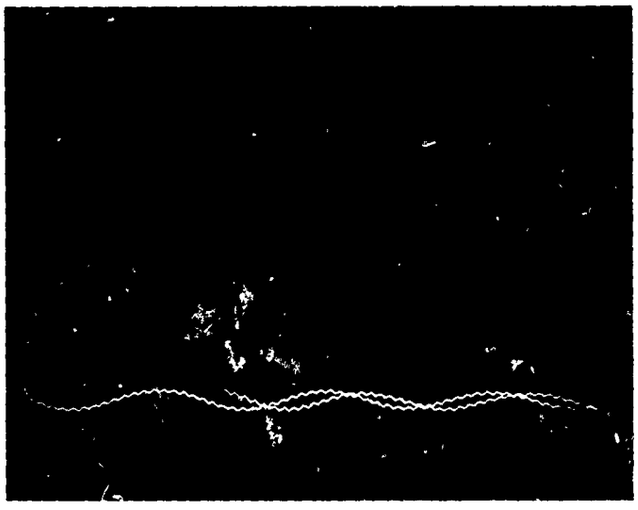

Figure 4.1.4.10-2. Thrust Proximity Probe Signal, 60.8-watt Load, Cryogenic Temperature, 179,340 Rpm, Oscilloscope Sensitivity 400 Microinches per Centimeter

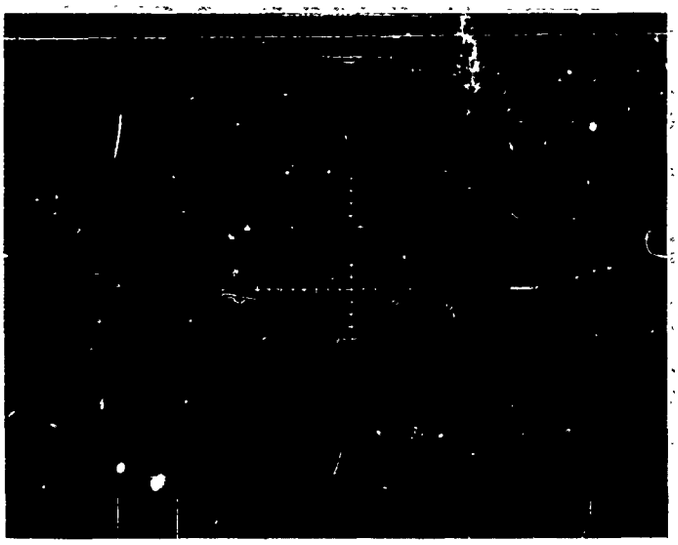

Figure 4. 1. 4. 10-3. Signals from Shaft Orbit Proximity Probes at 60. 8-watt Load, Cryogenic Temperature, 179, 340 Rpm, Oscilloscope Sensitivity 400 Microinches per Centimeter (Smallest Orbit Turbine End)

the turboalternator was turned off and restarted to retest the ability to start at the low temperature. The results agreed very closely with the test made after Test Run 105. The unit restarted with a turbine inlet pressure of 4. 4 inches of mercury and coasted down very smoothly after the inlet pressure was turned off.

After completion of Test Runs 105 through 109, the turboalternator was disassembled for inspection. The outer thrust bearing and nozzle were removed. There were no signs of dirt particles present at either end of the turboalternator and no visible signs of wear. The total testing time for the last five test runs was approximately 10 hours. From all indications, the porous wire mesh helium gas filters used seemed to be sufficient for continuous operation.

The unit was then completely disassembled and parts were further inspected for signs of wear. There was a slight amount of wear noticed near the inside diameter of the inner thrust bearing and also on the corresponding surface of the shaft inner thrust runner surface. This type of slight wear is considered normal and is believed to be caused by starting and stopping the turboalternator. There were no other indications of wear on the components.

4.2 TURBOALTERNATOR TEST EVALUATION

In the following paragraphs, performance tests conducted and described in section 4.1.4 are evaluated. Performance data obtained was reduced with the data reduction programs of Appendix I. All these computer program data reduction results are included in Appendix II. A summary of turboalternator tests was listed in Table 4.1.4-1.

Performance results have been plotted for evaluation purposes. Results from different runs were combined in many cases from similar test runs. A summary of the performance test results curves is shown in Table 4.2-1 for no-load operation and on Table 4.2-2 for load operation.

4.2.1 Room-Temperature No-load Operation

No-load tests were conducted at both room and cryogenic temperatures for a range of speeds from 92,280 rpm to 249,540 rpm. Results at cryogenic temperatures were very poor due to the problem of measuring the temperature drop across the turbine. The instrumentation accuracy of measuring these low temperatures was very close to the values expected for the turbine wheel temperature drop. This can be seen by examination of the data of Runs 103 and 108 in Appendix II. Therefore, only room-temperature no-load performance results are presented.

Figure 4.2.1-1 shows the various levels of power at no load for Run 100, with the shaft magnetized. The wheel power is from the test data, as determined by the flow through the turbine wheel and the measured temperature drop across the wheel. The core loss and bearing and windage friction powers shown were computed and based on the computer turboalternator design program. The total of these two calculated values should equal the wheel power measured; the agreement looks good.

Run 104 results are shown on Figure 4.2.1-2 for the unmagnetized shaft condition. Agreement is not as good as in the previous run, and there were no apparent reasons why there should be the differences shown.

Figure 4.2.1-3 represents a set of data for Run 106 similar to Run 100, but with two differences: the data of Run 106 is with the unit horizontal and with a larger wheel-to-nozzle clearance, but neither of these effects should significantly affect the results. The curves shown represent a reasonable correlation and compare well with the results of Figure 4.2.1-1.

A composite plot of all three runs is shown in Figure 4.2.1-4, where Runs 100 and 106 show reasonable correlation for both measured wheel power and calculated friction power. Of course the data of Run 104 do not provide good correlation.

Table 4.2-1

NO-LOAD PERFORMANCE CURVE SUMMARY

Temperature	Run	Temperature Drop Efficiency Flow Factor, Alternator/Turbine Flow Ratio versus Velocity Ratio	Wheel Power Friction, Power versus Speed	Core Loss and Friction Power Wheel Power, Friction Power Core Loss versus Speed
Room	100	X	X	X
Room	104	X Combined	X Combined	Shaft not magnetized
Room	106	X	X	X
Cryogenic	103*			
Cryogenic	108*			

*No curves (unreliable data)

Table 4.2-2

LOAD PERFORMANCE CURVE SUMMARY

Temperature	Run	Total Electrical Power Versus Speed	Alternator/Turbine, Flow Ratio and Overall Efficiency Versus Velocity Speed	Flow Factor Versus Pressure Ratio	Temperature Drop Efficiency Versus Velocity Ratio	Overall Efficiency, Electromagnetic Efficiency Versus Total Electrical Power	Voltage Versus Current	Volts per Cycle Versus Current
Room	101	X	X	X	X		X	X
Room	102	X Combined	X Combined	X Combined	X Combined		X Combined	X Combined
Room	107	X	X	X	X		X	X
Cryogenic	103	X	X	X		X		X
Cryogenic	105	X Combined	X Combined	X Combined		X Combined	Speed varied	X Combined
Cryogenic	109	X	X	X		X		X

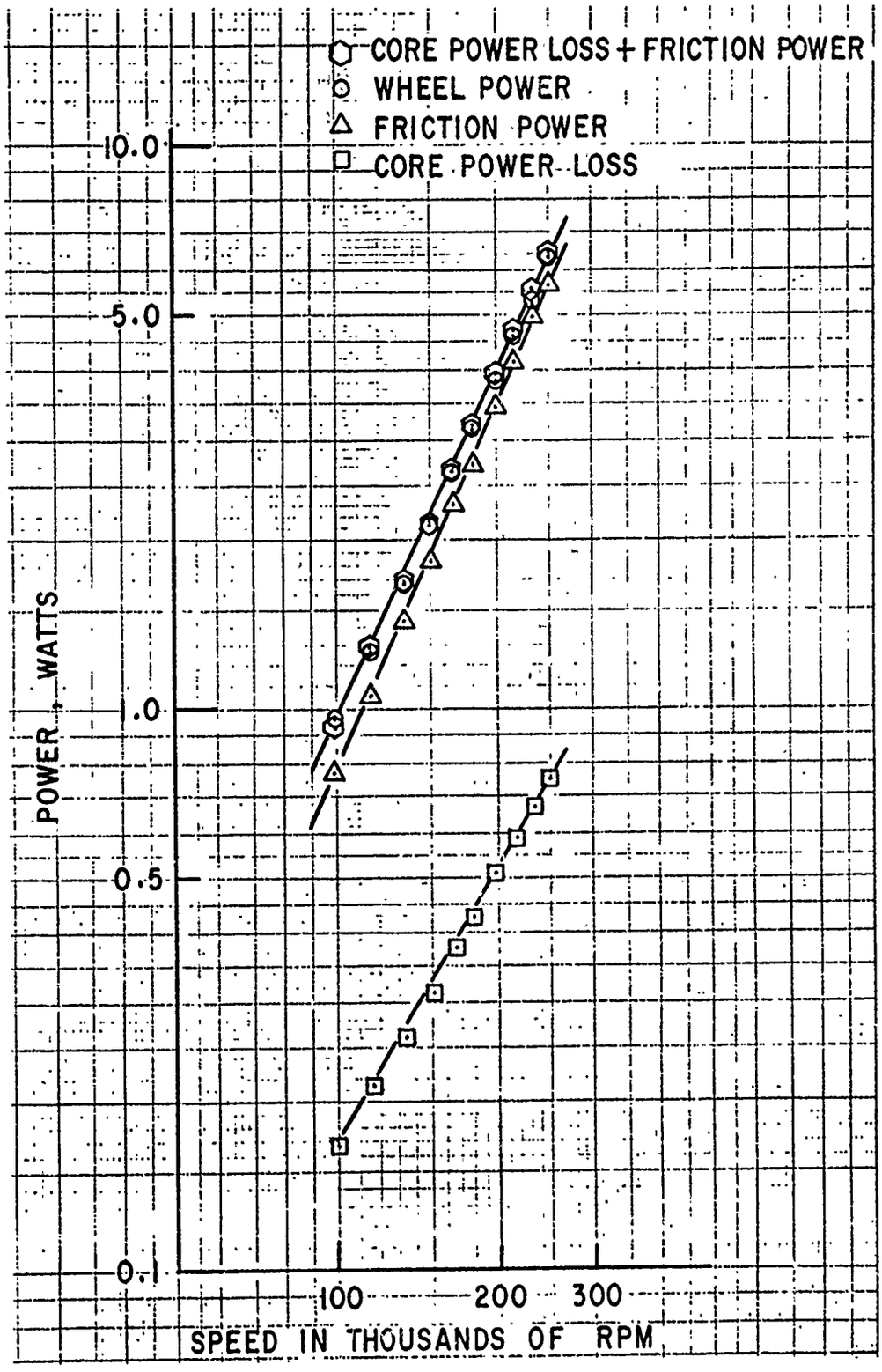

Figure 4.2.1-1. Room-temperature No-load Performance, Shaft Magnetized, Run 100

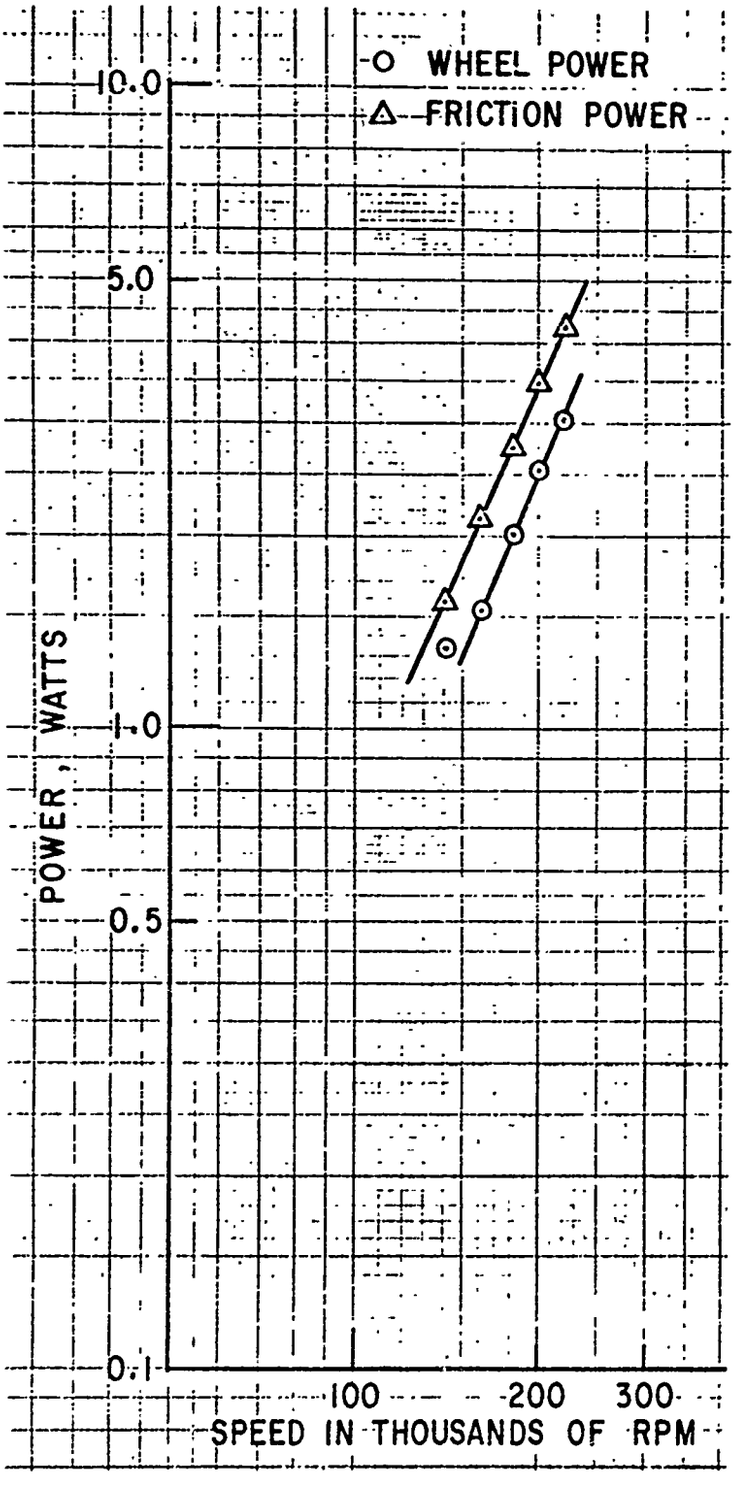

Figure 4.2.1-2. Room temperature, No-load Performance, Shaft Not Magnetized, Run 104

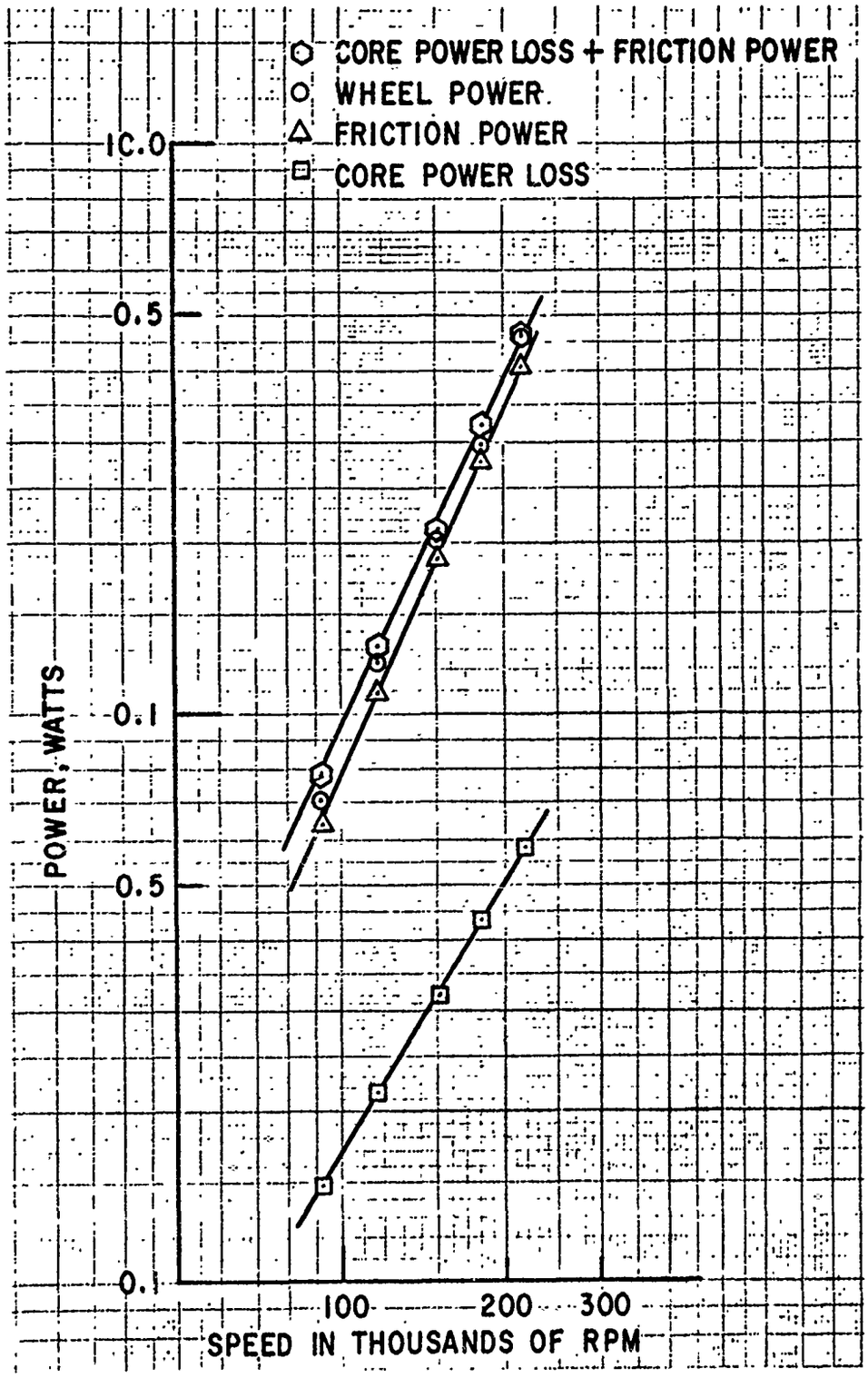

Figure 4.2.1-3. Room-temperature No-load Performance, Shaft Magnetized, Run 106

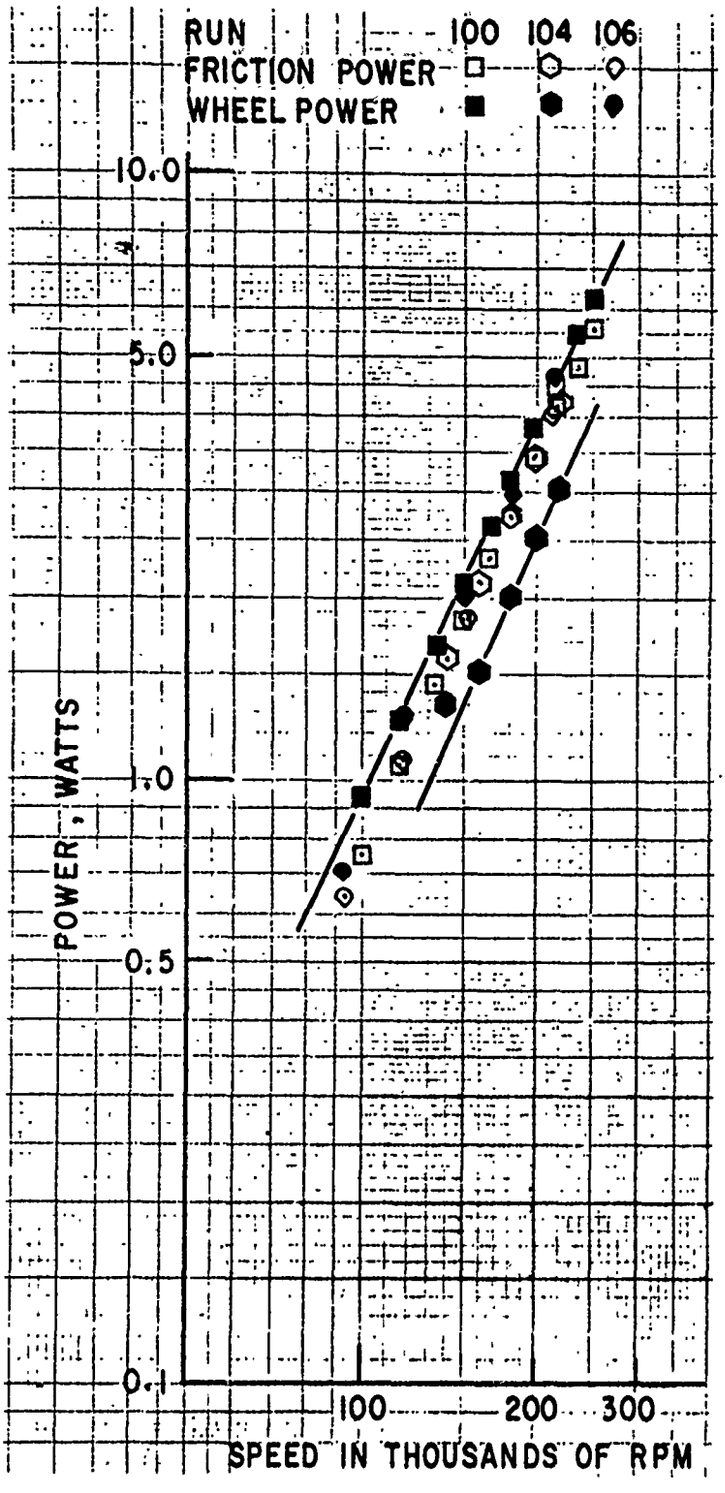

Figure 4.2.1-4. Room-temperature No-load Performance; Composite of Three Runs

For the three no-load tests, turbine performance parameters are shown in Figure 4. 2. 1-5. The poor correlation of the flow factor for Run 104 helps suggest why the wheel power and friction power did not match as well as they did in the other two runs. Because small values are being measured, some of the difference may be attributed to instrumentation accuracy, but possibly the flow factor is greater for Run 104 because of something like a small leak in a plumbing fitting to the turbine or at the nozzle-to-housing interface. The greater alternator bypass flow ratio for Run 106 appears reasonable because a 4-mil radial clearance was used, compared with a 2-mil radial clearance for Runs 100 and 104.

The turbine temperature drop efficiency appears reasonably consistent, at velocity ratios much larger than the design value of about 0. 30. Thus the flow to the blades was actually at a negative angle of attack. The data spread is reasonable considering the rather small temperature drops being measured, which ranged from 2°F to 8°F.

The pressure required to start the turboalternator has been of interest, to obtain a relative measure of the operating condition of the rotor bearing system. With no resistance load on the alternator stator, minimum starting pressures to the nozzle depend on the orientation. Typical results are:

Starting Pressure (Inches Mercury Gage)	Position	Test Temperature
2. 2	Vertical, turbine-end down	Room
3. 3	Horizontal	Room
4. 6	Horizontal	Cryogenic

After the turbine is started, the pressure is usually reduced because the starting torque is greater than the no-load running torque. Data for operation at constant speed were obtained for various orientations. Results are shown in Figure 4. 2. 1-6. The two upper curves show the pressure required to operate the unit vertically with the turbine end down. The only difference is that there is a slightly lower pressure required with the shaft not magnetized. The lowest curve is for horizontal operation with the rotor between pads for starting and with the shaft magnetized. A slightly lower characteristic should be obtained for operation on a single pad at each journal.

4. 2. 2 Room-temperature Load Operation

Alternator load tests were conducted at room temperature during Runs 101, 102, and 107.

Results of power output versus speed are shown in Figure 4. 2. 2-1. Runs 101 and 102 show fairly consistent data with solid constant load resistance lines

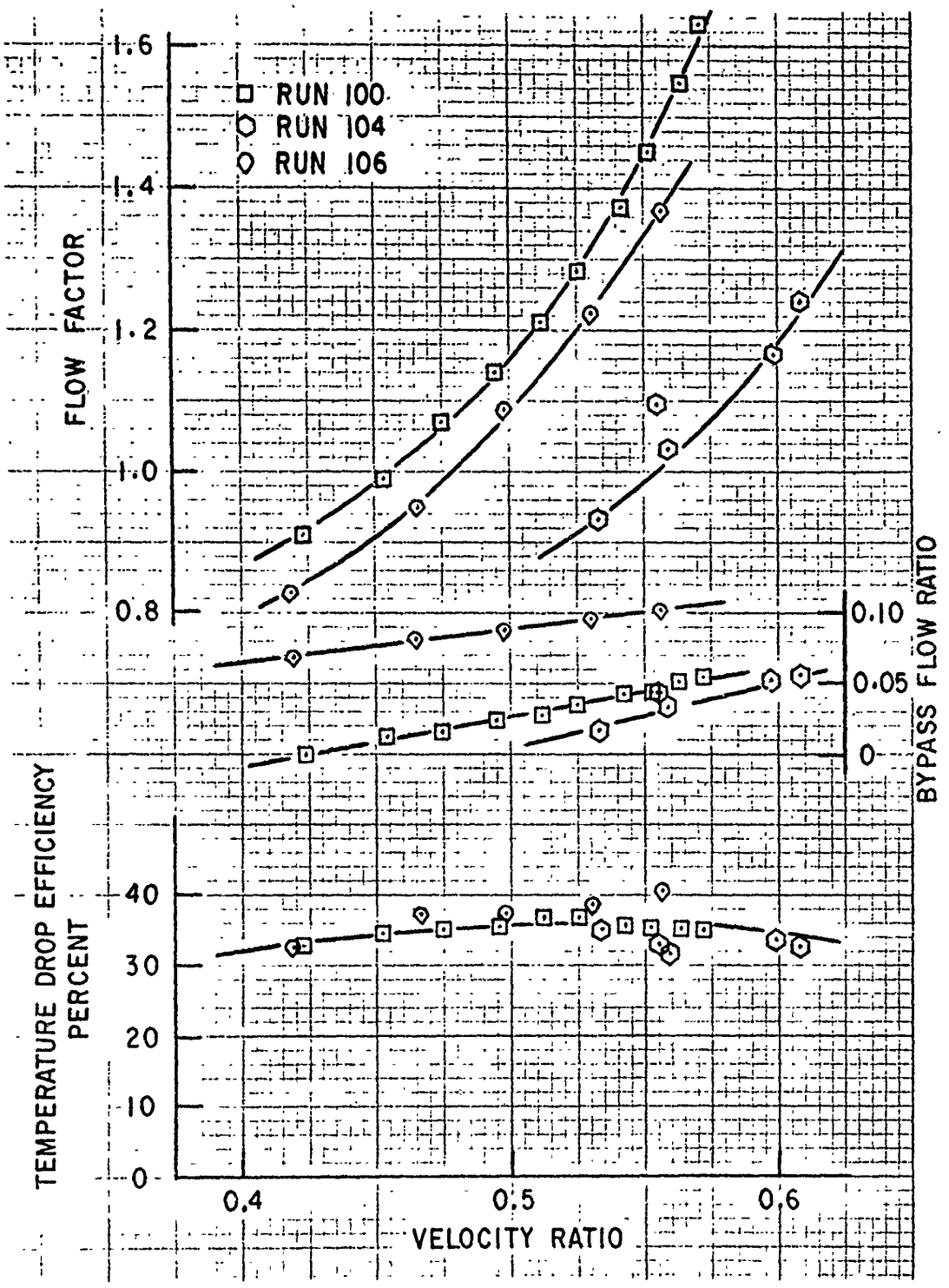

Figure 4.2.1-5. Room-temperature No-load Performance, Turbine Performance Parameters

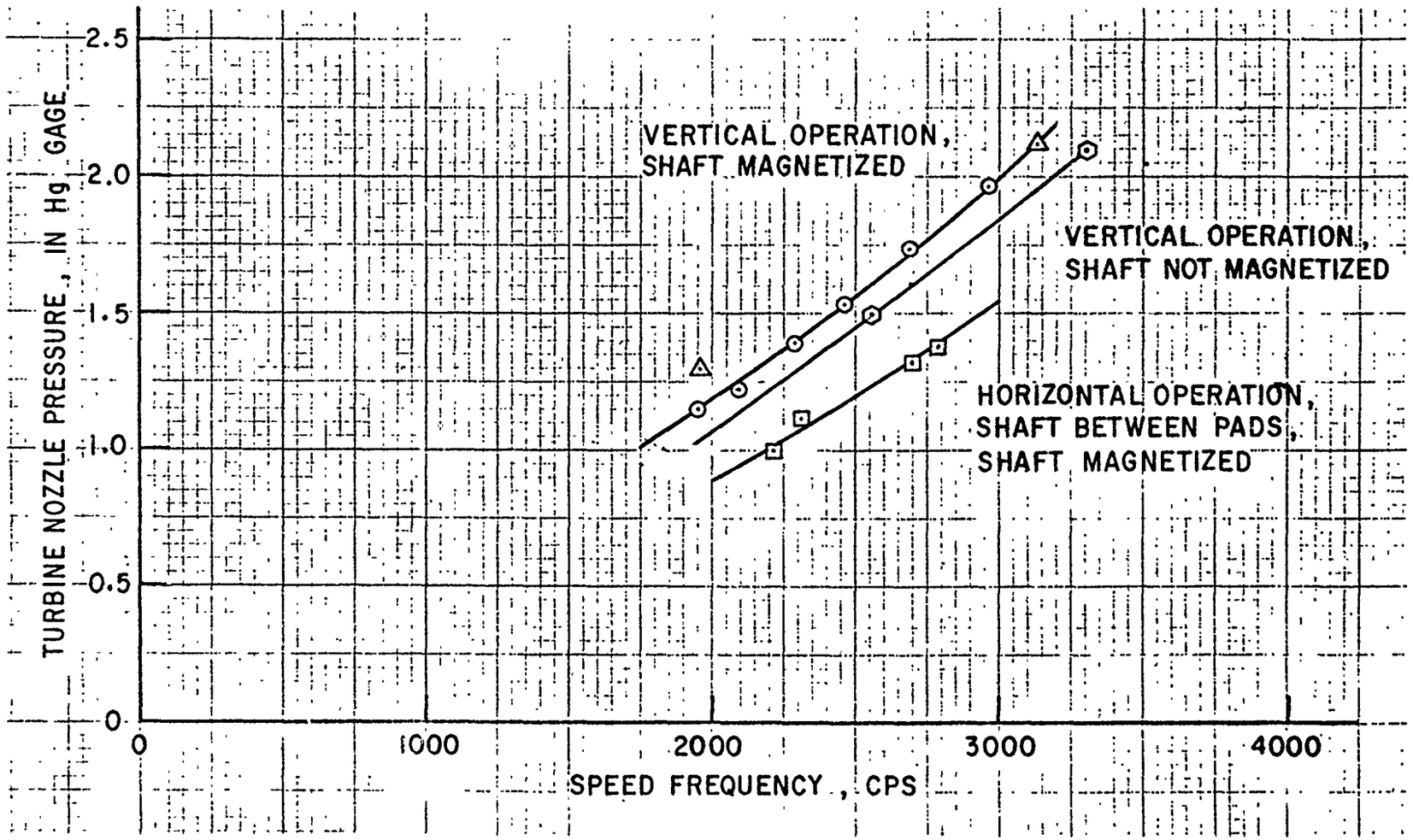

Figure 4.2.1-6. Room-temperature No-load Performance, Turbine Versus Speed

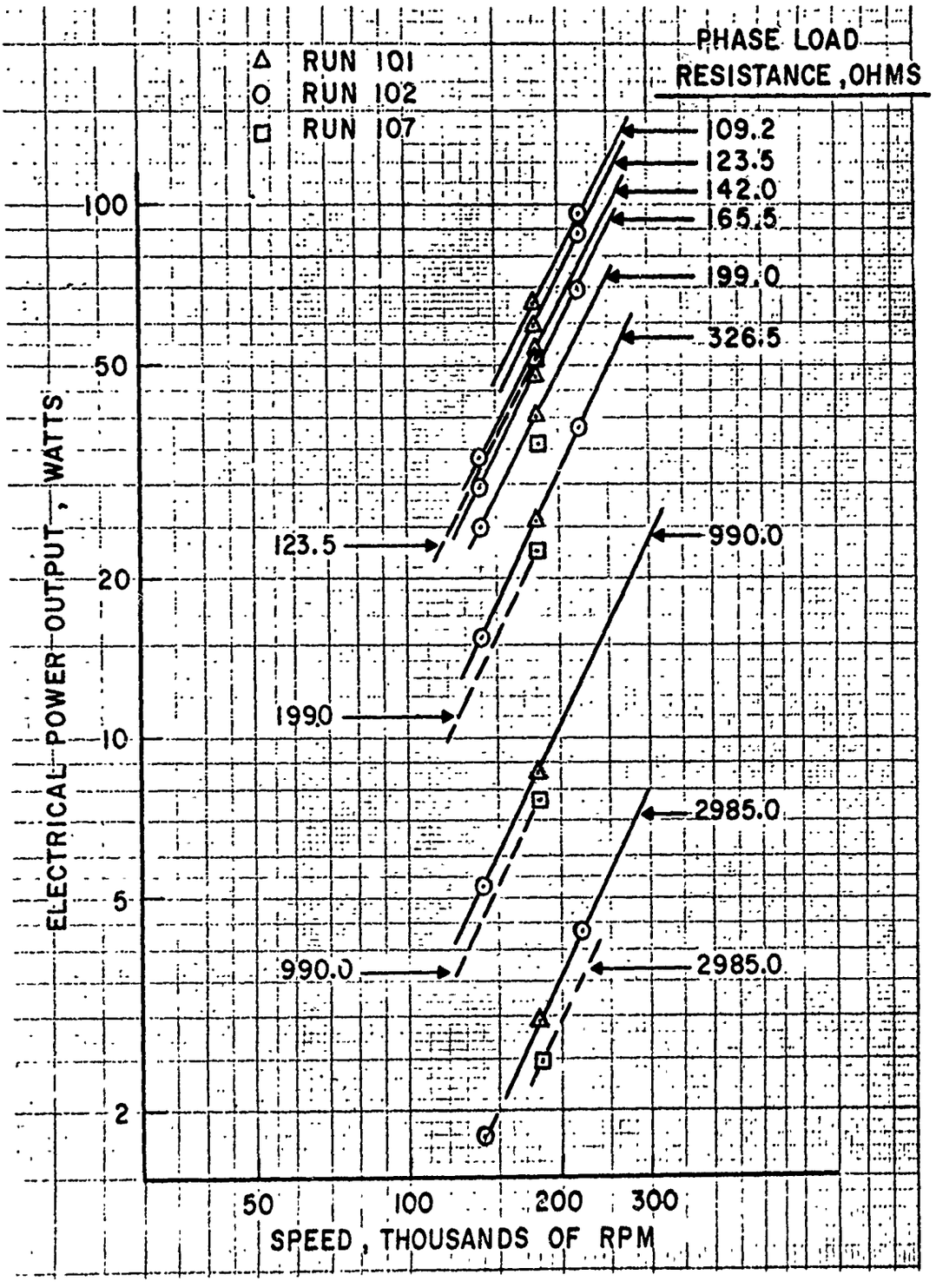

Figure 4.2.2-1. Turboalternator Room-temperature Performance, Power Output Versus Speed

connecting the data points at 140, 000, 180; 000, and 220, 000 rpm. The later data of Run 107 show a marked decrease. The differences in the turboalternator assembly can be seen on Table 4. 1. 4-1. The principal difference is in the shaft magnetization. The earlier runs had a magnet strength of 6070 gausses, while the magnet of Run 107 was 5510 gausses. The difference is believed to be a result of the process control during nitride hardening of the shaft.

Voltage regulation is demonstrated in Figure 4. 2. 2-2 for different speeds of the alternator. Runs 101 and 102 were with the same rotor and the load was unity power factor so the results are consistent. Figure 4. 2. 2-3 is a plot of the same data on a volts-per-cycle basis to rationalize the data. The results show that percent voltage regulation for unity power factor loads is very nearly the same for a given current, regardless of speed.

Turboalternator performance is shown in Figure 4. 2. 2-4. The overall efficiency, based on the actual electric power output, is shown as a function of velocity ratio. The best efficiency is with the larger wheel-tip-to-nozzle radial clearances of Run 107. This may be attributed to a better tangential flow redistribution at the nozzle discharge before the flow enters the wheel. At the same time, there is no increase in bypass flow ratio at the peak efficiency point, shown on the upper curve of Figure 2. 2. 2-4.

Figure 4. 2. 2-5 shows the temperature drop efficiency versus velocity ratio, which is the ratio of actual measured temperature drop to the isentropic temperature drop across the wheel. Again the greatest efficiency is with the larger turbine wheel radial blade clearance. The peak temperature drop efficiency is at a higher velocity ratio than the peak overall efficiency. This trend is a consequence of the higher bypass flow and friction power losses at higher velocity ratios, and the temperature drop efficiency is not affected by these losses.

It should be noted that the efficiency-versus-velocity-ratio curves are ideally parabolas for operation at constant pressure ratios. However, tests conducted were not held at constant pressure ratio, because constant speed was required and fixed resistant load steps were used. Therefore, the parabolic curves faired through the data points only suggest the appropriate trends.

The turbine nozzle flow factor characteristic is shown as a function of overall turbine pressure ratio in Figure 4. 2. 2-6. The lower flow factor at a given pressure ratio is from the higher efficiency unit. Again, this difference in characteristic can be a result of the nozzle-exit-to-wheel-inlet flow distribution due to the differences in wheel-tip radial clearances.

4. 2. 3 Cryogenic-temperature Load Operation

Turboalternator performance tests were conducted at cryogenic temperatures. Alternator electrical power outputs up to 109 watts and speeds up to 220, 000

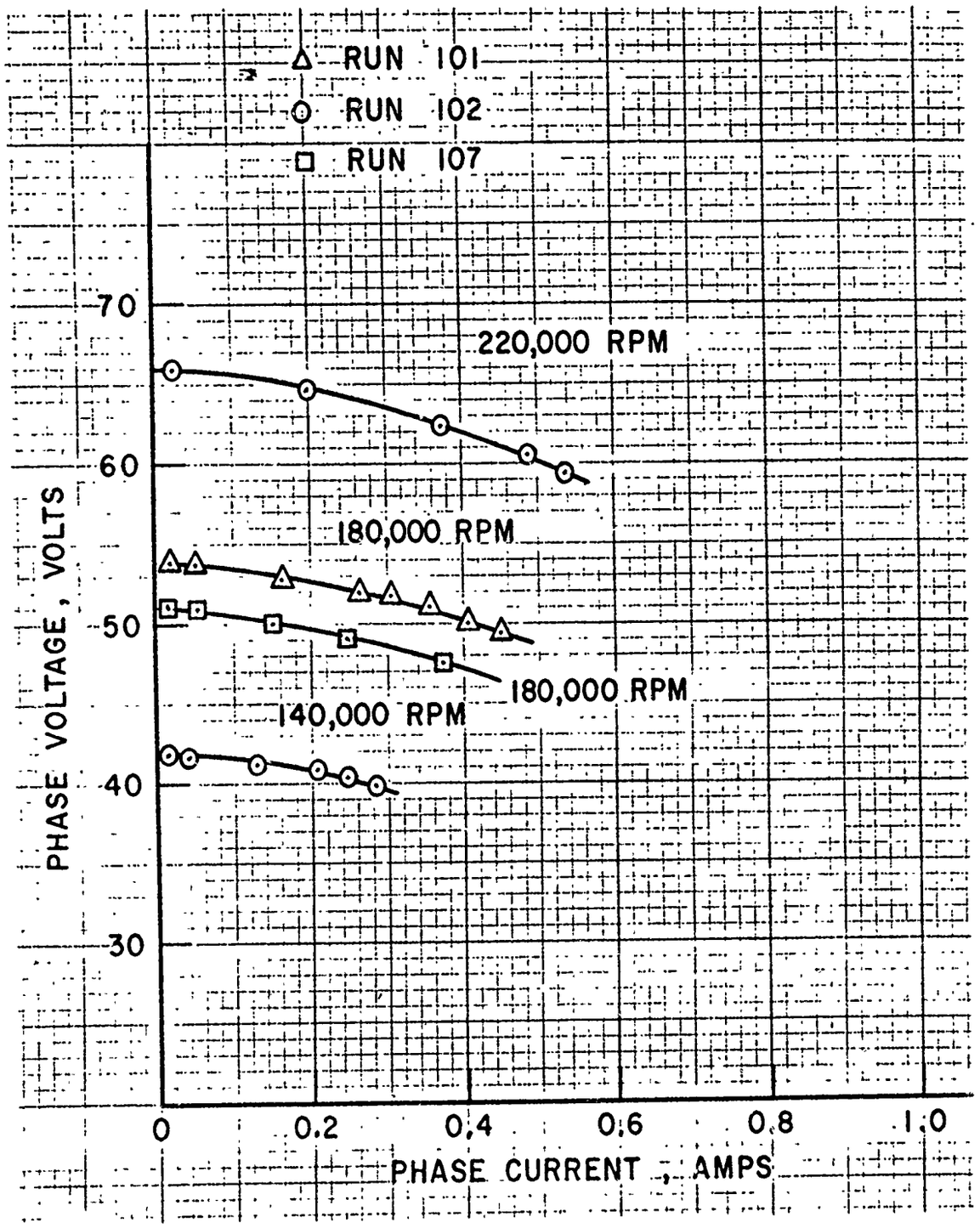

Figure 4.2.2-2. Turboalternator Room-temperature Performance, Voltage Versus Current

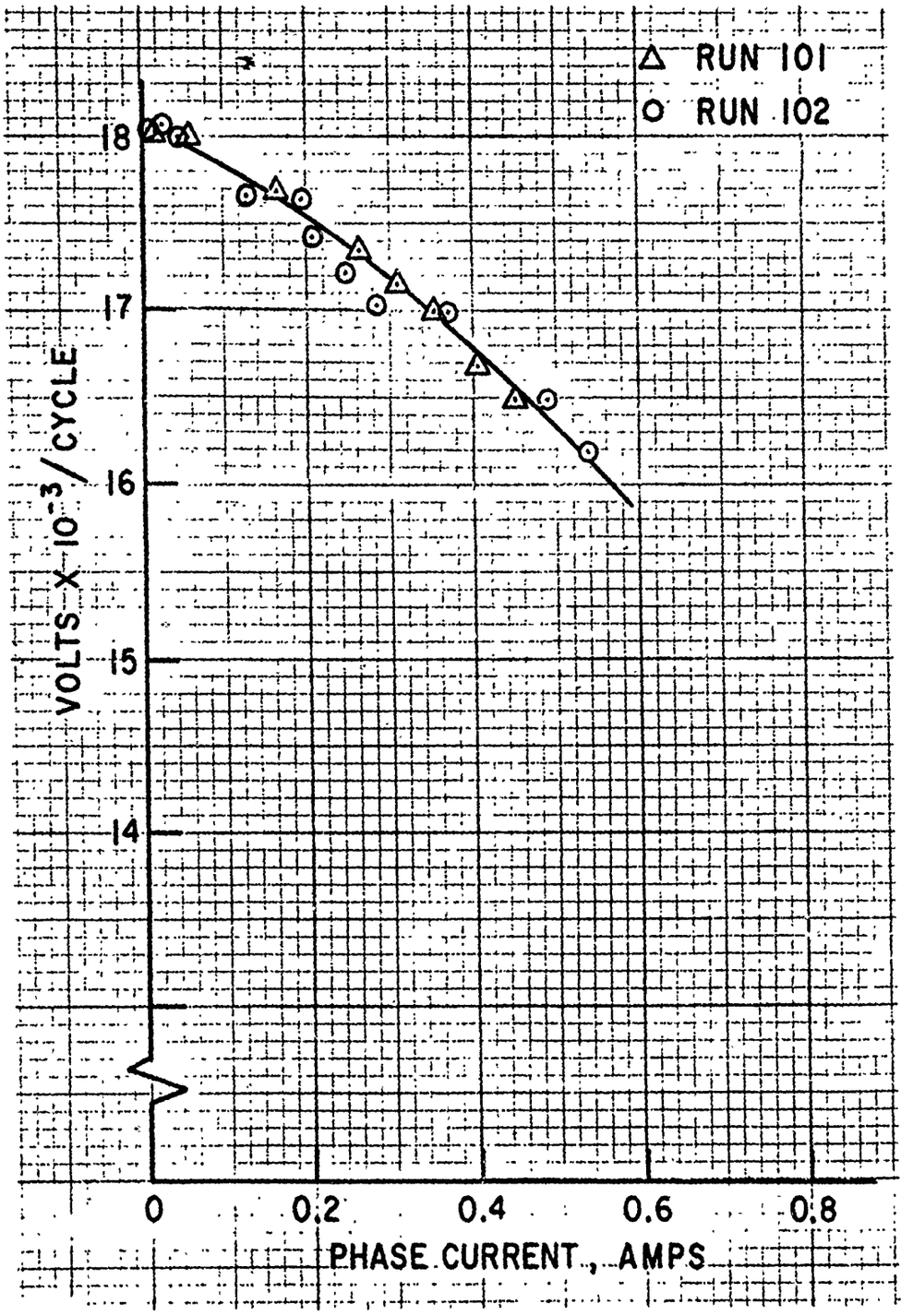

Figure 4.2.2-3. Turboalternator Room-temperature Performance, Voltage per Cycle Versus Current

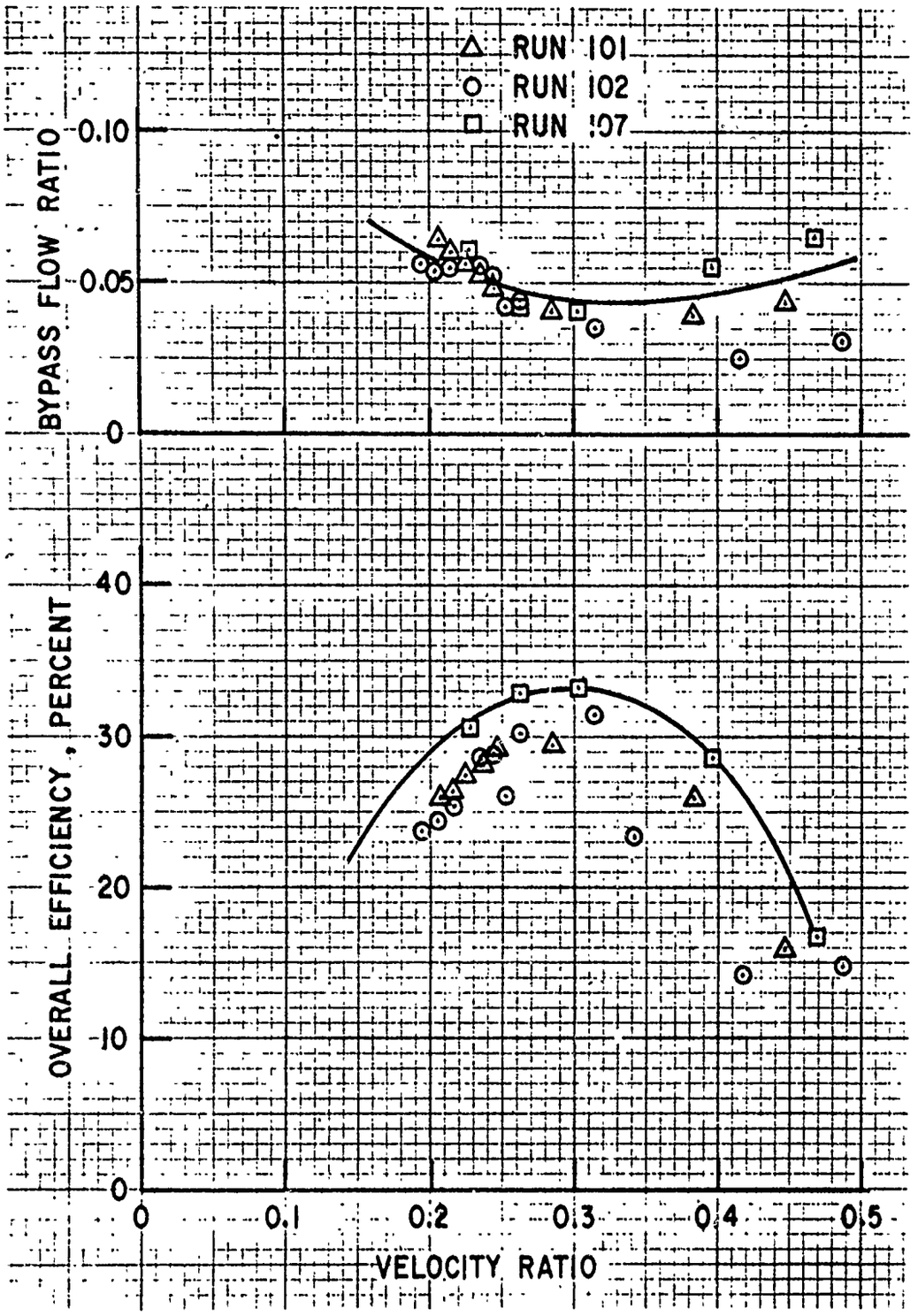

Figure 4.2.2-4. Turboalternator Room-temperature Performance, Efficiency and Bypass Flow Versus Velocity Ratio

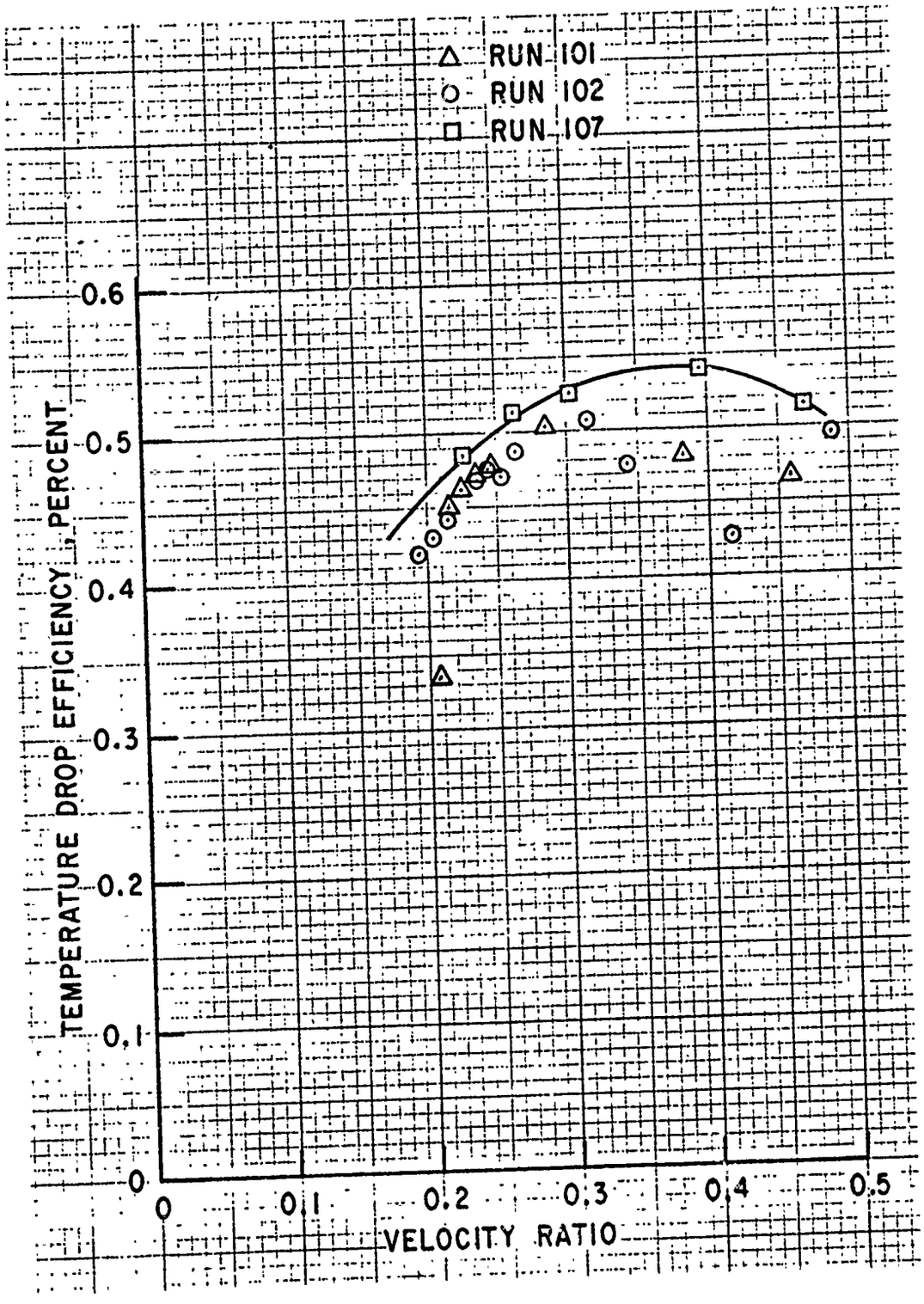

Figure 4.2.2-5. Turboalternator Room-temperature Performance, Temperature Drop Efficiency Versus Velocity Ratio

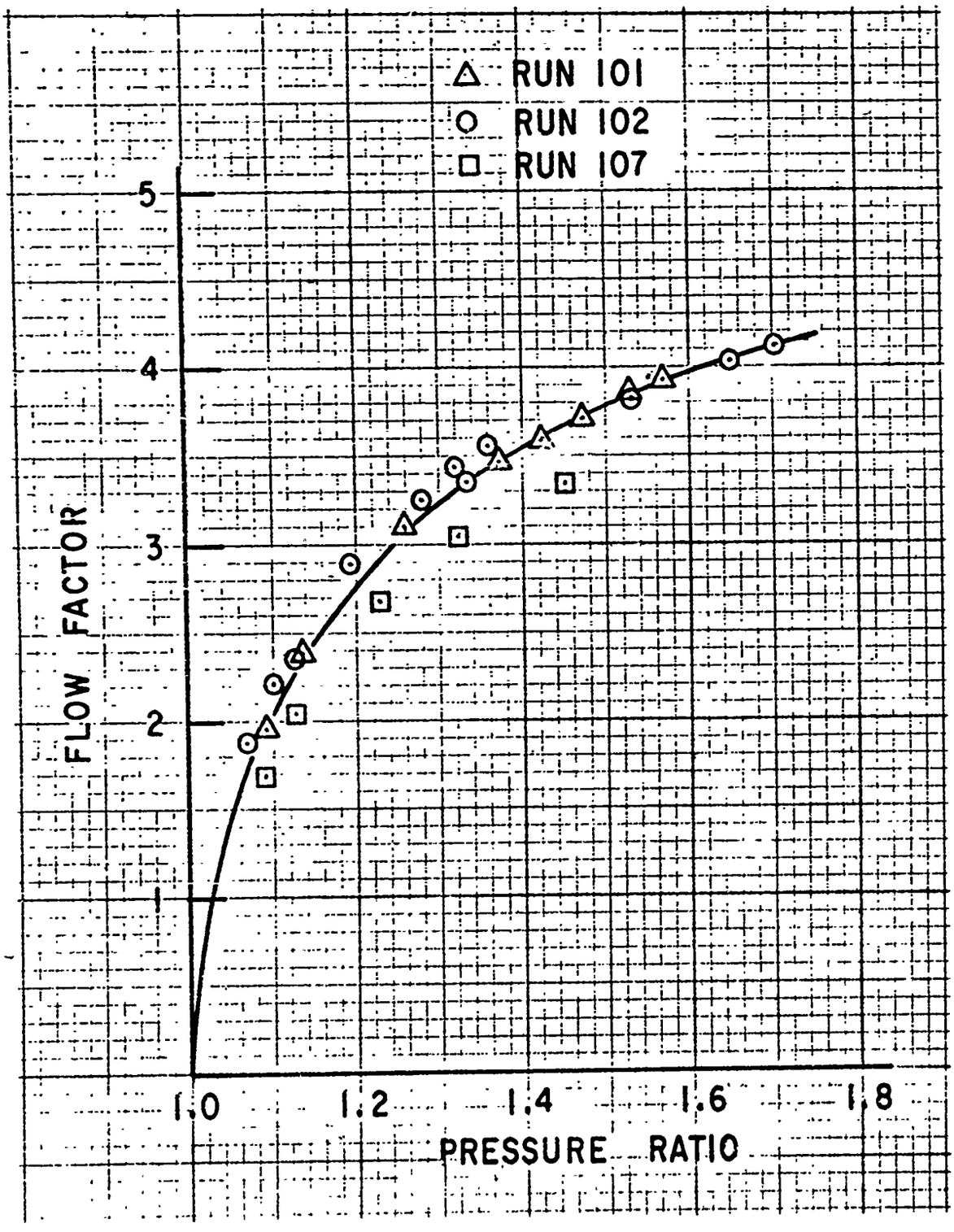

Figure 4.2.2-6. Turboalternator Room-temperature Performance, Flow Factor Versus Pressure Ratio

rpm were obtained. Most of the tests were conducted at unity power factor, but some special tests were conducted at leading and lagging power factors.

With the turboalternator tested open cycle, the cryogenic temperature level at any specific operating condition depended upon the length of time at the particular condition and the flow rate. During testing, the time at temperature had little effect because operation was fairly stable before recording the data. The flow rate to the turbine did have a marked effect on the cryogenic temperature. Tests with the largest helium gas mass flows provided a lower operating temperature environment, because more helium gas was available to cool the entire turboalternator assembly.

A spectrum of all the unity power factor cryogenic test data points is shown on Figure 4. 2. 3-1 with electrical power output as a function of speed. Data points with the same load resistances are connected with the constant load resistance lines identified.

Figure 4. 2. 3-2 shows the effect of load power factor on voltage regulation. These data were obtained with rotor 11B. Lagging power factor adversely affects voltage regulation. More leading power factor load would improve voltage regulation even more. However, this is not necessarily consistent with our goal of optimum performance in regard to minimum losses in the alternator. A leading power factor load results in better efficiency than a unity power factor load at about 40 watts and above.

The test condition data from Run 105 are summarized in Table 4. 2. 3-1 along with the calculated and tested terminal voltage. Fifteen load points -- 3 capacitive, 3 inductive, and 9 resistive -- are reported.

Reactance calculations for the permanent magnet alternator differ in one important respect from conventional methods. Permeability for the magnet approaches that of air. A 1000-Hz impedance test showed little change with insertion of the field magnet. End turn and slot leakage reactances predominate. Validity of this concept was to be verified by full-frequency dynamic tests.

The most severe condition for testing for the effect of reactance is a lagging power-factor load. Terminal voltage sags most for this condition. If voltage regulation can be accurately predicted, then we can be sure the method for calculating reactance is reasonably correct.

Stator resistance is about 0. 84 ohms, compared to a reactance of about 24. 7 ohms. The analysis included the exact stator resistance for the temperature of that particular test. Increased field strength at low temperature and the field strength of the particular rotor used (11B) was also incorporated into the analysis.

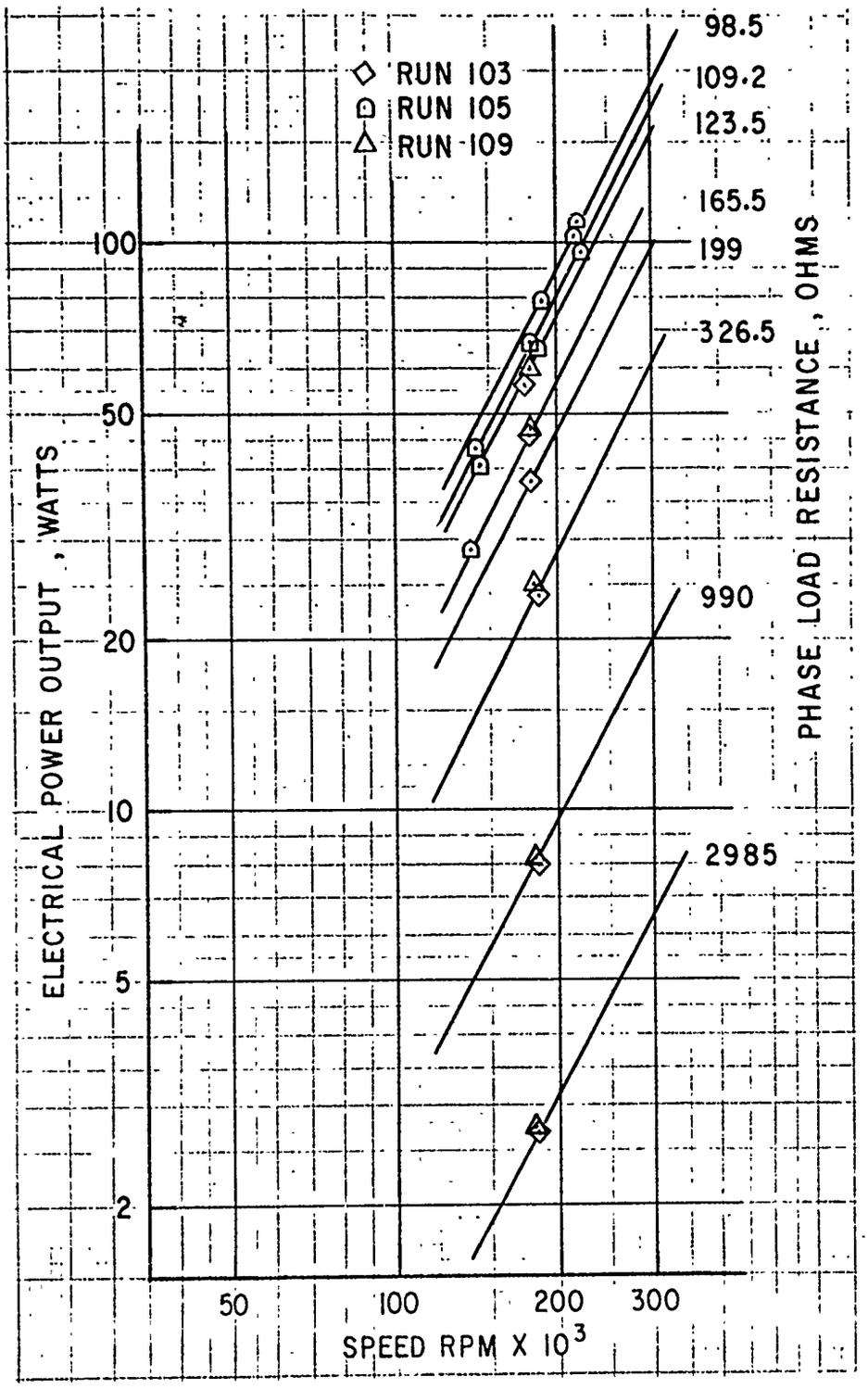

Figure 4.2.3-1. Turboalternator Cryogenic-temperature Performance, Power Output Versus Speed

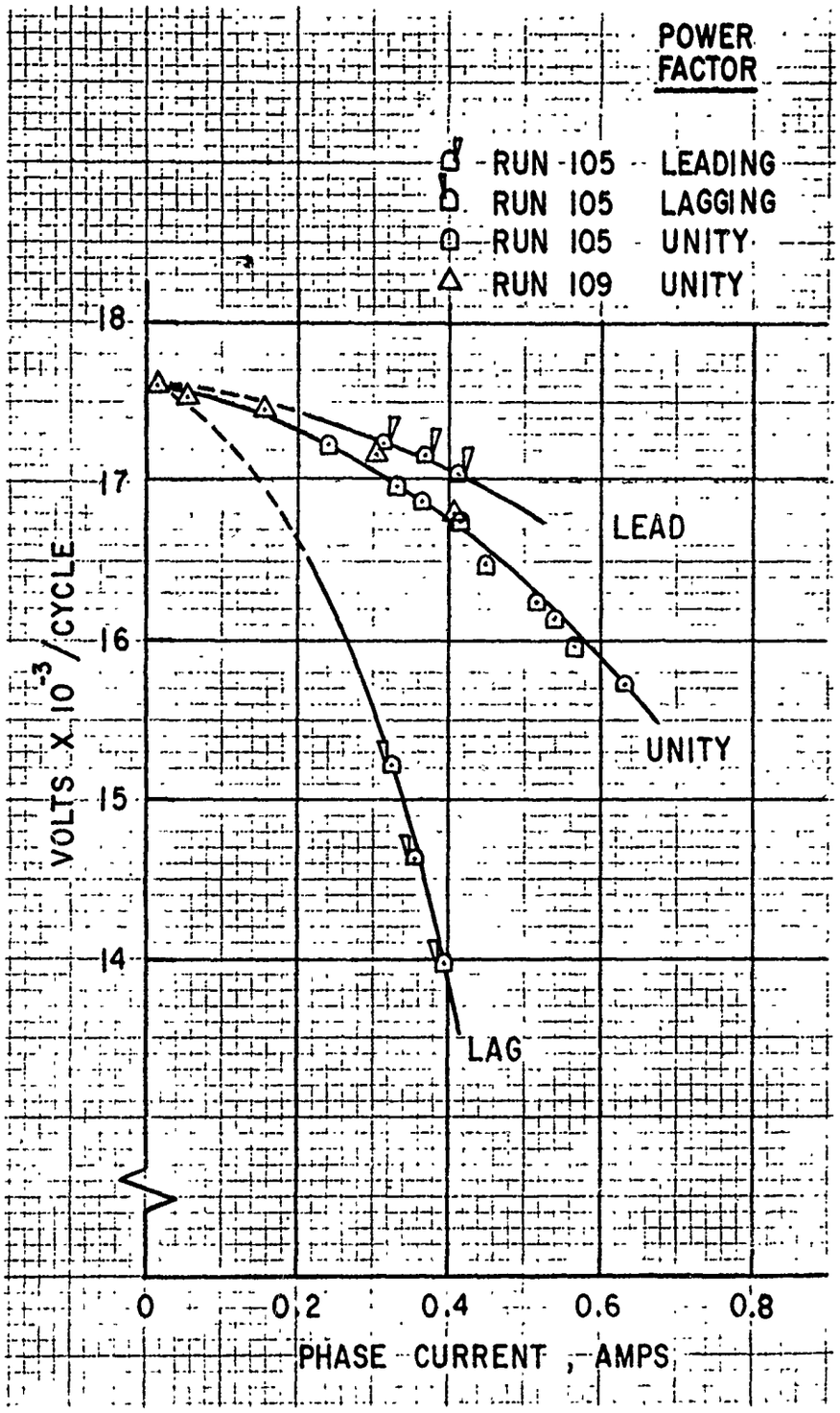

Figure 4.2.3-2. Turboalternator Cryogenic-temperature Performance, Voltage per Cycle Versus Current

Table 4.2.3-1

CHARACTERISTICS OF ALTERNATOR
DESIGN D-90702 WITH ROTOR 11B

Point	Phase (Volts)	Ampere	Power Factor	Power Out	Rpm	Terminal Voltage	
						Calculated	Measured
1	57.0	0.417	0.913 lead	65.1	183,060	56.5	57.0
2	56.6	0.367	0.930 lead	57.8	183,480	55.9	56.6
3	55.5	0.316	0.948 lead	49.7	182,820	55.0	55.5
4	47.2	0.393	0.918 lag	50.9	185,580	47.1	47.2
5	47.6	0.357	0.936 lag	47.6	182,100	47.4	47.6
6	48.6	0.324	0.951 lag	45.0	182,100	48.4	48.6
7	51.5	0.416	1.000 unity	64.2	184,320	51.1	51.5
8	51.2	0.519	1.000 unity	79.6	189,000	51.5	51.2
9	49.4	0.447	1.000 unity	66.3	179,640	49.3	49.4
10	59.4	0.540	1.000 unity	96.2	220,680	59.4	59.4
11	58.1	0.583	1.000 unity	101.6	218,220	58.1	58.1
12	57.2	0.635	1.000 unity	109.0	218,220	57.2	57.2
13	40.0	0.240	1.000 unity	28.8	139,320	39.8	40.0
14	40.6	0.331	1.000 unity	40.7	144,600	40.8	40.6
15	39.8	0.364	1.000 unity	43.3	141,480	39.6	39.8

Based on the results of these 15 load points, which are summarized in Table 4. 2. 3-1, it appears that calculated values of phase voltage can be as much as 1 percent low for a leading power-factor load. Calculated phase voltage for lagging and unity power factor loads will usually be much less than 1 percent low. Reactance calculations are sufficiently accurate for the present state of the art.

The results of an analysis for point 4 for an inductive load is shown in Table 4. 2. 3-2. The nomenclature is defined in Figure 2. 1. 1. 17-1.

Table 4. 2. 3-2

CHARACTERISTICS OF ALTERNATOR FOR POINT 4 LOAD

Characteristic	Analysis Result
Winding temperature	181 °R
Phase resistance	1. 573 ohms
Recoil permeability	1. 12
Phase reactance	25. 4 ohms at 185, 580 rpm
Ea (no load)	54. 0
Ea (internal voltage)	52. 4
Bq (quadrature)	188 gausses
Bd (direct)	4661 gausses
Bg (air gap)	4665 gausses
Armature reaction (A) before separation	351 ampere-turns per ampere

Overall efficiency of the turboalternator is shown in Figure 4. 2. 3-3 as a function of velocity ratio. With reference to Table 4. 1. 5-1, the higher efficiencies are for the later assemblies with the larger 4-mil radial turbine blade clearance and with the lower magnet strength. Another difference in the higher efficiency data points is that they are from operation at predominantly greater power levels.

The upper curve of Figure 4. 2. 3-3 shows that there is little difference in bypass flow among the sets of data for the three different runs. The characteristic of the curve is reasonable because at low velocity ratios, the inlet incidence angle to the turbine blades is high; therefore the pressure is high, causing a greater leakage flow to the alternator housing. As the incidence angle decreases with increased velocity factor, the flow leakage is a minimum at the velocity factor near peak efficiency. Then, as the blade incidence becomes negative, the bypass leakage increases as the velocity factor increases.

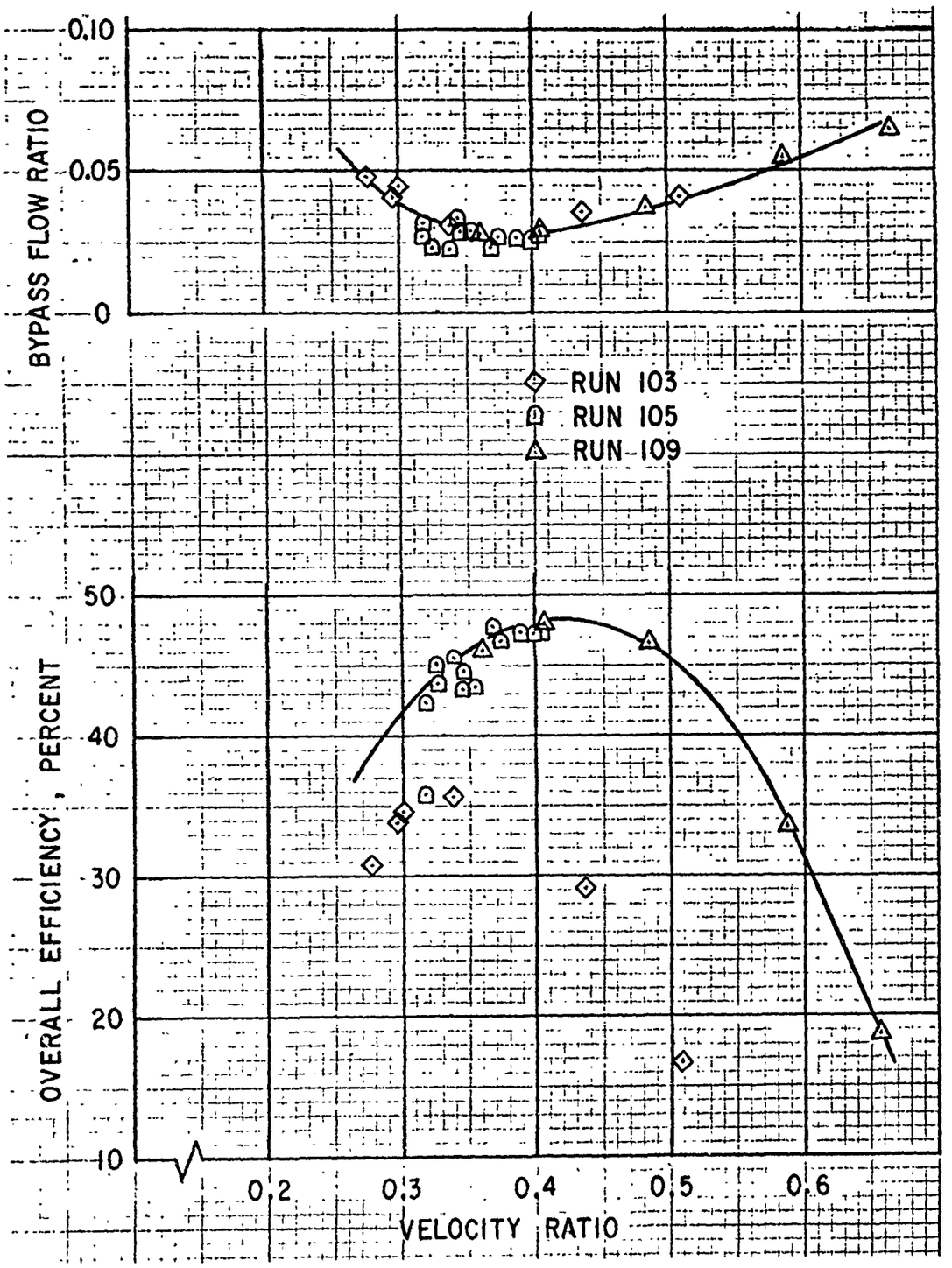

Figure 4.2.3-3. Turboalternator Cryogenic-temperature Performance, Efficiency and Bypass Flow Versus Velocity Ratio

A comparison with the room-temperature test results shows that the performance at cryogenic temperatures obtains a higher efficiency at a higher velocity ratio. The peak overall efficiency at room temperature is 33 percent, and at cryogenic temperatures the peak overall efficiency is 48 percent. The peak velocity factor at room temperature is about 0. 3 and at cryogenic temperature it is about 0. 4. Part of this improvement can be attributed to the decreased bypass flow leakage at cryogenic temperatures, because it is reduced by about half.

The lower efficiency data of Run 103, Figure 4. 2. 3-3, can be partially excused for two reasons. First, the wheel-tip-to-nozzle clearance was only 2-mils compared with the later higher efficiency data with a 4-mil clearance. Second, as can be seen on Figure 4. 2. 3-4, the flow factor at low pressure ratios for the lower efficiency Run 103 is much larger, which would lower the efficiency. Of course, the larger clearance and flow factor characteristics are interrelated. For purposes of this comparison, it is of interest to note that there is an apparent worthwhile performance improvement possible with the increased turbine-wheel-to-nozzle radial clearance.

For the cryogenic temperature tests conducted, a comparison of efficiencies as a function of electrical power output is shown in Figure 4. 2. 3-5. The electromagnetic efficiency is shown to remain high except for the very lowest power level. There is also a trend showing that the magnet with the greater magnet strength of 5700 gausses, Run 103, results in a lower electromagnetic efficiency than the later runs with a lower magnet strength of 5510 gausses.

However, the principal differences are that Run 103 data were at a higher operating temperature, resulting in greater Joule losses.

The overall efficiency includes the electromagnetic efficiency but the effect is not very great because the aerodynamic efficiency has many loss elements much greater than the electromagnetic losses. The low overall efficiency, at the lowest power output values shown, follows from the fact that bearing and windage friction losses are a significant proportion of shaft power. At the higher power levels, the overall efficiency should remain about constant at the 48-percent level. The principal reason for the slight efficiency decrease with increased power is that the turbine was not operating at the velocity factor for best overall efficiency. In other words, the 48-percent efficiency should be obtainable as a minimum at the larger power levels, if the turbine were to be designed and operated specifically for the higher power conditions. Actually, with the proper design conditions, the overall efficiency should increase with increasing power levels.

Electromagnetic efficiency of the alternator is not unlike other electromagnetic devices in that it peaks when fixed losses (core loss) about equal the variable losses (copper loss). The curve for electromagnetic efficiency in Figure 4. 2. 3-5 follows this general rule and peaks in the vicinity of 50 watts output.

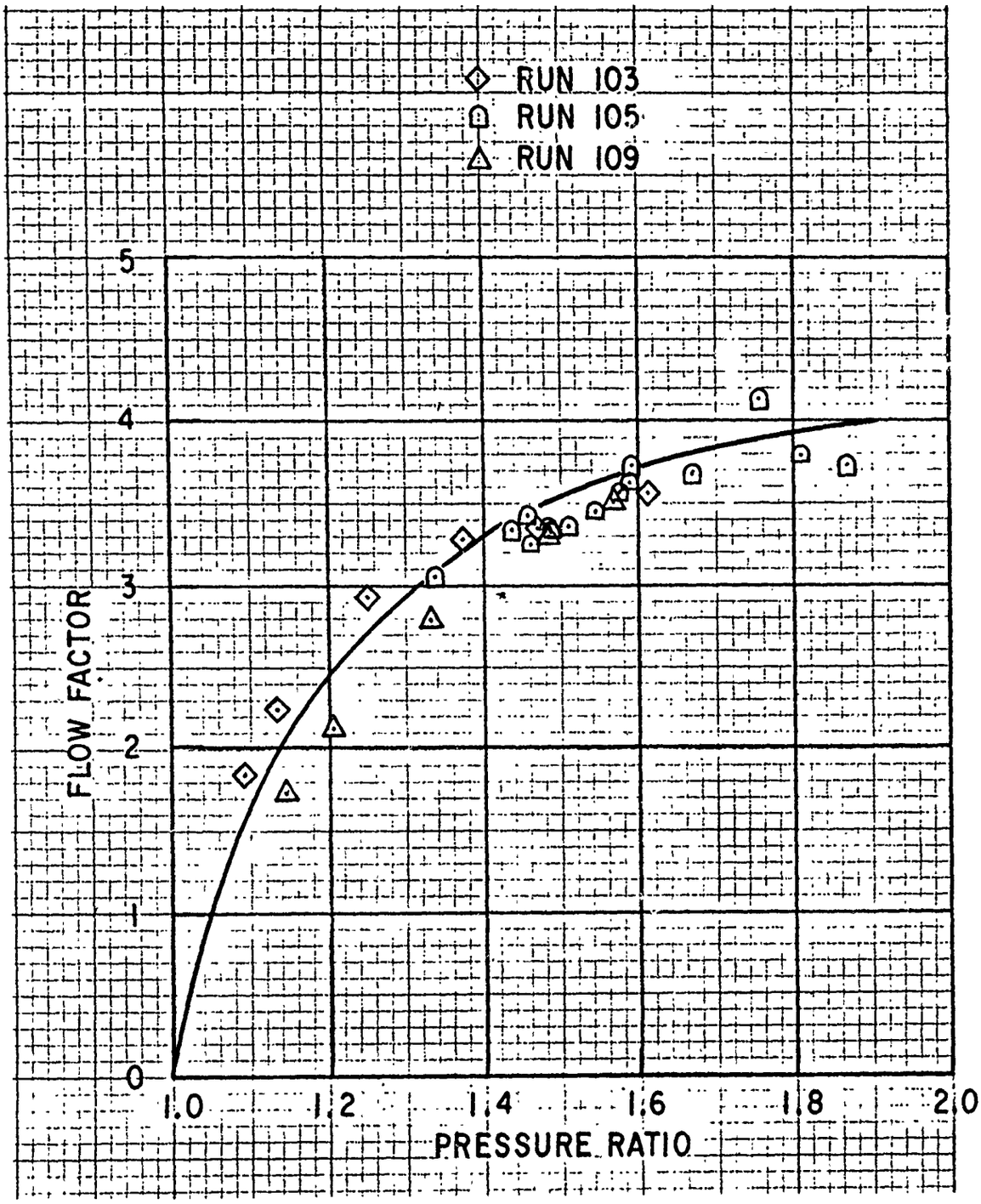

Figure 4.2.3-4. Turboalternator Cryogenic-temperature Performance, Flow Factor Versus Pressure Ratio

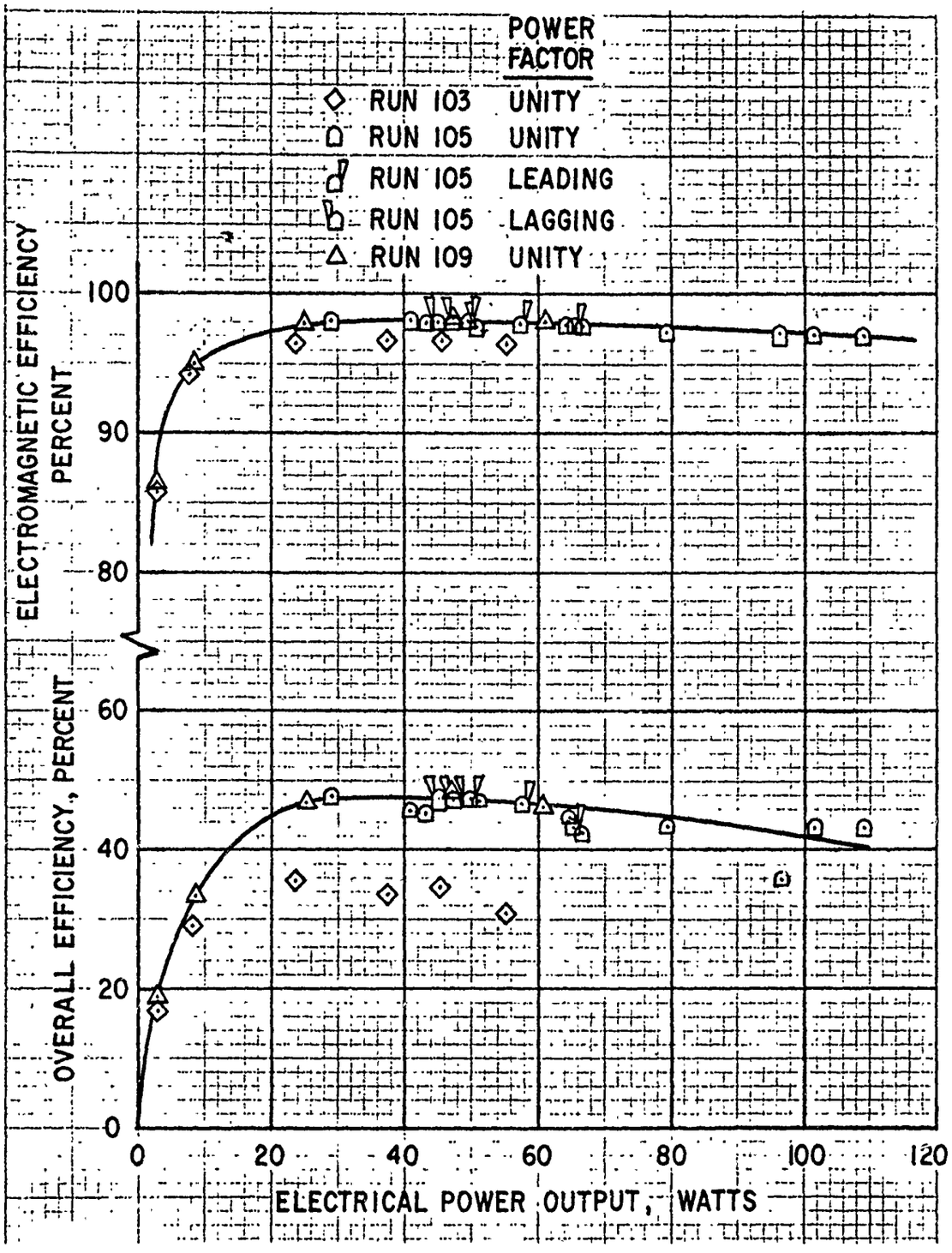

Figure 4.2.3-5. Turboalternator Cryogenic-temperature Performance, Electromagnetic and Overall Efficiency Versus Power Output

If the speed were increased 41 percent, the resulting efficiency would peak at twice the power and the losses would quadruple for that operating condition. Conversely, if the speed were reduced to 70 percent, the resulting efficiency would peak at half the power and the losses would quarter.

A comparison of measured alternator temperature shows poor correlation with the thermal analysis values shown in section 2. 3. 5. The design values for 100 watts power output are compared with values obtained at 79. 61 watts, the highest power reached near the design speed. The alternator temperatures are listed as the temperature rise above the turbine inlet gas temperature. Only one end turn at the gas inlet to the stator showed a 0. 65°K temperature rise, compared to the thermal analysis value of 3. 16°K (Table 4. 2. 3-3). At the largest power tested, 109. 03 watts, no great improvement is shown. At room temperature, the largest power obtained near design speed showed some temperature rises, but are below values that would be expected.

It is believed that the difficulty in adequately correlating the thermal analysis temperature values are:

- Difficult thermocouple installation relative to the element being sensed, compared to the large cooling gas stream
- Relatively low-sensitivity temperature-measuring capability at cryogenic temperatures

4. 3 TURBOALTERNATOR CONTAMINATION INVESTIGATIONS

During the turboalternator tests, considerable effort was expended toward getting the turboalternator to function properly, especially at cryogenic temperatures. Many individual component parts of the turboalternator were suspect from the information that could be deduced from the instrumentation installed to observe turboalternator operation. Eventually, though, the principal operating problems were traced to contamination particles brought into the turbine with the helium gas. These particles were eventually traced to various filter elements.

Prior turboalternator development programs were conducted successfully with no apparent problems of gas contamination. General Electric turbines were tested open cycle during many performance evaluation tests (Ref. 3). Then a General Electric turboalternator was installed in an 80°K closed-cycle refrigerator and was operated successfully for at least 100 hours. Open loop cryogenic temperature performance tests were also conducted on two turboalternators for the U. S. Air Force (Ref. 4). All of these tests may have been affected by contaminating particles, but there were no operating problems that were traced directly to contaminants.

During turboalternator testing, three sources of contamination were eventually identified.

Table 4.2.3-3

COMPARISON OF DESIGN AND TEST ALTERNATOR TEMPERATURES

Characteristic	Thermal Analysis Value	Test Values		
		Cryogenic (Greatest Power Output at Design Speed)	Cryogenic (Greatest Power Output Recorded)	Room Temperature
Electrical power output (watts)	100	79.61	109.03	66.87
Speed (rpm)	180,000	189,000	218,220	180,120
Inlet temperature (°K)	80.0	120.1	121.9	301.0
Pressure ratio	2.075	1.399	1.866	1.569
Total mass flow (pounds per hour)	19.2	12.399	14.314	7.899
Bypass flow (pounds per hour)	1.2	0.371	0.480	0.506
Alternator temperature rise above turbine inlet temperature (°K)				
End turn at gas inlet (S0 and S1)	3.16	0.65, 0	1.04, 0	0.854, 0
Slot copper (S4 and S5)	6.00	0, 0	0, 0	0.455, 0.500
End turn at gas outlet S8 and S9)	8.14	0, 0	0, 0	1.63, 1.78
Core	3.42			
Shell (S2 and S3)		0, 0	0, 0	-1.71, -2.94
Run		105	105	101
Data point		8	12	8

Moisture in the helium gas was an early suspect. Grade A helium was used, and the amount of moisture is shown in Table 4. 3-1. Also shown are more expensive grades that have less moisture.

Table 4. 3-1

COMMERCIAL HELIUM BOTTLED GAS SPECIFICATIONS

Grade	Dew Point (°F)	Moisture (Pounds per 1000 cubic feet)	Standard Cubic Feet per Bottle	Cost per Bottle	Vendor Information Source
A	-62	0. 0030	230	$14. 59	Linde Company
B	-86	0. 0007	262	$25. 40	J. T. Baker Company
C	-92	0. 0004	262	$92. 50	J. T. Baker Company

Charcoal filters were used to absorb the moisture, with the filters at liquid-nitrogen temperatures. Charcoal particles caused operating problems.

Five porous wire mesh filters were also used after the charcoal filters to stop any particle that could harm turboalternator operation. At first, this type of filter was found to contribute to the contamination problem, because epoxy particles used to fill large wire mesh holes came off at cryogenic temperatures and entered the turboalternator. After this problem was discovered and rectified, these wire mesh filters were found to be satisfactory.

4. 3. 1 Turboalternator Tests

During the initial turboalternator tests, a number of severe problems were encountered. At that time, these difficulties and many of the apparent problems were blamed on the turboalternator itself. In the course of solving these problems, it was concluded that the actual cause was contamination of the turbine gas supply by small particles.

In the presentation of test results in section 4. 1. 4, the problems were only briefly mentioned. Because many of the problem causes and effects were difficult to isolate, the operating difficulties are described in more detail.

A chronological history of the turboalternator development steps in conjunction with the contamination-induced operating problems follows.

At room temperature, turboalternator tests were conducted in steps from no load to about 70 watts at 180, 000 rpm. No load and part load tests were also conducted at speeds of 140, 000 rpm and 220, 000 rpm. At cryogenic temper-

atures, initial tests were at 180, 000 rpm and were conducted in steps from no load up to about 60 watts load. Tests were interrupted to evaluate test data.

After tests were resumed, problems were encountered with the turboalternator. Operation at first was not successful at cryogenic temperatures and no load. Test operation symptoms indicated that the shutdown, due to rubbing of the turbine wheel and tip, was possibly caused by:

- Close wheel clearance setting
- Possible ice or dirt interference
- Journal bearing tilting pad flutter
- Relaxing of thrust bearing gimbal pivot seats from temperature changes

In an attempt to correct this, the turbine wheel diameter was reduced, the gas feed lines were cleaned, and the gimbal pivot assembly torque values were checked. Also, to assure that there was no adverse influence from the alternator stator, it was left out of the assembly. After assembly, the unit was operated and it was found that there was considerable pad flutter, which could be corrected by increasing the clearance toward a more stable tilting pad preload value. Stable operation was obtained at room temperature and down to the lowest temperature tested at 100°K. Without a turbine load, lower temperatures could not be obtained because of the limited cooling gas available.

The alternator stator was then installed, and all phases were checked and found to be as originally assembled. Room temperature and cryogenic temperature operation was satisfactory up to a resistance load of 123 ohms. Then the turboalternator stopped. It was found that the turbine wheel rubbed on the tip again. Possible causes for this malfunction include:

- Journal pad flutter and clearance changes due to rough pivot to socket finish
- Misalignment of turbine wheel and rotor in the assembly
- Turbine wheel to shaft fit

These continued problems were surprising because the turboalternator assembly, except for the new stator design, was identical to a unit previously developed and tested successfully in the General Electric 80°K laboratory refrigerator.

To investigate turbine wheel clearances, a large radial clearance between the wheel and the nozzle was used. A 0.615-inch-diameter General Electric aluminum wheel was used in a General Electric housing that had previously been successfully used. No turbine wheel rubbing resulted during testing at room temperature with this nominal 5-mil radial clearance.

In order to minimize pad flutter, the pad socket base was made flat by electrodeposit machining and polishing. The thrust bearings were lapped down from the initial 2. 5-mil to a 1. 7-mil groove height to increase load capability. No alternator stator was installed.

Test results, with 350- and 315-microinch bearing clearances were good and no pad vibrations were observed. A summary of this test setup and results are shown as test A in Table 4. 3. 1-1.

The bearing clearances were then increased to 512 and 551 microinches, and no operating problems were observed at all the speeds tested up to 220, 000 rpm. These results are shown as test B on Table 4. 3. 1-1.

All the above parts were then installed in the U. S. Army turboalternator housing for test C with the alternator stator, but the rotor was not magnetized. With the turboalternator vertical and the turbine end down, there was no pad vibration with clearances of 407 and 399 microinches for the entire speed range tested up to 220, 000 rpm. Oscilloscope photographs were taken to compare test results. Figure 4. 3. 1-1 shows the speed trace from the Y probe of the X-Y set of probes on the turbine end. The speed is 180, 000 rpm based on the sweep rate shown. A typical proximity probe calibration results in a 1875-microinch-per-volt calibration. Figure 4. 3. 1-2 shows the two 90-degree X-Y probe traces forming the two journal orbits. The amplitude was 400 microinches per centimeter. These very small orbits represent what is considered to be a very good rotating assembly balance condition. The small thrust-end orbit is actually a circle, even though an instrumentation shadow is evident. A proximity probe to measure the leading edge of a single tilting pad was located at the leading edge of one of the pads of the thrust-end journal bearing. A resulting scope trace is shown on Figure 4. 3. 1-3. The particular sweep rate shows very slight once-per-revolution vibration at the 180, 000-rpm operating speed.

The thrust bearing trace used with the calibrations is shown in Figure 4. 3. 1-4. The probe location is such that the probe measures the plug in the end of the shaft and, with the turboalternator operating vertically, this probe essentially measures the inner thrust bearing motion. A once-per-revolution trace is shown with very low amplitude.

Test D was conducted with the same assembly, but with larger 528- and 489-microinch bearing clearances. Pad vibrations could be induced by tapping the turboalternator housing. Proximity instrumentation trace results at the 180, 000-rpm operating speed are shown in Figures 4. 3. 1-5 through 4. 3. 1-8. There was a slight increase in journal orbit sizes. The turbine-end orbit is shown on the bottom. The pad vibration shown in Figure 4. 3. 1-7 is 12, 000 cycles per minute, or one fifteenth of the operating speed of 180, 000 rpm. This same vibration is shown superimposed on the shaft speed in Figure 4. 3. 1-8. The pad fluttering could be stopped by pressing on one of the tur-

Table 4.3.1-1

TURBOALTERNATOR DEVELOPMENT TESTS SUMMARY

Date	Building	Test	Rotor Magnetized	Temperature	Journal Bearing Radial Clearance (Microinches)		Figure	Results
					Turbine End	Thrust End		
3 April	36	A	No	Room	350	315		No problem
3 April	36	B	No	Room	512	551		No problem
4 April	37	C	No	Room	407	399	4.3.1-1 through 4.3.1-4	No problem
4 April	37	D	No	Room	528	489	4.3.1-5 through 4.3.1-8	Could induce pad vibrations at high speeds
4 April	37	E	No	Room	304	286		No problem
7 April	37	F	No	Cryogenic	304	286		No problem
8 April	37	G	Yes	Cryogenic	304	286	4.3.1-9 through 4.3.1-12	Stopped suddenly; possibly dirt
8 April	37	H	Yes	Room	304	286		Would not start
9 April	37	I	No	Room	300 (approximately)	300 (approximately)		Would no start
10 April	37	J	No	Room	293	309		No problem
10 April	37	K	Yes	Room	293	309		No problem
16 April	37	L	Yes	Cryogenic	293	309		Stopped suddenly; thrust bearing dirt
18 April	37	M	No	Room	324	327		No problem
18 April	37	N	Yes	Room	324	327		No problem
21 April	37	O	Yes	Cryogenic	324	327		Satisfactory load tests

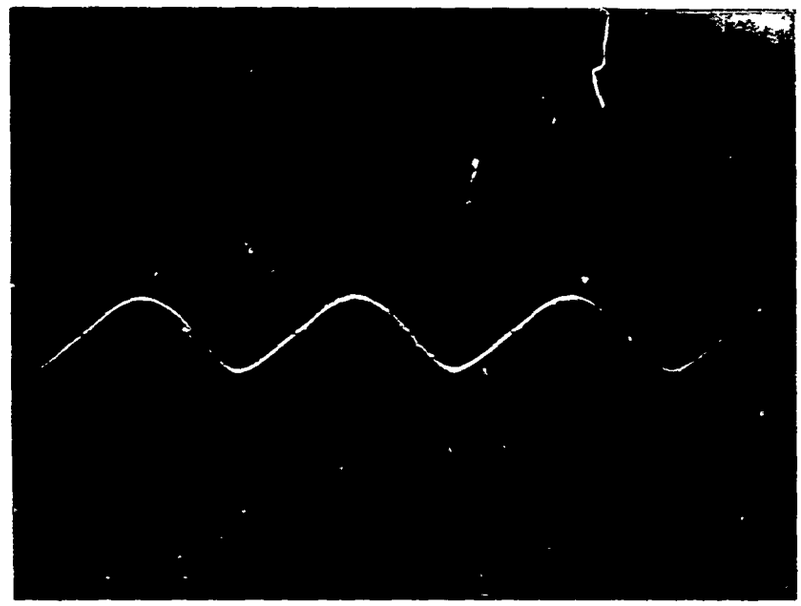

Figure 4.3.1-1. Shaft Speed Trace (Sweep -- 0.1 Millisecond per Centimeter; Amplitude -- 0.02 Volt per Centimeter)

Figure 4.3.1-2. Journal Orbit Traces (Left -- Thrust End; Right -- Turbine End), 400 Microinches per Centimeter

Figure 4.3.1-3. Journal Pad Trace (Sweep -- 0.1 Millisecond per Centimeter; Amplitude -- 0.1 Volt per Centimeter)

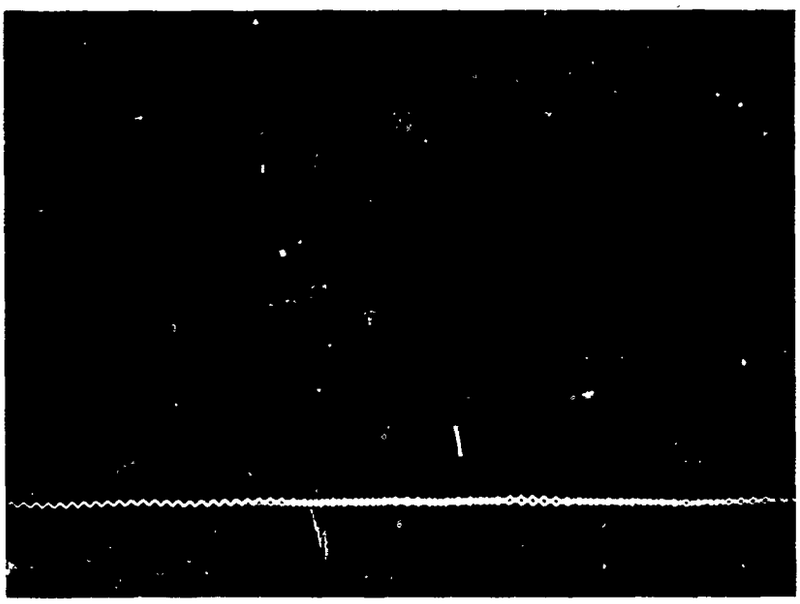

Figure 4.3.1-4. Thrust Bearing Trace (Sweep -- 2.0 Milliseconds per Centimeter; Amplitude -- 0.2 Volt per Centimeter)

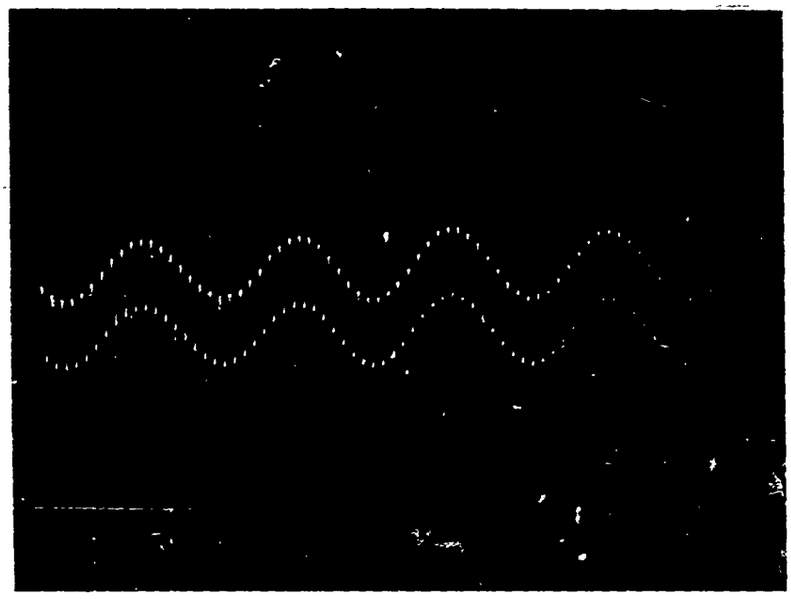

Figure 4.3.1-5. Shaft Speed Trace (Sweep -- 2.0 Milliseconds per Centimeter ; Amplitude -- 0.02 Volt per Centimeter)

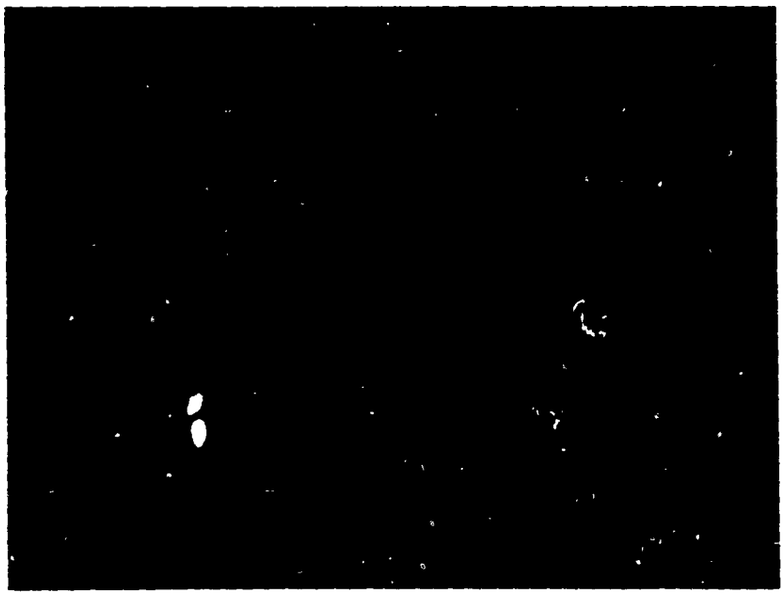

Figure 4.3.1-6. Journal Orbit Traces (Top -- Thrust End; Bottom -- Turbine End), 0.2 Volt per Centimeter

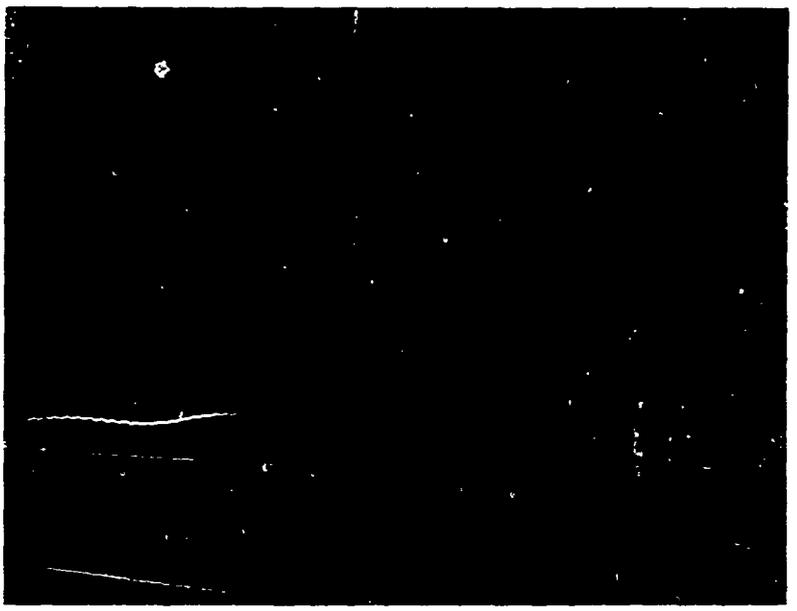

NOT REPRODUCIBLE

Figure 4.3.1-7. Journal Pad Trace (Sweep -- 2.0 Milliseconds per Centimeter; Amplitude -- 0.1 Volt per Centimeter)

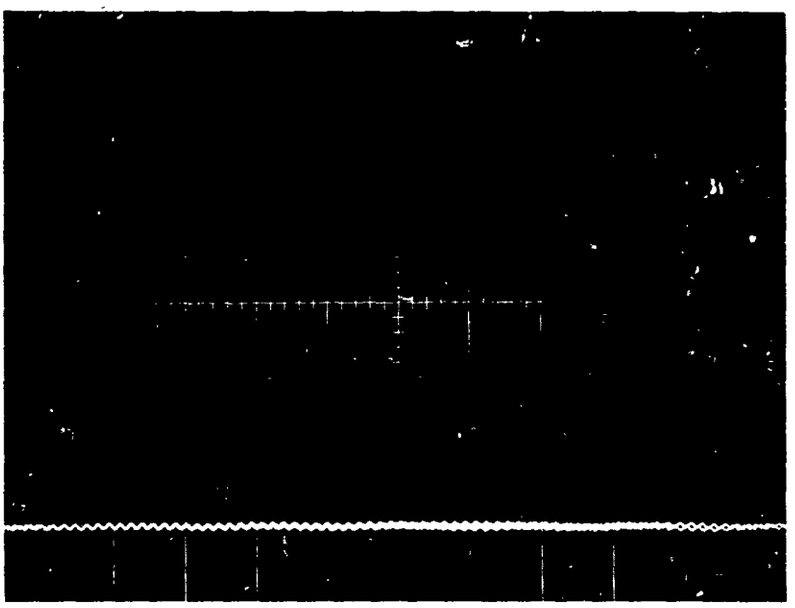

Figure 4.3.1-8. Thrust Bearing Trace (Sweep -- 2.0 Millisconds per Centimeter; Amplitude -- 0.2 Volt per Centimeter)

bine-end pad stems in a direction tangent to rotation. No change in speed from about 100, 000 rpm to 220, 000 rpm would stop this vibration.

The journal bearing clearances were then decreased to 304 and 286 microinches. There was no evidence of pad flutter in the vertical position in spite of attempts to induce vibration. Also, in the horizontal position, with rotation in all attitudes, there was no evidence of pad flutter. Results of scope traces at 180, 000 rpm were photographed and are virtually identical to Figures 4. 3. 1-1 through 4. 3. 1-4 for test E.

Next, with test F, the turboalternator was operated vertically (turbine end down) and at cryogenic temperatures without the rotor magnetized. A low temperature of 110°K was reached. There were nc operating problems.

The rotor was then removed and magnetized. It was seen that the bluing dye had completely eroded from the inside circumference of the nozzle block. This 0. 070-inch ring, which includes the eight nozzle openings, is adjacent to the turbine wheel blades. Two small charcoal filters were added in series to the large filters used on the previous test. The objective was to minimize the probability of moisture being carried in with the gas stream, resulting in the formation of solid particles at cryogenic temperature.

With the shaft magnetized, cryogenic test G was conducted. After 30 minutes, 114°K was obtained, and at 180, 000 rpm, scope-record photographs were taken (Figures 4. 3. 1-9 through 4. 3. 1-12). Operation at low speed and at high speed (up to 220, 000 rpm) was also satisfactory. Some small alternator loads were applied. Then, the turboalternator stopped abruptly and could not be started again at either cryogenic or, after being warmed up, at room temperatures.

Upon disassembly, it was observed that the bluing dye had eroded to a greater extent than before. Also some black particles were found in the nozzle plenum.

All parts were cleaned, and test H was attempted. The turboalternator would not start in any position or attitude.

It was again disassembled, and the shaft was demagnetized. The journal bearings were each set at about 300 microinches. The turboalternator would still not start for test I.

Upon disassembly, five black particles were found embedded in the inner thrust bearing. These were removed, and test J was conducted with no operating problems. The rotor was then magnetized, and test K showed no turboalternator operating problems at room temperature.

As a result of the above series of tests, it was tentatively concluded that particle contamination might be the cause of difficulties, and it was decided to evaluate the extent of contamination in gas which was being supplied to the turbine.

NOT REPRODUCIBLE

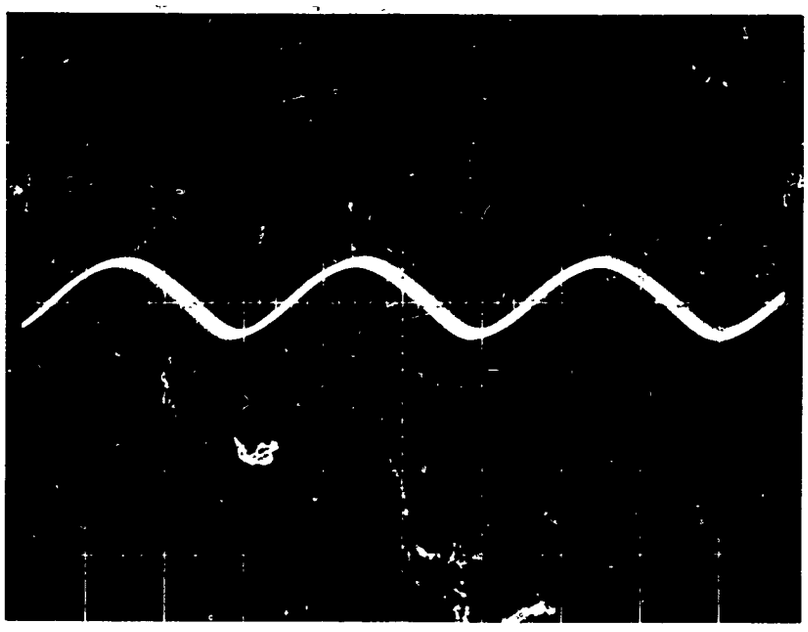

Figure 4.3.1-9. Shaft Speed Trace (Sweep -- 0.1 Millisecond per Centimeter; Amplitude -- 0.02 Volt per Centimeter)

Figure 4.3.1-10. Journal Orbit Traces (Top -- Thrust End; Bottom -- Turbine End), 0.2 Volt per Centimeter

NOT REPRODUCIBLE

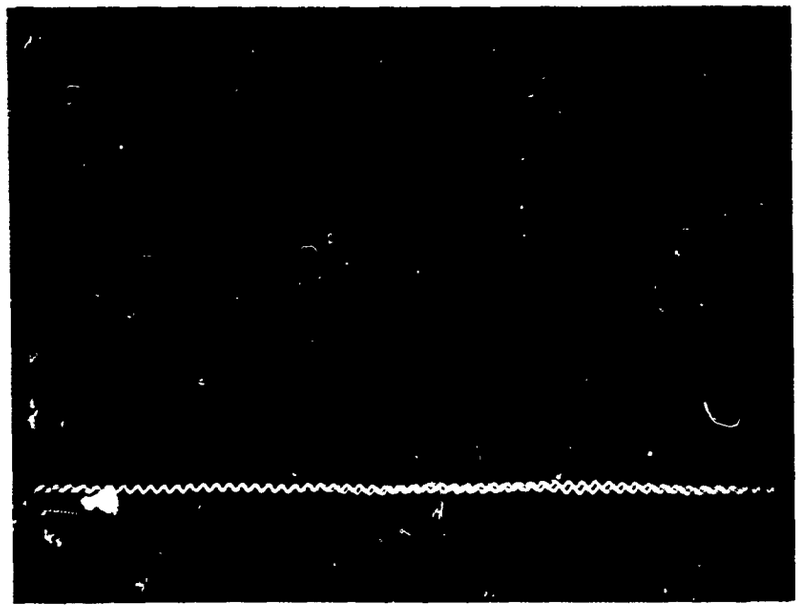

Figure 4.3.1-11. Journal Pad Trace (Sweep -- 2.0 Milliseconds per Centimeter; Amplitude -- 0.1 Volt per Centimeter)

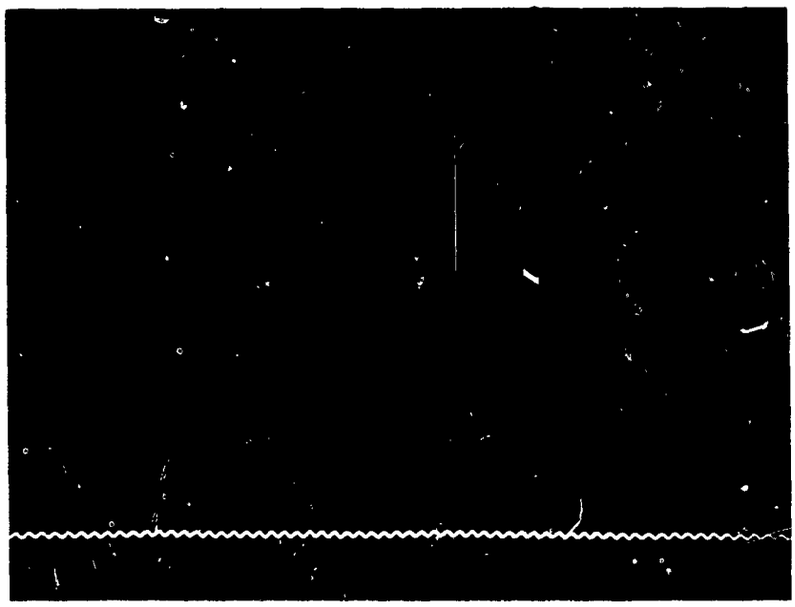

Figure 4.3.1-12. Thrust Bearing Trace (Sweep -- 2.0 Milliseconds per Centimeter; Amplitude -- 0.2 Volt per Centimeter)

The test arrangement shown in Figure 4. 3. 1-13 was used. The cold gas entered through tubing to an inverted funnel. The gas was reduced in velocity and passed through the filter paper and screen used to back up the filter. The filter paper used was from a vacuum cleaner bag, because laboratory filter papers were too dense. The cold gas was exhausted to the room underneath the bell jar because both the bell jar and funnel were glass, any moisture forming inside the funnel or on the filter paper could be seen.

The first system tested was tested with one large and two small charcoal traps, and the plumbing was as that used on recent turboalternator test K. A run of 1 hour and 25 minutes was made. The last 30 minutes was made at cryogenic temperatures, with a flow rate about the same as that required for the turboalternator at the highest cryogenic load point experienced (approximately 60 watts). There was no indication of moisture condensing, but six small black specs were found on the filter paper.

The next test for dirt was made with only the large charcoal trap and a single porous metal filter made by Aircraft Porous Media, ACL-3102-65A-6, which is rated at a 5-micron (98 percent removed) and 18-micron maximum. The charcoal and glass wool were removed from the porous metal filter assembly. The filter was in the cold gas stream, downstream of the charcoal trap, and a 1/4-inch-diameter tube was used for a cooling coil. A test of 1 hour and 27 minutes was conducted. The last 30 minutes at cryogenic temperatures were with the high flow rate comparable to a 60-watt turbine load at cryogenic temperature. No signs of moisture or black particles were observed from this test.

In order to decrease the filter and cooling coil pressure drop, three of the porous filters were connected in parallel and a 3/8-inch-diameter cooling coil was connected in series.

Tests were conducted across the filter paper test rig for 1 hour and 27 minutes. The last 30 minutes were with high helium gas flow rates. No moisture or black particles were seen after this test.

With the three-filter-plus-one-charcoal-trap gas system, the turboalternator was again tested (test L Table 4. 3. 1-1). At cryogenic temperatures and no load, the inner thrust bearing touched and bounced, and the unit came to a complete stop. The turboalternator could not be started cold or at room temperature. Upon disassembly, four black particles were seen on the inner thrust bearing.

The inner thrust bearing was replaced, and the unit would not start in any position. It was tentatively concluded that dirt on the journals could be the cause. So, the unit was completely disassembled, cleaned, and reassembled. It was tested at room temperature, test M, without problems.

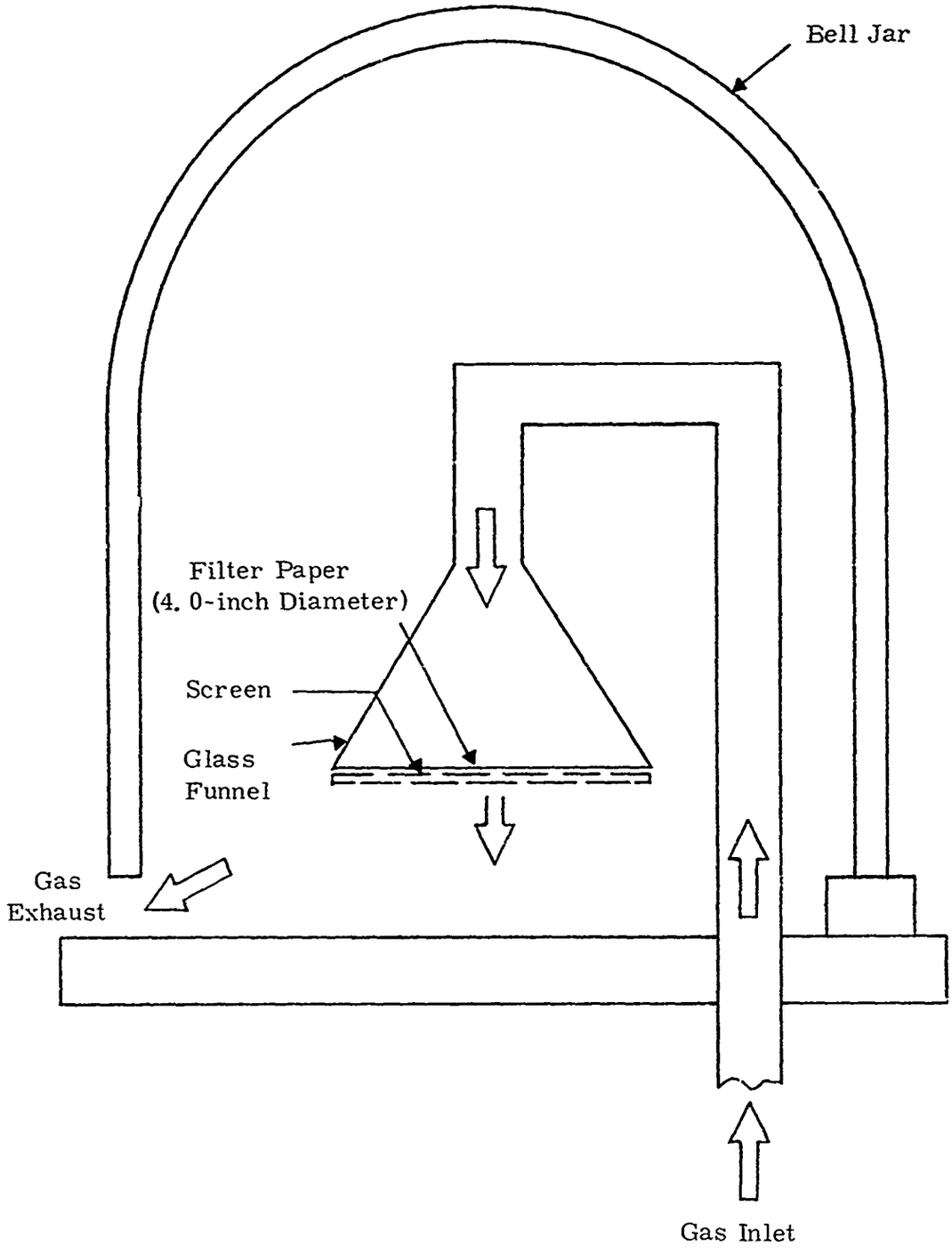

Figure 4. 3. 1-13. Turboalternator Gas System Cleanliness Test Arrangement

Then the rotor was magnetized and test N was conducted at room temperature without problems.

Because black particles were still evident, even with the porous metal filters after the charcoal trap, a test without the charcoal trap was made. With the three filters in parallel, gas was ducted to the inverted funnel of the test rig in Figure 4. 3. 1-13. It was postulated that any moisture in the gas would be frozen in the coil upstream of the filters, and, if carried with the gas stream, would be stopped by the three filters. Tests at cryogenic temperatures and high flow rates were made, and no evidence of moisture or particles was observed.

Test O, with the turboalternator at cryogenic temperatures, was then conducted at two load points at 23. 8 and 56. 2 watts. Mild but sporadic low-frequency flutter was observed from the pad probe, but the journal orbits did not enlarge much, and tests were not curtailed. The load point above 56. 2 watts was equivalent to the greatest load point previously run. It was decided to terminate the test with an operable turbine and prepare for performance tests.

After purging the bell jar with bottled nitrogen for 10 minutes, the turboalternator was started at 180, 000 rpm with no resistance load. The turboalternator was run for 15 minutes, under the above conditions, to thoroughly purge the system before adding liquid nitrogen to the dewar containing the cooling coil. As the liquid nitrogen was added, the load on the turboalternator was increased to 326 ohms, with capacitors in each line to provide a 0. 95 leading power factor at 180, 000 rpm. The turboalternator operated satisfactorily for 30 minutes as it cooled to nearly liquid nitrogen temperature. Then, the following conditions were observed:

- The pad probe signal suddenly went off of the scope.
- A noise that sounded like the turboalternator touching was heard.
- The thrust bearing probe scope signal became very rough.
- The shaft orbit signals on the scope became rough.

The turboalternator was quickly shut down and, with a bottled nitrogen gas purge, was warmed to room temperature.

The turboalternator was started at room temperature with no load. The thrust bearing and shaft orbit probes showed rough operation on the scope, so the turboalternator was again shut down. The capacitance probes were backed out slightly and the turboalternator was started again. The probe scope traces still indicated rough operation and the unit was turned off. An attempt was made to operate the turboalternator in the horizontal position, but the unit would not start.

The turboalternator was disassembled and the parts were examined. The parts were found in the following condition:

- The Y-axis orbit probe at the thrust end of the shaft indicated the possibility of a rub. All other probes looked good.
- The outer thrust bearing showed no sign of wear.
- The dye on the inside of the nozzle assembly showed two circular rub marks directly under the area where the turbine wheel blades rotate. One rub mark was 1/32 inch in from the nozzle inside diameter and the other was 1/16 inch in.
- The turbine wheel also showed rub marks, across the turbine blades, which corresponded to the same marks indicated on the nozzle. This and the previous item suggest the possibility of a dirt particle coming through the gas stream and becoming lodged between the nozzle and blades.
- Several dark particles were found on the shaft around the diameter at the thrust end of the magnet. The inner thrust surface of the shaft showed considerable wear. The journal pad sections on the shaft showed only a very slight amount of wear.
- The inner thrust bearing showed slight wear on the outside diameter and considerable wear on the inside diameter. Examination under a microscope showed several black smears embedded into the inner thrust bearing surface.
- The housing inside diameter showed no apparent wear, indicating that the back of the turbine wheel did not touch.
- No wear was shown on the journal pad bearings. A shiny material was noted on the top, or thrust side, of all the journal pads. This material appeared to be beryllium copper and probably came from the wear seen on the beryllium copper inner thrust bearing. No other signs of wear or dirt were found in the turboalternator.

The shaft and inner thrust bearing were sent to the Materials and Processes Laboratory of the General Electric Company to analyze the dirt particles found on the shaft and the black smears on the inner thrust bearing. Their report identified both particles as stainless steel of the 300 series, with a high percentage of oxygen present. The positions of the particles on the shaft indicated that they were magnetic. The turboalternator shaft is made from 304 stainless steel, and the surfaces are nitrided. It is possible that the particles analyzed originated from the inner thrust surface of the shaft because considerable wear was noted in that area. The particle sizes fell predominantly into the 21- to 60-micron range.

The three porous metal filters of stainless steel wire mesh connected in parallel just upstream of the turboalternator were disassembled. Several particles were found in the filters, both on the inlet and outlet plumbing tees. Several particles were also found in the copper lines on each side of the filter. These particles were collected and examined and it was found that predominant particle sizes were in the 21- to 250-micron range, with a few larger particles.

Tests were then conducted with the three porous wire metal filters to determine if the filters were breaking apart and producing particles as they were cycled between room temperature and liquid-nitrogen temperature. The steps taken were:

1. The three porous metal filters, the copper tubing connecting the filters in parallel, and the cooling coil were thoroughly washed in a solution of chlorothene and blown out with clean Freon* gas.
2. The cooling coil was connected directly to a helium gas cylinder with a short length of clean plastic tubing.
3. The three porous metal filters were connected in parallel to the output side of the cooling coil with a valve on the end of the line to simulate operation with the turboalternator.
4. A copper-constantan thermocouple was attached to the output side of one of the filter lines to indicate when the gas reached liquid-nitrogen temperature.
5. The helium gas flow was started with the system at room temperature, and liquid nitrogen was added to the dewar containing the cooling coil until the thermocouple output stabilized at liquid-nitrogen temperature for approximately 10 minutes. The helium gas was then turned off and the cooling coil was removed from the liquid nitrogen until the system warmed up to room temperature.
6. The filters were cycled three times between room temperature and liquid-nitrogen temperature.

After the above test, the three porous metal filters were disassembled. Some particles were found in the filters. These particles were sent to the Materials and Processes Laboratory for analysis and particle size determination.

Results of the particle analysis are shown in Table 4. 3. 1-2. The large number of 21- to 250-micron particles, in addition to some larger particles suggested the possibility that the filter element actually produced the contaminants, since translucent and black particles are included.

One additional check on contamination was made. On the section of copper tubing from the turbine inlet valve, through the cooling coil, and up to the three wire mesh filters, the line was flushed with distilled water. The particles collected were analyzed and found to be in the 21- to 105-micron range.

All of these results may be compared with the filter rating of 5 microns (98 percent) and 18 microns absolute. The possibility of the filters breaking apart was discussed. At first, the vendor could not think of any reason why the

*Trademark of E. I. du Pont de Nemours and Company, Inc.

Table 4.3.1-2

PARTICLE STUDY REPORT

Lab: 69C-864
Date received: 2 June 1969
Sample: Inside filter after cleaning

Particle Size (Microns)	Number (100 Milliliters)	Remarks
1-5		
6-11		
12-20		
21-60	100	Mostly black and opaque
61-105	130	
105-250	30	
250-500	3	
500-1000	7	
1000-2000	4	One black oxidic, 1650 x 660 microns One translucent, 1000 x 450 microns One shiny nonmagnetic, 1000 x 20 microns One transparent (like glass chip) 1200 x 900 microns
2000	1	330 x 200 microns, shiny, nonmagnetic, oxidic
Fibers	25	

sintered stainless-steel mesh elements would generate particles when the units are cycled between room temperature and liquid nitrogen temperature.

However, when it was mentioned that some of the filters appeared to be partially coated with an epoxy, the vendor said that the filter elements are tested under a pressure of up to 10-1/2 inches of water in a solution of Solox* 190 alcohol. If bubbles appeared, the larger openings in the mesh, which cause the bubbles, are sealed with an epoxy containing indicator dyes which glow in ultraviolet light. The vendor also said that they normally limit this epoxy coating to a maximum of 5 percent of the filter element area. The vendor said that the possibility of the epoxy flaking off when the units are cycled down to cryogenic temperatures had not been considered.

With this information, the filter elements were examined in ultraviolet light, showing that the three elements were coated with epoxy over 20 percent, 5 percent, and 3 percent of the filter areas.

Because the epoxy could be detected in ultraviolet light, the particle samples taken from the shaft, filters, and copper lines were also examined in that light. All the samples, except those from the copper line between the flowmeter and the control valve, showed at least three or four epoxy particles.

Considerable effort was expended to get these filters replaced to perform the proper function. A complete discussion on the remedial steps taken is discussed below. Also, use of a contamination particle counter to assure a contamination-free filter system was incorporated. A description of this equipment appears in 4. 3. 2 below.

New wire mesh filters were obtained with no epoxy coating, and tests were resumed.

Preparations were made to reassemble the turboalternator. The circular rub marks on the nozzle were polished out to remove any possible burrs. A new inner thrust bearing was installed. All parts were cleaned ultrasonically, with the exception of the alternator stator, which was carefully blown out with clean Freon gas.

The turboalternator was assembled to the point of installing a new shaft. During this assembly, the threads on the turbine end of the shaft were damaged. The threads were found to be very brittle, and pieces broke off while attaching the turbine wheel nut. This problem had been experienced in the past and was caused by nitriding the threads. The shafts now used have had the threads copper plated to prevent this condition during the nitriding process, after which the copperplating was removed. From all indications, the copperplating protected the threads on other shafts. However, this shaft may have

*Trademark of the U. S. Industrial Chemicals Company

had a thinner copperplating and therefore may not have been as completely protected.

The journal bearing pad clearances were adjusted to approximately 300 microinches, the turboalternator was operated with the shaft unmagnetized, and it ran very well. The shaft orbits were exceptionally small, the thrust end orbit was about 80 microinches, and the turbine end was about 40 microinches.

The turboalternator shaft was then magnetized and tested at room temperature to an approximate 63-watt load, operating at 180,000 rpm. The turboalternator operated very well at room temperature under load conditions. This unit had an exceptionally smooth coastdown at low speed. One hundred and eighty Hz (10,800 rpm) was noted on the counter as the turboalternator coasted to a stop.

The turboalternator was then operated at liquid-nitrogen temperature. During cooldown, the turboalternator was operating with a load of 492 ohms, and suddenly the turbine orbit increased in size from 40 microinches to approximately 140 microinches. The turboalternator load was quickly reduced to 2985 ohms and the turbine orbit returned to normal. Cooling was continued for about 10 minutes; then the load was increased to 123.5 ohms without problems. The change in the turbine orbit size may have been caused by a transient temperature gradient in the shaft.

After the above test, the turboalternator was turned off. The unit was then restarted at the cold temperature, and its operation was considerably different. The turboalternator appeared to have a weak inner thrust. The thrust probe showed slight touching. The turboalternator was turned off and allowed to warm up to room temperature. At room temperature, the turboalternator operated satisfactorily. From all indications, it was advisable to continue testing and obtain the required performance evaluation data. Performance tests were then resumed without problems, as reported in section 4.1.4.

4.3.2 Particle Counter Investigation

A suitable means for measuring contamination level was established with a commercially available particle counter. Use of this equipment with the proper procedures resulted in methods that could establish the level of contamination, and hence prevent contamination problems with miniature turbomachinery refrigerator components. A General-Electric-owned particle counter (Model PC200A, manufactured by Royco Instruments, Inc. of Menlo Park, California) was used.

The particle counter measures the quantity and diameter of the micron- and submicron-size particles present in the air. It counts all particles within one or more size ranges and provides a separate total for each range, and it counts all particles larger than any selected size. Particle sizes counted are 0.32-micron diameter and larger.

For measurement of particles within a particular size range, 15 individually selectable channels cover a band from 0. 32 microns to 8 microns and above. Any of these ranges may also serve as the minimum size level for a total count of all larger particles. The 15 channels are:

- 0. 32 to 0. 4 microns
- 0. 4 to 0. 5 microns
- 0. 5 to 0. 64 microns
- 0. 64 to 0. 8 microns
- 0. 8 to 1. 0 microns
- 1. 0 to 1. 3 microns
- 1. 3 to 1. 6 microns
- 1. 6 to 2. 0 microns
- 2. 0 to 2. 5 microns
- 2. 5 to 3. 2 microns
- 3. 2 to 4. 0 microns
- 4. 0 to 5. 0 microns
- 5. 0 to 6. 4 microns
- 6. 4 to 8. 0 microns
- 8. 0 microns and larger

Because this particle counter had not been used recently, methods of calibration were established. From Royco Instruments, Inc., standard particles were purchased in the following sizes: 1. 171, 2. 68, 19 to 20, and 28 microns. The 1. 171- and 2. 68-micron sizes are in solution. From the Particle Information Service, Los Altos, California, fluorescent particles of zinc cadmium sulfide in the 3- to 5-micron range and the 6- to 13-micron range were purchased.

The particle counter has a built-in field calibration mechanism to check the optical and electronic components. This field calibration test was made and the instrument appeared to be in good operating condition.

A means of injecting the standard particles into a clean gas had to be developed. Although Royco Instruments, Inc. sells an aerosol generator for this purpose, it was believed that the standard particles could be injected into the gas for an accurate calibration check.

First, the turboalternator helium gas supply was tested with the particle counter. The helium gas system had a King Engineering Corporation filter in the line, which should remove better than 98 percent of all particles down to 0. 5 micron at room temperature. The particle counter was purged on the

helium gas for half an hour. Then a test was made for 1/2 hour, using particle sizes in the instrument range of 1.0 to 1.3 microns. Seven particles were counted during this period, indicating the helium gas source was quite clean in the above particle range.

Figure 4.3.2-1 shows the system and method used to inject the standard particles of the 1.171- and 2.68-micron sizes. Because these particles were supplied in solution, a few drops of the solution containing the particles were put onto a 1.75-inch-diameter Millipore* filter paper, No. HABG 04700 (0.45-micron pores). The filter papers were covered with a clean glass disc and allowed to dry overnight.

The system shown in Figure 4.3.2-1 was cleaned and assembled with the exception of the filter paper and particles. After purging the system for half an hour, a test was made with the particle counter before and after adding Freon. The test showed only a couple of particles present (0.8 micron and larger) for 5-minute periods.

The filter paper with the dry 1.171-micron particles was installed in the system. Then, before turning the Freon gas on, the gas in the system was retested after approximately 10 minutes of purging with the helium gas. One particle on the 0.8- to 1.0-micron counter range was measured in 5 minutes, and one particle on the 1.0- to 1.3-micron counter range was measured in 2 minutes. The particles were then introduced into the bell jar by momentarily aiming the Freon gas at the back of the filter paper. The results of this test are shown in Table 4.3.2-1. The flow through the Royco particle counter was 250 cc's per minute.

Table 4.3.2-1

1.171-MICRON PARTICLE TEST
(Freon to Back of Filter Paper 30-second Test Period)

Royco Particle Range (Microns)	Royco Particle Count
1.0 to 1.3	19
1.3 to 1.8	2
0.8 to 1.0	22
1.0 to 1.3	74
1.3 to 1.6	9
0.8 to 1.0	13
1.0 to 1.3	36

*Trademark of the Millipore Corporation

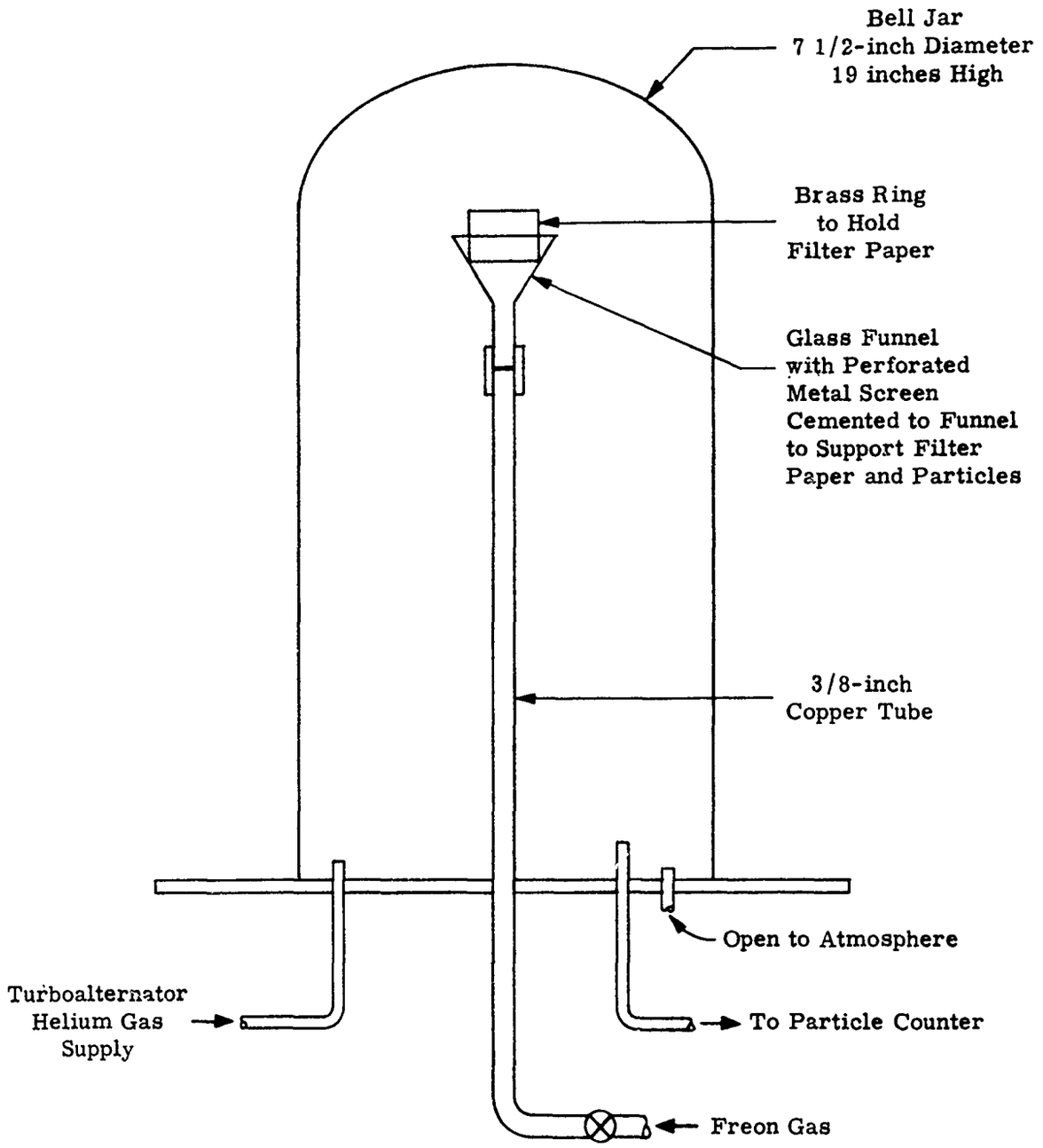

Figure 4.3.2-1. Equipment for Injection of 1.171- and 2.68-micron Particles into Gas Stream

The highest count was found to be in the 1.0- to 1.3-micron range indicating the instrument calibration is fairly accurate, or within ± 0.2 micron.

A similar test was made with the 2.68-micron particles. The system was purged for 10 minutes after the previous test, and the background was tested before the particles were introduced in the gas. Two particles were counted during an 8-minute period on the 0.8 and larger micron counter range. The results of this test are shown in Table 4.3.2-2. The flow through the Royco particle counter was 250 cc's per minute. The results show that the calibration might vary approximately 1/2 micron in this test.

Table 4.3.2-2

2.68-MICRON PARTICLE TEST
(Freon to Back of Filter Paper, 1-minute Test Period)

Royco Particle Range (Microns)	Royco Particle Count
2.5 to 3.2	0
2.0 to 2.5	19
2.5 to 3.2	9
1.6 to 2.0	4
2.0 to 2.5	7
2.5 to 3.2	3

Tests were also made with the 19- to 20-micron particles to be certain that the instrument would detect particles of this size on the 8.0-micron and larger counter range.

The system used in Figure 4.3.2-1 was not sufficient to introduce the larger particles into the gas for sampling. Therefore, another method was used (Figure 4.3.2-2). A 0.25-inch tube was shaped to blow the Freon gas across the bottom of a small jar and carry the particles up into the helium gas stream. This test showed that the larger particles would be detected on the 8.0-micron and larger range.

From the above tests, it was concluded that the Royco particle counter was operating satisfactorily.

4.3.3 Wire Mesh Filters

Problems with the wire mesh filters contaminating the turboalternator were covered in the previous section. Methods of testing for contamination and pressure drop test results follow.

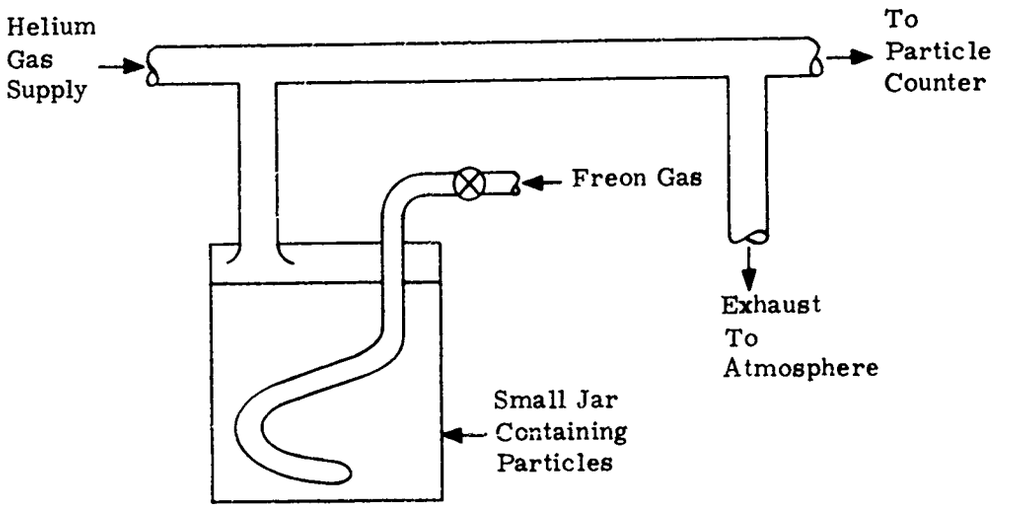

Figure 4. 3. 2-2. Method of Introducing Large Particles into Gas Stream

The porosity of the filter elements was tested in a solution of Solox 190 alcohol as outlined by the vendor, Aircraft Porous Media Division of the Pall Corporation. For the rating of this filter, no bubbles should appear as the pressure of the element is increased up to 10 inches of water with the elements 0. 5 inch below the surface of the Solox. The results of the test are:

Filter	Inches of Water Pressure when Bubbles Appeared
1	4. 5
2	3. 7
3	7. 0

The filter that showed bubbling at 3. 7 inches of water pressure was then assembled and connected in the helium gas line, between the connection for the jar containing the 19- to 20-micron particles and the particle counter connection. The particle counter measured 64 particles coming through the filter after one brief shot of Freon gas.

The ratings of these filters are 5 microns nominal (98 percent) and 18 microns absolute. The vendor claims that with gas, this filter will have a revised rating of 3. 5 microns nominal (98 percent) and 13 microns absolute.

Because both tests indicated that the filters were not acceptable, the filter vendor was again contacted. The vendor could not understand why the new filters were in such poor condition. However, the vendor agreed to personally prepare four new filters, three good filters and one bad one, to see if our testing methods were valid. The vendor would also make a particle test to be certain of the Solox testing method.

Three new filter elements were received. The elements were inspected with a black light and there was no indication of epoxy. The porosity of the filter elements was then tested by placing the elements horizontally in a solution of Solox 190 alcohol, as outlined by the vendor. The results of the tests are:

Element	Inches of Water Pressure when Bubbles Appeared
5	11.9
7	9.4
9	12.2

Elements 5 and 9 looked very good, on the basis of the above pressure test, because a pressure of 10 inches of water is the requirement for the rating of this filter with the element submerged 1/2 inch below the level of the Solox. Element 7 was not acceptable.

The filters were assembled and individually connected into the helium gas line, by injecting particles of the 3- to 5-micron range and 6- to 13-micron range with the Royco Particle Counter connected on the downstream side of the filter. Filters 5 and 9 passed several particles in the 3- to 4-micron range, a few in the 4- to 6-micron range, and very few above 6 microns. Filter 7 seemed to pass more particles in the 5- to 6-micron range than the above two units, but very few above 6 microns.

The filter vendor was then contacted to compare test results, and results closely agreed.

Pall's particle test is much more elaborate. They use a standard particle dust with known percentages of particles in given ranges per unit volume -- particle ranges of 0 to 5 microns, 5 to 10 microns, 10 to 15 microns, and on up to 40 microns. They measure a given amount of the dust, add it to the gas stream ahead of the filter, and use a Millipore filter after the test filter to trap the particles. The particles that are trapped on the Millipore filter are measured and microscopically examined to determine the maximum particle size coming through the filter and thus to obtain a nominal rating for the filter elements.

Pall tests showed that element 7 was allowing a few 13-micron particles through. The other two elements, 5 and 9, did not. The vendor tested two more filter elements to obtain a replacement unit for element 7.

The fourth filter element, number 6, was received from Pall and tested in the same manner as the above three elements. There was no indication of epoxy present on the element. Bubbling first appeared in the Solox when the pressure in the element reached 12.1 inches of water. The results of the particle test agreed very closely with filters 5 and 9.

From all test evidence, we now had three good filter elements which would remove 98 percent of the 3.5-micron particles and 13 microns absolute. This is also the rating claimed by Pall for gas; their new catalog will show this rating.

Pressure-drop considerations for the existing open-cycle tests and for future closed-cycle refrigerator tests prompted a pressure-drop evaluation.

Pressure-drop test data were reduced. These data represented single filter pressure drops plus cooling coils of 1/4- and 3/8-inch diameter. The catalog data for the filter (A. P. M. ACL-31902-65A) was also compared. Pressure-drop tests were then conducted on the filter alone. The results are shown in Figure 4.3.3-1.

Results of the three tests and the catalog information are shown in Table 4.3.3-1 for a common flow factor. The pressure drops with the coils are rather high compared with pressure drops when the filters are tested alone. The actual measured filter pressure drop is 16.7 times the catalog rating.

Table 4.3.3-1

COMPARISON OF PRESSURE-DROP TESTS
(Flow Factor of 1.0)

Pressure-drop Test	Dimensionless Pressure Drop
Filter plus 1/4-inch cooling coil	0.116
Filter plus 3/8-inch cooling coil	0.023
Filter alone	0.002
Catalog rating	0.00012

An additional analysis was carried out to compare the actual measured pressure-drop results with future pressure-drop requirements for complete closed-cycle refrigeration systems. A criteria for refrigeration system pressure drop can be based on the cryogenic exchanger design. The exchangers should cause a 1-percent, at the most, a 2-percent pressure drop. A larger pressure drop would substantially help reduce the exchanger sizes, but the overall system performance would suffer. Hence, any accessory-like filters or system plumbing should have pressure drops even below those of the exchangers. If cycle performance can be sacrificed, the greatest size and weight savings can be made in the exchangers.

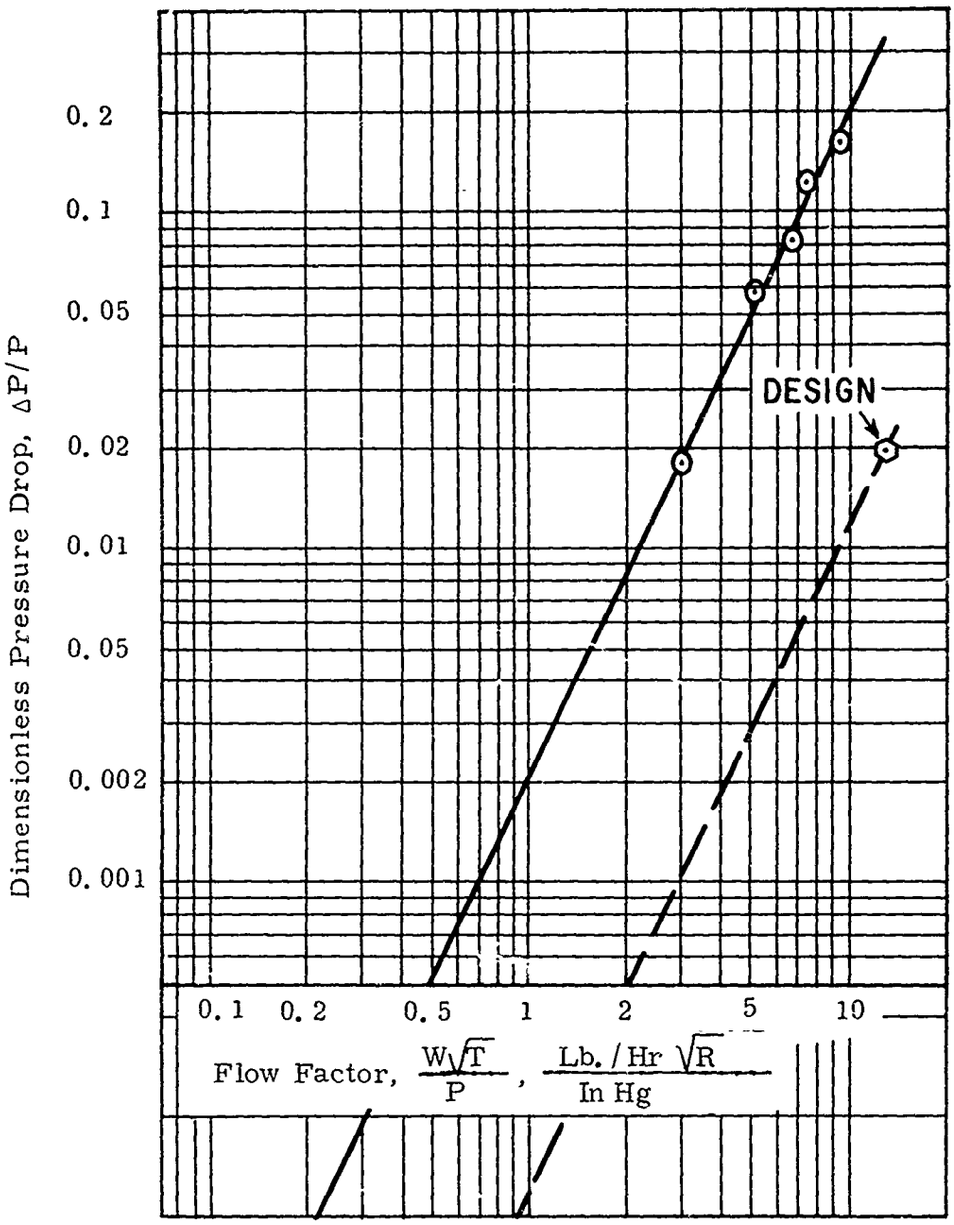

Figure 4.3.3-1. Filter Pressure Drop Test Results

'rom the filter pressure drop tests, the actual pressure drops using the subect filters are shown in Table 4. 3. 3-2. The first set of values is for operaion at the design temperature. Two filters appear adequate for the 80°K ystem, and one each at the three locations appear adequate in the 4. 4°K ystem.

Before design temperature conditions are reached, the gas volume flow is reater than at the design temperature Thus, the pressure drop is correspondingly greater. Calculations at room temperature operating conditions are hown at the bottom of Table 4. 3. 3-2. Hence, more filters in parallel are esirable, especially for the 80°K system for a rapid refrigerator cooldown.

. 3. 4 Alternate Filters

)uring the course of the problems with the wire mesh filters, alternate filters /ere investigated. A fiberglass material used for thermal insulation was recommended for cryogenic temperature service but was found unsuitable. Then . nuclepore membrane filter was investigated and designed, but not fabricated ecause the wire mesh filter problems discussed previously were corrected. \ description of these investigations follows.

. 3. 4. 1 Fiberglass Filter. An as alternate approach to solving the filter roblem, a fiberglass filter element was examined. The basis for selecting his was the fact that it is currently being used with helium gas at temperaures down to approximately 15°K, and the filter is claimed to be capable of topping particles 3 microns or larger.

The filter material is Johns-Manville Microlite* blanket-type thermal and coustical insulation made of fine glass fibers bonded with a thermosetting esin. Available densities are 0. 6, 0. 75, 1. 0, 1. 5, and 2. 0 pounds per ubic foot.

Tests were initiated to evaluate this material as a possible replacement for he wire mesh filter units. Filter capability, pressure drop, and lack of filter contamination particle generation at room and cryogenic temperatures were examined.

A filter assembly using a sample of Microlite 1 inch thick with a density of 0. 75 pound per cubic foot was made as shown in Figure 4. 3. 4. 1-1. All parts were cleaned except for the Microlite. The perforated screen and Microlite were sealed to the inside diameter of the can with General Electric silicone RTV cement. Because there is no means of cleaning the Microlite material, it was believed that the loose dirt particles would be blown out by actually operating the Microlite as a filter with a high gas flow through the unit.

The Royco particle counter was connected to the helium gas supply, as shown in Figure 4. 3. 4. 1-2. The connection for the Royco particle counter was made

*Trademark of the Johns-Manville Corporation

Table 4.3.3-2

FILTER PRESSURE DROPS RELATIVE TO REFRIGERATOR NEEDS

Refrigerator Location (Upstream of Component)	80°K System Turboalternator	4.4°K System		
		75°K Turboalternator	12°K Turboalternator	J-T Valve
Design operating conditions*				
Temperature (°K)	80.0	75.0	12.0	5.71
Temperature (°R)	144.0	135.0	21.6	10.3
Flow (grams per second)	2.78	0.730	1.265	0.788
Flow (pounds per hour)	22.0	5.79	10.03	6.25
Pressure (atmosphere)	2.90	2.87	2.85	2.85
Pressure (psia)	42.6	42.1	41.9	41.9
Flow factor	3.045	0.782	0.547	0.234
Number of filters in parallel	1 2	1	1	1
Dimensionless pressure drop	0.018 0.0045	0.00120	0.00060	0.00011
Pressure drop (psi)	0.767 0.192	0.0505	0.0252	0.0046
Approximate room temperature operating conditions**				
Temperature (°R)	560.0	560.0	560.0	560.0
Flow factor	6.00	1.595	2.79	1.743
Number of filters in parallel	1 2 3	1	1	1
Dimensionless pressure drop	0.072 0.018 0.008	0.005	0.015	0.0062
Pressure drop (psi)	3.06 0.767 0.350	0.210	0.629	0.0260

*From 24 March 1969 Progess Report: "High-speed Motor-driven Helium Compressor"
**Based only on the absolute temperature change from design conditions at cryogenic temperatures

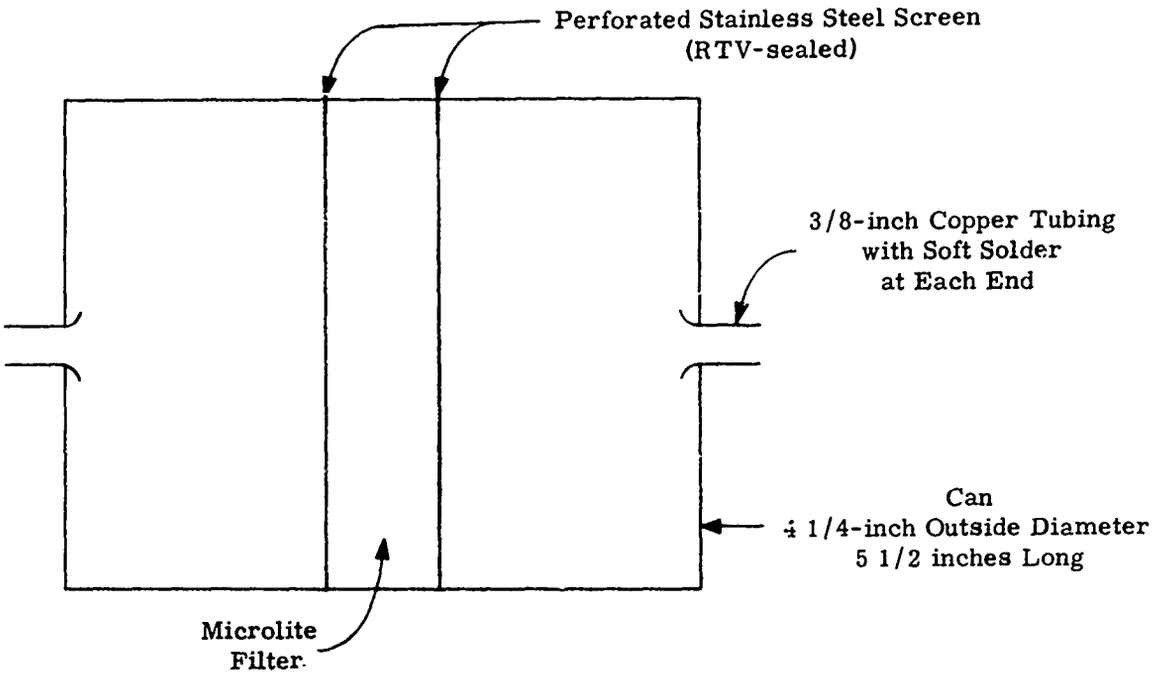

Figure 4. 3. 4. 1-1. Microlite Filter Assembly

to direct as many particles as possible toward the low partial flow going to the counter, because at the high flow rates required to operate the turboalternator at liquid-nitrogen temperatures, the counter would be sampling only a small percentage of the total gas flow. The gas flow through the system was measured on a Fischer and Porter flowmeter, FP-1/2-17G-10, GSVT-40, the same as that used in the turboalternator helium gas system.

The helium gas system and the line shown in Figure 4. 3. 4. 1-2 were purged for 1/2 hour before testing the gas with the Royco counter. Six particles were counted on the 2. 5-micron and larger range during a 10-minute period. After this test, the helium gas line was tapped several times with no increase in the particle count measured.

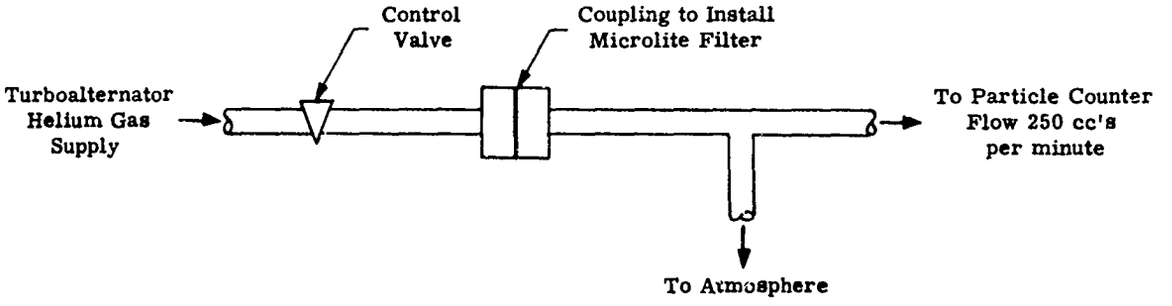

Figure 4. 3. 4. 1-2. Microlite Filter Gas Test Assembly

Then, the coupling in the gas line (Figure 4. 3. 4. 1-2) was opened, the Microlite filter was installed, and the helium gas flow was adjusted to approximately 6 percent on the flow tube. At this low helium flow, only two particles were measured on the 2. 5-micron and larger range for a 1-hour period. However, tapping the filter unit slightly increased the particle count to a reading of 60 particles. The Royco particle counter range was changed to 8. 0 microns and larger. No particles were measured until the filter was tapped; then the count went up to 124 particles.

The gas flow through the filter was increased to 70 percent and the filter was tapped several times until it appeared that no further particles were coming out of the filter at this flow. The helium flow rate was decreased to approximately 6 percent and cycled up to 30, 40, 50, and 60 percent several times. At each flow rate, the Royco particle counter would measure 7 to 35 particles on the 8. 0-micron and larger range every time the filter was tapped.

The above tests show that the Microlite filter either contains many particles or that the fiberglass breaks apart at the high flow rates when the filter is tapped.

Therefore, it was concluded that Microlite cannot be successfully used as a filter element for the turboalternator or refrigerator system tests. Further, it was concluded that any filter material that is subject to producing contaminants by routine handling cannot be used.

4. 3. 4. 2 Nuclepore Membrane Filter. As a backup to the wire mesh filters, Nuclepore membrane filter material was investigated to establish an alternate means of satisfying the requirements.

The General Electric Company's Nuclepore membrane filter provides an advanced medium for microfiltration. This unique porous material is a transparent polycarbonate plastic film penetrated with uniform cylindrical holes.

The holes produce a sieve-like filtering action, ideal for large-volume filter applications. This filter material allows filtration passes quickly and eliminates clogging experienced with cross-hatched filters.

The special holes in a Nuclepore filter result from a nuclear track registration and chemical etching process. First, a tape of the material is exposed to charged particles in a General Electric nuclear reactor. These fission fragments drill linear damage tracks in the plastic Nuclepore membrane. A chemical solution is then used to bath etch the tracks into uniform pores. Hole sizes of 0. 8, 0. 5, 1. 0, 2. 0, 5. 0, and 8. 0 microns are available.

Two membrane sizes of interest are 5. 0 and 8. 0. Characteristics of the two sizes are:

Pore Size (Microns)	Pores Per Square (Centimeter)	Thickness (Microns)	Tensile Strength (Psi)
5.0	400,000	11	15,000
8.0	100,000	11	20,000

The membrane pressure drop characteristic is shown in Figure 4.3.4.2-1 for helium gas, based on measured data for air. In order to check whether pressure drop results could be predicted, a calculation was made using the known physical dimensions of the 5-micron-hole Nuclepore filter. Conventional friction-factor correlations for fully developed flow through circular channels were used. For the single case calculated, the predicted and actual pressure drops were within 10 percent. It is surprising that the results were as close as this, considering the extremely small diameters and short lengths. It was not determined whether predictions based upon this method would be accurate throughout the entire range of hole diameters available.

A preliminary design for a filter with a Nuclepore membrane element was established and a preliminary drawing made, Figure 4.3.4.2-2.

From the above table of wire mesh filter tests, the greatest flow factor for testing turboalternators in the 80°K refrigeration system is 6.0. For the pressure drop ratio of 0.01, a 27.25-square-inch filter element would be required. This is the approximate size of the conical element shown in Figure 4.3.4.2-2. However, a backup plate with holes or a wire mesh screen should be used to support the thin membrane. At the same time, a more compact filter element design should be considered. A 45-percent open aluminum sheet with holes of 0.038-inch diameter may be a suitable material.

In order to use this membrane material in a filtering system, a reliable means of bonding and sealing had to be established. A tentative design plan was to try solvent cementing of the membrane material to itself and to a Lexan* ring.

Several small samples were made up, cementing the membrane to itself and onto 1/16-inch-thick Lexan. Trichloroethene was used as the solvent. With a small brush, a thin coating of the solvent was put onto both surfaces to be cemented together. The surfaces were pressed together and allowed to cure for 30 minutes at 90°C.

The samples of the membrane cemented to the Lexan were excellent. The samples of the membrane cemented to itself seemed to produce excellent bonds; however, the samples curled considerably during curing. This problem could be solved by clamping the cemented sections during the curing period.

---

*Trademark of the General Electric Company

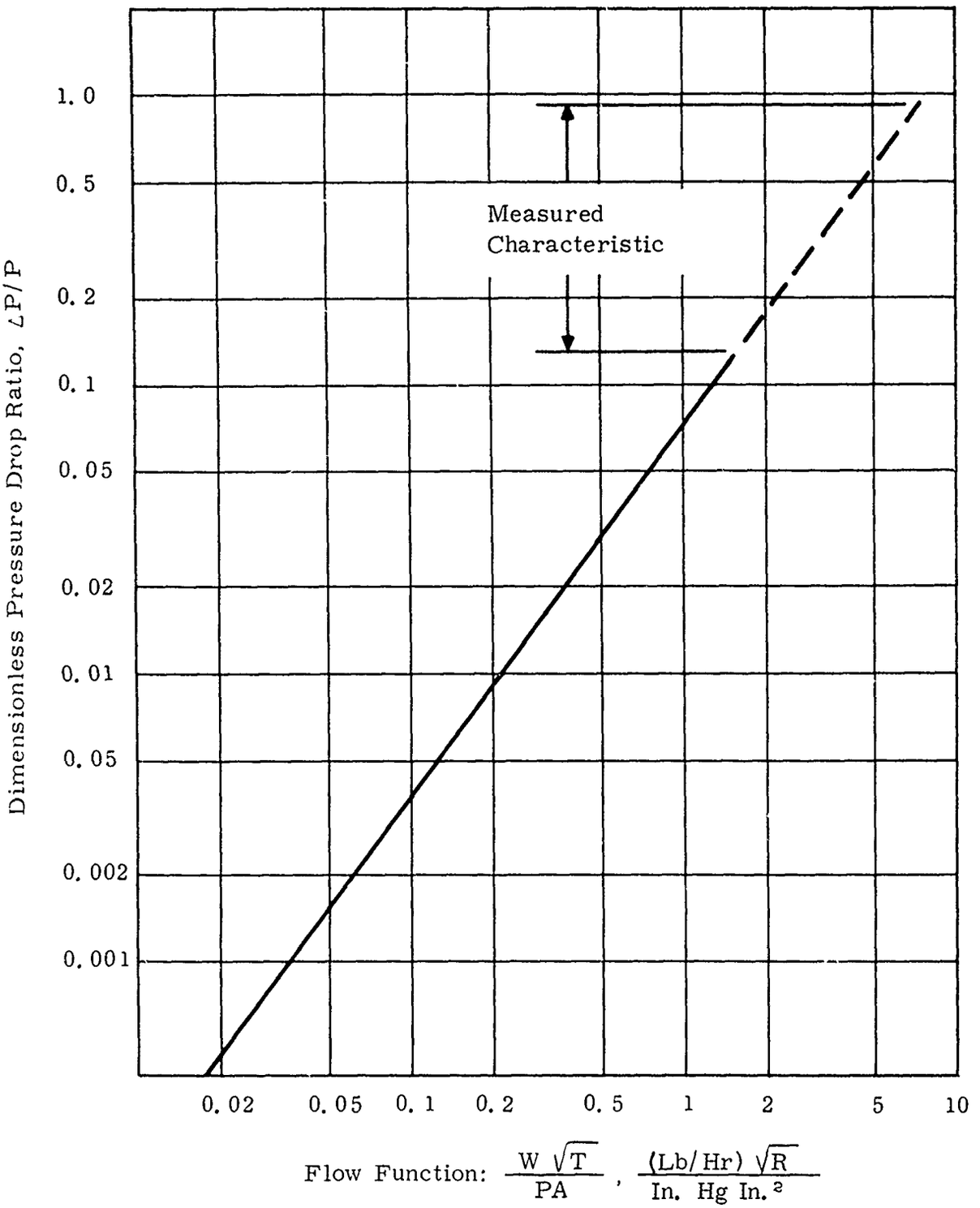

Figure 4. 3. 4. 2-1. Nuclepore Membrane Filter, Preliminary Design

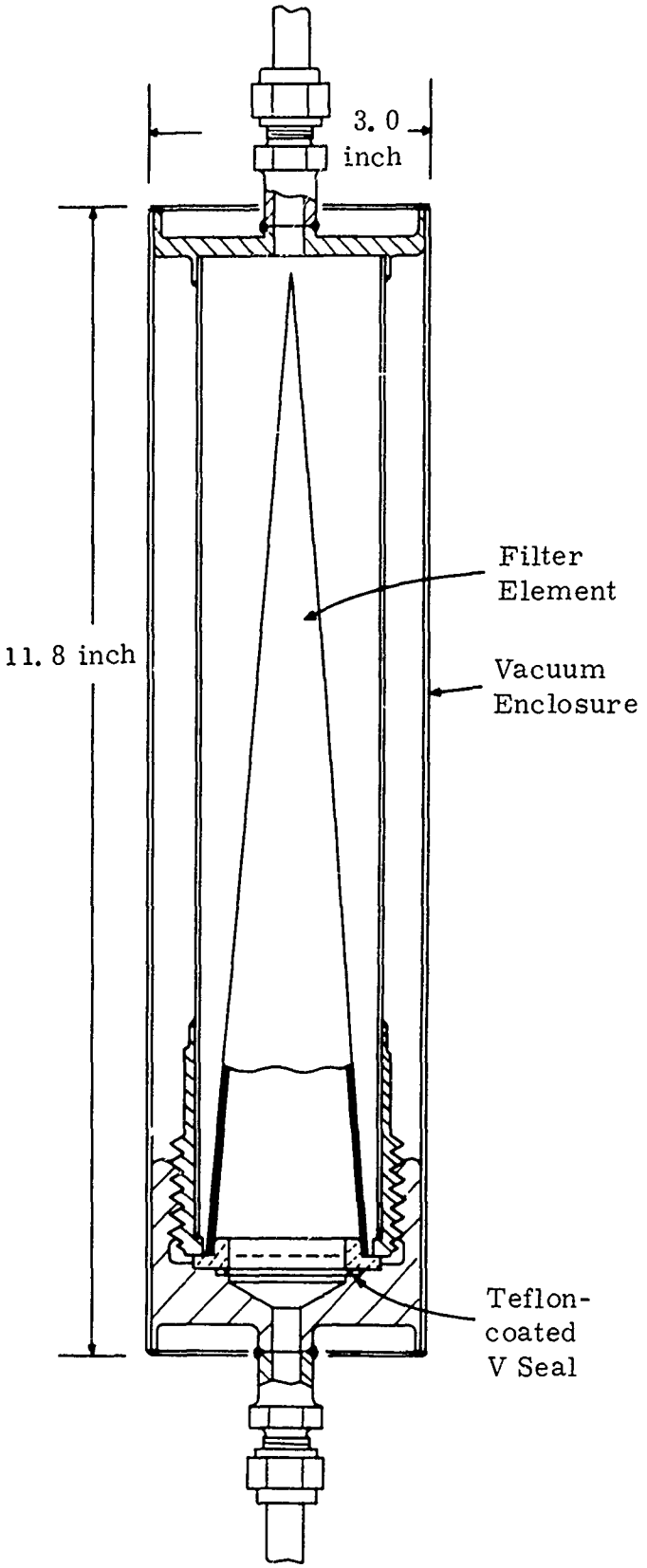

Figure 4.3.4.2-2. Nuclepore Membrane Filter Pressure Drop Characteristic (Five-micron Hole Size, Helium Gas)

The cemented samples were also cycled between room temperature and liquid-nitrogen temperature several times. There were no indications of the cemented joints being affected. The membrane material remained flexible at liquid-nitrogen temperature.

Eventually, for a 4.4°K refrigerator, flows of the required three filters were less, and smaller filters would be adequate. On the basis of the pressure drop characteristic shown in Figure 4.3.4.2-1, and requirements shown in Table 4.3.3-2, for a pressure drop ratio of 0.01, Nuclepore membrane filter elements of 10.22 square inches with five-micron hole size would be a typical solution.

No further attention was given the Nuclepore membrane filter design because the apparent progress with the wire mesh filters satisfied the immediate requirements.

43,704—Ft Belvoir